Multimodal magnetic nanostructures

A thesis submitted to the University of Dublin in application for
the degree of Doctor of Philosophy

Renata Tekoriute

School of Chemistry
University of Dublin
Trinity College
November 2009
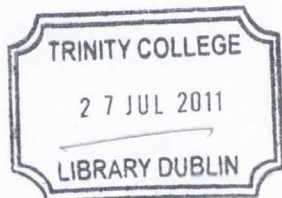
Declaration

This thesis is submitted by the undersigned to the University of Dublin, Trinity College for the examination of Doctorate of Philosophy. Except as otherwise indicated, the author carried out the work described here in alone and has not submitted as an exercise for a degree to any other university.

The author agrees that the Library may lend or copy the thesis upon request. This permission covers only single copies made for study purposes, subject to normal conditions of acknowledgement.
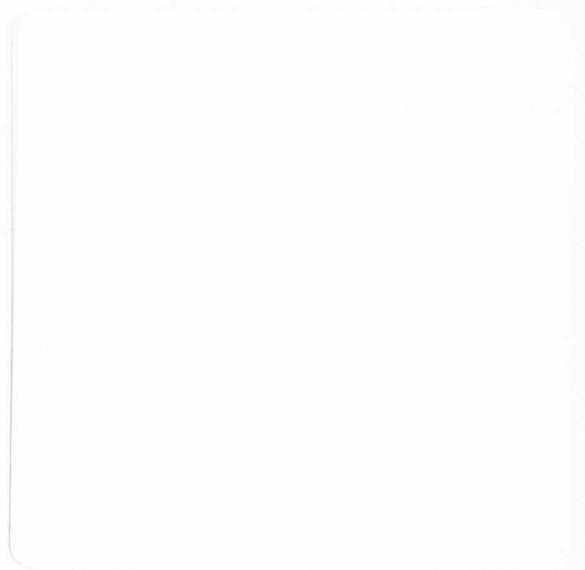
List of symbols and abbreviations

A – Absorbance

Å – Angstrom

Ar – Argon gas

AO - Acridine orange

Au - Gold

Ag – Silver

AMF – Alternating magnetic field

AC -Alternating current

c - Concentration

cm – Centimeter

cm^{-1} – Wavenumbers

CB - Conductive band

CM - Confocal microscopy

°C – Degrees Celsius

φ$_f$ - Quantum yield or fluorescence efficiency

d - Distance between planes

DDS - Drug delivery system

DNA - Deoxyribonucleic acid

ssDNA - single stranded Deoxyribonucleic acid

dsDNA – double stranded Deoxyribonucleic acid

e$^-$ -Electron

eV - Electron volt

E – Energy

ε- Extinction coefficient

ε - Dielectric constant

fcc - Face centred cubic structure

FTIR - Fourier Transform Infrared spectroscopy

FLIM - Fluorescent Lifetime Imaging

FRET - Förster resonance energy transfer

g – Grams

GI - Gastrointestinal tract

H – Magnetic field

HOMO - Highest occupied molecular orbital

HDD - Hard disk drive

Hc - Coercivity

h$^+$ - Photon

JCPDS - Joint Committee on Powder Diffraction Standards

K - Kelvin

kOe – KiloOersteds

kHz – Kilohertz

kg - Kilograms

l – Length of the cuvette

L - Distance between electrodes

LbL – Layer-by-Layer deposition

LUMO - Lowest unoccupied molecular orbital

λ - Wavelength

λ$_{ex}$ - Excitation wavelength

λ$_{ex}$ – Emission wavelength

m – Meter

mg – Milligram

μm – Micrometer

μL - Microliter

mL – Millilitres

mmoL – Milimoles

mT - Millitesla

mV – Millivolts

M – Molar concentration

M – Magnetisation

MW – Molecular weight

MS - Mössbauer spectroscopy

Me – Metal

M$_R$ - Remnant magnetisation

Ms - Saturation magnetisation

MRI - Magnetic Resonance Imaging

MI - Magnetoimpedance

MPa - Mega Pascales

MHz- Megahertz

n - Number of planes

n/a – Not applicable

nm – Nanometer

NPs **-** Nanoparticles

NMRD – Nuclear Magnetic Resonance Dispersion

η - Viscosity of the solution

pH – Acidity or basicity of the solution

PE - Polyelectrolytes

PAH - Poly(allylamine hydrochloride)

PSSS - 4 (poly(sodium 4 styrenesulfonate)

PMI - 2,6-diisopropylphenyl)-perylene-3,4-dicarbonacidimide

PVA - Polyvinyl alcohol

PCS - Photon Correlation Spectroscopy

PL – Photoluminescence spectroscopy

PDI - Poly-dispersion index

Θ **-** Reflected angle

QDs - Quantum dots

r_1 - Relaxivity

RES - Reticuloendothelial system

RNA - Ribonucleic acid

RS - Raman spectroscopy

RhB - Rhodamine B

s – Seconds

SEM – Scanning Electron Microscopy

SPIO - Superparamagnetic iron oxide

SQUID - Superconducting quantum interference device magnetometer

T – Tesla

T_1 – Spin lattice relaxation time

$T_{1(diam)}$ - Relaxation time of the supporting fluid

T_2 – Relaxation time

T_C - Curie temperature

TGA - Thermogravimetric analysis

TGA* - Thioglycolic acid

TEM - Transmission electron microscopy

TOTO - Thiazole orange

UV-vis - Ultraviolet-visible spectrophotometry

USPIO - Ultrasmall superparamagnetic iron oxide

υ - Speed of the particle

V – Voltage

VB - Valence band

W - Watt

XRD - X-ray powder diffraction

YOYO - Oxazole yellow

ζ – Zeta potential

Acknowledgments

Summary

The objectives of this thesis are to develop new iron oxide and cobalt ferrite ($CoFe_2O_4$) based nanocomposites and their fluorescent-magnetic derivatives with a range of potential biomedical applications. The major aims are: (i) to prepare magnetic iron oxide based nanoparticles and nanocomposites by co-precipitation techniques using Deoxyribonucleic acid (DNA) and various polyelectrolytes as stabilisers; (ii) produce new stable magnetic fluids based on functionalised iron oxide nanoparticles for Magnetic resonance imaging (MRI) and other potential biomedical applications; (iii) to develop new "two-in-one" fluorescent/magnetic nanocomposites using magnetic nanoparticles and fluorescent dyes or Quantum dots (QDs) for intracellular visualisation, manipulation and diagnostics; (iv) to characterise the nanoparticles, nanocomposites, and magnetic fluids fully using different instrumental techniques (e.g. Transmission electron microscopy (TEM), Scanning Electron Microscopy (SEM), Fourier Transform Infrared spectroscopy (FTIR), Raman, Ultraviolet-visible spectrophotometry (UV-vis), photoluminescence spectroscopy (PL), X-ray powder diffraction (XRD), Photon Correlation Spectroscopy (PCS), Thermogravimetric analysis (TGA), Nuclear Magnetic Resonance Dispersion (NMRD), magnetisation measurements (SQUID).

Chapter 1 gives a brief overview of the main principles of nanotechnology and provides an introduction to magnetic nanoparticles and fluorescent nanocomposites. This also includes a description of new fluorescent-magnetic bimodal nanomaterials, which combine magnetic and luminescence species in a single nanostructure. These new nanomaterials show great potential in biomedicine, exhibiting new properties and could be used as a sensitive contrast agents for two very powerful and highly complementary imaging techniques such as fluorescence imaging and MRI.

Chapter 2 gives detail with the synthesis and various experimental procedures, techniques that were used to characterise the prepared materials. These techniques include FTIR and Raman spectroscopy, XRD patterns, magnetisation measurements, NMRD techniques and Electron Microscopy and some others (see above).

Chapter 3 describes the preparation and investigation of cobalt ferrite

polyelectrolyte ((Poly(allylamine (PAH)) nanocomposites. The composites have been prepared by modified co-precipitation technique. Careful examination using Electron microscopy (TEM), FTIR, Raman spectroscopy, XRD, SQUID were performed to optimise the synthesis condition for the preparation of room temperature superparamagnetic cobalt ferrite nanoparticles.

The second part of this chapter deals with the preparation and investigation of cobalt ferrite nanocomposites with DNA. Similar to PAH stabilised cobalt ferrite nanoparticles, the morphology, crystalline and magnetic properties of cobalt ferrite-DNA nanoparticles were examined by variety of techniques in order to compare and determine the optimum synthesis conditions for superparamagnetic cobalt ferrite-DNA nanoparticles. The effect of an external magnetic field on the fabrication of chain-like nanostructures from the cobalt ferrite-DNA nanoparticles was also investigated.

The preparation of other type of iron oxide - magnetite (Fe_3O_4) is described in **Chapter 4**. The poly(sodium styrene sulfonate) (PSSS) stabilised Fe_3O_4 nanoparticles were prepared by an aqueous co-precipitation technique in different synthesis conditions. The morphology, physical and magnetic properties of the nanoparticles, colloidal stability of the magnetic fluids were investigated by described techniques including electron microscopy (SEM TEM), PCS and Zeta potential, NMRD studies. It is expected that these optimised synthesis conditions can be used for the preparation of new magnetite based magnetic fluids as a potential candidates for MRI.

The second part of **Chapter 4** discusses modified synthesis approach for the fabrication of bimodal magnetic luminescent nanomaterials based on magnetite (Fe_3O_4) nanoparticles and colloidal TGA* (thioglycolic acid) capped Cadmium Telluride (CdTe) QDs. The morphology and optical properties of Fe_3O_4-PSSS_PAH/PE$_{10}$-QDs were investigated by variety of techniques.

Chapters 5 deals with the development of new synthetic methods for the fabrication of bimodal magnetic luminescent nanocomposites based on superparamagnetic oxides Fe_3O_4 and $CoFe_2O_4$ and Rhodamine B (RhB) dye. This chapter presents new approaches for the production of fluorescent-magnetic nanocomposites, which consist of RhB coated polyelectrolyte stabilised magnetic nanoparticles. Fe_3O_4-PSSS and $CoFe_2O_4$-PSSS nanoparticles were used as templates. These new nanomaterials

have been studied using TEM, FTIR, Raman spectroscopy, XRD, SQUID, PCS and Zeta potential studies, NMRD, confocal (CM) and light microscopy were performed to investigate the properties of magnetic luminescent nanocomposites. The effect of time on the optical properties of new magnetic luminescent nanocomposites was also examined. One of the most interesting developments was the utilisation of Fe_3O_4-PSSS_PAH/PE$_{10}$-RhB nanocomposites as quite effective cell labelling agents. It is expected that this approach can be used to develop a new generation of bimodal magnetic luminescent nanostructures with a broad range of potential applications.

Chapter 6 describes the production and investigation of new magnetite-DNA based luminescent magnetic nanocomposites. Intercalation studies of Acridine Orange (AO) into double stranded DNA (dsDNA) and single stranded (ssDNA) stabilised Fe_3O_4 nanoparticles were carried out in order to prepare the new magnetic-luminescent nanostructures. The morphology and optical properties of nanocomposites have been investigated by a variety of techniques.

Chapter 7 provides the conclusions of this work and also an outlook of future studies to be carried out to develop new magnetic nanostructures.

Finally **Chapter 8** contains appendices.

Table of Contents

Chapter 1

Chapter 2

6. Chapter 6

Chapter 7

Chapter 8

Chapter 1

"Nanotechnology has given us the tools... to play with the ultimate toy box of nature - atoms and molecules. Everything is made from it... The possibilities to create new things appear limitless. Imagine superconductivity without the need for temperatures of minus 400 degrees, or films that allow materials to change behaviour depending on the environment, or the ability to store all of mankind's written knowledge on a device the size of a pinhead, or miniature implants that replace nerve functions in the body, or molecular sized computers that are more powerful than any we have ever known. All of this has implications for our lives and can make them better...

Horst Stormer.

1. Introduction

1.1. Brief introduction to nanoparticles

The term "nanotechnology" is used to describe materials with a size less then 100 nm. A nanometre, 10^{-9} m, is about ten times larger then the size of the smallest atoms, such as hydrogen and carbon [1]. A human hair is approximately 80,000 nm wide, and a red blood cell approximately 7000 nm wide. **Fig. 1.1** shows the nanometre in context.
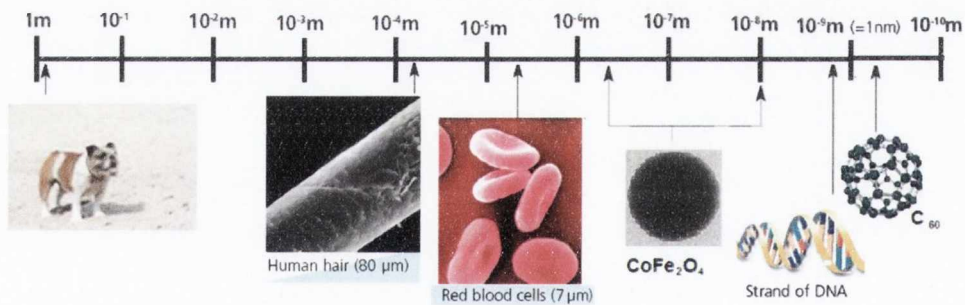
Figure 1.1. Length scale showing the nanometre in context. The length scale at the top ranges from 1 m to 10^{-10} m, and illustrates the size of a dog compared to a carbon 60 (C60) molecule, also known as a buckyball. For comparison the world is approximately one hundred million times larger than a dog, which is in turn one hundred million times larger than a buckyball. The length scale of interest for nanoscience and nanotechnologies is from 100 nm down to the atomic scale - approximately 0.2 nm [2].

Small nanometre-sized crystals of a substance are called nanocrystals or nanoparticles. Nanospheres, nanorods, nanocups, nanodiscs, nanorods, nanocubes, and nanowires are just a few of the shapes that have been produced [1-3]. Metal,

dielectric and semiconductor nanoparticles have been formed, as well as various hybrid structures (e.g., core-shell nanoparticles) [4, 5].

This project is focused on the investigation of new magnetic nano sized materials for potential applications in biotechnology and information technology.

1.2. Magnetism and magnetic materials

It is well known that electrons in materials rotate around the atom's nucleus. This rotation (spin) produces a small magnetic moment. In bulk materials electron spin is arranged in regions called domains.

Depending on the spin orientation mmaterials can be classified by their response to an applied external magnetic field as diamagnetic (opposes magnetic fields), paramagnetic (magnetised in the direction of and proportional to the applied field) or ferromagnetic (the largest effect which may be magnetised by orders of magnitude greater than the applied field).

In a diamagnetic material the atoms have no net magnetic moment when there is no applied field. Under the influence of an applied field (H) the spinning electrons (spins) process and this motion, which is a type of electric current, produces a magnetisation (M) [6] in the opposite direction to that of the applied field. All materials have a diamagnetic effect; however, it is often the case that the diamagnetic effect is masked by the larger paramagnetic or ferromagnetic term. The value of susceptibility is dependent on temperature.

Paramagnetic materials have permanent magnetic moments, which are randomly oriented in the absence of an external magnetic field. When an external magnetic field is applied the magnetic moments are aligned in the same direction as the applied field.

Below a certain characteristic temperature (the Néel or Curie temperature), paramagnetic materials may undergo a transition to a magnetically ordered state and become ferromagnetic, antiferromagnetic, or ferrimagnetic (**Table 1.1**). Those substances have a domain structure.

Ferromagnetic behaviour is exhibited by materials containing unpaired electrons as a result of interactions between neighbouring spins at least partially aligned by a magnetic field.

In antiferromagnetic materials, spins are aligned in opposite directions and the magnitudes of their magnetizations are equal. It results in a close to zero net magnetic moment even in the presence of an external magnetic field.

Ferrimagnetic materials also possess opposed spin alignment, but the magnitude of magnetic moments pointing in one direction differs from those pointing in the opposite direction. This creates a considerable net magnetic moment but is still lower than that for ferromagnetic material [6].

When a ferromagnetic material is magnetised by an increasing applied field and then the field is decreased, the magnetisation does not follow the initial magnetisation curve obtained during the increase. The irreversibility is called hysteresis. Hysteresis is related to the existence of magnetic domains in the material. At large fields, the magnetisation approaches the maximum value, called the saturation magnetisation (M_S). A ferromagnetic material has a residual magnetisation at zero external fields, called the remnant magnetisation ("memory" of the previous state of magnetisation) (M_R). Therefore ferromagnetic materials are not fully demagnetised due to the partial domain reorientation, which is called coercivity (H_C). H_C characterises the reverse-field strength needed to reduce the magnetisation to zero. **Fig. 1.2** shows M_S, M_R, and H_C on a hysteresis loop [1]. The shape of the hysteresis loop is determined by the particle size. If particles are large (1 μm) a narrow hysteresis is seen, while for smaller ones (of the order of 10 nm) there is no hysteresis observed due to a phenomenon called superparamagnetism.
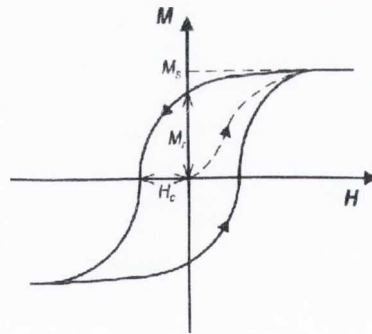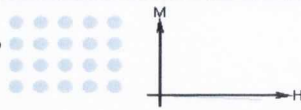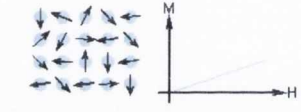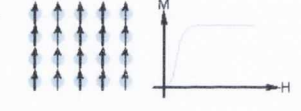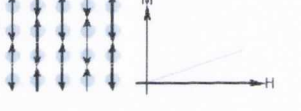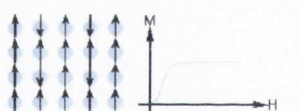
Figure 1.2. Schematic presentation of the hysteresis loop.

Superparamagnetism is an effect occurring when the particles constituting the material are so small (nanoparticles) that the thermal energy can destroy magnetisation at a temperature below the Curie temperature [7]. The Curie temperature (T_C) is the temperature above which the thermal energy of the material is sufficient to overcome the magnetic alignment of the spins. The resulting fluctuations in the direction of magnetization cause the magnetic field to average to zero. The material

thus adopts a paramagnetic behaviour. This parameter affects ferromagnets. A summary of different types of magnetic behaviour is presented in **Table 1.1**.

Table 1.1. Summary of different types of magnetic behaviour [6].

Type of Magnetism	Susceptibility	Atomic / Magnetic Behaviour		Example / Susceptibility	
Diamagnetism	Small & negative	Atoms have no magnetic moment		Au Cu	-2.74×10^{-6} - 0.77×10^{-6}
Paramagnetism	Small & positive	Atoms have randomly oriented magnetic moments		β-Sn Pt Mn	0.19×10^{-6} 21.04×10^{-6} 66.10×10^{-6}
Ferromagnetism	Large & positive, function of applied field, microstructure dependent	Atoms have parallel aligned magnetic moments		Fe	~100,000
Antiferromagnetism	Small & positive	Atoms have mixed parallel and anti-parallel aligned magnetic moments		Cr	3.6×10^{-6}
Ferrimagnetism	Large & positive, function of applied field, microstructure dependent	Atoms have anti-parallel aligned magnetic moments		Ba ferrite	~3

1.3. Magnetic fluids

Magnetic fluids are normally dispersions of stable magnetic nanoparticles with special magnetic properties. The magnetic moments are fully randomised without an external magnetic field and are not magnetised. The magnetic moments of small particles have the ability to rotate along the gradient of the applied field and have the ability to increase the overall magnetic strength. Superparamagnetic fluids possess magnetic moments that totally randomize once the field is removed (**Fig. 1.3**). These materials usually exhibit high magnetic susceptibility, and they do not show magnetic hysteresis.

4

Magnetic field

| fluid without an external magnetic field | fluid under an external magnetic field (H) | fluid after removal an external magnetic field |
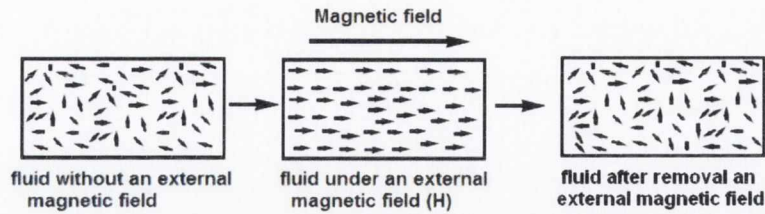
Figure 1.3. Scheme of superparamagnetic fluid without and under an external magnetic field.

A typical ferrofluid contains 5 % ferromagnetic nanoparticles, 10 % surfactant, and 85 % carrier fluid by volume [7]. The stability of the magnetic fluids depends on particle size and other factors. Very frequently small particles tend to form agglomerates to reduce the energy associated with the high surface area/volume ratio of the nanosized particles. As a result, it is important to develop coating strategies to chemically improve the stability of the magnetic nanoparticles in solution.

The synthesis of superparamagnetic nanoparticles is a complex process because of their colloidal nature. The possibility exists to prepare monodisperse inorganic nanoparticles of pure materials in the sub-20 nm size regime, associated with the capping of these particles by (typically) functionalised higher-molecular weight material (organic molecules) [8]. Then if high-molecular-weight polymer is added to a colloidal dispersion, it might possibly attach to the particle surface and increase colloidal stability of magnetic nanoparticles due to polymer's long flexible molecules [9].

There are two basic steps for the preparation of a ferrofluid: synthesis of the magnetic solid, for example magnetite (Fe_3O_4), followed by suspension with the aid of various surfactants as stabilizers. [10] However, stabilised magnetite nanoparticles in organic media can have only very limited applications in the biomedical field.

Preparation of stable water based magnetic fluids is of renewed interest especially to biomedical applications [11]. Therefore there are various methods for preparation of water-dispersible magnetite [12]. Some of these methods will be discussed later in this chapter.

1.4. Iron oxides

Magnetite (Fe_3O_4) and maghemite (γ-Fe_2O_3) are two different forms of iron oxide. They are usually synthesised as thin films or nanoparticles (or nanorods) and used in many technological fields [10]. The model of crystal structure is described in a

5

Fig. 1.4. Ordered systems of magnetite nanocrystals are also widely found in nature, including biological organisms [13]

Iron oxide nanoparticles of Fe_3O_4 and γ-Fe_2O_3 are commonly employed for various biomedical applications [14]. Magnetite nanoparticles have been found to be physiologically well tolerated as they show very small measurable toxicity [15, 16].

Figure 1.4. Structural formula of magnetite (Fe_3O_4), where iron exists as Fe^{2+}, which preferentially occupies the octahedral site and Fe^{3+}, which shows no preference and occupies both the tetrahedral and octahedral sites.

1.5. Cobalt ferrite

Cobalt ferrite ($CoFe_2O_4$) is considered as a potential candidate for high-density recording due to its unique magnetic properties such as strong anisotropy and hence high coercivity at room temperature and moderate saturation magnetisation, along with good mechanical hardness and chemical stability [17]. Cobalt ferrite nanoparticles crystallise in the cubic crystal system. The structure is described in **Fig. 1.5**. Cobalt atoms create a face centred cubic (*fcc*) structure subdivided in eight equal units. These units are alternately occupied by two other cubic structures. The first one is a tetrahedral cubic structure containing one cobalt ion for four oxygen ions. The second one is an octahedral structure that contains four iron ions for four oxygen ions. These two structures are included in the cobalt *fcc* with a special way: each structure cannot share a common face with another one of the same type [18].

6
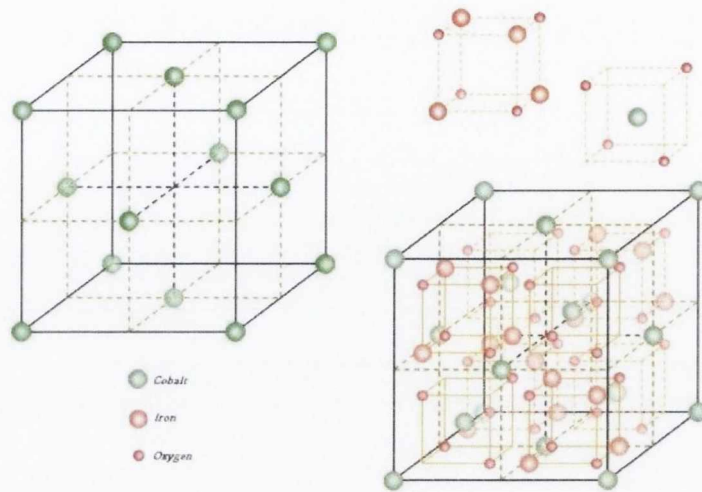
Figure 1.5. Models of the cobalt iron oxide ($CoFe_2O_4$) inverse spinel structure [18].

1.6. Preparation and coating (stabilisation) of magnetic iron oxide based nanoparticles

In the past decade a lot of study has been done on development of the methods for the preparation and coating of magnetite nanoparticles to control stability of these particles and avoid their agglomeration or precipitation. There are various chemical approaches aimed at synthesizing magnetic nanoparticles for a wide range of applications. Traditional synthetic methods for the fabrication of magnetic nanomaterials include co-precipitation, hydrothermal and high-temperature processing, sol-gel processing, microemulsion methods, flow injection syntheses, sonolysis and elecrospray synthesis amongst others [19]. However, we will focus on synthetic methods, which have been adapted to prepare magnetic nanoparticles for biomedical applications.

The co-precipitation technique is the most commonly used method and preferred synthetic approach to prepare magnetite nanoparticles for medical applications. [20]. The preparation of magnetite nanoparticles by co-precipitation involves the simultaneous precipitation of iron (II) and iron (III) salts in deoxygenated water by the addition of ammonia [21] or sodium hydroxide [22] solution. Although the co-precipitation method enables the variation of the average size of nanoparticles being produced by adjusting the pH, the ionic strength and the temperature of aqueous media, it has only limited control over the size distribution of the particles [23]. Traditionally magnetite nanoparticles prepared via aqueous co-precipitation are

7

cheaper, safer, easer to prepare and manipulate than other methods. Another advantage of the co-precipitation process is that a large amount of nanoparticles can be synthesized. However, the control of particle size distribution can be limited, because only kinetic factors are controlling the growth of the crystal.

Coating of a magnetic nanoparticle usually has an influence on the magnetic properties. Magnetic nanoparticles can be coated during (*in situ*) or after the synthesis. The selection of coating frequently depends on the final application of the particles. Three main types of coatings are used to stabilize nanoparticles in aqueous solutions; these are monomeric organic stabilisers, polymeric stabilizers and inorganic coatings [24]. Organic surfactants are frequently employed for stabilisation and coating of magnetic nanoparticles. The addition of chelating organic anions (carboxylate or R hydroxy carboxylate ions, such as citric, gluconic, or oleic acid) during the formation of magnetite can help to control the size of the nanoparticles. This coating provides further stability of the magnetic fluids in water [23]. The surfactant acts as a stabiliser, which passivates the surface of the nanoparticles during the synthesis procedure and prevents agglomeration and clustering [25-31]. Usually electrostatic interaction or steric stabilisation takes place to disperse nanoparticles and keep them in a stable colloidal suspension. Both electrostatic and steric stabilisation factors are necessary to obtain stable suspensions of magnetic nanoparticles. An illustration of stabilisation of magnetic nanoparticles by electrostatic and steric repulsion is presented in **Fig. 1.6**.
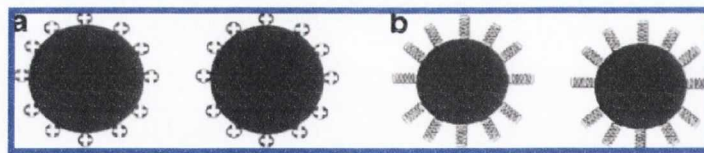
Figure 1.6. a) Particles stabilised by the electrostatic layer. b) Particles stabilised by steric repulsion [20].

The stability of a colloidal suspension (ferrofluids) is a crucial requirement for the application of magnetic nanoparticles. For example, smaller particles can circulate in the blood for longer periods of time, which allows for imaging of different tissue types [23]. Polymer coated magnetic nanoparticles can be prepared using various strategies. A well-known and fairly simple method is coating or encapsulating nanoparticles with preformed polymers [32]. Due to their good solubility in water and biocompatibility, polysaccharides such as dextran or carboxydextran are among the

8

most popular polymer coatings used for stabilisation of magnetic nanoparticles. Other suitable polymers for coating include starch, poly(pyrrole), poly(aniline), poly(alkylcyanoacrylates), poly(methylidene malonate), and polyesters, such as poly(lactic acid), poly(glycolic acid), poly(e-caprolactone), and their copolymers [33-37] or surface complexing agents (carboxydextran).

Inorganic coatings for magnetic nanoparticles include silica, carbon, precious metals (such as gold and silver) or metal oxides [24]. Following coating and stabilisation, magnetic nanoparticles can be utilised for various applications. However, further functionalisation, and targeted vectorisation, of the particles is normally necessary to improve performance for biomedical and in particularly for specific cellular and molecular imaging applications.

1.7. Deoxyribonucleic acid (DNA)

Deoxyribonucleic acid (DNA) is the biomolecule inside the nucleus of cells that carries genetic information. 25 years ago nucleic-acid-nanotechnology pioneer Ned Seeman of New York University began envisioning another realm of applications for them - as construction blocks, perhaps even in machines [38].

By partially unzipping a double-stranded DNA molecule, its branches can be potentially attached to oppositely charged particles [38, 39]. Denaturation of DNA is usually achieved by heat treatment or high pH; this involves the breaking of hydrogen bonds between the bases in the duplex, which causes the double-stranded helix to dissociate into single strands. DNA thermal denaturation occurs typically at temperatures in the range of 60-80 °C. **Fig. 1.7** shows schematic preparation of single stranded DNA molecules [39].
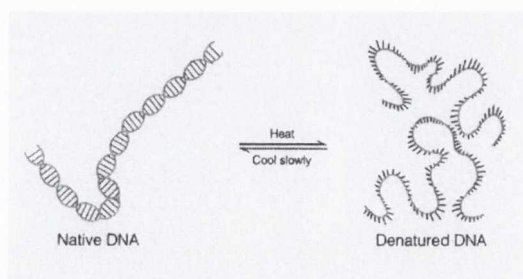
Figure 1.7. Schematic presentation of thermal denaturation of DNA.

The DNA molecule has an overall negative charge and it might be used in a process called self-assembly. When DNA is placed in a solution with magnetic

particles that have a positive charge, the particles are automatically attracted to the DNA strands, which act as tiny scaffolds for creating wires. Magnetic components are essential for computer memory, therefore these results demonstrate a potential for future applications of DNA-based structures in computers, sensors and other uses [38, 39].

1.8. Applications of magnetic nanoparticles

1.8.1. Drug delivery

One of the major disadvantages of chemotherapies is that they are often non-specific. When the therapeutic drugs are administrated intravenously in the patient, they lead to a general distribution, which attacks the targeted tumour cells as well as the normal and healthy ones. Therefore, traditional cancer treatment methods have significant side effects. Magnetic nanoparticles have been envisaged as drug carriers to target specific sites (generally cancerous tumours) within the body. The primary objective is to reduce the amount of systemic distribution of the cytotoxic drug in order to reduce the associated and damaging side effects. The second one is to reduce the dosage of drug required by increasing their efficiency by the targeting of drugs [40-43].

The carrying of the drug to the targeted region of the body is based on magnetic properties of nanoparticles. They can be coated with a biomolecule; resulting in a biocompatible magnetic carrier on which is attached a cytotoxic drug. These drug/carrier complexes - usually in the form of a biocompatible ferrofluid are injected into the patient via the circulatory system.

Particles are concentrated to a specific target site within the body by means of a gradient of external magnetic fields. The drug is then released either via enzymatic activity or changes in physiological conditions and taken up by the cancer cells.

Iron based nanoparticles can be used as delivery vehicles for drugs or radiation without damaging nearby healthy tissue by guiding the particles up the bloodstream to a tumour with magnets [40, 43]. Iron oxide nanoparticles covered by starch derivatives with phosphate groups, which bound mitoxantrone, have been used as chemotherapy. [44]

1.8.2. Hyperthermia treatment

Ferrofluids are not only a very powerful material for diagnosis using MRI, but they can be used also for therapeutic purposes. Cancer can be treated by artificially induced hyperthermia. The procedure consists of dispersing magnetic nanoparticles (*e.g. iron oxides*) to the targeted region of the body then heating them by applying an alternating current (AC) magnetic field. Tumour cells are more sensitive to a temperature increase than healthy ones. This implies the destruction of the cancer if the temperature can be maintained up to 42 °C for at least 30 minutes. However, this method is not sufficient in eliminating all cancerous cells and usually coupled with other techniques such as irradiation or chemotherapy. Ordinary hyperthermia is not well developed because of unacceptable heating of healthy tissue. Hyperthermia treatment using magnetic particles offers a way to damage only targeted tissue. However, only first clinical trials have been started recently [45-47].

For these purposes, researches are focused on finding appropriate materials from which enough heat would be generated with external AC magnetic fields of strength and frequency low enough to avoid damaging physiological responses. Ferrofluids and superparamagnetic particles are more likely to achieve this function [40, 43]. **Fig. 1.8** presents schematic illustration of the therapeutic strategy using magnetic particles.
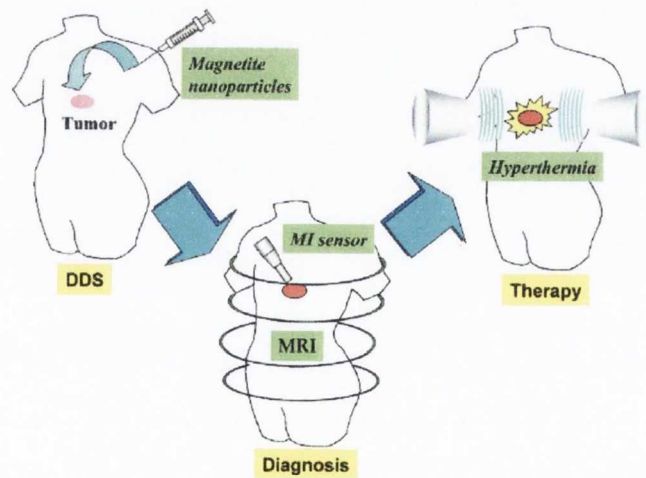
Figure 1.8. Schematic illustration of the therapeutic strategy using magnetic particles. Functionalised magnetic nanoparticles accumulate in the tumour tissues via the drug delivery system (DDS). Magnetic nanoparticles can be used as a tool for cancer diagnosis by magnetic resonance imaging (MRI) or for magnetoimpedance (MI) sensor. Hyperthermia can then be induced by an alternating magnetic field (AMF) exposure [47].

11

Superparamagnetic colloids can be seen as a very promising agent for hyperthermia therapy, but this new field of application requires an improvement of the reproducibility and the size control during the synthesis of particles.

1.8.3. Magnetic resonance imaging (MRI) contrast agents

Magnetic resonance imaging (MRI) is an imaging technique, which was introduced in the 1970's by Lauterbur [48]. This technique is based on the principles of nuclear magnetic resonance (NMR), which allows identification of the relaxation of a particular nucleus, as the strength of the field is proportional to the radio frequency used. The idea of using this technique in medical diagnostics was to produce images of different organs and tissues the inside of the human body due to nuclear magnetic relaxation times (**T**). Images of healthy tissues and diseased tissues or tumors are different [49, 50]. In the 1980's, medical MRI scans commenced and since then MRI has become an essential tool which is becoming more widespread in forming diagnoses in medicine (clinical oncology) [51, 52].

Specifically, the use of ferromagnetic and superparamagnetic nanoparticles as contrast agents can induce a more than ten-fold increase in proton relaxivities [53]. In the presence of a paramagnetic or superparamagnetic material, the relaxation properties, named spin-lattice or longitudinal relaxation time (T_1), the spin-spin or transverse relaxation time (T_2) and T_2* ($1/T_2$* = $1/T_2$ + $1/T_2$', with T_2' being a time constant arising from magnetic field inhomogeneity), of proton nuclear spins are shortened to some extent. Superparamagnetic iron oxides (SPIO) affect the T_2 relaxation time more significantly than T_1, whereas gadolinium chelates predominantly affect T_1. This shortening of T_2 results in a darkening of the image where the SPIO's are located, referred to as negative contrast [23].

Contrast agents are used to highlight different tissues in the body or to help distinguish between healthy and diseased tissue. Tumour cells do not have the effective reticuloendothelial system of healthy cells, so the contrast agent does not alter their relaxation times. Transverse relaxation results in signal loss (negative contrast) in T_2-weighted images.

SPIO nanoparticles are the most commonly used T_2 contrast agents in clinics [52, 53]. SPIO act by altering the magnetic resonance relaxation times of the water in the tissues surrounding the agent, and hence cause an increase (or decrease) in the intensity of the water signal in these tissues. SPIO can differ in their core size, coating

thickness, and coating material, all of which affect where the SPIO's end up *in vivo*. The uptake of nanoparticles by the tissue depends on their size. Large particles (300 nm to 3.5 μm) coated with an insoluble layer are used to image the gastrointestinal (GI) tract [54]. Particles ranging in size from 60-150 nm are quickly sequestered by the body's reticuloendothelial system (RES), rapidly appearing in the liver and spleen. Even smaller particles under clinical investigation (referred to as ultra small superparamagnetic iron oxide (USPIO's)) are typically 10-40 nm; these particles circulate in the blood stream for much longer than larger particles, can cross capillary walls, and are often taken up extensively by lymph nodes and bone marrow [23]. Some particles have been approved for clinical application or are being clinically tested (**Table 1.2**) [19].

Table 1.2. Characteristics of USPIO and SPIO agents: Commercial or under Clinical Investigation [19]

Name	Company	Applications	Relaxometric properties x 1.5 $T mM^{-1}s^{-1}$	Coating agent	Hydrodynamic size (nm)
Ferumoxides AMI-25 Endorem/Feridex	Guerbet, Advanced Magnets	liver imaging, cellular labelling	r_1=10.1 r_2=120	Dextran T10	120-180
Ferumoxtran-10 AMI-227 BMS-180549 Sinerem/Combidex	Guerbet, Advanced Magnets	metastatic lymph, node imaging macrophage imaging blood pool agent cellular labelling	r_1=9.9 r_2=65	Dextran T10, T1	15-30
Ferumoxytol Code 7228	Advanced Magnets	macrophage imaging blood pool agent cellular labelling	r_1=15 r_2=89	Carboxylmethyl-dextran	30
Ferumoxil AMI-121 Luiren/Gastromark	Guerbet, Advanced Magnets	oral GI imaging	n/a	silicone	300
Ferucarbotran SHU-555A	Schering	liver imaging cellular labelling	r_1=9.7 r_2=189	carboxydextran	60
Resovist SHU-555C Supravist	Schering	blood pool agent cellular labelling	r_1=10.7 r_2=38	carboxydextran	21
Feruglose NC100150	GE-Healthcare (abandoned)	blood pool agent	n/a	pegylated starch	20
Clariscan Ferristene Abdoscan	GE-Healthcare	oral GI imaging	n/a	sulphonated styrene-divinylbenzene copolymer	3500
VSOP-C184	Ferropharm	blood pool agent cellular labelling	r_1=14 r_2=33.4	citrate	7

Bulte, *et al.* studied the bio distribution of stem cells [55] after implantation by non-invasive monitoring of their migration and trafficking to determine the success of cell-transplantation therapy over six weeks [56] (see **Fig. 1.9**).
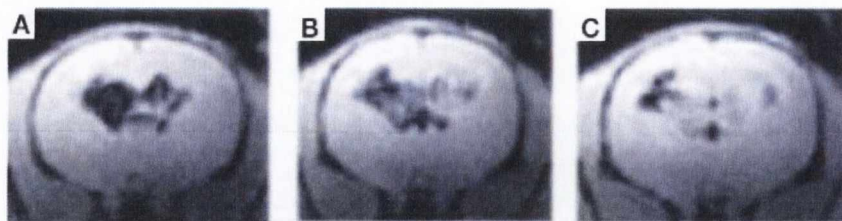
Figure 1.9. Sequential *in vivo* MRI images, obtained at a field strength of 4.7 T, of a rat brain after transplantation of oligodendroglial progenitor cells containing SPIO (dark areas, because of the negative contrast of the transplanted cells). These images were obtained six weeks after stem cell transplantation.

SPIO can be utilised in three distinctive neurological, which includes tracking transplanted cells (e.g. stem cells), identifying transcription efficiencies, and detecting amyloid beta peptides in diseased brains [57].

Recently it has been shown that new magnetic fluids based on iron oxide nanowires can be used as commercial MRI agents. Thus our water stable colloidal solutions based on magnetic nanowires could potentially serve as excellent contrast agents for MRI [58].

1.8.4. Magnetic recording devices

Magnetic storage is extremely important for every modern information processing system. The hard disk drive (HDD) that stores a large amount of information for computers and networks is a crucial device for modern information technology. Data storage in modern HDDs is based on films of cobalt alloys, which are made up of 15-20 nm magnetic grains, whose magnetic orientation can be guided by a recording head positioned above the film. A bit of information may then be stored as a common orientation of hundreds of these grains [59]. One of the main goals in this area is to achieve the control of the orientation of smaller and smaller magnetic particles in disk drives in order to increase their data storage capacity. One of the successful high-density storage technologies involves the utilisation of 4 nm FePt magnetic nanoparticles coated with oleic acid and oleylamine stabilisers [60]. These particles were annealed at 560 °C for 30 minutes and formed a smooth ferromagnetic film. Recording studies carried out showed that the particles could support stable magnetisation reversal transitions (bits) at room temperature allowing a very high-density magnetic recording.

1.8.5. Catalysis applications

Magnetite nanoparticles with core–shell structure have also been used for the development of a new type of catalyst. The shell consists of the catalytically active species, and the magnetic core can act as anchor to separate and recycle the catalyst. Magnetically separable mesoporous carbons constructed from mesocellular carbon and Fe/Fe_3O_4 core–shell ferromagnetic ferromagnetic nanoparticles (30 nm in size) show good electron conductivity, large pore size, and large pore volume [61].

Other work of group of S. Connon and co-workers synthesised heterogeneous catalyst highly active and recyclable, which could be used as a promoter of six different reactions at loadings between 1 and 10 % and could be recovered and recycled over 30 times without any discernible loss of activity [62]. Nanoparticle-supported chiral DMAP analogue showed highly active excellent recyclability [63].

1.9. Fluorescent materials and luminescence

Fluorescent materials emit light as a result of absorption of incident light of a shorter wavelength [64]. For better understanding of the nature of the fluorescent materials a brief summarised description of different types of luminescence is presented below:

• **Luminescence** is the general term to describe the processes leading to the emission of light. This production of light is most commonly associated with a process involving heat or electric current, but there are some cases in which this emission is not associated with thermal or electrical energy. Different types of luminescence are distinguished by the addition of a prefix to denote the type of energy involved, like bioluminescence, chemiluminescence or radio-luminescence.

• **Photoluminescence** is a luminescence, which is generated by illuminating a compound with UV-Vis radiation (200-800 nm) [64-66]. After the material absorbs light it is causing the process called photo-excitation. When this happened electrons are moved to the permissible excited states. After these electrons return to their equilibrium states, the excess energy is released and may lead to the emission of light (a radiative process) or may not (a non-radiative process).

• **Fluorescence** is a type of photoluminescence which is distinguished from others by the fact that the excited molecule or nanostructure relaxes to its ground state immediately after excitation, the time spent in the excited state being typically of the

order of 10^{-8} s and is called the fluorescence lifetime. It varies over several orders of magnitude, depending on the sample [64-66].

In the past, organic pigments were commonly used in the production of fluorescent coloured materials. These pigments typically absorbed invisible ultraviolet (UV) light (wavelengths less than 400 nm) and re-emitted light somewhere in the visible spectrum (400-700 nm). These organic fluorescent dyes tend to quickly degrade with continuous exposure to natural sunlight [3].

In many cases the general chemical structure of the dyes and pigments are similar. The dyes, unlike pigments, do dissolve in the medium in which they are incorporated. During dissolving process dyes lose their crystal structure. The pigments (fine solid particles) are typically insoluble in the liquid (water, oil). The dispersed particles (vehicles) in suspension could selectively scatter, reflect, absorb or transmit certain wavelengths of light. This physical process is different from fluorescence, phosphorescence, and other forms of luminescence, were material emits light.

Schematic illustrations of the electronic states of the semiconducting material and possible transitions between them going from the bulk to the nanoscale are presented in **Fig. 1.10**. The photon absorption excites the fluorescent molecule, which enters a high-energy state. This state is not favourable to be in for long periods of time. After a certain time the exciton will fall down as the charge carriers recombine with each other, losing their energy as a photon. As well as this though, both the electron and the hole can combine with various traps in the semiconductor. These traps are defects, interstitial atoms, impurities and dislocations in the crystal and the resulting recombinations can be either radiative or non-radiative processes, as shown in **Fig. 1.10.**

1: hυ induced excitation (E > E_g)   **2:Exciton recombination: luminescence**

3: Deep trap (defect) emission   **4: Radiationless transition**

5: Surface state emission

Where: **h⁺** - photon, **e⁻** -electron, **VB** - valence band, **CB** - conductive band, **E** – energy, **HOMO** - highest occupied molecular orbital, **LUMO** - lowest unoccupied molecular orbital.
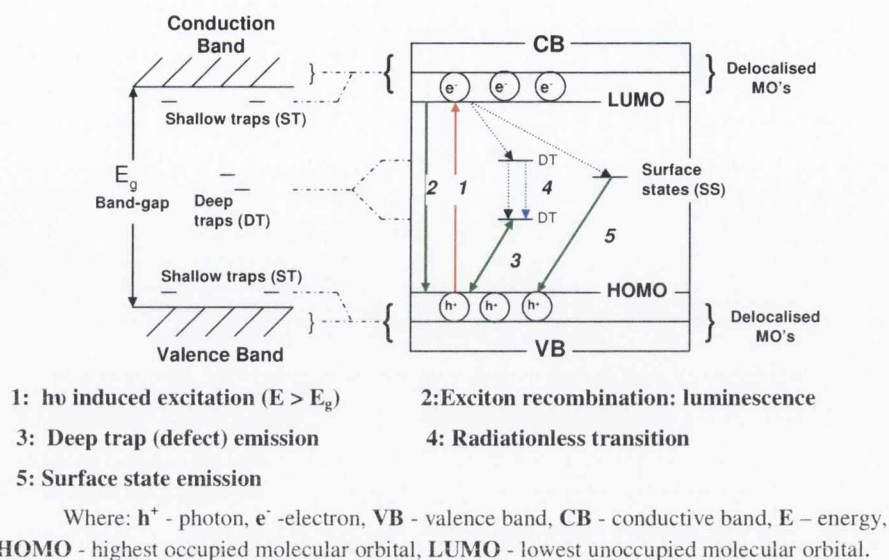
Figure 1.10. Schematic representation of the band gap (E_g) structure of a semiconducting material and the change in that structure on going from the bulk to the nanoscale. The absorption and leading emission pathways upon excitation by a photon are also shown. Adapted from the literature [64-66].

Therefore over the last decade a lot of investigation was done on light emitting quantum dots (QDs) or semiconductor nanocrystal II-VI group materials (e.g. CdTe, CdSe, PbSe, ZnS, others) [3, 66]. These fluorescent colloidal nanoparticles (QDs) showed outstanding photophysical properties. Fluorescent colloidal QDs (selenides and tellurides of cadmium, lead, mercury and zinc, II-VI semiconductors) can absorb light in the broad range of wavelength depending on their size [67]. Quantum confinement (QC) is a process, which appears in small sized (2-10 nm) semiconductor crystals due to their size similarity to Bohr radius (QDs typically exist as a small sphere). When QC takes place, more energy than normal is required to force the electrons out of the ground state, so when the electrons return to ground state, the photons they release have more energy (shorter wavelength than normal). There is a simple linear relationship between crystal size and colour: the smaller the size, the shorter the wavelength of emission.

There are a multitude of potential applications for these light emitting nanoparticles including uses in optoelectronic, biochemical and electronics applications [66].

1.9.1. Stokes Shift and Stokes fluorescence

Examination of the Jablonski diagram (**Fig. 1.10**) reveals that the energy of the emission is usually smaller than of the absorption. Fluorescence occurs at the lower energies of the longer wavelengths, when a system (molecule or atom) absorbs a photon; it increases energy and enters an excited state. One way for the system to relax is to emit a photon, thus losing its energy (another method would be the loss of heat energy). When the emitted photon has less energy than the absorbed photon, this energy difference is the Stokes shift (**Fig. 1.11**). If the emitted photon has more energy, the energy difference is called an anti-Stokes shift [65].
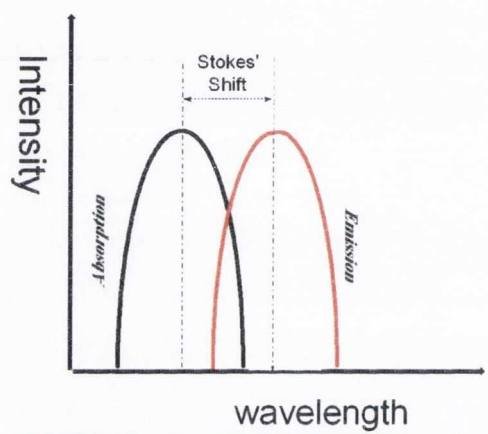
Figure 1.11. Stokes shift is the difference, in wavelength unit, between positions of the band maxima of the absorption and emission spectra of the same electronic transition.

In fluorescence, the molecular absorption of a photon triggers the emission of another photon with a longer wavelength (lower frequency). The energy difference between the absorbed and emitted photons ends up as molecular vibrations or heat. Usually the absorbed photon is in the ultraviolet range, and the emitted light is in the visible range [66, 67].

Both absorption and radiation (emission) of energy are unique characteristics of a particular molecular structure.

1.9.2. Quantum yield

Before a molecule can emit radiation by the fluorescence process it must be able to absorb radiation, but not all absorbed radiation is emitted. Frequently, some part of absorbed radiation is lost in various non-radiative processes and only a portion

of the radiation is emitted. The quantum yield or fluorescence efficiency, φ_f, of a compound is defined as the fraction of the incident radiation, which is re-emitted as fluorescence.

$$\Phi_f = \frac{\text{no. of photons emitted}}{\text{no. of photons absorbed}} = \frac{\text{intensity of fluorescence}}{\text{intensity of absorption}}$$

Values of Φ_f fall in the range 0 to 1 and are an inherent property of a molecule determined to a large extent by its structure [66].

The maximum fluorescence Φ_f is 1.0 (100 %); every photon absorbed results in a photon emitted. A high value of near 1.0 is generally observed with molecules having large, planar conjugated systems, which are relatively rigid. More flexible molecules are more likely to have low values of Φ_f while molecules whose lowest excited state is achieved by an n$\rightarrow\pi^*$ transition or which contain heavy atoms like bromine and iodine are usually non-fluorescent.

1.9.3. Quenching

Quenching is the process leading to the decrease of fluorescence intensity of the fluorophore. The different types of quenching of the fluorescence luminescence are presented below:

• **Collisional quenching** appears due to collisions of the molecules (atoms) with other neighbours that result in the loss of excitation energy as heat instead of as emitted light. Collisional quenching is a transient excited state interaction and does not affect the absorption spectrum. This process is present in samples, which are in solution; species that are particularly efficient in inducing the process are referred to as collisional quenchers (e.g. iodide ions, molecular oxygen (O_2), nitroxide radical [66, 65]).

• **Static quenching** appears due to the interaction of the fluorophore with the quencher, to form a stable non-fluorescent complex. The non-fluorescent complex usually has a different absorption spectrum from the original fluorophore (longer wavelength). A special case of static quenching is **self-quenching**, where the fluorophore (excited atom, molecule) and quencher are the same species. Self-quenching is mainly obvious in very concentrated solutions of dyes [66, 65].

• **Förster resonance energy transfer (FRET)**. This type of quenching is similar to collisional quenching. FRET could appear between two participating molecules

(atoms) do not undergo collisional quenching (strong interaction). One molecule (donor) is excited by absorption of a photon, but instead of emitting it, the excitation is transferred by electronic coupling to the other molecule (acceptor). As a result changes in fluorescence intensity could be seen: either fluorescence at longer wavelength (compared to the spectrum of the original donor) or no fluorescence, depending on whether the acceptor is itself fluorescent or non-fluorescent. The possible quenchers of fluorescence are various paramagnetic species (including magnetic nanoparticles) [3, 65, 66].

- **Photobleaching** is a photochemical process (light exposure), which causes the destruction of a fluorophore. The destruction leads to the loss of the ability of the fluorophore to absorb light of a particular wavelength. As a result total loss of fluorescence could be observed [66].

1.9.4. Overview of some selected applications of QDs

Many applications of QDs can be found in optics including lasing media, optically addressable storage devices, light-emitting diodes, fluorescent labels and barcodes.

QDs are also useful in the biological sciences [67]. Recent studies of QDs have resulted in developing of new fluorescence probes for *in vivo* studies and biolabelling applications, cell tracing, cellular imaging, cell uptake [67], immunoassays [68].

For example, in the work of Kobayashi of *et al.*, the conjugation of carboxyl groups to QDs produced *in vivo* fluorescence images to study the individual and composite drainage patterns towards primary lymph nodes (**Fig. 1.12**). This research is the first application of *in vivo* imaging that employs five different reporter QDs.
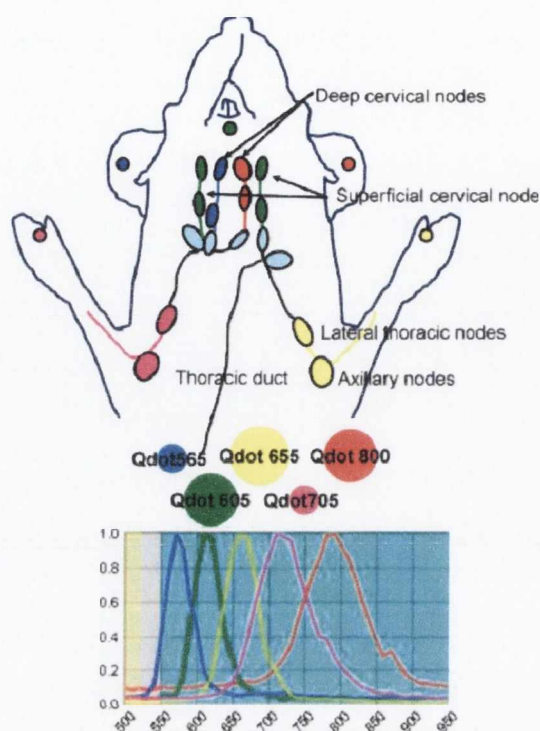
Figure 1.12. Anatomy of the lymphatic system in the upper body of the mouse and a schematic of five-colour spectral fluorescence imaging, with a graph of the emission spectra of each of the five carboxyl quantum dots used (QD 565, blue; QD 605, green; QD 655, yellow; QD 705, magenta; QD 800, red). The coloured lymph nodes are the draining lymph nodes visualised in this study [69].

1.10. Luminescent -Magnetic Nanostructures

In recent years, a lot of effort in nanoscience has been devoted to develop new nanocomposites: luminescent magnetic nanostructures in which the fluorescent modality can be originated by organic dyes or QDs [70]. It is expected that the combination of magnetic and fluorescent properties in one nanocomposite would open up great prospects both in nano- and bio- technology, enabling the engineering of unique targeted, nanoscale photonic devices, which could be manipulated using an external magnetic field. The major difficulty in the preparation of "two-in-one" magnetic fluorescent nanocomposites is the risk of quenching of the fluorophore on the surface of the particle by the magnetic core. The problem of quenching can be resolved by providing the magnetic nanoparticle with a stable shell prior to the introduction of the fluorescent molecule, or by first treating the fluorophore with an appropriate spacer.

The control of the properties of the new nanostructures are strongly related to the preparation method, the choice of the starting materials (components), especially fluorophores (QDs organic dye, silica) and magnetic nanoparticles, the type of surface coatings, the spacer molecules, and so on [71]. The different strategies of the preparation of "two-in one" magnetic-luminescent nanostructures are summarised and presented below.

1.10.1. Fabrication of Luminescent -Magnetic Nanostructures

a) Encapsulation

In this method the magnetic and the fluorescent entities are embedded together in a nano- or a micro-sized shell [72-78]. This general strategy works by filling preformed nanocapsules, which have channels of appropriate pore sizes, with the magnetic and the fluorescent nanoparticles.

As an example, 50 - 500 nm porous nanocapsules have been prepared by the reaction of hydrazined styrene with acrylamide copolymers The pores of these capsules were loaded with hydrophobic QDs (diameter 3-6 nm) and Fe_3O_4 (diameter of 5–20 nm), which were embedded in such nanocapsules by a simple mechanical stimulation (via sonication) [70]. Also, fluorescent dye molecules [namely (2,6-diisopropylphenyl)-perylene-3,4-dicarbonacidimide (PMI)] and Fe_3O_4 nanoparticles have been encapsulated together in the same types of nanocapsules [78].

b) Functionalisation of silica coated magnetic nanoparticles

Silica is another biocompatible material that has been widely exploited as "shell" component in the synthesis of magnetic luminescent nanocomposites. In this case, the hydrophobic surface of magnetic nanoparticles is primed with organosilicon compounds, which promote the formation of a silica shell around the nanoparticles.

As an example, silica-coated magnetic nanoparticles functionalised with either FITC or rhodamine dyes have been previously prepared. Capsules with sizes ranging from 30 to 70 nm have been reported [78].

The main advantage of such an approach is the high colloidal and chemical stability of the resulting nanoparticles and the possibility to tune the average distance between luminescent and magnetic domains such that no complete fluorescence quenching takes place [79-80].

c) Polymer based coating

In this approach polymeric coatings around the magnetic nanoparticles provide a barrier to prevent quenching of the luminescence due to their magnetic properties. This has been carried out by a combined method using layer-by-layer (LbL) deposition, which leads to the formation of a protective shell of polymer [77, 79]. The LbL assembly is a technique of depositing multilayers. Although its progress has increased rapidly in recent years, the research can be traced back to the pioneering work of Iler *et.al.* in 1966 [80], who reported for the first time the fabrication of multilayers by alternating deposition of positively and negatively charged colloid particles. As Iler pointed out, a similar technique could be applied not only to colloid particles, but polyvalent ions, surfactants, water-soluble polymers, and even proteins. The method has several advantages including the possibility of tuning the thickness of the polymer-coating and allowing the deposition of a monolayer of charged particles or molecules.

d) Binding a fluorescent entity via a spacer

Direct linking of a fluorescent species to a magnetic core normally requires the use of a sufficiently long molecular linker in order to bypass any possible quenching by the paramagnetic core.

In this approach a magnetic nanoparticle bearing different functional groups is linked covalently to the fluorophore (again either a colloidal QD or a fluorescent organic dye). In some cases, direct linkage between the magnetic nanoparticles and the fluorophore cannot take place; cross-linker molecules therefore mediate bond formation. As an example, hydroxyl-functionalised Fe_3O_4 nanoparticles have been linked to the -hydroxysuccinimide esters of the Cy5.5 dye (NHS-Cy5.5) by means of intermediate functionalisation with amino-PEG-silane molecules. The PEG molecules were first linked to the surface of the nanoparticles through their silanol groups and then their terminal primary amines were reacted with NHS-Cy5.5 molecules [72].

e) Direct coating with fluorescent inorganic shell

Direct coating of magnetic nanoparticles by fluorescent inorganic shells using organometallic chemistry produced high-quality nanoparticles with controlled sizes

and shapes for a wide range of materials, including several types of magnetic nanoparticles, such as iron oxide (magnetite) nanoparticles [81-83].

Examples of bifunctional magnetic-fluorescent and all-inorganic nanocrystals, in such cases organised in core/shell types, are represented by $Fe_3O_4/CdSe/ZnS$ nanocrystals [81] and Co/CdSe nanocrystals [84].

The main advantages of all synthesis procedures described above are: high colloidal and chemical stability of the resulting nanostructures and the possibility to tune the average distance between the luminescent and the magnetic cores.

However, a majority of these compounds are toxic to living systems. To reduce the toxicity and increase biocompatibility, functionalisation of the surface of QDs is necessary by post coating with a biocompatible shell, which is commonly done by various organic compounds.

1.10.2. Applications of Hybrid Luminescent -Magnetic Nanostructures

The main advantage of combining into a single nano-object both magnetic and luminescent components is clearly to develop multimodal and multipurpose tools. As was reported above most of these new types of magnetic luminescent nanostructures are based on iron oxide nanoparticles combined with various luminescent nanospecies (QDs, organic dyes). Fabrication of new generation of magnetic luminescent nanostructures based on QDs would give new unique properties which clearly make them ideal candidates in medical and biomedical applications where traditional dyes have failed [71, 72].

Fluorescence microscopy and MRI are two major imaging techniques, which have had an incredible impact upon biomedical science in recent years. These imaging techniques are complimentary to each other and could be used for parallel detection to have a clearer picture and provide a correct diagnosis. In this case, hybrid luminescent magnetic nanostructures serve as new dual function contrast agents, which can be used simultaneously in confocal fluorescent microscopy and in MRI.

We would like to highlight some potential applications of such luminescent magnetic nanostructures in biomedicine, which would include the following [70]:

• The detection and separation of different biomolecules, such as enzymes, proteins, and genes.

• Identification of tumour cell populations in tissue samples.

• Controlled delivery of drugs and/or biomolecules (including genes) at specific sites of the body. In all cases, using one single reagent can carry out fluorescent labelling of specific biomolecules/cells and their magnetic separation. The luminescent species would act as a luminescent code skilled at reaching a number of targets. Then the nanoprobe would be recovered by the application of a magnetic field.

Fig. 1.13 presents some main applications of the hybrid luminescent magnetic nanostructures.
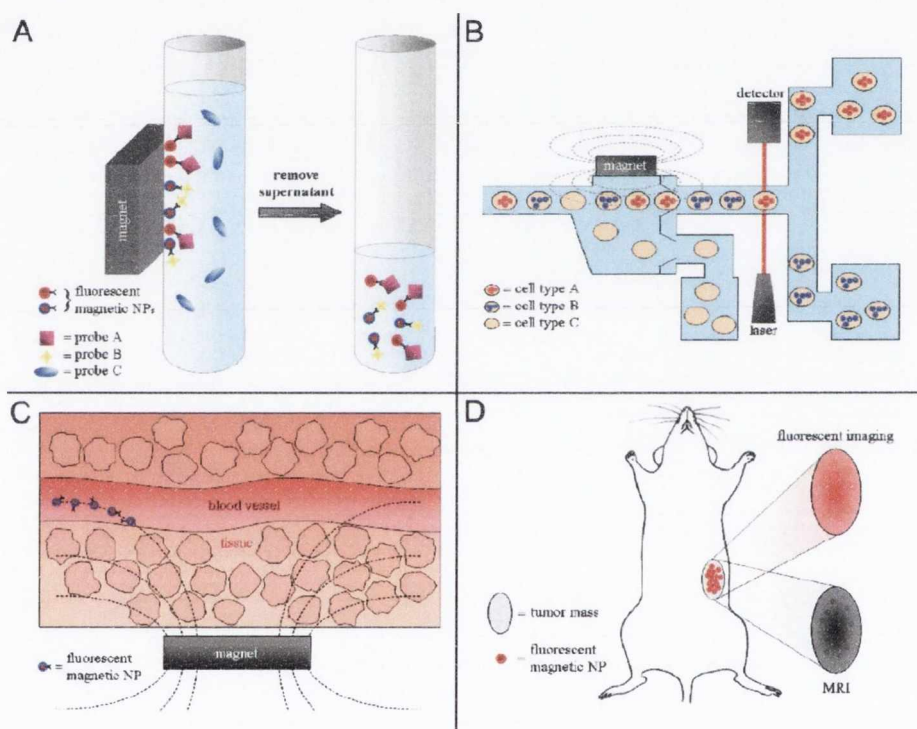
Figure 1.13. Cartoons highlighting the main applications of the hybrid luminescent magnetic nanostructures. a) Magnetic separation and luminescent detection of multiple targets and b) of different cell populations. c) *In vivo* manipulation of functionalised nanocomposites by applying an external magnetic field and optical detection of the treated area. d) Dual mode imaging system based on magnetic resonance imaging (due to the magnetic domain) and optical imaging (due to the luminescent domain [70].

Recent work has been done to investigate specific uptake of magnetic luminescent nanocomposites mediated by a large variety of receptor ligands for targeting different cell lineages. Specific ligands for tumour receptors, such as the

epidermal growth factor EGF [73], folic acid [78] and chlorotoxin [72], have been attached to the surface of nanocomposites to label and to separate different populations of tumour cells by applying a magnetic field.

Cellular uptake studies have been carried out by comparing cell populations that have a receptor for the ligand carried by the nanocomposites with cell populations that lacked such receptor [82, 83]. So far, two main aspects have been reported on this type of multimodal applications, one dealing with brain tumour studies [84] and the other one with imaging of sentinel lymph nodes in rats [83]. The group of Weissleder injected Cy5.5-arginyl-iron oxide nanocomposites, named as Cy5.5-arginyl-CLIO, under the skin of a mouse to visualize the lymph nodes by dual modality. The MRI images showed that the composites accumulate in the axillary and brachial nodes, which were visible as a small region of lower intensity [85, 86].

In another study, nanocomposites based on FeCo/graphitic shell were injected in a rabbit. The nanocomposites acted as good contrast agent at lower dosages than more standard contrast agents [87].

However, all these potential *in vivo* and *in vitro* applications for magnetic luminescent nanostructures also showed some limitations such as:

• Photobleaching (i.e., the loss of fluorescence upon continuous laser excitation), which makes them unsuitable for long-term imaging and tracking studies.

• Size of the nanostructures (i.e. should be big enough to avoid fast renal elimination and to guarantee long blood circulation life. At the same time, it should be small enough to elude the recognition processes operated by the phagocytes. The optimal sizes for intravenous injection range from 10 to 100 nm.

• Cytotoxicity it is critical to know whether these cytotoxic substances can leak out of the QDs particles over time, upon illumination or oxidation [88].

While iron oxide nanoparticles and some traditional dye molecules are now under clinical trial investigations, fluorophore probes based on QDs are far from being not toxic to living systems [70, 88] it is clear that *in vivo* studies on humans will never be carried out with such materials.

Thus great efforts have to be undertaken to understand the interactions of nanoparticles and live cells and to optimize conditions for the molecular interaction of particle-conjugated receptors or ligands *in vivo*. There is also a great challenge in finding new synthetic methods to produce bimodal magnetic luminescent hybrid

26

nanomaterials, which would be not only biologically active and non-toxic, but will also produce strongly luminescent signals.

1.11. Aims of this work

The main aim of this project is to develop new iron oxide and cobalt ferrite based nanocomposites and their fluorescent-magnetic derivatives with a range of potential biomedical applications. The major scientific and technical objectives of this work are to:

- Prepare magnetic iron oxide based nanoparticles and nanocomposites by co-precipitation techniques using DNA and various polyelectrolytes as stabilisers.

- Produce new stable magnetic fluids based on functionalised iron oxide nanoparticles for MRI and other potential biomedical applications.

- Develop new "two-in-one" fluorescent/magnetic nanocomposites using magnetic nanoparticles and fluorescent dyes or QDs for intracellular visualisation, manipulation and diagnostics.

- Carry out full characterisation on the nanoparticles, nanocomposites, and magnetic fluids using different instrumental techniques; including Transmission Electron Microscopy (TEM), Scanning Electron Microscopy (SEM), Fourier Transform Infrared (FTIR), Raman spectroscopy, Ultraviolet-visible spectrophotometry (UV-vis), Photoluminescence (PL) and Mössbauer spectroscopy, X-ray Powder Diffraction (XRD), Photon Correlation Spectroscopy (PCS), Thermogravimetric analysis (TGA), Nuclear Magnetic Resonance Dispersion (NMRD), and magnetisation measurements (SQUID).

Thanks to their controllable size, biocompatibility, and magnetic properties, these nanoparticles and nanocomposites present attractive applications in many fields of biotechnology and medicine. These materials are expected to provide new diagnostic tools for cell labelling and both the optical and magnetic detection of these cells. Magnetic fluorescent nanocomposites might also potentially serve as agents for "two-in-one" hyperthermia and photodynamic therapy.

Overall, the successful realisation of this project should result in development of new magnetic nanomaterials with a broad range of potential applications.

1.12. References:

1. E.L. Wolf., Nanophysics and Nanotechnology, (2005). 1-7, 10-12, 17-20, 25-40.

2. The Royal Society & The Royal Academy of Engineering. Nanoscience and nanotechnologies. Chapter 2. (2004). http://www.nanotec.org.uk/finalReport.htm.

3. G. Schmid., Nanoparticles. From Theory to Application., Wiley-VCH Verlag GmbH, (2004), 1-10, 12-17.

4. O. Pana, C.M. Teodorescu, O. Chauvet, C. Payen, D. Macovei, R. Turcu, M.L. Soran, N. Aldea, L. Barbu., *Surface Science.*, 601, (2007), 4352–4357.

5. W. Lu, B. Wang, J. Zeng, X. Wang, S. Zhang, and J.G. Hou., *Langmuir.*, 21, (2005), 3684-3687.

6. http://www.aacg.bham.ac.uk/magnetic_materials/type.htm, 13.12.2007.

7. V.E. Fertman., Magnetic Fluids Guidebook: Properties and Applications., Hemisphere Publishing Corporation. New York, (1990).

8. M. Shinkai., *Journal of Bioscience and Bioengineering.*, 94, 6, (2002), 606-613.

9. D. Myers. Surfaces., Interfaces, and Colloids. Principles and Application., Second Edition. (2002), 218, 223-225. 237-239.

10. L.A. Harris, J.D. Goff, A.Y. Carmichael, J.S. Riffle, J.J. Harburn, T.G. Pierre, and M. Saunders., *Chemistry of Materials.*, 15, 6, (2003), 1367–1377.

11. T. Neuberger, B. Schopf, H. Hofmann, M. Hofmann, B. von Rechenberg., *Journal of Magnetism and Magnetic Materials.*, 293, (2005), 483–496.

12. Y. Zhai, F. Liu, Q. Zhang, G. Gao., *Colloids and Surfaces A: Physicochemical and Engineering Aspects.*, 332, (2009), 98–102.

13. M. Hanzlik, C. Heunemann, E. Holtkamp-Rotzler, M. Winklhofer, N. Peterson and G. Fliessner., *Biometals*, 13, (2000), 325.

14. R.T.M. Cornell, U. Schewertmann., The Iron Oxides. Structure, Properties, Reactions, Occurrence and Uses. Wiley-VCH Verlag GmbH (2003), 7-9, 26-31, 58, 112-117, 128, 304, 340.

15. C.C. Berry and A.S.G. Curtis., *Journal of Physics D: Applied Physics.*, 36, (2003), 198–206.

16.   S.M. Kraemer., *Aquatic Science.*, 66, 1, (2004), 3–18.

17.   C.N. Chinnasamy, M. Senoue, B. Jeyadevan, O. Perales-Perez, K. Shinoda, and K. Tohji., *Journal of Colloid and Interface Science.*, 263, (2003), 80–83.

18.   M. Moloney., Properties and Characterisations of Magnetite and Luminescent Particles. Thesis for degree of Doctor of Philosophy. University of Dublin. Trinity College, (2006), 44.

19.   S. Laurent, D. Forge, D.; M. Port, A. Roch, C. Robic, L.V. Elst, R.N. Muller., *Chemical Reviews.*, 108, (6), (2008), 2064-2110.

20.   M. Ballauff, Y. Lu., *Polymer.*, 48, (2007), 1815-1823.

21.   S.E. Khalafalla, G.W. Reimers., *IEEE Transactions on Magnetics.*, (1980), 16, 178.

22.   Y.S. Kang, S. Risbud, J.F. Rabolt, P. Stroeve., *Chemistry of Materials.*, (1996), 8, 2209.

23.   L. LaConte, N. Nitin, and G. Bao., *Nanotoday.*, (2005), 32.

24.   A.H. Lu, E.L. Salabas, F.Schuth., *Angewandte Chemie International Edition.*, 46, (8), (2007), 1222-1244.

25.   J. Turkevich, P.C. Stevenson, J. Hiller, *Discussions of the Faraday Society*, 11, (1951), 55.

26.   G. Frens., *Nature - Physical Science.*, 241, (1973), 20.

27.   N. Moumen, P. Veillet, M.P. Pileni., *Journal of Magnetism and Magnetic Materials.*, 149, (1995), 67.

28.   K.S. Suslick, M. Fang, T. Heyon., *Journal of the American Chemical Society.*, 118, (1996), 11960.

29.   a) N. Moumen, M.P. Pileni., *Journal of Physical Chemistry.*, 100, (1996), 1867., b) N. Moumen, P. Bonville, M.P. Pileni., *Journal of Physical Chemistry*, 100, 14, (1996), 410.

30.   I. Lisiecki, F. Billoudet, M.P. Pileni., *Journal Physical Chemistry.*, 100, (1996), 4160.

31.   K.V.P.M. Shafi, S. Wisel, T. Prozorov, A. Gedanken., *Thin Solid Films.*, (1998).

32.   K. Ghosh., Functional Coatings. Wiley-VCH Verlag GmbH & Co. (2006), 85-165.

33.   W. Wang, Q. Zhang, B. Zhang, D. Li, X. Dong, L. Zhang, and J. Chang., *Chinese Science Bulletin.*, 53, 8, (2008), 1165-1170.

34. M. Wan, J. Li., *Journal of Polymer Science.*, 36, (1998), 2799.

35. M.D. Butterworth, S.A. Bell, S.P. Armes, A.W. Simpson., *Journal of Colloid Interface Science*, 183, (1996), 91.

36. P. Tartaj, M.P. Morales, T. Gonzlez-Carreno, S. Veintemillas- Verdaguer, C.J. Serna., *Journal of Magnetism and Magnetic Materials.*, 290-291, (2005), 28-34.

37. G. Barratt., *Cellular and Molecular Life Sciences.*, 60, (2003), 21.

38. C.M. Niemeyer., Nanobiotechnology: concepts, applications and perspectives. (2004), 200-201, 370.

39. D.W. Ussery., DNA Denaturation., *Academic Press.*, (2001).

40. I. Hilger, W. Andra, R. Hergt, R. Hiergeist, H. Schubert, W.A. Kaiser., *Radiology,.* 218, (2001), 570-575.

41. C.M. Niemeyer, C.A. Mirkin., Nanobiotechnology. Concepts, Applications and Perspectives., WILEY-VCH. (2004).

42. C.M. Niemeyer, C.A. Mirkin., Nanobiotechnology II. More concepts and Applications., WILEY-VCH, (2007).

43. R.T. Gordon, J.R. Hines and D. Gordon., *Medical Hypotheses.*, 5, (1979), 83-102.

44. C. Alexiou, R.J. Schmid, R. Jurgons, M. Kremer, G. Wanner, C. Bergemann, E. Huenges, T. Nawroth, W. Arnold and F.G. Parak., *European Biophysics Journal.*, 35, (2006), 446–450.

45. N. Kohler, G.E. Fryxell, M. Zhang., *Journal of the American Chemical Society.*, 126, (2004), 7206.

46. R. Hirsch, E. Katz, I. Willner., *Journal of the American Chemical Society.*, 122, (2000), 12053.

47. A. Ito, M. Shinkai, H. Honda, and T. Kobayashi., *Journal of Bioscience and Bioengineering.*, 100, 1, (2005), 1–11.

48. C. Lauterbur., *Nature.*, 242, (1973), 191–192.

49. Q.A. Pankhurst, J. Connolly, S.K. Jones, J. Dobson., *Journal of Physics - Applied Physics D.*, (2003), 167.

50. J.F. Schenck, and E.A. Zimmerman., *NMR in Biomedicine.*, 17, (2004), 433–445.

51. M. Bottrill, L. Kwok and N.J. Long., *Chemical Society Reviews.*, 35, (2006), 557–571.

52. I. Coroiu., *Journal of Magnetism and Magnetic Materials.*, 201, (1999), 449.

53. Y.X.J. Wang, S.M. Hussain and G.P. Krestin., *European Radiology.*, 11, (2001), 2319–2331.

54. P. Keston, A.D. Murray, A. Jackson., *Clinical Radiology.*, 58, 7, (2003), 505-513.

55. J.W. Bulte., *Nature Biotechnology.*, 19, 12, (2001), 1141.

56. J.W. Bulte., *Journal of Cerebral Blood Flow & Metabolism.*, 22, 8, (2002), 899.

57. C. Khemtong, C.W. Kessinger and J. Gao., *Chemical Communications.*, (2009), 3497–3510.

58. S.J. Byrne, S.A. Corr, Y.K. Gun'ko, J.M. Kelly, D.F. Brougham, S. Ghosh., *Chemical Communications.*, (2004), 2560-2561.

59. A. Roch, P. Gillis, A. Ouakssim, R.N. Muller., *Journal of Magnetism and Magnetic Materials.*, 201, (1999), 77.

60. R.F. Service., *Science.*, 287, (2000), 1902.

61. A.H. Lu, E.L. Salabas, F. Schuth., *Angewandte Chemie International Edition.*, 46, (2007), 1222–1244.

62. C. Dalaigh, S.A. Corr, Y. Gun'ko, S.J. Connon., *Angewandte Chemie.*, 119, (2007), 4407.

63. O.Gleeson, R. Tekoriute, Y.K. Gun'ko, S.J. Connon., *Chemistry - A European Journal.*, (2009), 5669–5673.

64. C. R. Ronda., Luminescence: from theory to applications., Wiley-VCH, Weinheim., (2007)., 3-4,

65. J.R. Lakowicz., Principles of fluorescence spectroscopy. 3rd ed. (2006), New York., Springer. 1-25. 675-678.

66. D. Rendell., Fluorescence and Phosphorescence, Analytical Chemistry by Open Learning. John Wiley & Sons. London. Crown Copyright., (1987).

67. M.A. Walling, J.A. Novak and J.R.E. Shepard., *International Journal of Molecular Sciences.*, 10, (2009), 441-491.

68. F. Tokumasu, R.M. Fairhurst, G.R. Ostera, N.J. Brittain, J. Hwang, T.E. Wellems, J.A. Dvorak., *Journal of Cell Science.*, 118, 5, (2005),1091-1098.

69. H. Kobayashi, Y. Hama, Y. Koyama, T. Barrett, C.A.S. Regino, Y. Urano, P.L.Choyke., *Nano Letters.*, 7, (2007), 1711-1716.

70.   A. Quarta, R. Di Corato, L. Manna, A. Ragusa, and T. Pellegrino., *IEEE Transactions on NanoBioscience.*, 6, 4, (2007).

71.   V. Salgueirino-Maceira, M.A. Correa-Duarte, M. Spasova, L.M. Liz-Marzan, and M. Farle., *Advanced Functional Materials.*, 16, (2006), 509–514.

72.   Veiseh, C. Sun, J. Gunn, N. Kohler, P. Gabikian, D. Lee, N. Bhattarai, R. Ellenbogen, R. Sze, A. Hallahan, J. Olson, and M.Q. Zhang., *Nano Letters.*, 5, (2005), 1003–1008.

73.   M.Q. Chu, X. Song, D. Cheng, S.P. Liu, and J. Zhu., *Nanotechnology.*, 17, (2006), 3268–3273.

74.   C.W. Lu, Y. Hung, J. K. Hsiao, M. Yao, T. H. Chung, Y. S. Lin, S.H. Wu, S.C. Hsu, H.M. Liu, C.Y. Mou, C.S. Yang, D.M. Huang, and Y. C. Chen., *Nano Letters.*, 7, (2007), 149–154.

75.   G.P. Wang, E.Q. Song, H.Y. Xie, Z.L. Zhang, Z.Q. Tian, C. Zuo, D.W. Pang, D.C. Wu, and Y.B. Shi., *Chemical Communications.*, (2005), 4276–4278.

76.   T.R. Sathe, A. Agrawal, and S.M. Nie., *Analytical Chemistry.*, 78, (2006), 5627–5632.

77.   X. Hong, J. Li, M.J. Wang, J.J. Xu, W. Guo, J.H. Li, Y.B. Bai and T.J. Li., *Chemistry of Materials.*, 16, (2004), 4022–4027.

78.   H.Y. Xie, C. Zuo, Y. Liu, Z.L. Zhang, D.W. Pang, X.L. Li, J.P. Gong, C. Dickinson, and W.Z. Zhou., *Small.*, 1, (2005), 506–509.

79.   V. Holzapfel, M. Lorenz, C.K. Weiss, H. Schrezenmeier, K. Landfester, and V. Mailander., *Journal of Physics: Condensed Matter*, 18, (2006), 2581–2594.

80.   R. K. Iler., *Journal of Colloid and Interface Science.*, 21, (1966), 569.

81.   J. Guo, W.L. Yang, C.C. Wang, J. He, and J.Y. Chen., *Chemistry of Materials.*, 18, (2006), 5554–5562.

82.   S.H. Sun and H. Zeng., *Journal of American Chemical Society.*, 124, (2002), 8204–8205.

83.   S.H. Sun, C.B. Murray, D. Weller, L. Folks, and A. Moser., *Science.*, 287, (2000), 1989–1992.

84.   J.H. Lee, Y.W. Jun, S.I. Yeon, J.S. Shin, and J. Cheon., *Angewandte Chemie International Edition*, 45, (2006), 8160–8162.

85.   M.F. Kircher, U. Mahmood, R.S. King, R. Weissleder, and L. Josephson., *Cancer Research.*, 63, (2003), 8122–8125.

86. L. Josephson, M.F. Kircher, U. Mahmood, Y. Tang, and R. Weissleder., *Bioconjugate Chemistry.*, 13, (2002), 554–560.

87. W.S. Seo, J.H. Lee, X.M. Sun, Y. Suzuki, D. Mann, Z. Liu, M. Terashima, P.C. Yang, M.V. McConnell, D.G. Nishimura, and H.J. Dai., *Nature Materials.*, 5, (2006), 971–976.

88. W.W. Yu, E. Chang, J.C. Falkner, J.Y. Zhang, A.M. Al-Somali, C.M. Sayes, J. Johns, R. Drezek, and V.L. Colvin., *Journal of American Chemical Society.*,. 129, (2007), 2871–2879.

Chapter 2

2. Experimental

2.1. General procedures and starting materials

All manipulations were carried out under vacuum or argon by standard Schlenk techniques using a vacuum manifold fitted with a liquid nitrogen trap. Deoxygenated under argon Millipore water of 18.2 MΩ was used. Ferric chloride hexahydrate (FeCl$_3$ 6H$_2$O), ferrous chloride tetrahydrate (FeCl$_2$ 4H$_2$O), iron (II) bromide, sodium tert-butoxide (NaO^{t}Bu) and cobalt (II) nitrate hexahydrate (Co(NO$_3$)$_2$ 6H$_2$O), Rhodamine B (Rhodamine B base), citric acid, disodium dihydrogenethylenediamine tetra acetate dehydrate (EDTA), sucrose anhydrous, sodium phosphate anhydrous (Na$_3$PO$_4$), sodium chloride (NaCl), Acridine Orange base (AO), were obtained as powders from Sigma-Aldrich. The materials were of analytical grade and used without purification. Ammonium hydroxide (NH$_4$OH, 10 M) was obtained for Sigma-Aldrich. Herring sperm deoxyribonucleic acid (DNA) was obtained in dry form and was stored at 4 °C. Poly(allylamine hydrochloride) (PAH), poly(sodium styrene sulfonate) (PSSS) in powder form and of an average molecular weight of 70,000 g were obtained from Sigma-Aldrich.

2.2. Experimental details for Chapter 3: Preparation and investigation of Cobalt ferrite composites

2.2.1. Preparation of cobalt ferrite nanocomposites using co-precipitation with NH$_4$OH

Cobalt ferrite nanoparticles were prepared by the co-precipitation method [1]. A three-necked 100 mL round bottomed flask was placed under vacuum and then flushed with argon. Iron (II) chloride (0.796 g; 40 mmoL) and cobalt (II) nitrate (0.582 g; 20 mmoL) were added to deoxygenated water (100 mL). The solution was stirred for 5 minutes using a magnetic stirrer at 300rpm and heated to 80 °C using an oil bath on a hot plate. PAH solutions of various concentrations (0 - 1.43x10^{-7}M) were prepared in 10 mL of degassed Millipore water. The PAH solution was then injected by syringe into the flask with Fe/Co salts solution and stirred for 15 minutes under argon gas. To precipitate the cobalt ferrite particles, 10 M NH$_4$OH solution (10 mL)

was added to the mixture and it was heated at 80-90 °C over oil bath for 2 hours. Then the suspension was cooled under argon, the precipitate was washed (5x20 mL Millipore water), centrifuged and finally dried under vacuum at 60 °C. The yield varied in the range of 61.2 - 72.3 % from batch to batch.

2.2.2. Preparation of cobalt ferrite nanocomposites using co-precipitation with NaOH

2 M NaOH was degassed *via* heating (80-90 °C) and subsequent cooling to remove any dissolved oxygen. The preparation of the particles was performed using a technique similar to that described above using NaOH solution in place of NH_4OH. The process resulted in black product. Yield: 40.2 - 47.3 %.

2.2.3. Preparation of DNA solution

The herring deoxyribonucleic acid (DNA) sodium salt (0.06 g) was dissolved in 100 mL of degassed water in a volumetric flask. The standard DNA solution was stored in a refrigerator (at about 4 °C). A range of various concentrations of DNA (0.06 – 1.2 mg/mL) were made and used for other syntheses.

2.2.4. Synthesis of cobalt ferrite - DNA composites

The required volume of Co/Fe solution was added into the 100 mL three-necked round-bottomed flask under argon. Single stranded DNA was prepared by boiling the solution for 10-15 minutes to denature the duplex strands, followed by quick cooling in ice bath. Single stranded DNA solution was used immediately after preparation. The required amount of the cold DNA solution was added into the flask with pink Co/Fe solution.

The mixture of DNA and Co/Fe solutions was heated up to 40 °C and 10 mL of 10 M ammonia (NH_4OH) was injected by syringe. The pink colour of Co/Fe solution immediately changed to dark-green and then black. The black precipitate was heated up to 80 °C into the oil-bath for one hour under argon and slowly cooled to the room temperature. The solvent was removed by syringe out of the black precipitate. The black precipitate was washed with Millipore water until neutral pH (12 x 40 mL) then dried under vacuum at room temperature. Yield: 24.7 - 27%.

2.3. Experimental details for Chapter 4: Preparation and investigation of "two-in-one" magnetic luminescent nanocomposites based on magnetite nanoparticles and QDs

2.3.1. Preparation of Magnetite Nanocomposites using PSSS Stabiliser

Magnetite nanoparticles were prepared by co-precipitation technique, which was reported earlier [2]. Iron (II) chloride (0.02 g, 0.13 mmoL) and iron (III) chloride (0.54 g, 3 mmoL) were added to 10 mL of degassed Millipore water in a three neck round bottomed flask under argon. PSSS (0.15 g, 2.14×10^{-8} moL) in 10 mL of Millipore water was added and the solution was stirred under argon for 15 minutes. Ammonium hydroxide (2 mL, 10 M) was added. The mixture was stirred for 1 hour under argon at the room temperature. The resulting magnetite nanoparticles were collected by magnetic precipitation using 0.5 T permanent magnet (permanent magnet). The black precipitate was washed with (4 x 20 mL) Millipore water and the last washings were retained for future NMRD analysis. The rest of the black product was dried under vacuum under ambient temperature. The experiment was repeated with different quantities of iron (II) chloride, iron (III) chloride, and PSSS according to **Table 4.1**. (**Chapter 4**)

2.3.1.1. Preparation of magnetic multilayered nanocomposites

0.003 g of Fe_3O_4-PSSS was dispersed in 10 mL of filtered distilled water. Fe_3O_4-PSSS nanoparticles were negatively charged, and were, therefore favorable for the deposition of positively charged PAH. LbL technique was used for the formation of multilayered nanocomposites. Using electrostatic interactions as the driving force, positively charged PAH (0.2 mL, 2.85×10^{-7} M) was added; the sample was sonicated for 10 minutes at room temperature. After the resulting PAH layer was deposited, negatively charged PSSS (1.2 mL, 2.85×10^{-7} M) was added into solution and sonicated again. To separate PAH coated magnetite-PSSS nanoparticles from free PAH magnetic separation was performed with the help of 0.1 T permanent magnet for 5 minutes. After a second layer of polyelectrolyte was deposited, the process was carried out in a cyclic method, until ten layers of polyelectrolytes producing multilayered magnetic nanocomposites. After deposition placing the sample onto a 0.1 T permanent magnet for 20 minutes, then removing the non-magnetic supernatant

magnetically separated nanocomposites. The magnetic precipitate was re-dispersed in 10 mL of degassed distilled water.

2.3.1.2. Preparation of magnetic luminescent nanostructures with various types of QDs

Gelatine (Gel) and non-gel thioglycolic acid (TGA*) capped CdTe QDs were prepared by Dr. S. Byrne and V. Gerard according to procedure published by Gaponik et al. [3]. Synthesised gel, non-gel TGA*CdTe QDs were characterised by UV-vis, and PL. Sizes of the QDs were determinate using empirical graph relating absorption λ_{max} with the size determined by TEM. Quantum Yields of Gel CdTe QDs were calculated from the absorption and integrated emission data of the QDs and organic dye (Rhodamine B). Stock solutions of QDs were stored in the fridge at 4 °C and used for the future synthesis.

Magnetic luminescent nanostructures were prepared according **Table 2.1**. Various types of CdTe QDs (Gel or non-gel) were added in 4 mL of filtered distilled water. Required amount of PAH (2.85×10^{-7} M) in the rage of 200-500 µL were added to QDs solution. Prepared stock QDs solutions were mixed with 3 mL (1×10^{-3} g/mL) of multilayer magnetic structures for 14-16 hours in darkness at the room temperature to produced samples. The sample was placed onto 0.1 T permanent magnet for 20 minutes, then the supernatant (nonmagnetic suspension containing unreacted QDs was removed). The collected luminescent magnetic nanostructures were dispersed in 5 mL distilled degassed water. Final fluorescent suspensions were stored in the dark to prevent photochemical decomposition. All samples, unless otherwise noted, were used for spectroscopic studies within 24 hours of the preparation time.

Table 2.1. Synthesis conditions for the preparation of magnetic luminescent nanostructures with various types of CdTe QDs.

Sample	Type of CdTe QDs	Conc. of CdTe QDs (M)	Volume of CdTe QDs (µL)	Added PAH (µL)	Volume of mag. nanocomposites (mL)	Time (hours)
10	Gel TGA	1.4×10^{-4}	300	30	3	14
11	Non gel TGA	2.35×10^{-4}	200	30	3	14
12	Gel TGA	1.4×10^{-4}	300	30	3	14
13	Non gel TGA	3.71×10^{-5}	500	52	3	14
14	Non gel TGA	3.71×10^{-5}	500	30	3	14

2.4. Experimental details for Chapter 5: Bimodal luminescent magnetic nanocomposites

2.4.1. Preparation of Cobalt ferrite –PSSS nanoparticles

Cobalt ferrite nanoparticles were prepared by co-precipitation method similarly above. The required volume of Co^{2+}/Fe^{3+} solution (Ratio 1 : 2 mmoL) was placed into the 100 mL three-necked round-bottom flask under argon gas. Then the required volume of PSSS (0.25 g in 10 mL) solution was added to the mixture and it was stirred for 15 minutes. Ammonia (2 mL, 10 M) was injected by syringe until pH reached 9. The black precipitate was heated and stirred at 80 °C for 1 hour. Then the suspension was cooled under argon. The black precipitate was washed with Millipore water until neutral pH (5x20 mL). The obtained nanoparticles were dried under vacuum at room temperature for the following use. Yield: 35-42 %

2.4.2. Preparation of Cobalt ferrite –PSSS-RhB nanocomposites

0.0058 g of $CoFe_2O_4$-PSSS was dispersed in 10 mL of Millipore water. Then positively charged PAH (1 mL, $2.85x10^{-7}$ M) was added and the sample was sonicated for 10 minutes at 20 °C. Then the resulting PAH layer was deposited, negatively charged PSSS (2.3 mL, $2.85x10^{-7}$ M) was added into solution and sonicated again. After second layer of polyelectrolyte was deposited, the process was repeated in cycles, until multilayered magnetic nanocomposites with sixteen layers of polyelectrolytes have been prepared. After the deposition multilayered nanocomposites were magnetically separated, decanted and re-dispersed in 10 mL of degassed Millipore water. Rhodamne (RhB) solution ($2.9x10^{-4}$ M) was added (the amount was varied depending on experiment) to the suspension of magnetic multilayered nanocomposites and mixed overnight in darkness at the room temperature. The unreacted Rhodamine B in the resulting mixture was washed with Millipore water several times (4x5 mL), until the washings turned colourless. Freshly prepared luminescent magnetic nanocomposites were then removed by magnetic separation. The collected luminescent magnetic nanocomposites were dispersed in 5 mL degassed Millipore water and stored in darkness at the room temperature.

2.4.3. Preparation of Magnetite –PSSS-RhB nanocomposites

0.0058 g of Fe_3O_4-PSSS was dispersed in 10 mL of Millipore water. Positively charged PAH (0.6 mL, 2.85×10^{-7} M) was added, sample was sonicated for 10 minutes at 20 °C. Then the resulting PAH layer was deposited, negatively charged PSSS (1.2 mL, 2.85×10^{-7} M) was added into solution and sonicated again. After second layer of polyelectrolyte was deposited, the process was carried out in cycles, until magnetic nanocomposites with ten layers of polyelectrolytes were produced. After the preparation nanocomposites were magnetically separated, decanted and re-dispersed in 10 mL of degassed Millipore water. 2 mL (2.9×10^{-4} M) of RhB solution was added (the amount varies with the experience) to the suspension of magnetic multilayered nanocomposites and mixed overnight in darkness at the room temperature. The unreacted Rhodamine B in the resulting mixture was washed with Millipore water several times (4x5 mL), until the washings turned colourless. Freshly prepared luminescent magnetic nanocomposites were then removed by magnetic separation. The collected luminescent magnetic nanocomposites were dispersed in 5 mL degassed Millipore water and kept in darkness.

2.5. Experimental details for Chapter 6: Magnetite-DNA nanoparticles based magnetic luminescent nanocomposites

2.5.1. Preparation of Acridine Orange in citrate-phosphate buffer

- **Stock buffer I** (20 mM citrate-phosphate, 0.1 mM EDTA, 0.2 M sucrose) pH~3

In 200 mL volumetric flask was added 40 µL 0.5 M EDTA, 26.48 mL 0.1 M citric acid, 6.85 mL 0.2 M dibasic sodium phosphate, 13.69 g sucrose and degassed Millipore water. Solution was filtered through 0.2 µ filter and stored at 4 °C.

- **Stock buffer II** (10 mM citrate-phosphate, 0.1 M NaCl) pH ~3.8)

In 200 mL volumetric flask was added 10 mL of stock buffer I, 9.92 mL 0.1 M citric acid, 5.46 mL 0.2 M dibasic sodium phosphate, 1.7 g NaCl, degassed Millipore water. Solution was filtered through 0.2 µ filter () and stored at 4 °C for the period of two weeks.

2.5.2. Preparation of Acridine Orange in phosphate buffer

2 mg of Acridine Orange base (AO) was suspended in 1 mL degassed Millipore water and diluted 1:100 in Stock buffer II and stored at 4 °C.

2.5.3. Preparation of magnetite-DNA nanoparticles

The herring deoxyribonucleic acid (DNA) sodium salt 0.0053 g was dissolved in 25 mL of degassed water in a volumetric flask. The standard DNA solution (0.0030 M) was stored in a refrigerator (at about 4 °C). Single stranded DNA was prepared by boiling the solution for 10-15 minutes to denature the duplex strands, tracked by quick cooling in ice bath. Single stranded DNA solution was used immediately after preparation. Freshly prepared single stranded and double stranded DNA was used for the synthesis. The concentration of the stock DNA solution was determined spectrophotometrically using extinction coefficient 6600 $M^{-1}cm^{-1}$ of at 260 nm.

FeCl$_3$.6H$_2$O (0.33 g; 4 mmoL) and FeCl$_2$.4H$_2$O (0.12 g; 2 mmoL) were dissolved in 30 mL deoxygenated water. DNA solutions were added to of Fe^{3+}/Fe^{2+} solution as shown in **Table 2.2**.

Table 2.2. Summarised experimental data for magnetite DNA samples.

Name	Iron concentration (M)	Volume of DNA (mL)	DNA concentration (M)	Metal:PSSS ratio
Sample 7 (ssDNA)	0.006	15	0.003	2
Sample 8 (dsDNA)	0.006	15	0.003	2

The solutions were allowed to stir at room temperature for 15 minutes. Magnetic nanoparticles were precipitated *via* the addition of ammonia solution until the pH reached 9. The black precipitate was washed with degassed Millipore water until neutral pH (4 x 20 mL) then dried under vacuum at room temperature. The final washes used in next experiments and TEM analysis.

All titrations were performed at room temperature. Absorbance, emission and excitation spectra were measured for 0 – 200 μL AO in the samples.

2.5.4. Fabrication of Magnetite-dsDNA-AO nanocomposites

500 µL of sample was placed in a glass cuvette and diluted to 2 mL with Millipore water. Magnetite-dsDNA sample was spectroscopically titrated against the AO in phosphate buffer solution.

2.5.5. Fabrication of magnetite-ssDNA-AO nanocomposites

50 µL of magnetite-ssDNA sample was diluted up to 2 mL in a glass cuvette. Solution was titrated against the Acridine Orange solution in phosphate buffer. Absorbance, emission and excitation were measured for the range 0-10 µL of AO added.

2.6. Experimental details for Chapter 7: Conclusions and future work

2.6.1. Preparation of iron metallorganic precursor, [(THF)NaFe(OBu^t)$_3$]$_2$

Sodium *tert*-butoxide (NaOBu^t) (3.022 g, 0.014 mmoL) was dissolved in 80 mL of dry tetrahydrofuran (THF) at room temperature. The suspension was stirred at room temperature until all NaOBu^t was completely dissolved. Then anhydrous iron (II) bromide (FeBr$_2$) was added into the suspension of NaOBu^t/THF. The colour of the suspension changed to greyish. Final precipitate was stirred for 24 hours at the room temperature. The solvent was removed. Crystals of [(THF)NaFe(OBu^t)$_3$]$_2$ were dried for 2 hours under vacuum. The synthetic scheme is presented in **Chapter 7**.

2.6.2. Preparation of Fe$_3$O$_4$ from metallorganic precursor, [(THF)NaFe(OBu^t)$_3$]$_2$

[(THF)NaFe(OBu^t)$_3$]$_2$ (0.45 g) was dissolved in 60 mL of dry toluene. The flask with the dark brown solution was placed in an ultrasonic bath and various volume of degassed Millipore water (0.05, 0.1, 0.2 mL) were injected into the 3 shlenks. The resultant mixture was then ultrasonically treated at the 50 °C for 1 hour to give a black precipitate. Black precipitate was washed 3x10 mL of dry THF under argon and then dried under vacuum.

2.7. Instrumental techniques

This part of Chapter 2 is dedicated to the methods chosen to be suitable for the studies of phase characterisation of new magnetic, magnetic luminescent nanomaterials, suspension colloidal stability, size of the nanoparticles, theirs optical and magnetic properties.

The basic principles of Raman, Infrared (FT-IR), Ultraviolet-Visible (UV), Fluorescence spectroscopy, Transmission Electron (TEM), Scanning electron microscopy (SEM), Confocal microscopy (CM), Zeta potential and Photon Correlation Spectroscopy (PCS) measurements, Nuclear magnetic resonance dispersion (NMRD), X-ray powder diffraction (XRD), Thermogravimetry (TGA), Superconducting Quantum Interference Device Magnetometry (SQUID).

2.7.1. Transmission electron microscopy (TEM) measurements

The transmission electron microscopy (TEM) is the most direct tool and time-consuming process to analyse the size distribution in nanomaterials (nanocrystals, nanoparticles, etc). Moreover, *in situ* monitoring of growing particle in solution is obviously beyond scope of TEM.

The TEM operates on the same basic principles as the light microscope but uses electrons instead of light. TEM's use electrons as "light source" and their much lower wavelength make it possible to get a resolution a thousand times better than with a light microscope. A thermionic gun (electron source) offers a stream of electrons, which are then accelerated towards the sample using a positive electrical potential. Electron beam is focused and narrowed on the sample using two condenser lenses. The first lens determines the spot size and the second lens allows the spot to be pinpointed onto the sample. When the electron beam is transmitted through the sample, only the electrons, which are not blocked by the sample, are allowed through. This produces an image, which is passed down through the column through a series of other lenses. When the electrons reach the bottom, screen generates light, which allows the user to see the image.

TEM is used to analyse the crystallographic structure, microstructure, and the composition of a wide range of organic and inorganic materials. Analysing objects could be seen to the order of a few angstrom (1 $\overset{\circ}{A}=10^{-10}$ m). For example, study could be done on small details in the cell or different materials down to near atomic levels.

The possibility for high magnifications has made the TEM a valuable tool in both medical, biological and materials research [4]. Schematic presentations of the series of interactions occur between the sample and the electron beam in TEM and Scanning electron microscopy (SEM) is shown in **Fig. 2.1**.
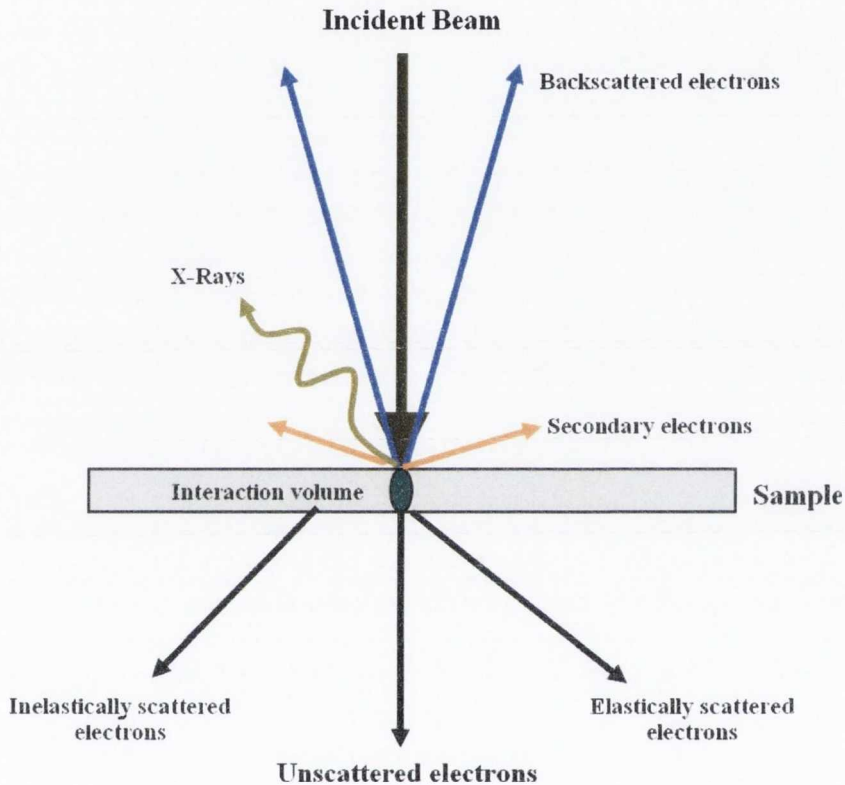
Figure 2.1. Different types of electron interactions, which occur in electron microscopy.

- **Unscattered electrons** are transmitted through the sample without any interactions with the specimen.

- **Elastically scattered electrons**, which are scattered according to Bragg's Law without energy lost. These electrons will be scattered by the same angle when they come into contact with the same atomic spacing. These elastically scattered electrons can be collected to form a diffraction pattern of the sample.

- **Inelastically scattered electrons** are similar to those above, except in this case there is a loss of energy to the environment. The energy lost can excite vibrations at the surface of the sample and the resulting energy loss peaks can be observed. The magnitude of the energy loss is different for the various elements the electrons have

interacted with. The energy lost can excite vibrations at the surface of the sample and the resulting energy loss peaks can be observed. This technique is called Electron Energy Loss Spectroscopy (EELS) [4 b)].

The sizes, shapes and arrangements of the particles in our experiments were analysed by Jeol 2100 Transmission Electron Microscope (TEM). Samples were prepared by ultrasonically dispersing powder samples in Millipore water. Then one drop of the solution (5 μL) was placed onto a formvar-coated copper or carbon-coated TEM grid. The grid was then dried in air. Set of the samples were placed in a parallel 0.5 T magnetic field and slowly dried at the room over night. Particle sizes were determined by manually counting over 100 particles in different regions of a given TEM grid.

2.7.2. Scanning electron microscopy (SEM) measurements

The SEM technique designed for direct studying of the surfaces of solid objects. SEM microscope the same as TEM uses electrons to form an image. The most important interactions of the electrons in SEM are leading to the emission of backscattered electrons, secondary electrons and x-rays [4].

• **Backscattered electrons** are produced when electrons interact with the sample, (bump into the nuclei of atoms). The production and number of backscattered electrons produced depends on the atomic number of the specimen being imaged and the angle close to that of the incident beam. The higher the atomic number, the more likely it is to have an interaction of the electrons with the nucleus. Backscattered electrons may be used to produce an image, which will give details of the specimen in terms of the elements, which make it up - a brighter image will be found for higher atomic numbered elements [4, 5].

• **Secondary electrons** (lower energy) are produced and then collected by a detector near the surface (applying positive potential) of the sample without interaction with the atom nucleus in the sample. These give an impression of the topography of the surface and are most important in the SEM technique.

• **X-Rays** - are produce as an excess of the emitted energy from the secondary electron of the ionised atom creating the vacancy. Electron with higher energy can "fall" down to the lower level and fill this vacancy. As the electron falls, it emits its excess energy in the form of X-rays. The X-rays are characteristic of the element in

the sample and can be detected and separated into an energy spectrum, to give an elemental composition of the sample in a technique called Energy Depressive X-ray Analysis (EDX).

In our experiments 200-400 µL of the selected samples were put onto the 2 mm glass slides. Slides were kept overnight in 0.5 T parallel magnetic field (permanent magnet) at the room temperature. SEM was performed using Hitachi S-4300 Field Emission Scanning Electron Microscope, in high vacuum mode.

2.7.3. X-ray powder diffraction (XRD) measurements

X-rays are relatively short electromagnetic radiation of wavelength about 1 Å (10^{-10} m), which is about the same size as an atom. They occur in that portion of the electromagnetic spectrum between gamma-rays and the ultraviolet. The discovery of X-rays in 1895 enabled scientists to probe crystalline structure at the atomic level. X-ray diffraction has been in use in two main areas, for the fingerprint characterisation of crystalline materials and the determination of their structure. Each crystalline solid has its unique characteristic X-ray powder pattern, which may be used as a "fingerprint" for its identification. Once the material has been identified, X-ray crystallography may be used to determine its structure, i.e. how the atoms pack together in the crystalline state and what the interatomic distance and angle are etc.

W.L. Bragg (1913) was the first to show that the scattering process, which leads to diffraction, can be visualized as a reflection from imaginary planes. *Bragg's* law (1) allows us relate the distance between a series of planes in a crystal and the angle at which these planes will be diffract X-rays of a particular wavelength. **Fig. 2.2** presents set of atomic planes [6, 7].

$$n\lambda = 2d\sin\Theta \qquad\qquad (1)$$

were: **n** - number of planes, λ - wavelength, **d** - distance between planes, Θ - reflected angle.
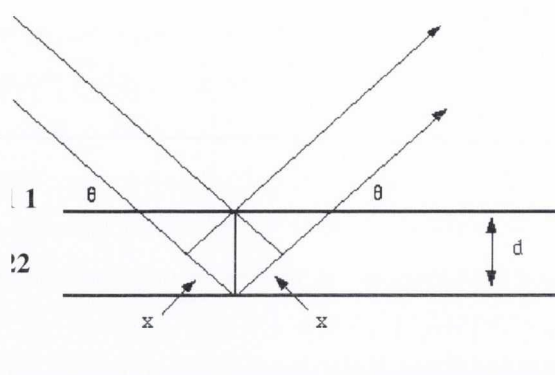
Figure 2.2. Reflection of x-rays from two planes of atoms, 1, 2 – planes.

X-ray diffraction is one of the most important characterization tools used in solid state chemistry and materials science. We can determine the size and the shape of the unit cell for any compound most easily using the diffraction of x-rays [7].

In our experiments samples in the powder form were spread onto the XRD slide with a very thin layer of vacuum grease. XRD was performed using a Siemens-500 X-Ray diffractometer, which uses Cu cathode $K_{\alpha1}$ with a wavelength ($\lambda_{K\alpha}$) of 1.54056 Å. The diffraction patterns were taken in the range of $5° < 2\theta < 90°$ using step of $0.02°$ (2Θ) for 1 hour. All samples were scanned at room temperature. The phases were identified by comparison of the sample data (peaks and intensities) with the set of the standard references provided by the Joint Committee on Powder Diffraction Standards (JCPDS) database.

2.7.4. Superconducting quantum interference device magnetometer (SQUID) measurements

The superconducting quantum interference device (SQUID) device consists of the semiconducting rings (Josephson junctions). Josephson junctions are separated by a thin insulating layer, which allows electrons (current) to cross through. In the absence of the magnetic field the maximum current (Josephson current) flows is equal to the twice the current passing through each of junctions. The Josephson current is extremely sensitive to magnetic fields. Then the magnetic field is applied to the perpendicular to the plane of the ring, the magnetic vector (A) is parallel to the current of the one arm and opposite to another. The meeting point were two currents interfere gives the shift of the phase through the individual junctions. This interference of two current in the arms of the rings was named - superconducting quantum interference

device [8]. A SQUID measures magnetic signals on the order of 10^{-9} Tesla and less [8, 9]. Schematic illustration of direct use of Josephson junctions in SQIUD is presented in **Fig. 2.3**.
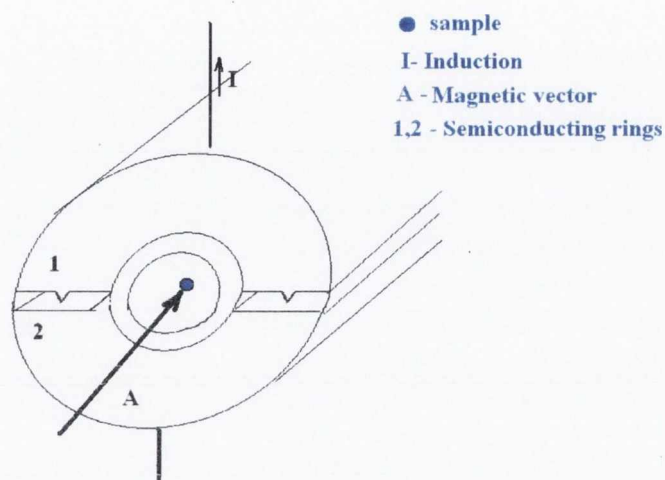
Figure 2.3. Schematic illustration of the basic principal work of the SQUID.

SQUID is used to measure magnetic signals, which is extremely valuable for magnetic nanoparticle analysis.

Magnetisation measurements were carried out on the selected samples on a SQUID magnetometer with a 5 T magnet and a magnetic field of 10^{-8} amps/m. Temperatures can be varied from 1 to 300 K. The magnetisation curves M (H_c) were obtained after cooling the sample to the measurement temperature in zero fields and then increasing the field from 0 to 50 kOe. In all cases, the powders were moderately compacted into the sampling tubes. The device operates typically with samples of mass 1.4 - 4 mg.

2.7.5. Fourier Transformed Infrared spectroscopy (FTIR) measurements

Infrared spectroscopy (IR) is a technique used to identify various functional groups in unknown substances through the identification of different covalent bonds that are present in the compound. The term "infra red" covers the range of the electromagnetic spectrum between 0.78 and 1000 μm. These atoms in the molecules are oscillating around average positions. With the vibration, the length of bond and angles are continuously changing due to this vibration (see **Fig. 2.4 (b)**). A molecule absorbs infrared radiation when the vibration of the atoms in the molecule produces

an oscillating electric field with the same frequency as the frequency of incident IR. Molecules have two types of vibration: stretching and bending (see **Fig.2.5**). A stretch produces a change of bond length.

bond strech   **normal bond**   **bond compressed**

(b)   (a)   (c)
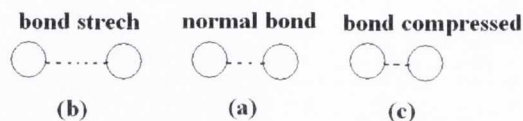
Figure 2.4. Stretching vibrations of covalent bonds. a) bond stretched b) normal bond, c) bond compressed.

A bending vibration produces a change of bond angle. They are called scissoring, rocking and "wig wag" motions.

(a)   (b)   (c)
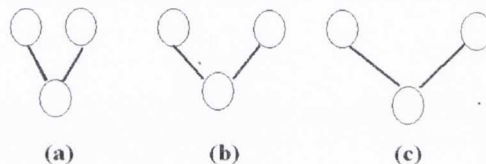
Figure 2.5. Scissoring of bending vibrations of covalent bonds. a) Bond angle compressed b) Normal bond angle c) Bond angle widened.

By comparing the absorptions seen in an experimental spectra to the literature absorptions of various functional groups, could be determined a list of possible identities for the bonds present [10].

Potassium bromide (KBr, for IR spectroscopy, Fluka) was used to prepare disks of the samples by pressing at a pressure of 8 MPa for 2-5 minutes. IR spectra were recorded between 4000-500 cm^{-1} by diffuse reflectance using a Perkin Elmer Spectrum One FT-IR.

2.7.6. Raman spectroscopy (RS) measurements

When light is scattered from a molecule most photons are elastically scattered. The scattered photons have the same energy (frequency) and, therefore, wavelength, as the incident photons. However, a small fraction of light (approximately 1 in 10^7 photons) is scattered at optical frequencies different from, and usually lower than, the frequency of the incident photons. The process leading to this inelastic scatter is the termed the Raman effect. Raman scattering can occur with a change in vibrational, rotational or electronic energy of a molecule (see **Fig. 2.6.**). Chemists are concerned

primarily with the vibrational Raman effect. The difference in energy between the incident photon and the Raman scattered photon is equal to the energy of a vibration of the scattering molecule. A plot of intensity of scattered light versus energy difference is a Raman spectrum.
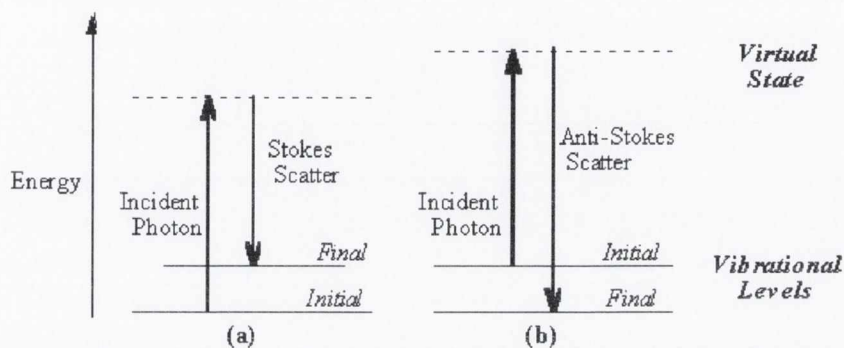
Figure 2.6. Energy level diagram for Raman scattering: a) Stokes Raman scattering b) anti-Stokes Raman scattering.

Chemists generally prefer a quantum-mechanical approach to Raman scattering theory, which relates scattering frequencies and intensities to vibrational and electronic energy states of the molecule. The standard perturbation theory treatment assumes that the frequency of the incident light is low compared to the frequency of the first electronic excited state. The small changes in the ground state wave function are described in terms of the sum of all possible excited vibronic states of the molecule [11, 12].

In all our experiments, samples in the powder from were placed onto 1.2 mm glass slide. Raman spectra were recorded between 1000 and 4 cm^{-1} at room temperature using Renishaw 1000 micro-Raman system. Raman spectra were fitted using the GRAM/386 software. The excitation wavelength was 457 nm from an Ar$^+$ ion laser (Laser Physics Reliant 150 Select Multi-Line) with a typical laser power of ~ 17 W cm^2 in order to avoid excessive heating. The 100x-magnifying objective of the Leica microscope was capable of focusing the beam into a spot of approximately 1 μm diameter. To have high signal–noise ratio, each RS spectrum is the average of 3 successive scans.

2.7.7. Thermogravimetric analysis (TGA) measurements

Thermogravimetric analysis (TGA) is an analytical technique used to determine a material's thermal stability and its fraction of unstable components by monitoring

the weight change that occurs as a specimen is heated. The measurement is normally carried out in air or in an inert atmosphere, such as Helium or Argon, and the weight is recorded as a function of increasing temperature. Sometimes, the measurement is performed in a lean oxygen atmosphere (1 to 5 % O_2 in N_2 or He) to slow down oxidation [12]. Samples of approximately 2-3 mg are recommended for the measurement. Considering stability of modern TGA instruments, this quantity of material (1 mg) is still acceptable, but should be an absolute minimum. The TGA profile could be electronically recalculated (differentiated) into derivative thermogravimetric (D-TGA) profile.

Our TGA experiments were carried out in air for all the samples using a Perkin Elmer Pyris 1 TGA with a temperature scan rate of 10 °C min^{-1}. The analysis was performed in air on a sample of approximately 2-3 mg.

2.7.8. Photon Correlation Spectroscopy (PCS) measurements

Photon correlation spectroscopy (PCS) has become a mature and popular technology for probing the diffusion of particulate materials either in solution or in suspension. When a beam of light passes through a colloidal dispersion, the particles or droplets scatter some of the light in all directions. The Brownian motion of the particles in solutions causes a Doppler shift in the incident light frequency by angle Θ. The amount of frequency shift is related to the frequency of the Brownian motion, which is related to the size of the particles. When the particles are very small compared with the wavelength of the light, the intensity of the scattered light is uniform in all directions (Rayleigh scattering); for larger particles (above approximately 25 nm).

Schematic illustration of the light scattering by particles in solution is presented in **Fig. 2.7.** The advantages of PCS, which include the fact that it is a non-invasive absolute technique requiring only a small amount of sample, and does not require extensive sample preparation, have made this technology the method of choice for sizing submicron particles. PCS is particularly suited to determining small changes in mean diameter such as those due to adsorbed layers on the particle surface or slight variations in manufacturing processes [13].
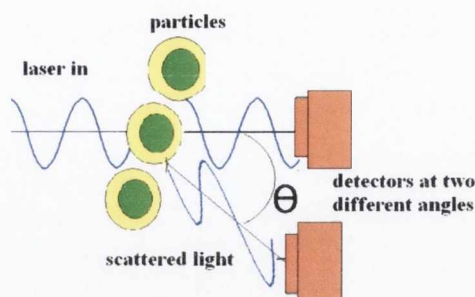
Figure2.7. Schematic illustration of the light scattering by particles in solution.

PCS measurements were carried out for all samples in air at 25 °C using fluorimeter low volume polystyrene cuvette at a backscatter angle of 173 ° for all samples using a Malvern Zetasizer Nano ZS instrument.

2.7.9. Zeta potential (ζ- potential) measurements

Most particles dispersed in an aqueous system will acquire a surface charge, principally either by ionisation of surface groups, or adsorption of charged species. The double layer model is used to visualise the ionic environment in the surrounding area of a charged particle. These surface charges modify the distribution of the surrounding ions, resulting in a layer (fixed layer) around the particle that is different to the bulk solution. When a voltage is applied to the solution of the charged particles; particles would be attracted to the opposite charged electrode. Outside the fixed layer, there are varying compositions of ions of opposite charges, forming a cloud-like area (diffuse double layer). The double layer is formed in order to neutralise the charged surface. If the particle moves, under Brownian motion for example, this layer moves as part of the particle. The zeta potential is the potential at the point in this layer where it moves past the bulk solution. Zeta potential depends on number of parameters such as surface charges, ions absorbed at the interface and nature of the composition. The zeta potential is calculated according *Smoluchowski's* formula (2):

$$\zeta = (4\pi\eta\upsilon L/\varepsilon V) \times 300 \times 300 \times 1000 \qquad (2)$$

were: ζ - Zeta potential, η - viscosity of the solution, ε - dielectric constant, υ - speed of the particle, V - voltage, L - distance between electrodes.

The main reason to measure zeta potential is to predict colloidal stability. The interactions between charged particles play an important role in colloidal stability.

Positively or negatively charged particles with a high zeta potential (<-30mV and >+30mV) will stay well dispersed in solution. At the same time electrostatic repulsion of colloidal particles affect suspension stability (aggregation might appear). The smaller is the particles' size the better they (mass) would be distributed in suspension (solution). The better mass is distributed in solution the lower kinetic energy it has to affect electrostatic repulsion between particles. The zeta potential is a measure of the repulsive forces between interacting particles. In aqueous colloidal suspensions particles are stabilised by electrostatic repulsion, the larger the repulsive forces between particles, the less possibility that particles will come close together and form an aggregate. Thus, the more stable a colloid will be [14, 15].

Sample (~1 mL working volume) was injected into a disposable capillary cuvette and zeta potential measurements were carried out in air at 25 °C for using a Malvern Zetasizer Nano ZS.

2.7.10. Ultraviolet-visible Spectroscopy (UV-vis) measurements

Many molecules absorb ultraviolet or visible light, and they absorb radiation of different wavelength. An absorption spectra shows a number of absorption bands corresponding to structural groups within the molecule. The *Beer-Lambert* Law (3) shows the relation between the absorbance, the extinction coefficient, the path length and the concentration of the compound in solution. The relation is:

$$A = \varepsilon cl \tag{3}$$

where: **A** – Absorbance, ε - extinction coefficient, **c** - concentration of the compound in solution (in mol/L), **l** - the path length of the sample.

The ultraviolet (UV) region scanned is normally from 200 to 400 nm, and the visible portion is from 400 to 800 nm.

The absorbance depends on the total quantity of the absorbing compound in the light path through the cuvette. When the energy is sufficient to promote or excite an outer electron to a higher energy orbital, we can observe a peak on the spectrum [absorbance (A) versus wavelength (nm)]. As a rule, energetically favoured electron promotion will be from the highest occupied molecular orbital (HOMO) to the lowest unoccupied molecular orbital (LUMO). There are three types of electronic transition, which can be considered (a) transitions involving π, σ and n electrons; (b) transitions

involving charge-transfer electrons and (c) transitions involving d and f electrons. When an atom or molecule absorbs energy, electrons are promoted from their ground state to an excited state. This is what we observe as our peak in the absorbance spectrum [16].

In our experiments samples were diluted with known concentration in a quartz cuvette (2 mL working volume, 10 mm path length) and analysed with Varian Cary 50 UV-vis spectrophotometer with 150W Xenon lamp as a light source. UV-Visible absorption spectra (200-800 nm) were recorded against blank sample (cuvette). All scans were performed at the room temperature.

2.7.11. Photoluminescence Spectroscopy (PL) measurements

Samples were prepared the same way as for UV-vis. PL measurements were performed by using Varian Cary Eclipse Fluorescence Spectrophotometer with Xenon lamp as a light source. Luminescence was recorded perpendicular to excitation, with both excitation and emission monochromators slit-width set to 5 nm. All scans were performed at the room temperature.

2.7.12. Nuclear Magnetic Resonance Dispersion (NMRD) measurements

One of the important biochemical applications of magnetic fluids is their use as MRI contrast agents. As the particles dispersed in the fluid are superparamagnetic they are not as susceptible to aggregation as larger particles. These contrast agents may be used to localise and diagnose brain tumours, cardiac infarct liver lesions [17-20]. The NMRD technique allows the monitoring of the magnetic interaction of magnetic species with their surrounding water molecules. This was carried out by testing the dependence of the proton relaxation on the applied magnetic field. The spin-lattice, R_1, is related to the observed spin lattice relation time T_1 as follows:

$$R_{1(obs)} = \frac{1}{T_{1(obs)}} = \frac{1}{T_{1(diam)}} + \frac{1}{T_{1(para)}} = \frac{1}{T_{1(diam)}} + r_1[Fe] \qquad (3)$$

where: $T_{1(diam)}$ - the native relaxation time of the supporting fluid (water in this case) and r_1 - the relaxivity of the agent, [Fe] - iron concentration [21].

2 mL of magnetic fluid was added into 10 mm MNR tube. T_1 and T_2 measurements by NMRD were made using Spinmaster FFC-2000 Fast Field Cycling NMR Relaxometer operating at the frequency of 9.25 MHz with a 90 ° pulse of 6 μs. T_1 measurements were performed as a function of external field, B_0, with standard pulse sequences incorporating B_0 field excursions. A field switching rate of 20 MHz/ms ensured measurement of T_1 relaxation times as low as 1 ms were possible. The field range covered on the Stelar Spinmaster was from 10 kHz to 20 MHz. For the field range 35–60 MHz, T_1 measurements were performed on a reconditioned Bruker WP80 variable field magnet, using the saturation recovery pulse sequence. For all experiments presented, the temperature of the samples was maintained at 25 °C and controlled within ±1 °C by use of a thermostatted air flow system.

2.7.12.1. Determination of Iron Content

To determinate the amount of iron present in the samples used in NMRD studies, a known volume was taken (0.3-0.5 mL) immediately after NMRD measurements. Total iron content was determined by atomic absorption spectroscopy. Samples were prepared for analysis as follows. Concentrated HCl (0.5 mL) and 1 mL of distilled H_2O, 300 μL of Triton X-100 were added to a small aliquot (300 μL) of magnetic suspension of the nanoparticles. Triton X-100 was used as a detergent to ensure dissolution of the organic component (PSSS), confirmed that the C18 surfactants do not interfere with the iron determination.

The mixture was heated until only 1 drop of liquid remained, at which time 25 mL of distilled water was added. The solution was heated to boiling and then immediately removed from heat and allowed to cool to room temperature. The volume was adjusted to 100 mL. Spectra were recorded on a Varian SpectrAA spectrometer fitted with a single slit burner. The light source was a Fe-cathode lamp with a wavelength of 248.3 nm. The resulting atomic absorption of the solution was measured against a set of standard solutions (0.5 – 2.5 mM iron). An example of one of the calibration curves is presented in **Fig. 2.8**.
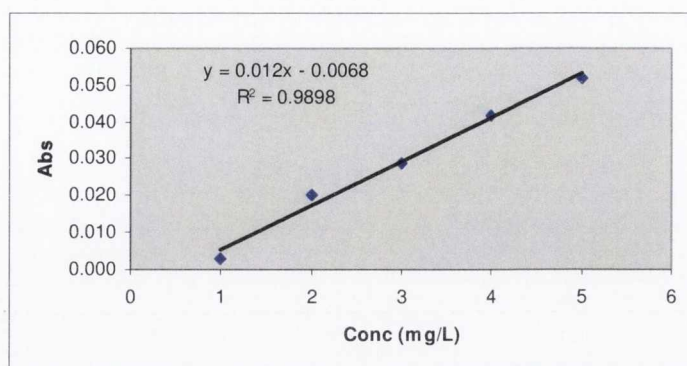
Figure 2.8. Standard calibration curve for iron concentration determinations in the range 0.5-2.5 mM iron by atomic absorption spectroscopy.

2.7.13. Fluorescent microscopy measurements

Fluorescence spectroscopy is a non-destructive method of probing the electronic structure of materials. Electrons are excited to the conduction band by light absorption. Light is directed onto the sample, where it is absorbed and imparts excess energy into the material, it is the photo-excitation. One way this excess energy can be dissipated by the sample is through the emission of light, or luminescence. In the case of photo-excitation, this luminescence is called photoluminescence. The photo-excitation causes electrons within the sample to move into permissible excited states. When these electrons return to their equilibrium states, the excess energy is released and may include the emission of light. The photoluminescence is used to determine the band gap, to detect impurity levels and defect, in recombination mechanisms and to determine the quality of a material [16]. In the case of magnetic luminescent nanomaterials, the photoluminescence spectroscopy is used to determine if magnetic nanoparticles are coated with fluorescent material.

300 μL of the sample was placed onto 1.2 mm glass slide and dried in 0.5 T parallel magnetic field at the room temperature. Samples were examined using Olympus BX51M microscope fitted with the Mercury burner USH-103 OL as a light source. Images were taken using different magnifications (x50, x100).

2.7.14. Confocal microscopy (CM)

Confocal fluorescence microscopy is rapidly becoming a powerful tool in cell biology for analysing biological structure and function at the cellular level, since elimination of out-of-focus fluorescence improves clarity of structures that previously

were unobservable with conventional epifluorescence microscopy. Confocal imaging is a technique in which an object is illuminated with a small (diffraction limited) spot, usually derived from a focused laser beam. The illuminated spot is viewed with a spatially restricted optical system so that only signals emanating from this spot are detected. An image of the complete specimen is built up by a raster scan. Both the intensity of illumination and the sensitivity of the detector fall rapidly with distance away from the plane of focus. This contrasts with conventional epifluorescence methods, where the specimen is bathed in an essentially uniform flux of excitatory illumination.

The advantage of fluorescence for microscopy: a) fluorescent dye molecules could be attach to specific parts of the sample, so that only those parts are the ones seen in the microscope, b) more than one type of dye and thin section of the sample could be analysed.

300-400 μL (magnetite-DNA samples Chapter 7) of the sample was placed onto 18 mm VWR micro cover glass slide and dried in 0.5 T parallel magnetic field at the room temperature. Images were taken on a Zeiss LSM Meta-510 confocal microscope.

- **Analysis of magnetic luminescent nanostructures internalisation**

Primary rat cortical mixed glia cells were washed twice with ice-cold PBS buffer (137 mM NaCl, 2.7 mM KCl, 8.1 mM Na_2HPO_4, 1.5 mM KH_2PO_4, pH 7.3) and then fixed with ice-cold methanol. Cells were washed three times with PHEM buffer (60 mM PIPES, 25 mM HEPES, 10 mM EGTA, 2mM $MgCl_2$, pH 6.9). The cover slips were mounted onto glass slides for confocal microscopy (Zeiss, Axioplan 2).

2.7.15. Cytotoxicity studies

The cytotoxicity of the nanostructures was evaluated by measuring the inhibition of cell proliferation using the MTT assay (Cell Proliferation Assay, Promega). Cells were incubated for the different period of time 2 - 48 hours in the presence of nanostructures (1, 5, 10 or 20 μM). Cell viability was assessed by calculating the ratio of the number of viable cells in the nanostructure-treated culture with the non-treated culture.

2.8. References:

1.   T. Fried, G.Shemer, G. Markovich., *Advanced Materials.*, 13, (2001), 1158.

2.   S.J. Byrne, S.A. Corr, Y.K. Gun'ko, J.M. Kelly, J. M. D.F. Brougham, S. Ghosh., *Chemical Communications.*, 22, (2004), 2560.

3.   N. Gaponik, D.V. Talapin, A.L. Rogach, K. Hoppe, E.V. Shevchenko, A. komovski, A. Eychmuller,. *Journal of Physical Chemistry B*, 106, 29 (2009), 7177-7185.

4.   a) J.B. Wachtman, Z.H. Kalman., Characterization of materials., Butterworth-Heinemann., (1992). b) P.J. Goodhew, F.J. Humphreys, R. Beanland., Electron microscopy and analysis., 3rd Edition, (2001), 20-34, 66-67, 122-124.

5.   E. Lifshin., Materials Science and Technology. Characterization of Materials., Part I. WILEY-VCH. 2, (1992).

6.   E.Lifshin., X-ray characterization of materials., Weinheim, New York. Wiley-VCH, (1999).

7.   G. Gao., Nanostructures & Nanomaterials. Synthesis, properties and applications., Imperial College Press. (2004).

8.   C.G. Sammis, T.L. Henyey., Methods of Experimental Physics., Geophysics., Volume 24-A. (1987)., 343, 352-255.

9.   R.T.M. Cornell, U. Schewertmann. The Iron Oxides. Structure, Properties, Reactions, Occurrence and Uses., Wiley-VCH Verlag GmbH, (2003), 128.

10.   R.G.J. Miller and B.C. Stace., Laboratory Methods in Infrared Spectroscopy., Heyden & Son Ltd., London, New York-Rheine. 2 nd ed., (1972).

11.   J.W. Robinson, E.M. Skelly Frame, and G.M. Frame., Undergraduate Instrumental Analysis., Sixth Edition., Taylor &Francis e-Library, New York, (2005).

12.   M. Jonasz and G.R. Fournier., Light scattering by particles in water: theoretical and experimental foundations., Amsterdam; London. Academic Press, (2007).

13. J. Koetz, S. Kosmella., Polyelectrolytes and nanoparticles., Springer Berlin Heidelberg NewYork. (2007).

14. http://www.malvern.com/LabEng/technology/zeta_potential/zeta_potential_L DE.htm, 12.08.2009.

15. a) D. Rendell., Fluorescence and Phosphorescence, Analytical Chemistry by Open Learning., John Wiley & Sons. London.Crown Copyright., (1987). b) C. R. Ronda., Luminescence: from theory to applications., Wiley-VCH, Weinheim., (2007)., 3-4, c) J.R. Lakowicz., Principles of fluorescence spectroscopy. 3rd ed., (2006), New York., Springer.

16. J.R. Albani., Principles and Applications of Fluorescence Spectroscopy., Wiley-Blackwell., (2007).

17. S.J. Wright, J.S. Walker, H. Schatten, C. Simerly, J.J. Mc Carthy, and G.D Schatten,. *The Journal of Cell Science.*, 94, (1989), 617-624.

18. J.G. White, W.B. Amos, and M. Fordham., *The Journal of Cell Biology.*, 105, (1987), 41-48.

19. S.K. Das, S.U.S. Choi, W. Yu, T. Pradeep., Nanofluids., Science and technology. WILEY-VCH. (2008).

20. G. A. Webb., Nuclear magnetic resonance., *The Royal Society of Chemistry.*, 34. (2005).

21. J. Bogaert, S. Dymarkowski, A.M. Taylor., Clinical cardiac MRI: with interactive CD-ROM., Springer- Verlag Berlin Heidelberg (2005), 1-7.

Chapter 3

3.1. Preparation and investigation of cobalt ferrite–polyelectrolyte nanocomposites

3.1.1. Introduction

DNA and polyelectrolyte materials have been demonstrated to serve as excellent templates for the preparation of self assembled nanostructured materials in recent years [1-3]. Nevertheless, controlling the formation and stability of the suspensions is difficult, as the complex microscopic events of nucleation and growth proceed far from equilibrium and these processes are strongly influenced by the concentration and chemi- and physisorption characteristics, including the charge of the polyelectrolyte and the ions. Previously the formation of ordered nanowires of magnetite nanoparticles on the backbone of single stranded herring DNA, and their alignment in a magnetic field have been reported [4]. These nanowire-like assemblies also provided us with a stable magnetic fluid, which gave unprecedented high relaxivity at low field. We believe magnetic fluids of this type could have an important application as low field MRI contrast agents.

Polymers are frequently used as stabilizers and cross-linking agents in the preparation of magnetic nanoparticle assemblies [5-10]. Several researchers have found strong indications that using synthetic polyelectrolytes, which give finer control, due to their well-defined electrostatic charge and polymer length, can control the magnetic properties of the suspensions. For example, controlled clustering of magnetic particles using cationic-neutral block copolymers was reported for the preparation of magnetic fluids with improved contrast for MRI [11]. This type of block copolymer only self-assembles when there is an oppositely charged species present. When citrate-coated maghemite nanoparticles are mixed with the block copolymer, a stable suspension is formed. Two forms of the block copolymer are investigated, both with different charged monomer molecular weights.

Hatton and co-workers [10] have reported polyelectrolyte adsorbed polystyrene beads coated with maghemite nanoparticles. The beads were linked to a polyelectrolyte

patterned glass slide *via* a carbodiimide coupling reaction between the carboxylated beads (the final polyelectrolyte coating is polyacrylic acid) and the amine terminated glass surface. Chain formation was achieved by the addition of a cross-linker to form amide bonds between the beads. By applying an external magnetic field, the covalently linked beads formed chains. Variations of the applied field caused the chains to adopt different configurations, including hairpin and S-shaped loops. Random copolymers of acrylic acid, styrenesulfonic acid, and vinylsulfonic acid have also been used to stabilize magnetic nanoparticles and exert some control over the size of the resulting nanoclusters [12].

Linear chains of magnetite nanoparticles have also been prepared by using magnetic field induced self-assembly of citrate stabilized magnetite, by using poly(2-vinyl N-methylpyridinium iodide) as the template [13]. However, control over the emergent magnetic properties of the nanocluster suspensions continues to be crucial for the further development and MRI applications of nanoparticle based magnetic fluids.

Surface modification of pre-prepared magnetic iron oxide nanoparticles using polyelectrolytes has also been previously reported [14-16].

In our work we are going to develop a modified *in situ* co-precipitation approach, in which polyelectrolyte is added to the reaction mixture before the nanoparticle formation. We expect that charged macromolecules of polyelectrolyte would provide sites for particle growth and act as templates for nanoassembly formation. A polyelectrolyte as the stabilising reagent should also provide a high stability of the nanoparticles in water solution and enable us to prepare new magnetic fluids. Thus the main aim of this part of our project is to develop a new family of magnetic fluids based on cobalt ferrite-polyelectrolyte and cobalt ferrite-DNA nanocomposites using our new *in situ* approach and to demonstrate their utility for clinical MRI applications.

## 3.2. Synthesis of cobalt ferrite-PAH (CoFe₂O₄-PAH) nanocomposites

Poly(allylamine)hydrochloride (PAH) has a positively charged backbone (**Fig. 3.1**). This polyelectrolyte (average MW ~70,000) was added to a mixture of iron (II) chloride (40 mmoL) and cobalt (II) nitrate (20 mmoL) salts solution in an appropriate ratio in water. Then base (NH₄OH, 10 mL, 10 M) solution was added and the mixture

was heated to 80 °C for 2 hours resulting in the formation of black precipitate. The precipitate was then washed with Millipore water and separated by centrifugation. Finally the black product was dried under vacuum. The synthetic scheme is presented in **Fig. 3.2.** In this case PAH serves as a positively charged stabiliser, which can prevent the magnetic particles from aggregation and improves the dispersibility of the particles allowing them to form stable colloids [16-18]. All syntheses were repeated 3 times. The products have been characterised by XRD, FTIR and Raman spectroscopy, TEM and magnetisation measurements (see below).

In parallel, a series of experiments were performed using the same synthetic conditions for the preparation of PAH stabilised cobalt ferrite nanoparticles using 2 M NaOH as an oxidizing agent. Unfortunately, lower synthetic yields (~42 %) were obtained compared to the experiments where 10 M NH_4OH was used (Yields: ~72.3 %). This could be due to lower molarity of NaOH (concentration) in the system, which prevented full co-precipitation of all metal ions. Thus, 10 M NH_4OH was used for the future syntheses.

$$\left[\begin{array}{c} \cdot \ HCl \\ CH_2NH_2 \\ | \\ -\,CH_2CH\!\!-\!\!\!- \end{array} \right]_n$$
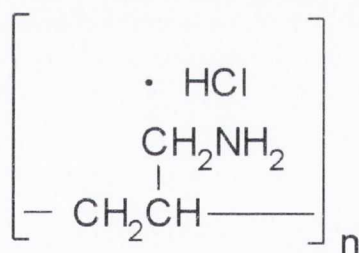
Figure 3.1. Chemical structure of poly(allylamine) hydrochloride (PAH).

Various concentrations of PAH in Millipore water were used to investigate and optimise the conditions for the preparation of cobalt ferrite nanoparticles of a uniform size and distribution. The main variable factor involved in the preparation of these particles was the ratio between the concentration of cobalt and iron solution and the concentration of polyelectrolyte. We have found that the addition of PAH results in a substantially improved stability of the particles in solution. Without the addition of PAH, cobalt ferrite particles are not stable in solution and can be easily precipitated. It was calculated that used PAH (average MW ~70,000 amu) has 750 head groups

(charge) per unit. The conditions and results of the particle size analysis (from TEM) are presented in **Table 3.1** below.

Table 3.1. Summary of results and analysis of the particle size for selected cobalt ferrite - PAH samples.

Sample	Total metal concentration (mol/L)	PAH concentration (mol/L)	Metal/ PAH ratio	Average particle size (nm)
RT100	3×10^{-3}	1.43×10^{-7}	2.1×10^{4}	20 ± 8
RT102	1.5×10^{-3}	1.43×10^{-8}	1.05×10^{5}	30 ± 13
RT103	4.5×10^{-3}	3.57×10^{-8}	1.26×10^{5}	39 ± 10
RT104	3×10^{-3}	1.43×10^{-8}	2.1×10^{5}	28 ± 17
RT105	1.5×10^{-3}	2.86×10^{-9}	5.2×10^{5}	87 ± 41
RT75	4.5×10^{-3}	0	-	74 ± 13
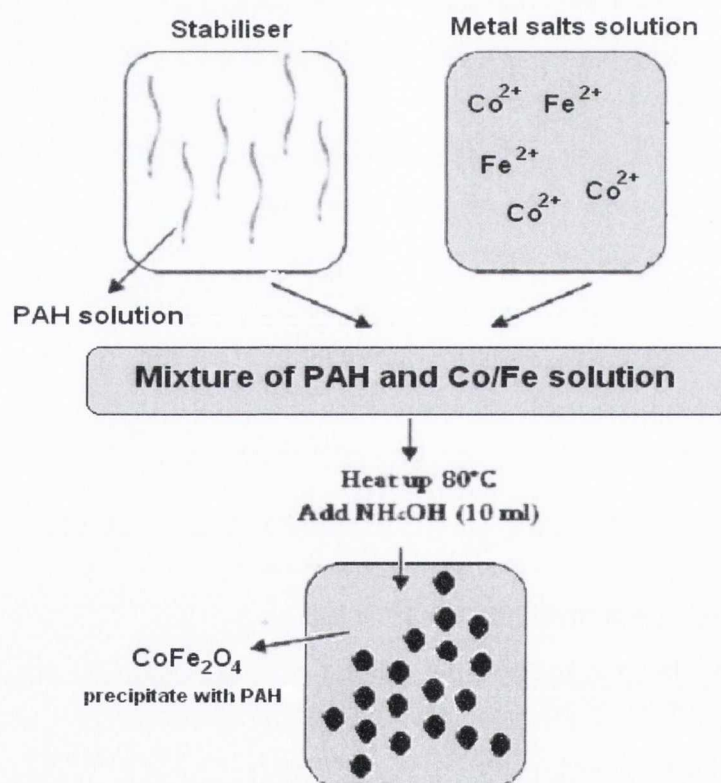
Figure 3.2. Schematic presentation of the preparation of cobalt ferrite-PAH particles.

3.2.1. Transmission electron microscopy (TEM) studies of PAH stabilised cobalt ferrite nanoparticles

As was mentioned above TEM was used as the main method to analyse particle size and distribution. TEM images of selected samples of cobalt ferrite-PAH composites are presented in **Fig. 3.3-3.4**.
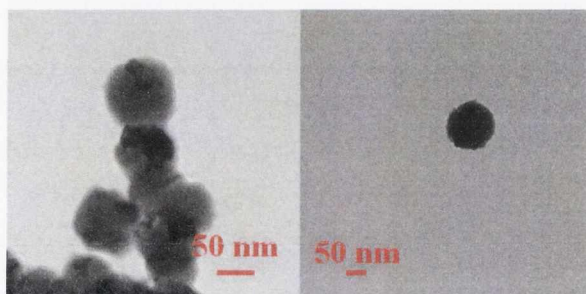
Figure 3.3. TEM images of functionalised cobalt ferrite samples without PAH stabiliser (sample **RT75**).

To investigate the effect of the PAH on the resulting particle size, a control sample without stabiliser (RT75) was prepared. The main difficulty in assembling and maintaining a nanometer scale material from molecular clusters is the tendency of aggregation to reduce the energy associated with the high ratio of surface area to volume. Without a stabiliser, the cobalt ferrite nanoparticles come into direct contact and tend to form aggregates. According to TEM an average particle size of cobalt ferrite prepared without PAH was 75 ±13 nm (**Fig. 3.3**). It was found that the particle size depends on metal/polyelectrolyte ratio. The addition of PAH (see **Table 3.1**) resulted in significantly reduced particle size, down to 20 ±8 nm. The smallest particles were synthesised at metal/polyelectrolyte ratio of 2.1×10^4. In this case the smaller size of the particles can be explained by the surface stabilisation and passivation by PAH coating. This prevents coalescence and further particle growth. In general an increase in the metal/polyelectrolyte ratio resulted in particle growth (up to 87 ± 41nm) and in a broader particle size distribution (higher standard deviation) (**Fig. 3.4. d).** We also observed some aggregation of nanoparticles for all samples most likely due to cross-linking by polyelectrolyte molecules. The aggregation of these nanoparticles may be ascribed to a combination of the magnetic interactions between the nanoparticles and

chemical cross-linking due the presence of PAH. The interaction of functional groups of the PAH with the surface of the particles can therefore play an important role. At highest PAH concentrations, PAH can affect the size of the particles. This involves their adsorption on the surface sites of the growing particles providing a better stability of the particles in solution. This stability of cobalt ferrite suspension is mainly due to electrostatic repulsions between charged particles. The best electrostatic stabilisation was achieved by functional groups of PAH adsorbed on particles at the pH 12. The stability of these solutions containing PAH was very high. In order to obtain powders for the further characterisation of structure, morphology, and magnetic properties of the sample, we used organic solvents (e.g., ethanol or acetone) to initialise the precipitation of PAH stabilised particles from these colloidal solutions.
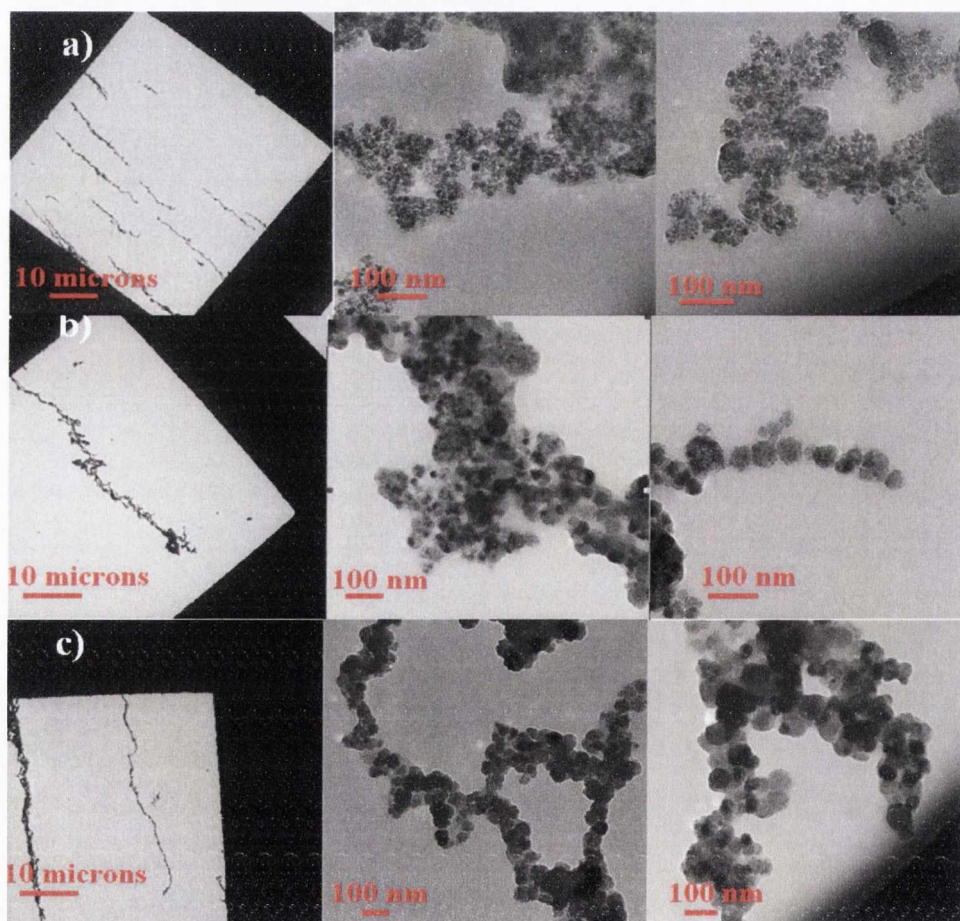
Figure 3.4. TEM images of selected cobalt ferrite-PAH nanocomposites in 0.5 T parallel magnetic field: (a) **RT104**, Metal/PAH ratio 2.1×10^5, (b) **RT100**, Metal/PAH ratio 2.1×10^4 (c) **RT105**, Metal/PAH ratio 5.2×10^5.

3.2.2. Fourier Transformed Infrared spectroscopy (FTIR) spectroscopy studies of PAH stabilised cobalt ferrite nanoparticles

FTIR spectra were recorded for all samples using KBr disk and have showed stretching frequencies at 570-580 cm^{-1}, which represent Fe-O and Co-O bonds, and a t 3440-3460 cm^{-1}, which represent water and OH^{-} groups (**Fig. 3.5**). According to literature data the faint absorption band at 667.05 cm^{-1} can be assigned to the stretching vibration mode of Co-O bond [5]. The effect of the ratio between the concentration of cobalt and iron solution and the concentration of PAH in samples. These spectra differ from those observed for cobalt ferrite particles prepared without any PAH stabiliser.
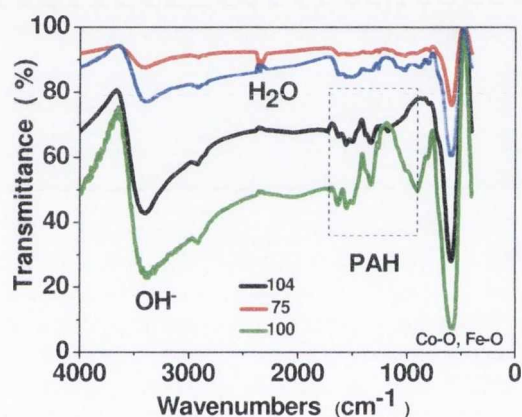
Figure 3.5 . FTIR spectra of selected cobalt ferrite-PAH samples. **Key**: (black) **RT104** Metal/PAH ratio 2.1x10^{5}, (red) **RT75** no PAH, (green) **RT100** Metal/PAH ratio 2.1x10^{4}, (blue) **RT100** total metal solution concentration 3x10^{-3} mol/L.

3.2.3. Raman spectroscopy results of PAH stabilised cobalt ferrite nanoparticles

Raman spectroscopy studies were carried out on all cobalt ferrite-PAH composites. CoFe$_2$O$_4$ has a cubic inverse spinel structure with O$_h^7$ (F3dm) space group. Typical Raman spectra (**Fig. 3.6**) of selected PAH stabilised cobalt ferrite sample show the presence of five bands at 200, 315, 476, 626, 685 cm^{-1}, which are in good agreement with five Raman active optical modes [19].
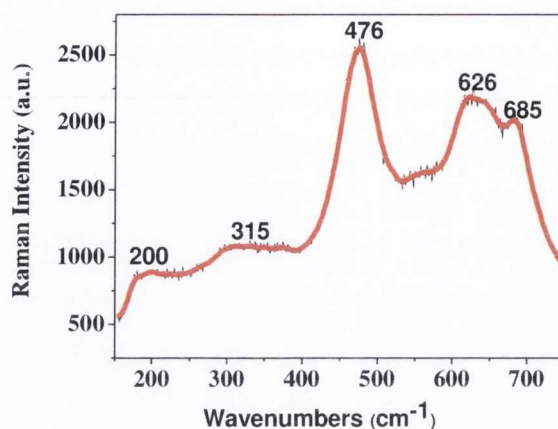
Figure 3.6. Typical Raman spectra of cobalt ferrite-PAH nanocomposite. (sample RT 100)

3.2.4. X-ray powder diffraction (XRD) analysis of PAH stabilised cobalt ferrite nanoparticles

X-ray of PAH functionalised cobalt ferrite nanocomposites (**Fig. 3.7**) showed typical spinel diffraction patterns [20] corresponding to the cobalt ferrite phase for all the samples. The reflection peaks can be readily indexed to the (220), (311), (400), (511) and (440) planes of non-stoichiometric spinel $CoFe_2O_4$ with a cubic symmetry .The sharpness of the major peaks and the diffraction are probably due to an increase in grain size [21].

At the same time this difference in intensity of the major peaks in XRD pattern of pure cobalt ferrite sample **RT 75** (**Fig. 3.7 a)**) and PAH functionalised cobalt ferrite nanoparticles are mainly due to the reduction of the crystallite sizes (increase of the surface area) and presence of PAH. The average size of the nanoparticles was not determined using Scherrer's formula due to very weak intensity and broadening of many of the characteristic peaks.
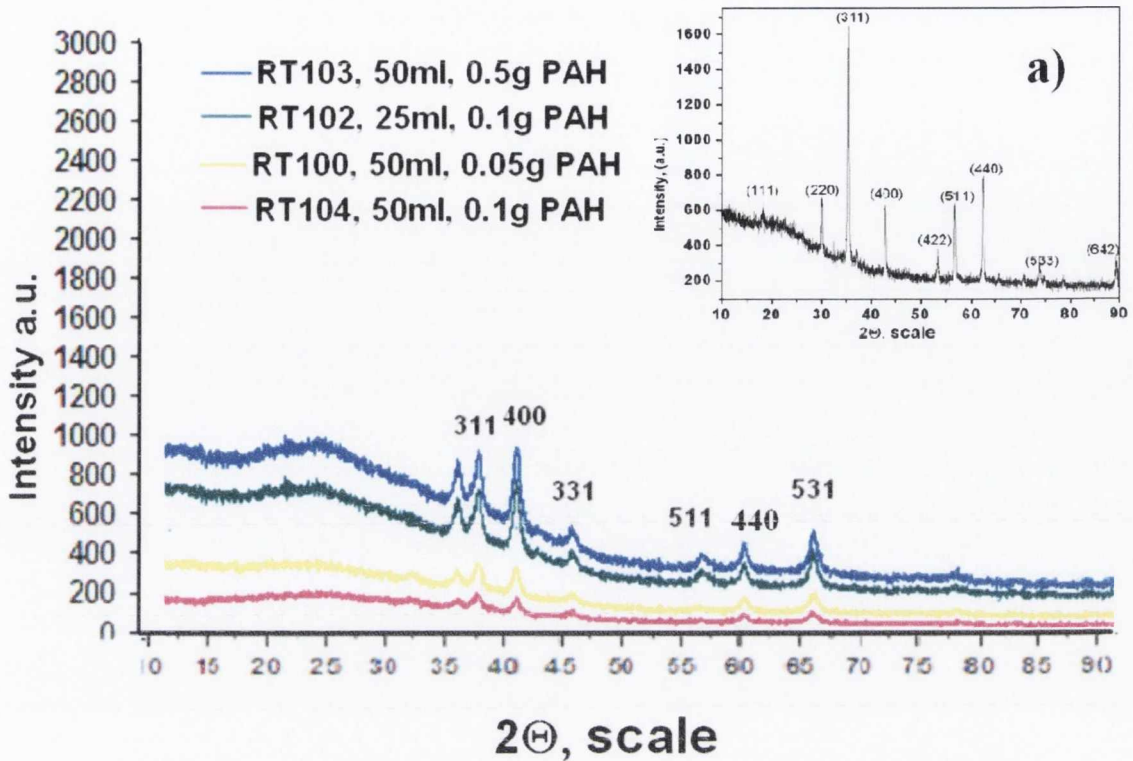
Figure 3.7. XRD patterns (λ=1.54056 Å) of cobalt ferrite-PAH samples. **Key**: (navy) **RT102**, Me/PAH ratio 1.05×10^5 (blue) **RT103**, Me/PAH ratio 1.26×10^5 (yellow) **RT100**, Me/PAH ratio 2.1×10^4, (magenta) **RT104**, Me/PAH ratio 2.1×10^5. a) Insert shows XRD patterns for sample **RT75** (no stabiliser).

In the XRD pattern of these samples, the strongest peak at $\theta = 35.5°$ corresponds to the (311) plane of the cubic structure of $CoFe_2O_4$ [22-24]. The presence of the peak around 32-33° in all XRD patterns is due to the machine contamination.

3.2.5. Investigation of magnetic properties of PAH stabilised cobalt ferrite nanoparticles using Superconducting quantum interference device magnetometer (SQUID) magnetometer

Fig. 3.8 shows typical magnetic hysteresis curves of cobalt ferrite [25]. The powders exhibited saturation magnetisation (M_s) and coercivity (H_c) in the range of 12–80 Am^2kg^{-1}, depending on the Metal/PAH ratio in solution. The magnetisation of the sample **RT105** is much higher and tend to be saturated at a high field. This can be

67

explained by the fact that this sample has the highest metal/polyelectrolyte ratio and the largest particle size. The smallest magnetisation value, for the sample **RT102** could be attributed to the variation of the average particle sizes in the sample (30 ±13 nm). When the sample consists of small nanoparticles, the total magnetisation decreases with decreasing particle size because some of the nanoparticles may be superparamagnetic (state where each of the particles acts as a spin). Overall, the saturation magnetisations observed for the samples is in good agreement with the reported value of 80 Am^2/kg for the pure inverse $CoFe_2O_4$ phase. A Summary of data on cobalt ferrite particles is presented in **Table 3.2**.
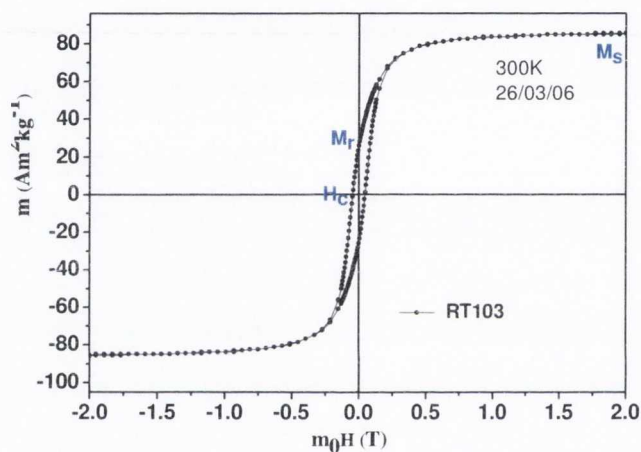
Figure 3.8. Magnetisation curve versus magnetic field for cobalt ferrite powders. Sample **RT103** total metal concentration 4.5×10^{-3} mol/L.

Table 3.8. Summary of magnetisation data for selected functionalised Cobalt ferrite-PAH samples.

Name	Mass (mg)	M_s (Am^2kg^{-1})	M_r (Am^2kg^{-1})	M_r/M_s	H_c (mT)	Average size of the primary particles by TEM (nm)
RT100	1.8	47	2	0.04	3	20 ±8
RT102	1.8	12	2.5	0.21	25	30 ±13
RT103	1.6	80	12	0.15	20	39 ±10
RT104	1.8	74	10	0.14	20	28 ±17
RT105	1.6	98	35	0.36	70	87 ±41
RT75	1.9	100	29	0.29	0	74 ±13

The coercive field (H_c) is a very important parameter in particular for magnetic storage media applications. The H_c value depends on the various factors including shape-dependency of the magnetic substances. In our samples H_c was in the range of 0.0452–0.036 kOe, depending on the PAH stabiliser concentration in the total metal concentration in solution. Very small changes in the coercivity value for samples **RT102**-**RT104** were observed. This could be attributed to the reduced particle size effect, a behaviour quite characteristic for the small particle systems about or below the critical single-domain size [26]. Only the sample **RT100** (**Fig. 3.9**) with the smallest particle size, did not show any hysteresis and almost zero coercivity indicating that these particles were superparamagnetic at room temperature (300 K). The variation of the saturation magnetisation with different concentrations of PAH or interactions between particles is possibly due to the rearrangement of the cation distribution, i.e. the degree of inversion, in $CoFe_2O_4$ in which there is the exchange of Co^{2+} and Fe^{3+} ions in the lattice [27, 28].
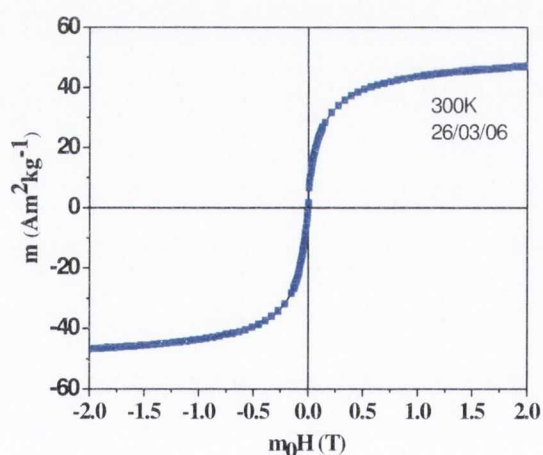

Figure 3.9. Magnetisation curves versus magnetic field for cobalt ferrite-PAH samples. **Sample RT100** total metal concentration 3×10^{-3} mol/L.

3.3. Preparation of cobalt ferrite - DNA nanocomposites

DNA can serve as a potential template for nanoassemblies due to its polymeric linear morphology and repeating structure (a helical pitch of 3.4 – 3.6 nm) and the variety of appropriate functional groups [29]. It is intriguing to consider whether DNA-

conjugated cobalt ferrite nanoparticles could serve as target-directed MRI contrast agents for cancer diagnosis. In this project we have used a long chain of single stranded herring DNA as both a stabiliser and template for the preparation and assembly of cobalt ferrite particles. DNA has an overall negative charge due to the polyphosphate chemical backbone [29].

The mixture of ssDNA and Co/Fe solution was heated up to 40 °C and an excess of aqueous ammonia solution was injected by syringe. The black precipitate was heated up to 80 °C into the oil-bath for one hour under argon and slowly cooled to the room temperature. The solvent was removed and the black precipitate was washed with Millipore water until neutral pH and then dried under vacuum at room temperature. The synthetic procedure is presented in **Fig. 3.10.**
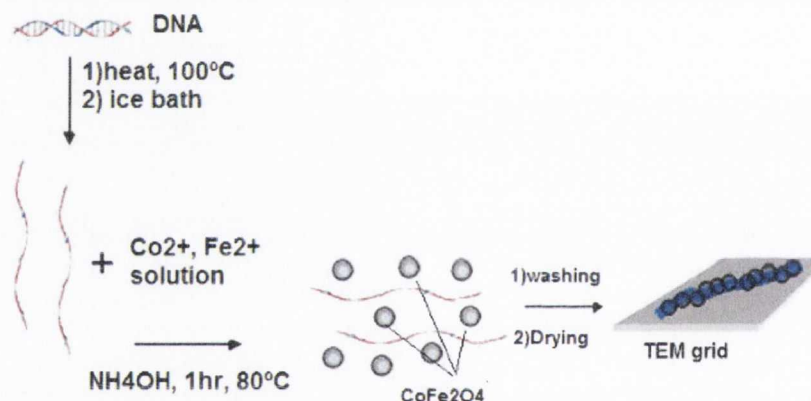
Figure 3.10. The schematic presentation of the preparation cobalt ferrite -single stranded DNA nanocomposites.

3.3.1. A statistical analysis for the preparation of cobalt ferrite-DNA nanocomposites

A statistical analysis of the preparation of functionalised cobalt ferrite-DNA composites was carried out in order to optimise the experimental conditions and to achieve particles with a uniform size distribution. The particle size was studied by TEM. The main variable factors involved in the preparation of these particles were the concentrations of metal (C(Fe/Co) and stabiliser in solution. In our work we have used 2^2 factorial design for experiments, where the factors can be changed simultaneously in

a systematic way (**Fig. 3.11**). This allowed us to check when we are approaching the optimum conditions in term of the particle size and distribution.

Summarised TEM data of experimental results and synthesis the conditions for prepared cobalt ferrite – DNA composites are presented in the **Table 3.3**.
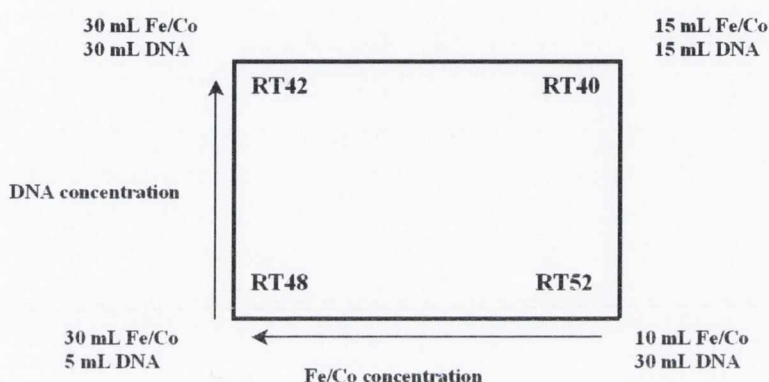
Figure 3.11. Statistical design for the preparation of cobalt ferrite composites with DNA. Total metal concentration 6×10^{-3} mol/L, DNA concentration 0.06 g/L.

Table 3.3. Summary of results of the conditions and analysis of the particle sizes (from TEM) for selected cobalt ferrite – DNA composites.

Sample	DNA in a sample (g)	Total Metal concentration (M)	Metal/DNA ratio	Average particle size (nm)
RT75	0	6×10^{-3}	-	74 ± 13
RT40	0.03	3×10^{-3}	0.1	49 ± 23
RT51	0.06	6×10^{-3}	0.1	49 ± 17
RT41	0.04	2×10^{-3}	0.05	57 ± 25
RT54 (rods)	0.045	6×10^{-3}	0.134	63 ± 20
RT50(rods)	0.04	6×10^{-3}	0.15	70 ± 56
RT52(rods)	0.03	6×10^{-3}	0.2	104 ± 42
RT42	0.02	6×10^{-3}	0.3	112 ± 73
RT47	0.015	6×10^{-3}	0.4	138 ± 54
RT48(rods)	0.0086	6×10^{-3}	0.7	227 ± 51

Selected TEM images of cobalt ferrite-DNA particles presented in **Fig.3.12, 3.13**. Analysing the results from **Table 3.3**, we found that particle size and distribution depend on the metal/DNA ratio. Higher metal/DNA ratios result in an increased average particle sizes and also in a broader particle size distribution. The smallest

average particle size (49±18 nm) was achieved for 0.1 metal/DNA ratio. High (e.g. 0.7) metal/DNA ratios gave quite big particles with broad distribution of sizes to 227±51 nm. We believe that higher concentration of DNA produced better coating of small nanoparticles (due to bonding to metal oxide surface), which preserves them from aggregation and further growth, providing greater stabilisation. However, some aggregation of nanoparticles into assemblies still observed at high DNA concentrations. This is caused by some cross-linking of cobalt ferrite nanoparticles by DNA strands. We have found that these assemblies can be aligned into linear parallel chains by drying the samples in an external perpendicular magnetic field (**Fig. 3.12** and **Fig. 3.13**). Only the sample **RT40** with the very low metal/DNA ratio did not show any clear chains of the particles in the parallel magnetic field (**Fig. 3.12 a**) and **Fig. 3.12 a**) (**i**)).
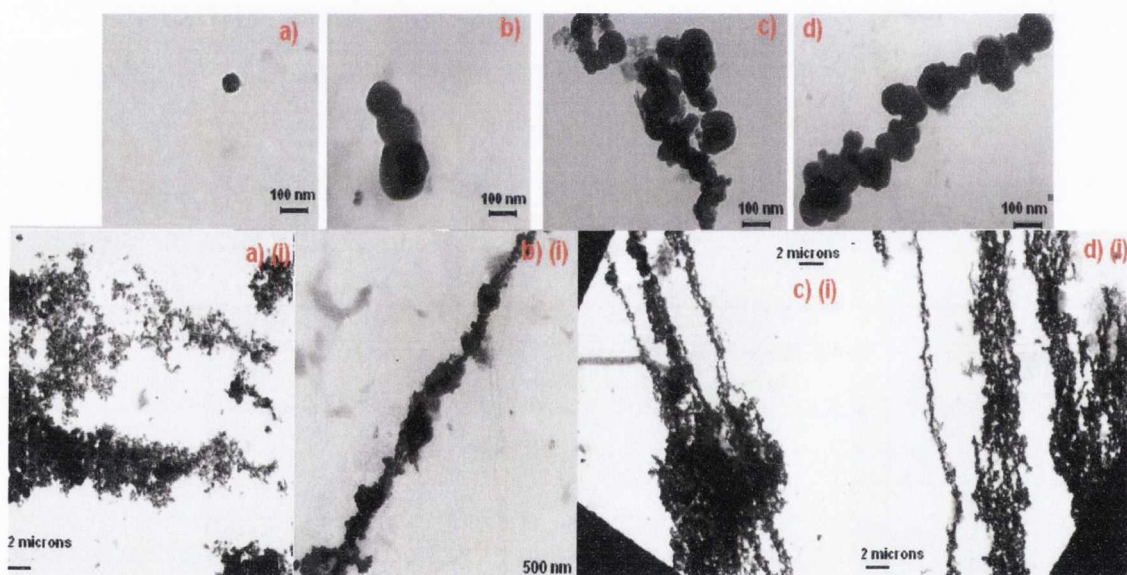
Figure 3.12. TEM images of samples for statistical study. (a) **RT40**, (b) **RT41**, (c) **RT42**, (d) **RT47** samples without presence external perpendicular 0.5 T magnetic field, (i) samples in the solution in perpendicular magnetic field.

TEM images show variations in particle size of the selected samples (**Fig. 3.14**). Cobalt ferrite - DNA nanocomposites in turn form long-range self assembles (26.6± 6 micron) under perpendicular external magnetic field. Note: that without presence of magnetic field the formation of much shorter in length self-assemblies was observed.
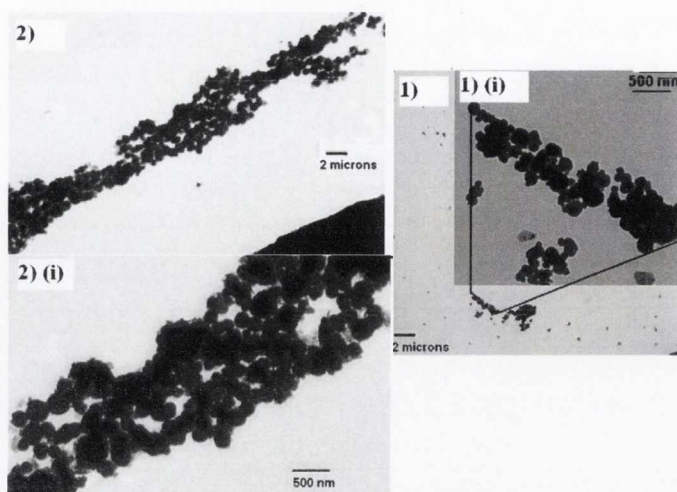
Figure 3.13. TEM images for statistical study. Sample **RT42** dried in a perpendicular magnetic field (i) samples in the solution without magnetic field increasing magnification.

Fig. 3.14 b) shows single spherical non-functionalised cobalt ferrite particles. Due to a strong magnetic interaction between single non-functionalised cobalt ferrite nanoparticles, they are aggregated together and as a result form lager particles. A lower concentration of metal solution implies the formation of bigger aggregates shown in **Fig. 3.14 a)**. Regarding these results, other samples were prepared using higher concentration of Fe/Co solution (6×10^{-3} mol/L) and variable concentrations of DNA for the following samples via the same experimental procedure.
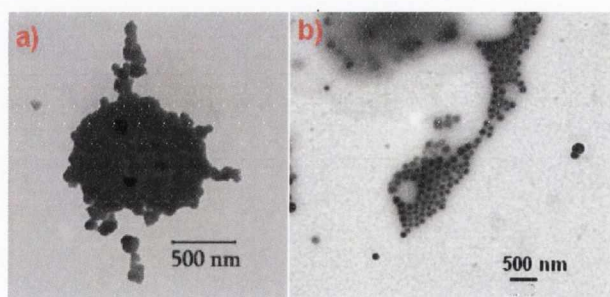
Figure 3.14. TEM images of $CoFe_2O_4$ particles prepared without DNA (a) 1.5×10^{-3} mol/L total metal concentration, (b) 6×10^{-3} mol/L total metal concentration.

An external parallel magnetic field (0.5 T) was applied to the samples to align the particles on TEM grids. TEM pictures of selected samples are presented in **Fig. 3.15**. Particles in aggregates in a particular samples vary in size from 300 to 500 nm (**RT40**,

73

RT41) and a wide size distribution spreading from 100 nm to 500 nm (**Fig. 3.15 c)**). However, the shape (spherical) of the particles seems to be relatively uniform for each sample.
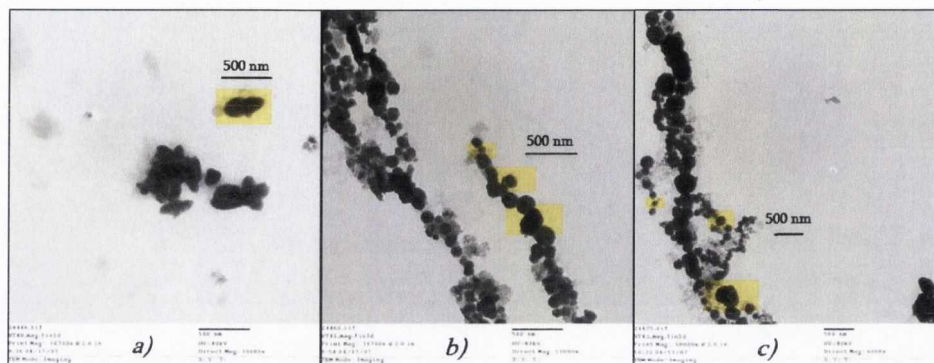
Figure 3.15. TEM images of the functionalised cobalt ferrite samples in 0.5 T parallel magnetic field (a) **RT40** (0.03 g DNA), (b) **RT41** (0.04 g DNA), (c) **RT42** (0.03 g DNA). (scale bar 500 nm).

Non-uniformly shaped particles occur when the nucleation and growth rates during the reduction process (**Fig. 3.16 a), b)**). Particles may be seen to be of different sizes and shapes (oval, rods). TEM images show quite big particles and nanorods, which are ranging in length from 100 to 250 nm. **Fig. 3.16 b)** presents **RT52** sample the size distribution is less wide (from 100 to 200 nm). Some nanorods are also observed in samples **RT51** and **RT54**, see **Fig. 3.16** highlighted **c)** and **d)**.
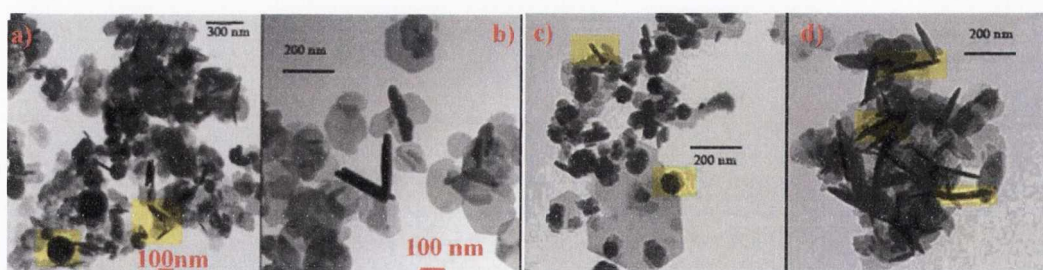
Figure 3.16. TEM images of cobalt ferrite samples without magnetic field. (a-b) **RT52** (0.03 g DNA), (c) **RT 51** (0.06 g DNA), (d) **RT 54** (0.045 g DNA).

The presence of the rod-like or needle- like structures can be explained by the formation of some amount of γ-Fe_2O_3 phase. It has been previously reported [27] that γ-

Fe_2O_3 nanoparticles can be formed as a side product in the preparation of cobalt ferrite at 80 °C, which have further been confirmed by Raman spectroscopy studies (see below).

PCS data showed different results with calculated size from TEM. **Fig. 3.17** (**Appendix 1**) represents the average hydrodynamic radius of size distributions of non-functionalised and functionalised cobalt ferrite-DNA composites in Millipore water and the TEM gives the average particle size of the dry media. The hydrodynamic radius of non-functionalised cobalt ferrite particles in Millipore water had an average value of 1070 nm (PDI = 0.119). Combining both data results (TEM, PCS) the behaviour of non-functionalised cobalt ferrite nanoparticles in solution could be explained by the formation of large aggregates due to the absence of the stabiliser. The evidence of the instability of the nanoparticle in suspension could be explained by the large average size of the nanoparticles, which was on the limit of detection for the machine. The average R_H value could be markedly reduced from 1000 to 250 nm even with a small amount of DNA (0.03 g, RT40) content in solution The sample RT42 showed a slightly higher value for average particle size probably due to cross linking or a larger standard deviation in the sample (see Table 3.3). For a better understanding of the role DNA concentration plays in cobalt ferrite solution stability, various concentrations of DNA were used for sample preparation. The effect of the DNA concentration in the sample was examined to clearly determine the relationship between DNA concentration and size of the particles.
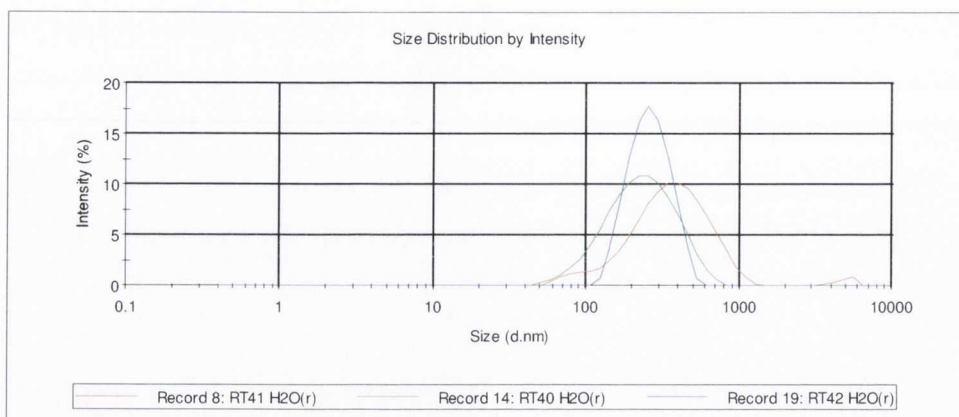
Figure 3.17. Hydrodynamic radius of size distributions of cobalt ferrite-DNA composites in Millipore water. (b) (green) **RT40** sample (0.03 g DNA), (red) **RT41** sample (0.04 g DNA), (blue) **RT42** sample (0.03 g DNA).

The average diameter of the particles size increased due to higher DNA concentration and agglomerates of primary particles (5–20 nm). The average of the nanoparticles in water 1050 nm, see **Appendix 2**. As PCS is a measure of the hydrodynamic size, its value reflects the presence of the DNA coating as well as any solvent (water) molecules associated with the tumbling particle. At the same time formation of chain-like assemblies and present of DNA in solution had significant influence on PCS performance (specific limit of detection).

3.3.2. FTIR spectroscopy results of cobalt ferrite-DNA nanocomposites

FTIR measurements have been performed on selected samples and **RT75** in addition to XRD analysis. The analysis of **RT75** shows the difference between samples functionalised with DNA or without DNA measured by FTIR spectroscopy (**Fig. 3.18**).
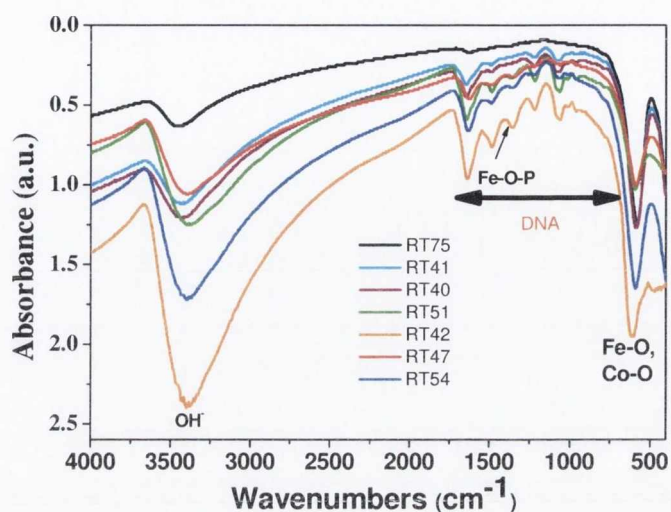
Figure 3.18. FTIR spectra of selected samples **Key**: (purple) **RT40** 0.03 g DNA, (cyan) **RT41** 0.04 g DNA, (orange) **RT42** 0.02 g DNA, (red) **RT47** 0.015 g DNA, (green) **RT51** 0.06 g DNA, (blue) **RT54** 0.045 g DNA, (black) **RT75** no DNA.

One of the strongest bands revealed by the FTIR corresponds to iron oxygen and cobalt oxygen bonds (Fe-O near 580 cm^{-1} and Co-O near 667 cm^{-1}). The single characteristic peak of Co-O bond is hidden due to the proximity with the peak of Fe-O bond (**Fig. 3.18**). Fe-O-P stretch 1157 cm^{-1} for DNA [4]. FTIR results for **RT75** sample reveal that this pattern does not show any peaks between approximately 740 and 1350 cm^{-1} as do other spectra in the **Fig. 3.18**. The peak between 3400 and 3500 cm^{-1} is attributed to the presence of OH$^-$ groups.

3.3.3. Raman spectroscopy studies of cobalt ferrite-DNA nanocomposites

Raman analysis of cobalt ferrite–DNA nanocomposites confirmed the formation cobalt ferrite ($CoFe_2O_4$) phase as expected. The main characteristic peaks of cobalt ferrite are present in all Raman spectra (~200, 315, 470, 627 and 688 cm^{-1}) (**Fig.3. 19**). However, the Raman spectrum of **RT51**, which showed the presence of nanorod-like structures in TEM, was rather different. In addition to the cobalt ferrite peaks, there were new peaks around 350 and 550 cm^{-1} (**Fig. 3.19**) due to presence of another phase, namely maghemite (γ-Fe_2O_3). Similar Raman spectra were also observed for **RT52** and **RT54** samples. Main DNA peaks were between 800-1700 cm^{-1}. The characteristic

77

symmetrical stretching vibrations of the orthophosphate (PO_2^-) and phosphodiester (C—O—P—O—C) group vibrations [28], generate intense Raman bands not present in the Raman spectra because spectra were taken in 900-100 cm^{-1} region.
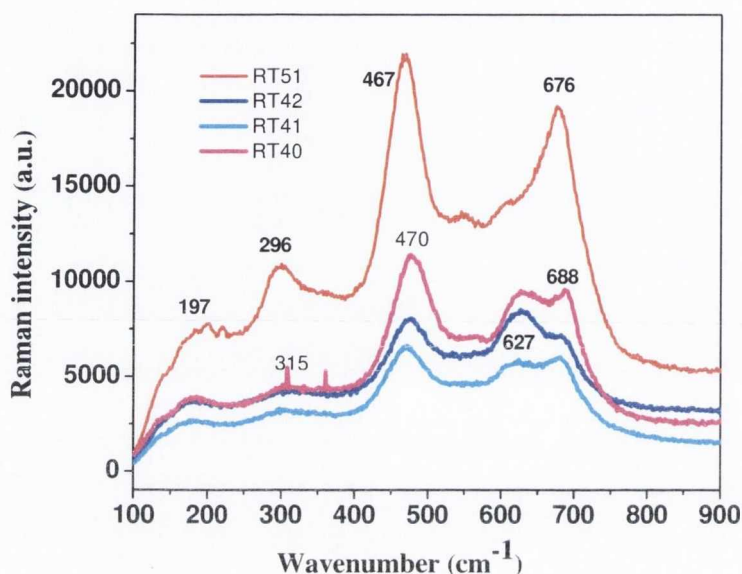
Figure 3.19. Raman spectra of selected cobalt ferrite-DNA nanocomposites. **Key**: (magenta) **RT40** 0.03 g DNA, (cyan) **RT41** 0.04 g DNA, (blue) **RT42** 0.02 g DNA, (red) **RT51** 0.06 g DNA.

3.3.4. XRD analysis results of cobalt ferrite-DNA nanocomposites

The main characteristic peaks (220), (311), (400), (511), (440) from the XRD pattern correspond to cubic spinel cobalt ferrite (**Fig. 3.20**). The XRD analysis for selected samples reveals that **RT 41** and **RT 42** have several similar peaks with **RT 75**. Thus XRD confirms the formation of cobalt ferrite phase. However, as expected peak intensities decrease with increasing DNA content in a sample.
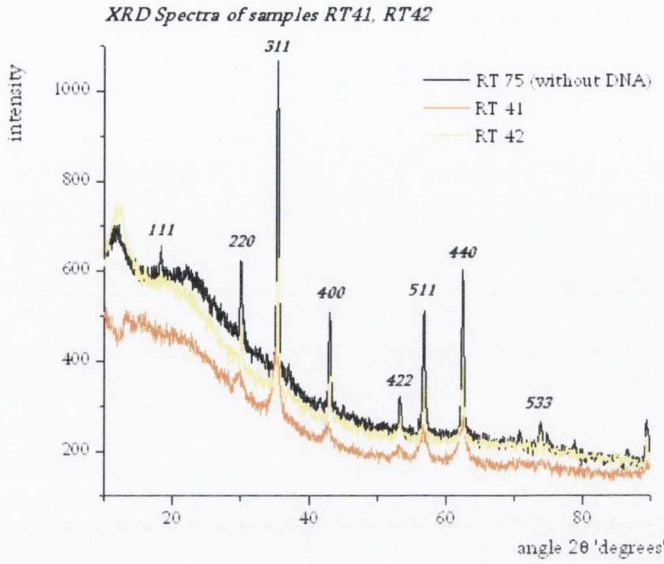
Figure 3.20. XRD patterns of selected samples (powders). **Key**: (orange) **RT41** 0.04 g DNA, (yellow) **RT42** 0.02 g DNA, (black) **RT75** no DNA).

Fig.3.21 shows a small shift of the main (311), (400), (511), (440), (533) peaks. This shift is about a half-angle caused by the presence of a small ammount of FeOOH phase [27].
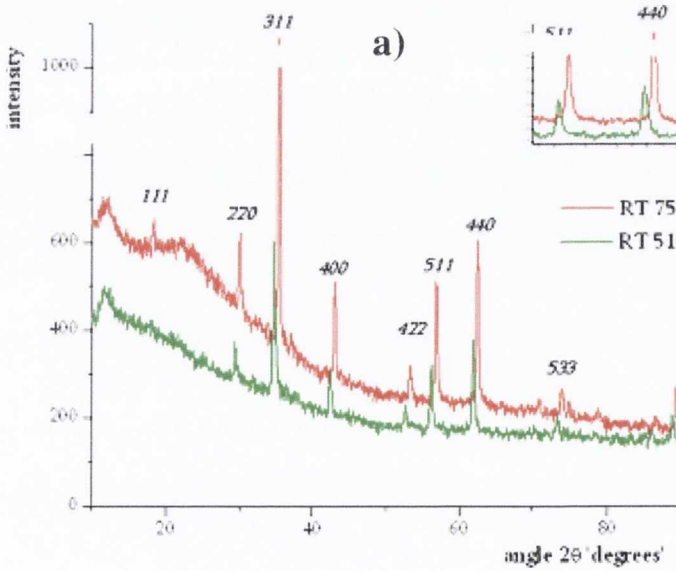
Figure 3.21. XRD patterns of selected samples **Key**: (green) **RT51** (0.06 g DNA) compared with the bulk $CoFe_2O_4$ (**RT 75**) (red).

The small shift of peaks is still present but does not disprove the conclusion about the nature of the material. Moreover, a new peak appears in the pattern of the sample **RT52** at $2\theta = 40°$ as shown by the enlargement in the top right hand corner of the **Fig. 3.22**. This peak detected coresponds to some presense of Fe_2O_3 phase [27]. The XRD data are consistent with Raman spectroscopy results and confirm the presence of an extra phase in the sample.
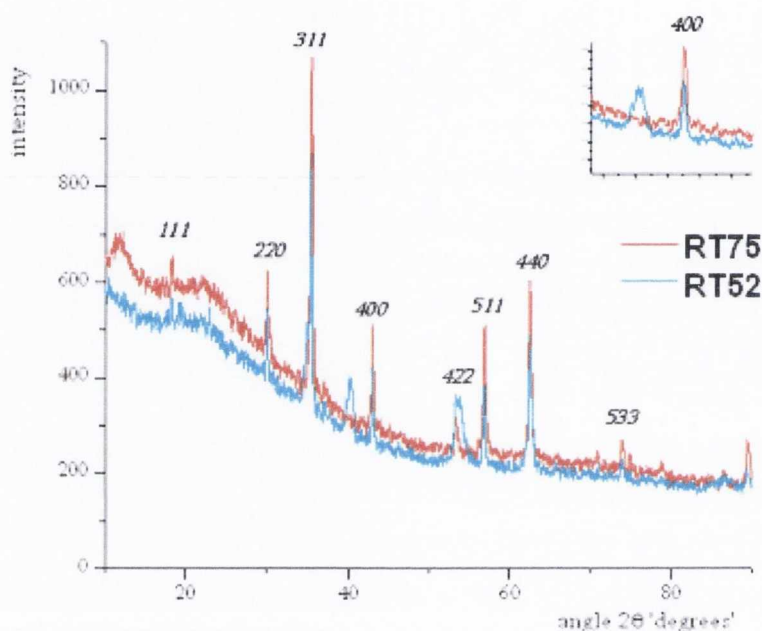
Figure 3.22. XRD patterns of functionalised cobalt ferrite- DNA nanocomposites. **Key**: (blue) **RT52** (0.02 g DNA), (red) **RT 75** bulk cobalt ferrite.

3.3.5. Thermogravimetric Analysis (TGA) of cobalt ferrite-DNA nanocomposites

The attachment of the DNA on the surface of the $CoFe_2O_4$ particle was further confirmed by TGA. The TGA for the pure $CoFe_2O_4$ and functionalised $CoFe_2O_4$ - DNA composites were performed. **Fig. 3.23 a)** and **b)** displays the samples weight loss as a function of temperature for **RT75** and functionalised cobalt ferrite-DNA sample. In the **RT75** sample, which does not contain DNA, TGA gave only one peak at 371 °C. Approximately 3 % weight loss was attributed to the dehydroxylation of the $CoFe_2O_4$ surface and dehydration in the process of crystal aggregation at this

temperature. For $CoFe_2O_4$-DNA nanocomposites (**Fig. 3.23**) the TGA has a shown more complex picture with several peaks. The curve of the cobalt ferrite- DNA sample consists of three steps degradation with total weights losses of ~ 14 %. The first step was observed around 60 °C (loss of adsorbed H_2O) then two weights losses at 168 ° C and 298 °C to the air oxidation of the total organic matter (DNA) on the particle surface. Thus TGA results clearly prove the presence of DNA in the samples.
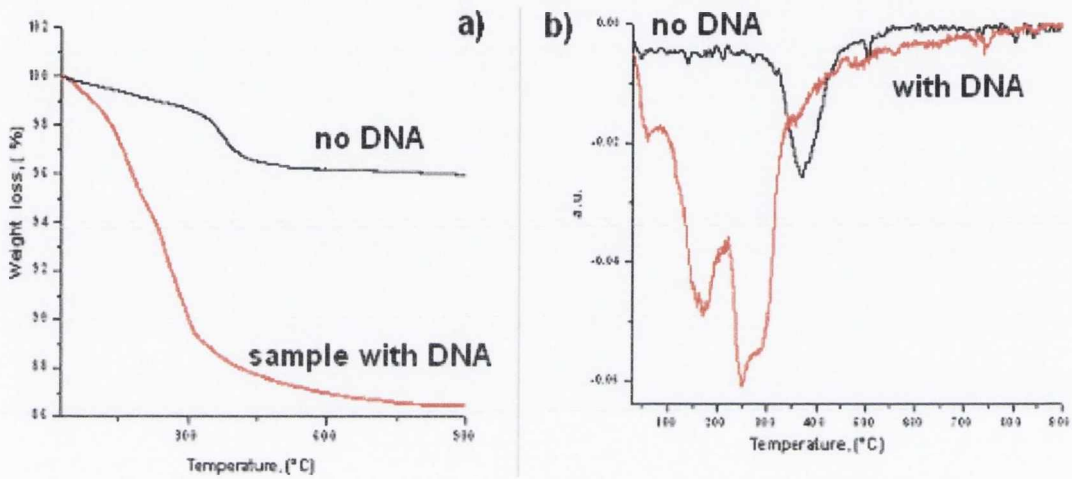
Figure 3.23. Typical TGA curves for the pure $CoFe_2O_4$ and selected functionalised $CoFe_2O_4$ - DNA sample. **Key**: (a) (red) 0.03 mg DNA in a sample, (black) pure cobalt ferrite (**RT75**) (b) D-TGA curves (red) functionalised cobalt ferrite-DNA sample, (black) pure cobalt ferrite **RT75**.

3.3.6. Magnetic measurements of cobalt ferrite-DNA nanocomposites using SQUID magnetometer

Figs. 3.24 and **3.25** show typical magnetisation curves of pure cobalt ferrite particles and selected $CoFe_2O_4$-DNA nanocomposites. Magnetisation measurements have demonstrated the clear ferromagnetic nature of the stabilised cobalt ferrite particles.
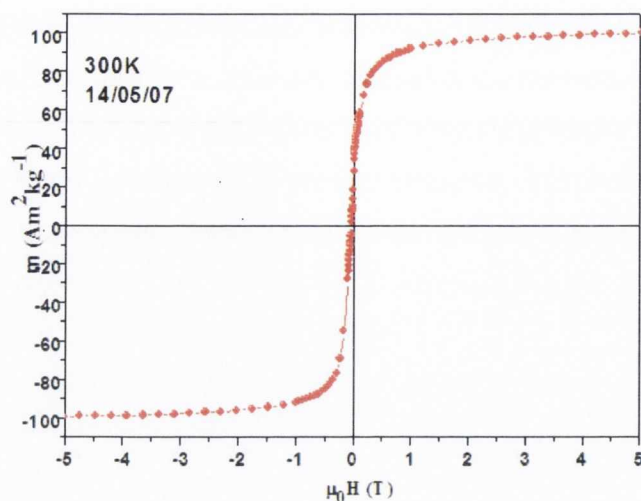
Figure 3.25. Magnetisation curves versus magnetic field for no-functionalised $CoFe_2O_4$ nanoparticles. (**RT75**)

Magnetisation (M_S) is 120 Am^2kg^{-1} and 104 Am^2kg^{-1} at respectively 4 and 300 K. These functionalised cobalt ferrite particles demonstrate hysteresis behaviour at both temperatures but at 4 K it reaches a higher value of (H_C) at 0.26 T, see **Fig. 3.26**. This behaviour can be explained by the presence of both small superparamagnetic nanoparticles as well as large ferromagnetic aggregates. The large moment is attributed to an unusual cation distribution and suppression of surface spin caused by the organic capping layer. [30]. These results are consistent with our TEM data.
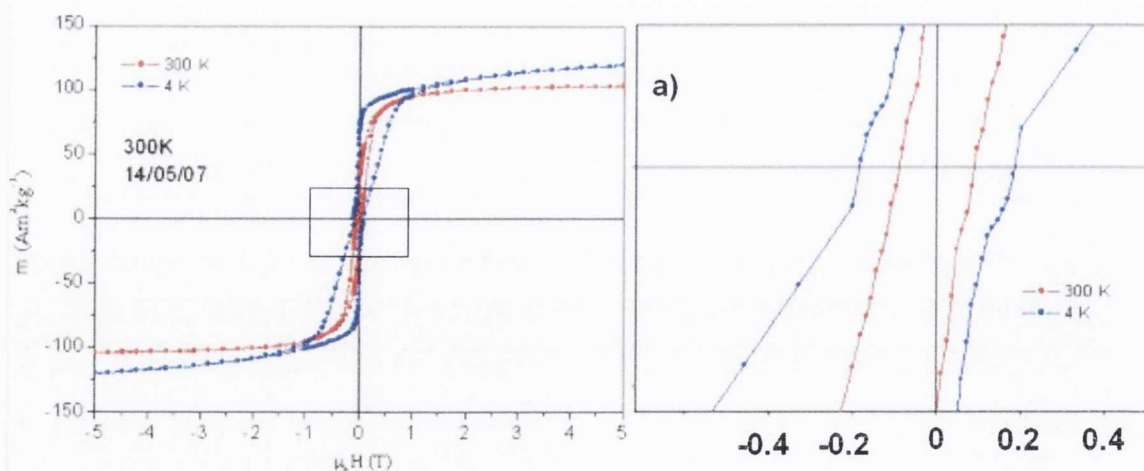
Figure 3.27. Magnetisation curves versus magnetic field for selected $CoFe_2O_4$-DNA nanocomposite. **Sample RT40**. **Key**: (red) at 300 K, (blue) at 4 K a) zoomed in view.

3.4. Conclusions

We have developed a new *in situ* co-precipitation technique for the preparation of polyelectrolyte (PAH) and DNA- cobalt ferrite nanocomposites. Therefore, by using this method, we have been able to effectively stabilize nanometer scale cobalt ferrite particles in aqueous solution.

It was found that the formation of the well-defined magnetic cobalt ferrite particles occurs at temperatures around 80°C. The phase composition of the particles were characterised using XRD, Raman spectroscopy, which showed that samples consisted of cobalt ferrite phase.

We have demonstrated that the higher concentration of polyelectrolyte results in formation of smaller particles. This can be explained by polyelectrolyte coating, which stabilises nanoparticles minimizing particle-particle interaction and as a result prevents their further growth.

According PCS data improvement of the colloidal stability of cobalt ferrite particles was observed after the addition of PAH stabiliser. However, it was found that polyelectrolyte (PAH) could also cause an aggregation of the nanoparticles via their cross-linking.

Cobalt ferrite samples with PAH stabiliser have shown clear ferrimagnetic behaviour. The magnetisation and the coercivity of cobalt ferrite samples strongly depended on the temperatures and concentration of PAH. This is directly related to the variation of cobalt ferrite particle sizes.

A similar strategy was used to prepare novel single stranded $CoFe_2O_4$-DNA nanocomposites. In these materials cobalt ferrite nanoparticles most likely bind to the DNA phosphate groups, acting as a cross-linker between strands, thereby increasing the size and chain lengths of the aggregates.

In the presence of an external parallel magnetic field cobalt ferrite-PAH and cobalt ferrite –DNA samples tend to form arranged nanowires aligned with the direction of the applied field. The arranged nanowires showed ability to remain aligned after the magnetic field was removed.

Similarly to PAH the addition of DNA results in smaller sizes of original nanoparticles, most likely due to their surface passivation by DNA that prevents further growth during the reaction in aqueous solution. Selected samples in dry form showed high magnetic moment and ferromagnetic properties at various temperatures (300 and 4 K). Unfortunately as was expected, $CoFe_2O_4$-DNA samples did not formed stable magnetic fluids for NMRD measurements.

These new magnetic cobalt ferrite nanoparticles and nanowires may be used as potential candidates for data storage devices.

3.5. References:

1. H. Yan, S.H. Park, G. Finkelstein, J.H. Reif, T.H. Labean., *Science.,* (2003), 301, 1882.

2. H.A. Becerril, R.M. Stoltenberg, D.R.Wheeler, R.C. Davis, J.N. Harb, A.T. Woolley., *Journal of Americal Chemical Society.,* 127, (2005), 2828.

3. N.C. Seeman, *Nature,* 421, (2003), 427.

4. S.J. Byrne, S.A. Corr, Y.K. Gun'ko, J.M. Kelly, D.F. Brougham, S. Ghosh., *Chemical Communications.,* 22, (2004), 2560.

5. J. Philip, O. Mondain-Monval, F. Leal-Calderon, J. Bibette., *Journal of Physics D: Applied Physics.,* (1997), 30, 2798.

6. E. Furst, C. Suzuki, M. Fermigier, A. Gast., *Langmuir.,* (1998), 14, 7334.

7. S.L. Biswal, A.P. Gast., *Physical Review Letters.,* (2003), 68, 021402.

8. C. Goubault, P. Jop, J. Baudry, E. Bertrand, M. Fermigier, J. Bibette., *Physical Review Letters,* (2003), 91, 260802.

9. C. Goubault, F. Leal-Calderon, J.-L. Viovy, J. Bibette., *Langmuir.,* (2005), 21, 3725.

10. H. Singh, P.E. Laibinis, T.A. Hatton., *Nano Letters.,* (2005), 5, 2149.

11. J.F. Berret, N. Schonbeck, F. Gazeau, D. El Kharrat, O. Sandre, A. Vacher, M. Airiau., *Journal of American Chemical Society.,* (2006), 128, 1755.

12. A. Ditsch, P.E. Laibinis, D.I.C. Wang, T.A. Hatton., *Industrial & Engineering Chemistry Research.,* 44, (2005), 6824.

13. R. Sheparovych, Y. Sahoo, M. Motornov, S.M. Wang, H. Luo, P.N. Prasad, I. Sokolov, S. Minko., *Chemistry of Materials.,* (2006), 18, 591.

14. S. Si, A. Kotal, T.K. Mandal, S. Giri, H. Nakamura, T. Kohara., *Chemistry of Materials.,* 16, (2004), 3489-3496.

15. S. Wan, J. Huang, M. Guo, H. Zhang, Y. Cao, H. Yan, K. Liu., *Journal of Biomedical Materials Research Part A.,* 80, (2006), 946–954.

16. M. Schonhoff., *Journal of Physics: Condensed Matter.,* 15, (2003), 1781–1808.

17. J.F. Liu, G. Min, and W.A. Ducker. *Langmuir.,* 17, (2001), 4895-4903.

18. S. Corr. New magnetic nanocomposite materials. Thesis for degree of Doctor of Philosophy. University of Dublin. Trinity College, (2006).

19. O.N. Shebanova and P. Lazor., *Journal of Solid State Chemistry.*, 174, (2003), 424–430.

20. Y. Qu, H. Yang, N. Yang, Y. Fan, H. Zhu, G. Zou., *Material Letters.*, 60, (2006), 3548–3552.

21. S. Ammar, A. Helfen, N. Jouini, F. FieAvet, I. Rosenman, F. Villain, P. Molinie, M. Danot., *Journal of Materials Chemistry .*, 11, (2001), 186-192.

22. S. Ardizzone, A. Chittofrati, L. Formaro., *Journal of the Chemical Society, Faraday Transactions.*, 83, (1987), 1159-1168.

23. Y.I. Kim, D. Kim, C.S. Lee., *Physica B: Condensed Matter.*, 337, (2003), 42–51.

24. P.D. Thang, G. Rijnders, D.H.A. Blank., *Journal of Magnetism and Magnetic Materials.*, 295, (2005), 251–256.

25. M. Grigorova, H.J. Blythe, V. Blaskov, V. Rusanov, V. Petkov, V. Masheva, D. Nihtianova, L.M. Martinez, J.S. Munoz and M. Mikhov, *Journal of Magnetism and Magnetic Materials.,*. 183, (1998), 163.

26. G.F. Goya, T.S. Berquo, F.C. Fonseca, M.P. Morales., *Journal of Applied Physics*, 94, (2003), 3520.

27. M. Chastellain, A. Petri, H. Hofmann., *Journal of Colloid and Interface Science.*, 278, (2004), 353–360.

28. J.M. Benevides, S.A. Overman and G.J. Thomas., *Journal of Raman Spectroscopy.*, 36, (2005), 279–299.

29. D.W. Ussery., DNA Denaturation. *Academic Press.* (2001).

30. A.E. Berkowitz, J.A. Lahut, I.S. Jacobs, L.M. Levinson, D.W. Forester., *Physical Review Letters.* 34 (1975), 594.

Chapter 4

4.1. Preparation and investigation of "two-in-one" magnetic luminescent nanocomposites based on magnetite nanoparticles and QDs

4.1.1. Introduction

This part of the work is focused primarily on combining various types of CdTe QDs with PSSS coated magnetite nanoparticles. The PSSS coated magnetite nanoparticles with controlled particle size described above showed great potential as magnetic templates for future synthesis of bimodal magnetic luminescent nanocomposites. Semiconductor nanocrystals (QDs) take advantage of the quantum confinement effect, giving the nanoparticles unique optical and electronic properties. QDs offer advantages over conventional dye molecules in that they have tuneable fluorescence signatures, narrow emission spectra, brighter emission and good photostability [1]. To avoid complete quenching of luminescence of QDs by the magnetic properties of magnetite nanoparticles, a detailed investigation was carried out to prepare stable magnetic fluids with low Fe/PSSS ratio.

It was expected that a modified layer-by-layer (LbL) approach [2] would allow the combination of PSSS stabilised magnetite nanoparticles with QDs and this in turn would lead to the formation of bimodal contrast agent that have two advantages: QDs would serve for fluorescent imaging, while the magnetic nanoparticle would be used for magnetic resonance imaging (MRI). Fabrication of bimodal magnetic luminescent nanocomposites would offer great advantages in a number of important potential applications in biology and biomedicine. However, synthesis of new bimodal magnetic luminescent nanocomposites can be problematic.

The initial aims of this part of our project were to develop a new family of magnetic fluids based on water-dispersible magnetite-polyelectrolyte nanocomposites and investigate their properties. We plan to use commercially available polyelectrolytes *in situ* for the preparation of magnetic nanoparticles by a co-precipitation technique. In this case, polyelectrolytes are expected to serve both as nanoparticle stabilisers and chemical linkers for magnetic nanowire assembly. We

plan to characterise the new nanocomposites using NMR methods (NMRD profiles for T_1 measurement) and to investigate them by transmission electron microscopy (TEM), Raman and FTIR spectroscopy and XRD techniques. After that we are going to use these nanocomposites and quantum dots to prepare new "two in on" magnetic-luminescent nanostructures and investigate their properties. We plan to optimise synthesis conditions for the preparation of new bimodal magnetic-luminescent nanostructures using modified LbL technique [2]. This could lead to a new strategy for the synthesis of new luminescent magnetic nanostructures for use as improved probes for biological detection and investigation.

The structure and properties of new synthesised nanostructures were investigated and characterized by TEM, SEM microscopy, PCS, Zeta potential, and PL, UV-vis, FT-IR spectroscopy, and TGA techniques.

4.2. Preparation of PSSS stabilised magnetite nanoparticles

The well know *in situ* co-precipitation technique [4] was used to synthesise magnetite nanoparticles in the presence of poly(sodium 4-stryene sulfonate) PSSS which was used as a stabiliser. It is important to stabilize the magnetic suspension of magnetic nanoparticles with an optimal amount of polyelectrolyte to produce magnetic fluids with high content of magnetic material. The main factors that can influence the stability and size of magnetite nanoparticles are the concentration of Fe^{2+} and Fe^{3+} and the concentration of PSSS added (**Table 4.1**). It was expected, that optimisation of the conditions would provide further information to improve stability of magnetic fluids and the control of the particle size.

All freshly prepared PSSS stabilised magnetite nanoparticle samples had high stability in aqueous solution. **Table 4.1** shows summarised experimental data of formed stable magnetic fluids with an average diameter of the primary magnetic particle are below 10 nm (from TEM). It was calculated that PSSS with the average molecular weight of 70.000g/mol has 340 head groups per unit.

Table 4.1. Summaries experimental data of the PSSS stabilised magnetite
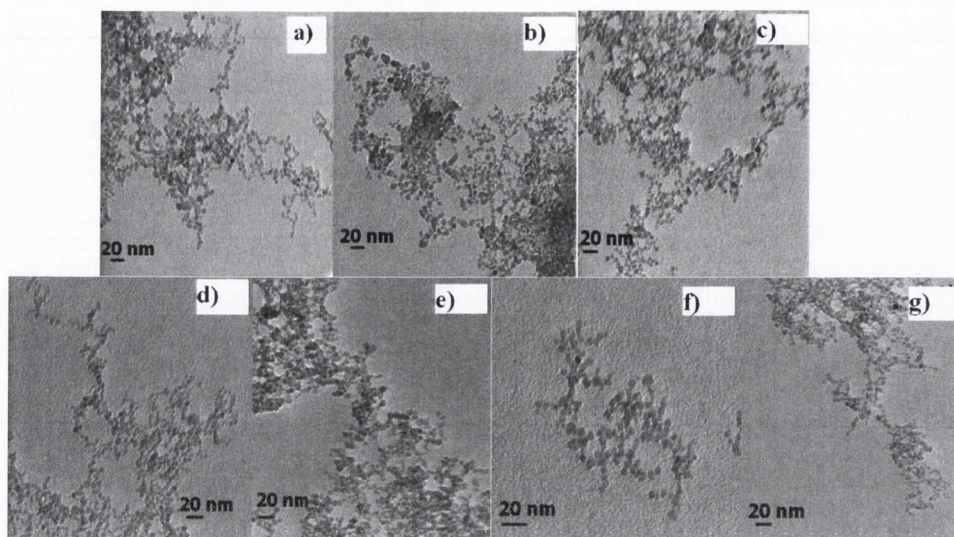nanoparticles.

Sample	PSSS (g)	PSSS (M)	Metal (M)	Metal/PSSS ratio	Zeta potential (mV)	PCS size (nm)	Size of primary NPs by TEM(nm)
a	0.15	2.1×10^{-6}	3.2×10^{-3}	1524	-53 ±5.2	225.1 (PDI 0.150)	5.9±1
b	0.15	2.1×10^{-6}	6.5×10^{-3}	30952	-52 ±4.4	232.5 (PDI0.170)	7±1.3
c	0.25	3.6×10^{-6}	3.2×10^{-3}	889	-39 ±4.4	383.7 (PDI 0.423)	5.4±1
d	0.25	3.6×10^{-6}	6.5×10^{-3}	1805	-55 ±6.2	164.9 (PDI 0.234)	6.4±0.8
e	0.25	3.6×10^{-6}	8×10^{-3}	2222	-56 ±5.3	256.3(PDI 0.117)	6.3±0.9
f	0.3	4.3×10^{-6}	1.8×10^{-3}	418	-49 ±5.5	239.8(PDI 0.145)	6.2±1
g	0.35	5×10^{-6}	6.5×10^{-3}	1300	-51 ±6.0	144.3(PDI 0.157)	5.6±0.9

4.2.1. TEM microscopy studies of PSSS stabilised magnetite nanoparticles

In order to obtain more direct information on PSSS coated magnetite
nanoparticle size and morphology, TEM was carried out on the final washes of the
samples. As expected, the calculated average size of magnetite nanoparticles from
TEM images revealed the presence of individual primary nanoparticles of small size
(7-5 nm), small standard deviation (±1.2 nm) and regular spherical shapes (**Fig. 4.1**).
Table 4.1, gives average size of the particles from TEM images and PCS
measurements. Note, that the average size obtained from PCS is different when
compared to sizes calculated from TEM due to the aggregation and cross-linking of
primary magnetite nanoparticles. TEM images clearly showed presence of cross-
linking of individual primary magnetite nanoparticles into the networks for all
samples due to the presence of PSSS. The degree of cross-linkage between magnetite
nanoparticles was strongly dependent on the PSSS concentrations and Metal/PSSS
ratio in aqueous solutions. The lowest concentration of PSSS in the samples showed
the highest cross-linkage. These cross-linked clusters of the nanoparticles probably
arose from an inadequate amount of the PSSS needed to stabilise the particles in
Millipore water. A Higher concentration of PSSS stabiliser in the sample prevents

further assembling between primary nanoparticles and formation of agglomerates to give more monodisperse spherical magnetite nanoparticles.

Figure 4.1. TEM images of PSSS stabilised magnetite nanoparticles with various amounts of iron and PSSS in the reaction solutions. a) **sample a**, b) **sample b**, c) **sample c**, d) **sample d**, e) **sample e**, f) **sample f**, g) **sample g**.

To investigate the effect of a magnetic field on the cross-linked PSSS stabilised magnetite nanoparticles sample were dried on TEM grids in a 0.5 T parallel magnetic field. All samples formed arranged chain-like 1-D nanowires under an external parallel 0.5 T magnetic field (**Fig. 4.2**).
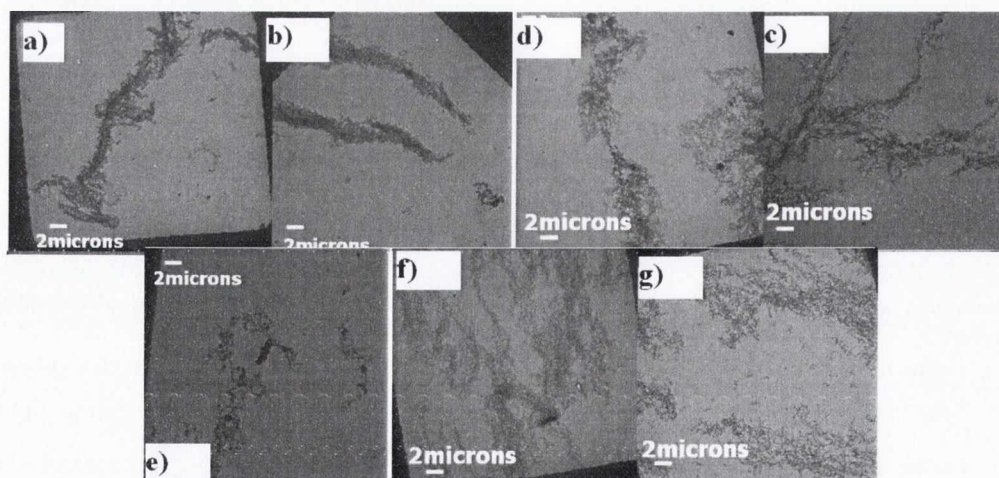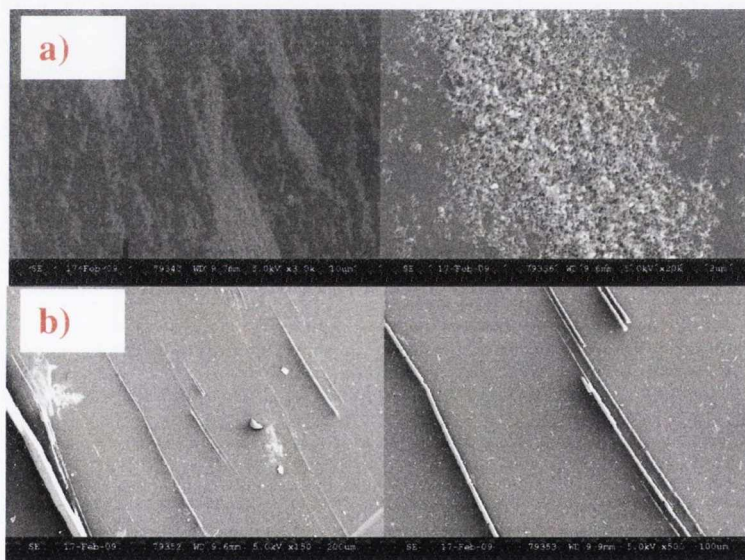

Figure 4.2. TEM images of PSSS stabilised magnetite nanoparticles with various amounts of iron and PSSS in the reaction solutions in 0.5 T parallel magnetic field. a) **sample a**, b) **sample b**, c) **sample c**, d) **sample d**, e) **sample e**, f) **sample f**, g) **sample g**.

Samples with a higher concentration of PSSS formed wider, longer and denser nanowires (see **Fig. 4.2 (f)**, **(g)**). Thus, nanoparticles were highly clustered, due to their cross-linking by polyelectrolyte molecules.

4.2.2. Scanning electron microscopy (SEM) studies of PSSS stabilised magnetite nanoparticles

Similar behaviour of PSSS stabilised magnetite nanoparticles under an external magnetic field was observed by SEM. **Fig. 4.3** presents selected SEM images of pattern formation of PSSS stabilised magnetite nanoparticles in a 0.5 T parallel magnetic field. Due to strong dipole-dipole interaction PSSS stabilised nanoparticles within each other neighbours tend to align in the orientated linear nanoassemblies (nanowires) with the direction of the applied magnetic field. Therefore, the formation of arranged clusters could be clearly seen in **Fig. 4.3 a)**.

Figure 4.3. SEM images of the selected PSSS stabilised magnetite nanoparticles under 0.5 T parallel magnetic field. a) **sample a** b) **sample f**.

4.2.3. PCS and Zeta potential studies of PSSS stabilised magnetite nanoparticles

PCS were performed on the last washes of each sample in order to investigate the size of cross-linked magnetite nanoparticles in water. PCS data for all samples, showed some variations of average nanoparticles size distributions in distilled water (**Fig. 4.4**). PCS measurements demonstrated that there was a big difference in the particle

sizes obtained from TEM. This could be simply explained: PCS is a method used to estimate the average particle size in solution whereas TEM is an analysis carried out on a dry media (dry sample). At the same time as was discussed above, the presence of long chain-like PSSS molecules in the system provided a negatively charged backbone for the formation of networks of Fe_3O_4 nanoparticles. The disagreement between PCS/TEM sizes arises because larger particles (clusters or networks of Fe_3O_4) scatter light more strongly than smaller particles (clusters), so the higher PCS size distribution might contribute more strongly to the scattering, resulting in a systematically high value of the mean particle size.
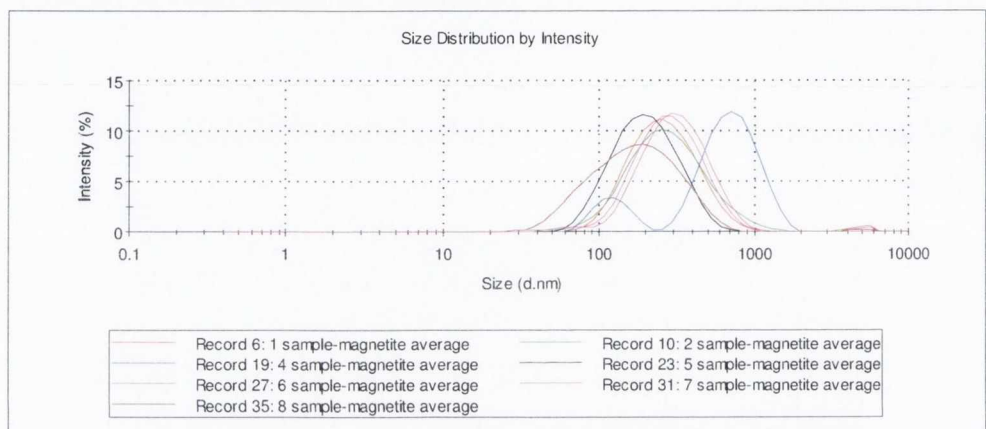
Figure 4.4. Hydrodynamic radius distributions of PSSS coated magnetite nanoparticles in distilled water. 1) **sample a**, 2) **sample b**, 4) **sample c**, 5) **sample d**, 6) **sample e,** 7) **sample f**, 8) **sample g**.

The presence of the two peaks in PSC data (**Fig. 4.4**, **sample c**) could be simply explained by the presence of high molecular mass polyelectrolyte (PSSS) in the system. Probably some long chains of the PSSS are not fully attached to the magnetite nanoparticles and could potentially fluctuate in solution. Further, their fluctuation is also affected by presence of the water molecules, which are bound or entrapped by PSSS. The average size in diameter of particles varied from 144.3 to 383.7 nm. There was not any specific trend depending on the PSSS concentration and Metal/PSSS ratio (**Table 4.1**). It was expected that PDI values would provide information concerning the degree of clustering in solution. It would allow us determine whether there are a large number of different size clusters. The results confirmed good dispersion stability of the magnetic fluids and cross-linking between magnetite nanoparticles with average range of PDI 0.117-0.225 in comparison with

Sample 4 which showed higher degree of clustering and agglomerates (PDI 0.450) and formation seen as dense different sized aggregates. The surface charge of nanoparticles was studied using zeta potential measurements. All freshly prepared magnetic suspensions were negatively charged, the charge varied from -39 to -57 mV, this indicates the formation of the stable magnetic solutions due to presents of PSSS stabiliser, no precipitation was observed (**Fig. 4.5**).
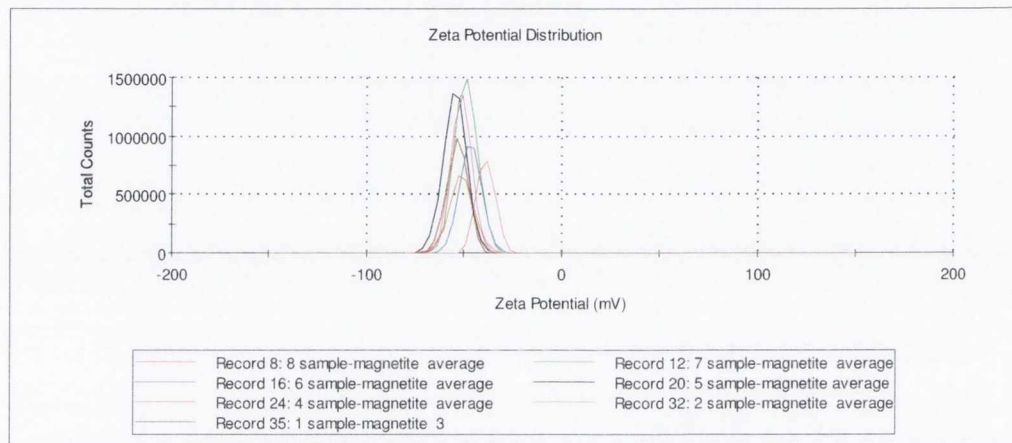

Figure 4.5. Zeta potential distributions of PSSS coated magnetite nanoparticles in distilled water. 1) **sample a**, 2) **sample b**, 4) **sample c**, 5) **sample d**, 6) **sample e**, 7) **sample f**, 8) **sample g**.

The **sample d, e** with the highest Metal/PSSS ratio gave the lowest zeta potential values (between -51 and -56 mV). The charged polyelectrolyte molecules coat the magnetite nanoparticles and prevent them from aggregating and falling out of solution. It is well known that the suspension stability is related to high zeta potentials. A large negative zeta potential was found to be advantageous for achieving lower particle sizes and good suspension stability, owing to the particles remaining separation without agglomeration [15].

4.2.4. FTIR and XRD studies of PSSS stabilised magnetite nanoparticles

FTIR spectroscopy was carried out in KBr matrix on all PSSS stabilised magnetite nanocomposites (**Fig. 4.6**). Spectra show presents characteristic peaks 1180-1008 cm^{-1}, which can be attributed to PSSS in all samples. Peaks at approximately 585 cm^{-1} and 460 cm^{-1} were attributed for Fe-O as expected for magnetite [16-18]. All samples gave approximately the same results.
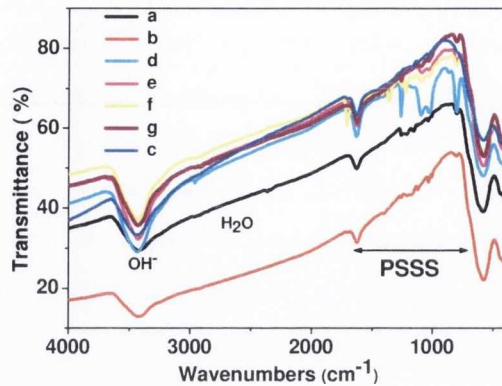
Figure 4.6. FTIR spectra of PSSS stabilised magnetite nanoparticles with various amounts of iron and PSSS in the reaction solutions.

An XRD pattern presented selected data for **samples f** and **d** (**Fig. 4.7**). Due to similar particles size, the XRD pattern for **sample f** is masked by the XRD pattern of **sample d**. No impurity was observed in the XRD patterns, the reflection peaks obtained were readily indexed to (531), (440), (400), (311), and (220) planes of inverse spinel magnetite (Fe_3O_4) [19]. The decrease of the intensity and widening of the characteristic reflection peaks indicates the small (below 10 nm) average size of Fe_3O_4 nanoparticles. The patterns were found to coincide with the JCPDS database for magnetite. The calculation of the average particle size from the (311) broadening XRD peak using Scherrer's formula did not produce accurate results due to the high noise/intensity ratio recorded during the measurement.
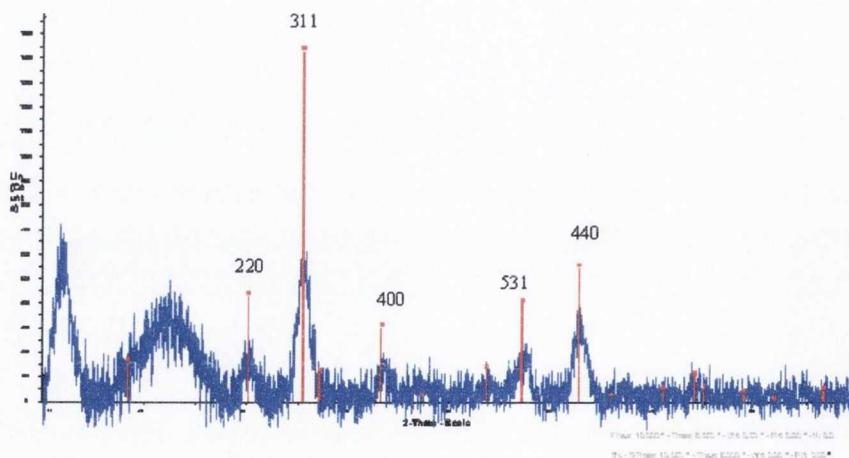
Figure 4.7. X-ray diffraction pattern of selected PSSS stabilised magnetite nanoparticles. Key: (black) **sample f**, (blue) **sample d**, (red) pattern magnetite from JCPDS database.

94

4.2.5. Magnetic resonance dispersion (NMRD) studies of suspension of PSSS stabilised magnetite nanoparticles

It is important to note that according to TEM images all samples form arranged nanowires in the present of the external magnetic field. In order to investigate the effect of these stable magnetic suspensions on the water proton spin lattice relaxation time T_1, nuclear magnetic resonance dispersion (NMRD) were performed to carry out a preliminary evaluation of these magnetic fluids as potential contrast agents for applications in low field MRI. The NMRD profiles of PSSS stabilised magnetite nanoparticles showed a monotonous increase of R_1 at the range 0.18 MHz reaching maximum at about 8 MHz with increasing magnetic field (**Fig. 4.8**). r_1 value was recalculated according equation:

$$r_1 = \frac{R_{1(obs)} - R_{1(solvent)}}{[Fe]}$$

Where: $R_{1(solvent)}$ - spin lattice relaxivity of water, r_1 - the relaxivity of the agent, [Fe] - iron concentration [17].

For all PSSS stabilised magnetite samples at the lower frequencies (< 4MHz), the principle mechanism leading the relaxation process is the Néel process (the movement of the nanoparticles' internal magnetic moment). This means that T_1 is shorter at the lower frequencies leading to the shapes of relaxivity curves seen in Fig. 4.8. This type of curve is noted for clustered material or aggregates of the small primary nanoparticles. It is important to maintain the optimal balance between iron and PSSS concentration in order to keep nanoparticles stable in solution. It was found that optimum metal/PSSS ratio gave highest relaxivity (r_1 ~21 $M^{-1}s^{-1}$). All curves confirmed TEM results demonstrating superparamagnetic size range of cross-linked iron oxide nanoparticles.
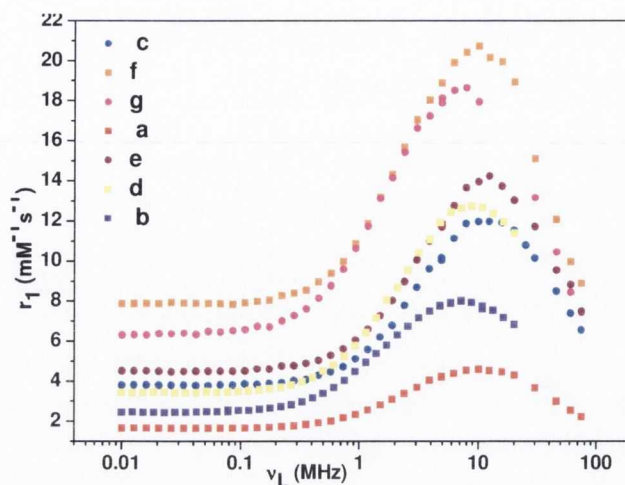
Figure 4.8. NMRD relaxation curves recorded at a measuring frequency of 20 MHz for PSSS stabilised magnetite nanoparticles in Millipore water. **Key:** (orange) **sample f**, (red) **sample a**, (blue) **sample** c, (purple) **sample e**, (magenta) **sample g**, (yellow) **sample d**, (violet) **sample b**. Measurements were carried out at 24.9 ±1°C.

Table 4.2. Summaries of experimental NMRD and PCS data of the PSSS stabilised magnetite nanoparticles.

Sample	Metal/PSSS ratio	TEM of primary NPs (nm)	r_1 (M^{-1}s^{-1})	Size according to PCS before NMRD (nm)	Size according to PCS after NMRD (nm)
a	1524	5.9±1	5.33	225.1 (PDI 0.150)	221.7 (0.138)
b	30952	7±1.3	8.63	212.7 (PDI 0.234)	178.5 (PDI 0.208)
4c	889	5.4±1	12.43	253.6 (PDI 0.387)	203.4 (PDI 0.407)
d	1805	6.4±0.8	13.12	184.6 (PDI 0.0.283)	164.7 (PDI 0.266)
e	2222	6.3±0.9	14.68	196.1 (PDI 0.307)	134.0 (PDI 0.523)
f	418	6.2±1	20.91	239.8 (PDI 0.145)	217.4 (PDI 0.262)
g	1300	5.6±0.9	18.89	210.2 (PDI 0.160)	170.6 (PDI 0.290)

No precipitations of the measured samples in solutions were observed after NMRD experiments. To obtain a more quantitative understanding of these results, PCS was performed after NMRD measurements. Note: that PCS data in **Table 4.2** are different in comparison in **Table 4.1** because measurements were performed on diluted samples. PCS data showed decrease in average sizes in diameter after NMRD

measurements had some influence on the cross-linkage between the PSSS stabilised magnetite nanoparticles (see **Table 4.2**). However the magnetic fluids were still stable.

4.2.6. Magnetic measurements of PSSS stabilised magnetite nanoparticles using SQUID magnetometer

Another important factor for practical applications of PSSS stabilised magnetite nanoparticles is their magnetic properties. Magnetisation measurements were performed using SQUID magnetometer. All our PSSS-magnetite samples showed superparamagnetic behaviour at 300 K, by the absence of magnetic remanence (Mr) and coercitivity (Hc). According results (**Fig. 4.9**), the saturation magnetisation varied for all PSSS stabilised magnetite nanoparticles from 28.8 - 63.5 Am^2kg^{-1}, which is lower than that of bulk magnetite 92 Am^2kg^{-1} [20] due to the particle size effects. The results of room-temperature magnetic measurements on PSSS stabilised magnetite nanoparticles are summarised in **Table 4.3**. The magnetisation values increase with increasing PSSS concentrations because the organic PSSS layer reduces the total magnetic moment of nanoparticles per unit weight.
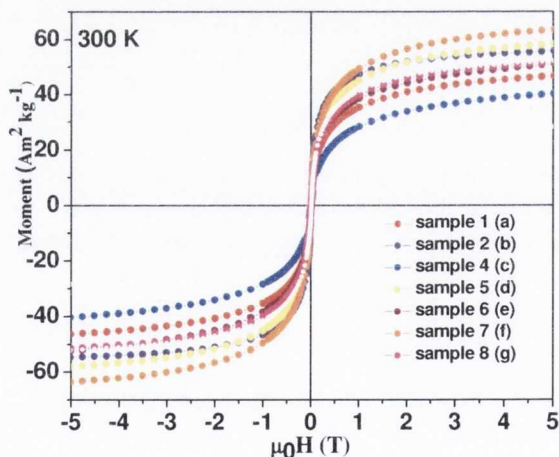
Figure 4.9. Room temperature magnetisation curves of PSSS stabilised magnetite nanoparticles. 1) **sample a**, 2) **sample b**, 4) **sample c**, 5) **sample d**, 6) **sample e,** 7) **sample f**, 8) **sample g**.

Though samples are phase pure, the drop in magnetisation with further reduction in size may be attributed to surface effects [21, 22]. The magnetisation near the surface is generally lower than that in the interior (different x values for the Fe_{3-}

$_x$O$_4$ stoichiometry occur on the surface layers). With size reduction, the surface effects become more predominant due to differences in surface magnetic anisotropy of the particles [23]. At the same time previous studies reported in the literature [24] also suggested that the decrease of the saturation magnetisation could be attributed to the presents of surfactants on the surface of nanoparticles. However, the Mössbauer studies are under future investigation to conduct the effect of the nanoparticle size on the magnetisation value.

Table 4.3. Summaries of experimental magnetisation data of the PSSS stabilised magnetite nanoparticles.

| Sample	Metal/PSSS ratio	Mass (mg)	Size according to TEM of primary NPs (nm)	M$_s$ (Am^{2}kg^{-1})
a	1524	3.8	5.9±1	46.8
b	30952	2.7	7±1.3	55.7
c	889	4.7	5.4±1	40.8
d	1805	1.4	6.4±0.8	58.3
e	2222	2.3	6.3±0.9	51.0
f	418	2.5	6.2±1	63.5
g	1300	2.4	5.6±0.9	51.5

4.3. Preparation and investigation of new magnetic luminescent nanostructures

4.3.1. Preparation of magnetic multilayered nanocomposites

Bimodal magnetic luminescent nanostructures were synthesised using a two-step (LbL) technique [25]. The first step was the fabrication of multilayered nanocomposites in addition to providing the frame for a fabrication core/shell (multilayered) structure. Second step was the addition of different sized CdTe QDs. In the first step PSSS coated magnetite (Fe$_3$O$_4$) nanoparticles were used as templates. It was expected that deposited multilayered shell of polyelectrolyte layers (PAH and PSSS) would allow us to prepare magnetic nanocomposites for the future synthesis of bimodal magnetic luminescent nanostructures. It was also anticipated that core/shell structured magnetic nanocomposites would prevent complete quenching of the luminescence of the QDs by the magnetic core in comparison with a single layer of PSSS coated Fe$_3$O$_4$ nanoparticles.

Superparamagnetic Fe$_3$O$_4$-PSSS nanoparticles with an average size of 8.6 ±1.7 nm in diameter were synthesised and used in this case for the production of

multilayered nanocomposites. To monitor the formation of the multilayer shell on Fe_3O_4-PSSS nanoparticles zeta potential measurements were performed. Due to the presence of a single layer of PSSS on the surface of the Fe_3O_4 nanoparticles, a negative zeta potential value was recorded (~ -42 ±3 mV). This negative charge causes a reversal in zeta potential to positive values after addition of 0.2 mL, 2.85×10^{-7} M PAH (+34 ±2 mV). Alternate layers of the polyelectrolytes: positively (PAH) or negatively (PSSS, 1.2 mL, 2.85×10^{-7} M) charged were deposited in a cyclic mode on the surface of Fe_3O_4-PSSS nanoparticles using electrostatic adsorption. The alternating zeta potential depends on whether nanoparticles are covered with PAH or PSSS as the outer layer and demonstrates a successful stepwise layer growth occurs on the nanoparticles. The difference in PAH (0.2 mL) used compared to PSSS (1.2 mL) used during the synthesis of multilayer structures could be attributed to the different number of charges per unit (PAH - 750, PSSS – 340 head groups).**Fig. 4.10** illustrates the formation of multilayered nanocomposites using the LbL technique.
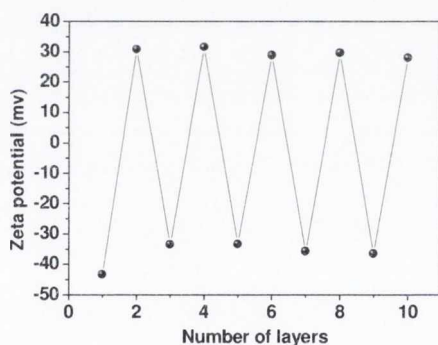
Figure 4.10. Zeta potential for each layer of polyelectrolyte coated PAH/PE$_{10}$ nanocomposites as a function of polyelectrolyte layers numbers for PAH/PSSS coatings.

For coating Fe_3O_4-PSSS nanoparticles with more the 10 layers of PE, it is hard to control the suspension stability due cross-linking and aggregation (PDI = 1, from PCS) following dramatic changes in zeta potential measurements (see **Appendix 3**). The zeta potential value of the magnetic suspension is not strongly positively charged (~+14 mV) and cannot provide an accurate value for charge of the multilayered magnetic nanocomposites. Thus, considering the previous findings an optimum 10 layers of polyelectrolytes (PSSS and PAH) have to be deposited on the surface of the Fe_3O_4 nanoparticles to prevent the complete luminescence quenching of the QDs. The zeta potential measurements showed that following the polyelectrolyte coating the

nanostructures were positively charged (+28. 8 mV) and this provided a counter charge for the deposition of the negatively charged QDs.

Freshly prepared multilayered magnetic nanocomposites were used for the second step preparation of "two-in-one" magnetic-luminescent nanostructures.

4.3.2. TEM microscopy studies of multilayered Fe_3O_4-PSSS nanocomposites

TEM images of the multilayered polyelectrolyte coated magnetite nanoparticles are presented in **Fig. 4.11**. Some slight decrease in the polydispersity of the primary PSSS coated magnetite nanoparticles was observed. This is most likely due to the dipole-dipole interactions between nanoparticles that results in their agglomeration. The average diameter of the nanocomposite was 9.6 ±2 nm. It is worth mentioning that the average hydrodynamic size of the nanocomposites (105 nm PDI0.132) measured by PCS is bigger than the average size estimated by TEM. This may be attributed to cross-linking between individual nanoparticles by polyelectrolyte molecules.
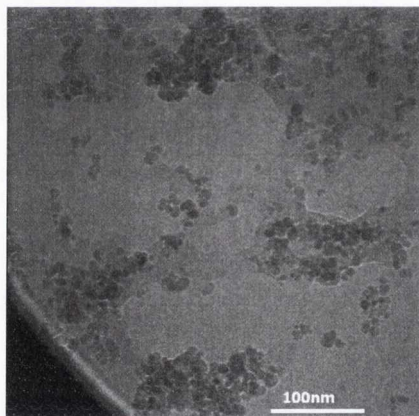
Figure 4.11. TEM image of multilayered nanocomposites (Fe_3O_4-PSSS) with 10 layers of PE.

### 4.3.3. Preparation and characterisation of multilayred structures with CdTe QDs

Thioglycolic acid (TGA*) capped CdTe QDs with and without Gelatine (gel) were synthesised according to previously reported procedure [26]. **Table 4.4** presents the summarised data on the different properties of the CdTe QDs, which were used for reaction with the multilayer nanocomposites. All samples of CdTe QDs used in the

synthesis of magnetic luminescent nanostructures showed narrow size distribution and a negative surface charge.

Table 4.4. Summarised data of the properties of various sized CdTe QDs used for the preparation of magnetic luminescent nanostructures.

Sample	QDs	UV vis (nm)	PL em. (nm)	QY (%)	Conc. (mol/L)	Size (± 0.1) (nm)	Zeta potential (mV)
VG006(7)	TGA QDs	531	556	43	8.11×10^{-5}	2.9	-31.2±6.5
VG006(6)	TGA QDs	552	584	34	3.71×10^{-5}	3.6	-36.5±7.6
Sb215(4)	TGA gel	584	600	33	1.4×10^{-4}	4.2	-35.0±5.1
Sb215(3)	TGA gel	572	614	47	1.10×10^{-4}	4.6	-49.6±4.8
TC58(2)	TGA QDs	602	609	30	2.35×10^{-4}	5.2	-47.1±7.3

Fig. 4.12 shows the room temperature absorption and photoluminescence (PL) spectra of various CdTe QDs used. **Fig 4.12** shows the typical absorption (panel 1) and PL emission (panel 2) spectra indicative of CdTe QDs. A range of sizes, as noted by the varying absorption and emission wavelengths (λ_{em} 556-614 nm) were used and quantum yields varied from 30-47 %.
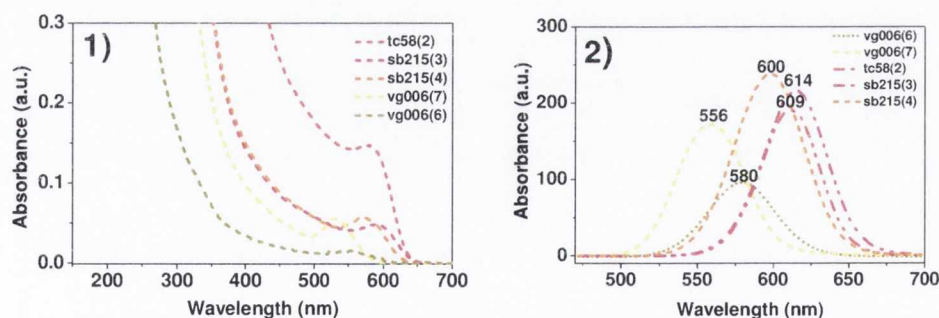
Figure 4.12. Room temperature absorbance and emission spectra of different sizes of CdTe QDs used. **Key: 1) Absorbance spectra** (yellow) Vg006(7) (2.9 nm), (dark yellow) Vg006(6) (3.6 nm), (orange) Sb215(4) (4.6 nm), (pink) Tc58(2) (5.2 nm), (magenta) Sb215(3) (4.2 nm). **2) Emission spectra** (yellow) Vg006(7) (2.9 nm), (dark yellow) Vg006(6) (3.6 nm), (orange) Sb215(4) (4.6 nm), (pink) Tc58(2) (5.2 nm), (magenta) Sb215(3) (4.2 nm). All samples were excited at λ_{ex}=450 nm.

Fig. 4.13 shows different sized gel and non gel QDs under UV light (λ=365
nm). Different sized CdTe QDs emit different coloured light due to quantum
confinement [27].
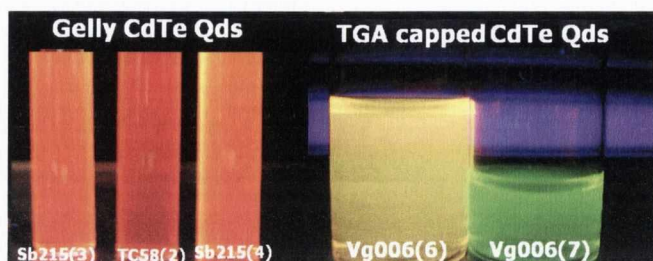
Figure 4 13. Colloidal CdTe QDs irradiated with a UV light.

A similar LbL deposition technique was used for the fabrication magnetic
luminescent nanostructures. The only difference was that poly(allylamine
hydrochloride) (PAH) (30-52 µL) was added to the various sized CdTe QDs before
preparation of the magnetic luminescent nanostructures. After the addition of 30-52
µL of PAH, no significant changes in emission intensity were recorded for all types of
our CdTe QDs.

Driven by electrostatic interaction, negatively charged CdTe QDs with PAH
were deposited on the oppositely charged multilayered nanocomposites. This kind of
interaction is extremely sensitive to the separation distance (number of deposited
layers) between the CdTe QDs and the magnetic cores. Degassed water was used
during all experiments as the presence of free oxygen in solution may result in a
quenching of the CdTe QD luminescence.

Schematic illustration of the synthesis of magnetic luminescent nanostructures is
presented in the **Fig. 4.14**.
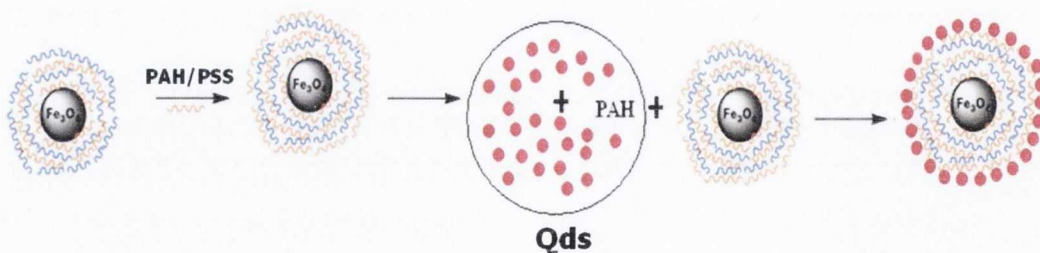
Figure 4.14. Schematic illustration of fabrication magnetic luminescent nanostructures
using the two-step LbL technique.

To investigate the effect of the PAH stabiliser on the formation of the magnetic luminescent nanostructures, a control experiment was run in tandem. The multilayered magnetic nanocomposites (**sample 15**) were reacted for the same period of time (14 hours) with a no gel QD suspension (1.1×10^{-8} M) without the extra addition of PAH.

Results for no gel CdTe QDs without the addition of PAH, showed no cases of electrostatic interaction between the CdTe QDs and the magnetic nanocomposites and no direct electrostatic adsorption onto the surface of the multilayered magnetic nanocomposites was observed. This suggests that electronic bonding of the CdTe QDs to the surface of the multilayered magnetite nanocomposites is directly related to the presence of PAH in the system. Addition of the positively charge PAH stabilizer to the CdTe QDs suspensions probably modifies or additionally caps the surface of the CdTe QDs, forming a thin monolayer. These results suggest that extra addition of PAH to the CdTe QDs suspensions should be used in further experiments.

Following this control experiment, a more systematic study (using PAH) was carried out to investigate the formation of magnetic luminescent nanostructures with different sized CdTe QDs. After 14 hours of mixing the gel and non gel CdTe QDs with multilayered magnetic nanocomposites, a change in zeta potential from positively charged +28.7 mV to negatively charge was observed. All freshly prepared samples exhibited negatively charged zeta potentials from the range -14 to -25 mV. This could be attributed to the successful deposition of the CdTe QDs onto the surface of the magnetic multilayered nanocomposites. PCS measurements showed a general increase in the average size and polydispersity index (PDI) of the samples (see **Table 4.5**). It must be noted that the data illustrates the effect of the PAH, as the control sample with no PAH was not luminescent after washing.

The physical properties of the new magnetic luminescent nanostructures with different CdTe QDs are summarised in **Table 4.5**.

Table 4.5 Physical properties of the magnetic luminescent nanostructures.

Name	PAH Present	QDs conc. (mol/L)	QDs volume added (mL)	Average size (nm)	Zeta potential (mV)
10 (Sb215(3))	Yes	1.1×10^{-6}	2	369.5 (PDI 0.359)	-19.5±3.2
11 (TC58(2))	Yes	2.35×10^{-6}	2	322.3 (PDI 0.238)	-24.9±3.8
12 (Sb215(4))	Yes	9.33×10^{-7}	2	265.4 (PDI 0.412)	-24.3±4.3
13 (VG006(6))	Yes	1.86×10^{-6}	2	284.9 (PDI 0.238)	-20.5±5.9
14 (VG006(7))	Yes	8.11×10^{-6}	2	1240 (PDI 0.549)	-14.5±4.8
Control 15 (Sb215(3))	No	1.1×10^{-6}	2	-	-

This process is accompanied by changes in the room temperature absorption and emission spectra (**Fig. 4.15, 4.16**) and can be monitored for all samples to compare to the original CdTe QDs.

Synthesised magnetic luminescent nanostructures in the presence of PAH had remnant luminescence, which was observed in absorbance and emission spectra. This emission, although greatly reduced when comparing to the original CdTe QDs indicates that the reaction between multilayered magnetic nanocomposites and QDs resulted in formation new magnetic luminescent nanostructures. The significant decrease in the emission (PL) intensity of the QDs can be attributed to static quenching cased by the presence of the superparamagnetic nanoparticles coupled to the fact that not all of the QDs were deposited onto the multilayer structures. The washings following deposition frequently contained non-deposited QDs.
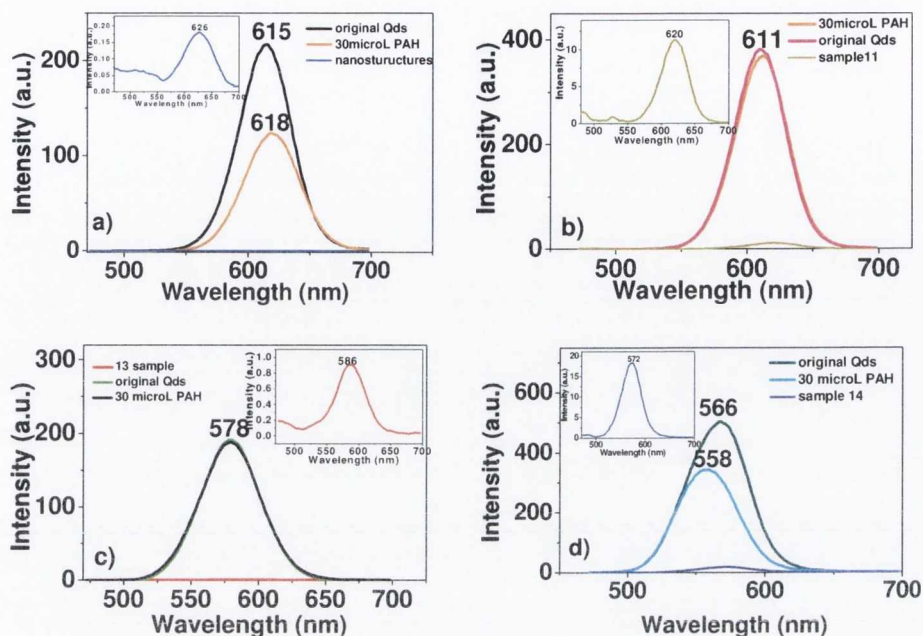
Figure 4.15. Room temperature emission spectra of selected magnetic luminescent nanostructures synthesised with different sized CdTe QDs. (λ_{ex}=450 nm). **Key: a) 10 sample, b) 11 sample,** c) **13 sample,** d) **14 sample.** Insert shows the changes in the main emission peak.

The appearance of red shifts ~4-6 nm in the PL curves for **samples 10, 11, 13, 14** can be accredited to the aggregation in the multilayered magnetic luminescent nanostructures. It was calculated from the PL data that 0.37 % (10 sample) 0.38 % (11), 0.48 % (13 sample), and 5.5% (14 sample) of the original CdTe QDs with PAH was incorporated (deposited) on the surface of nanostuctures. (see **Table 4.6**)

Table 4.6 Physical properties of the QDs and magnetic luminescent nanostructures

Sample name	PAH Present	QDs conc. Used (mol/L)	QDs volume added (mL)	Absorbance of original QDs	Absorbance of nanocom.	PL nacomposites/ PL QDs %
10 (Sb215(3))	Yes	1.1×10^{-6}	2	128	0.17	0.37
11 (TC58(2))	Yes	2.35×10^{-6}	2	365.4	14	0.38
13 (VG006(6))	Yes	1.86×10^{-6}	2	187.4	0.9	0.48
14 (VG006(7))	Yes	8.11×10^{-6}	2	345.6	19	5.5

UV-vis absorption spectra of selected samples are presented in **Fig. 4.16** a broadening of the characteristic absorption maxima was observed for all samples.
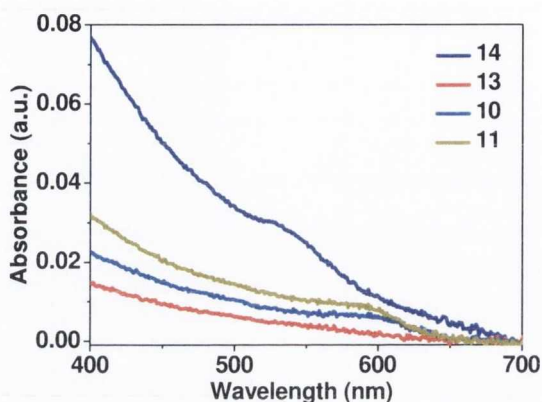

Fig. 4.16. UV-vis absorbance spectra of selected magnetic luminescent nanostructures synthesised with different sized CdTe QDs. **Key:** (red) **13 sample**, (dark yellow) **11 sample**, (navy) **14 sample**, (blue) **10 sample**.

The new magnetic luminescent suspensions showed some instability after 2-3 hours of storage, which were confirmed by PCS data and showed the coagulation of the colloidal suspension.

4.3.4. Visibility studies of the magnetic luminescent suspensions

Fig. 4.17 shows freshly prepared magnetic luminescent suspensions under UV radiation with and without the presence of an external magnetic field. Without the presence of an external magnetic field the magnetic luminescent suspensions are homogeneously dispersed. This behaviour is essential for magnetic separation techniques.
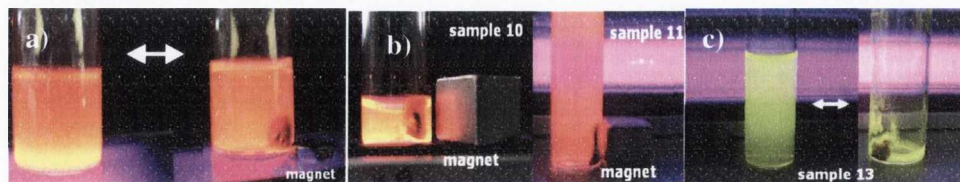

Figure 4.17. Fluorescing suspensions under UV radiation of magnetic luminescent nanocomposites with different sized gel CdTe QDs. (a) and (b) and non gel QDs: (c)

Following the addition of an external magnetic field the nanostructures are attracted toward the magnet due to their Fe_3O_4- core, thus demonstrating, that after the CdTe

QDs deposition they still maintained strong magnetic properties. The magnetic nanostructures were still highly luminescent under the influence of the magnetic field. This demonstrates the dual magnetic / luminescent characteristics of these nanostructures. These manipulations can be repeated many times without any loss of luminescence intensity.

The average hydrodynamic diameters of freshly prepared suspensions of the magnetic luminescent nanostructures with were recorded by PCS. However, this data (see **Table 4.5**) demonstrated that all samples most likely consist of agglomerates of primarily Fe_3O_4 nanoparticles electrostatically bonded with the CdTe QDs. The size of the magnetic core was determined by TEM.
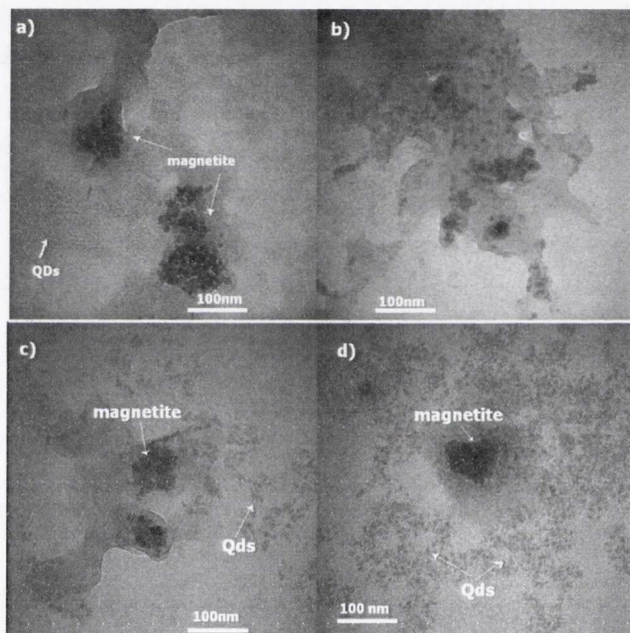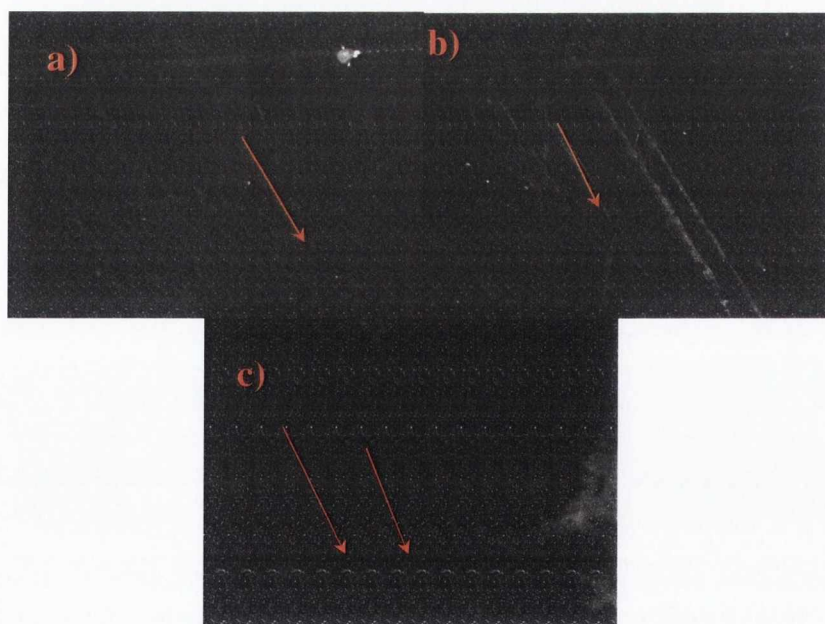

Figure 4.18. TEM images of magnetic luminescent nanostructures. a) **sample 10**, b) **sample 11**, c) **sample 12**, d) **sample 13**, e) **sample 14**.

TEM analysis was carried out on all samples and the corresponding images are shown in the **Fig. 4.18** with a zoomed image shown in **Fig. 4.19**. TEM results confirmed the PCS data. Aggregation and clustering of the magnetite nanoparticles were observed throughout. Final average clusters sizes were close to 100-150 nm, indicating that addition of the CdTe QDs had a significant influence on the final size of the nanostructures.
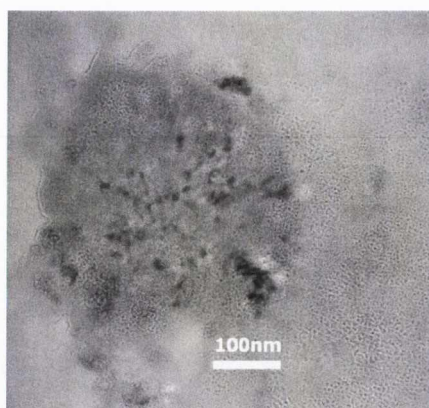
Figure 4.19. Zoomed TEM image of **sample 14**.

To investigate magnetic properties of these luminescent nanostructures, 500 µL samples were placed on a glass slide and kept in a 0.5 T parallel magnetic field overnight (see **Fig. 4.20**). The formation of aligned chains of magnetic luminescent nanostructures in the direction of the magnetic field demonstrates both the magnetic and luminescent modalities in one nanostructure. Note: fluorescent structures were seen under the microscope, however only black and white images could be taken by the camera. This visual detection method showed potential application for cell labelling and monitoring the location of the drug delivery system in the body.


Fig 4.20. Fluorescence microscope image of magnetic luminescent nanostructures. a) **sample 12,** b) **sample 13,** c) **sample 11.**

4.3.5. FTIR spectroscopy studies of magnetic luminescent nanostructures

FTIR studies were carried out to compare with PSSS coated magnetite and the magnetic fluorescent nanostructures (**Fig. 4.21**). As expected, all characteristic peaks for PSSS coated magnetite nanoparticles had a slight shift to lower wavenumbers due to the strong interaction between the CdTe QDs and surface of the magnetic multilayered nanocomposites. Most of characteristic stretching peaks of the PSSS: arenes group, S=O bonds are overlapping with amide group peaks for PAH, and gelatine. The main peaks for PAH and PSSS stabilisers are in the region between 1600-1000 cm^{-1} [28,29]. A weak peak at around 3425.37 cm^{-1} can be ascribed to the N-H stretching vibration, and bands ranging from 2920 to 3000 cm^{-1} capable to the hydrogen bonding between molecules or C-H vibration all verify the presence of PAH [29].
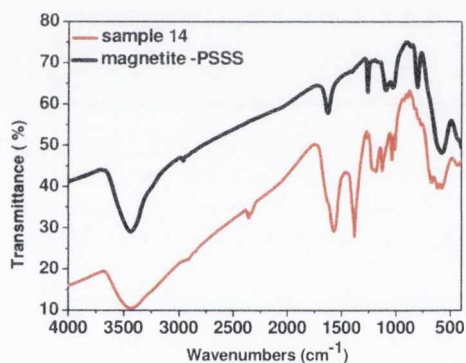

Figure 4.21. FTIR spectra of selected magnetic luminescent nanostructures. **Key**: (black) magnetite-PSSS nanoparticles, (red) **Sample 14**.

4.3.6. Thermogravimetric analysis (TGA) of magnetic luminescent nanostructures

Fig. 4.22 shows TGA and D-TGA curves for PSSS coated magnetite nanoparticles, magnetite nanocomposites with 10 PE layers and magnetic luminescent nanostructures from 30 up to 900 °C. From the curves (**Fig. 4.22 (1)**) multiple step thermal decomposition process are seen to be taking place. Firstly, a 2-3 % weight loss up to 100 °C can be attributed to the evaporation of absorbed water on the surface of nanoparticles and nanostructures. Results showed a similar general shape for both the magnetic and magnetic luminescent nanocomposites (**Fig 4.22 (1)** green and red).

The second step of weight loss at about 180-300 °C corresponds to the decomposition of the organic matter (extra PE layers) from the surface of magnetite. Weight loss at about 350-500 °C could be explained as possible low-temperature oxidation of colloidal magnetite particles to maghemite [30] (**Fig 4.22 (1)** green red curves).

We have found that multilayered nanocomposites (magnetite with 10 PE layers) had a total weight loss ~27 %, while for magnetic luminescent nanostructures this weight total loss was loss 62 %, where ~35 % was due to presence of thioglycolic acid and gelatine on the surface of the CdTe QDs. D-TGA curves (**Fig 4.22 (2)**) of magnetic luminescent nanostructures showed peaks at 304, 449, 646, 724, 756 °C which suggests that interpretation of the decomposition process is more complex due to presence of the CdTe QDs in the system (see **Fig. 4.22 (2)** red curve).
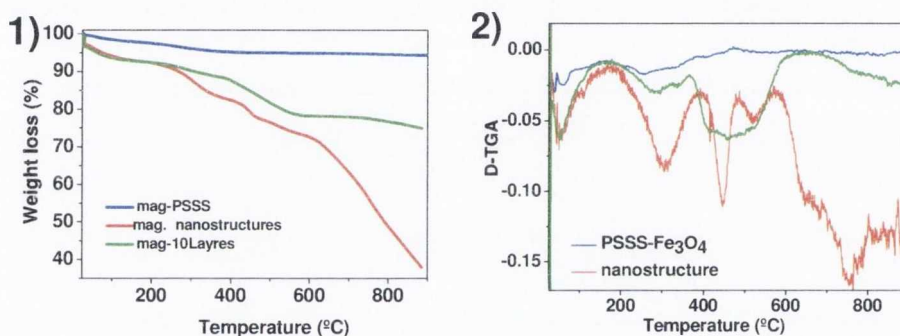
Figure 4.22. 1) TGA curve **2)** D-TGA curve. **Key**: (red) magnetic luminescent nanostructures (**sample 13**) (green) multilayered nanocomposites (blue) PSSS coated magnetite nanoparticles.

4.4. Conclusions

The aqueous *in situ* co-precipitation method allows for the synthesis of PSSS stabilised superparamagnetic nanocomposites and form very stable suspensions in water. This co-precipitation method has several advantages over other existing procedures: it is a quick, inexpensive one step experiment which is reproducible and whose parameters can be varied to produce various magnetic fluids. Thus, our approach uses a simple technique to control the particle size over a broad range, down to 10 nm primary particles. This is an exciting prospect as there is currently no reported method of a system, which allows tuning of the contrast agent relaxivity.

We have also demonstrated that by choosing appropriate iron and polyelectrolyte concentrations and ratios, we potentially can tune the magnetic properties and the nanocomposites and their relaxivities.

It was found that PSSS coated magnetite nanoparticles showed great potential as magnetic templates for the fabrication of "two-in-one" magnetic luminescent nanocomposites using LbL technique.

We demonstrated that various sized CdTe QDs coated with a stabilizer PAH could be linked to the surface of the multilayered core/shell magnetite nanoparticles and as a result produce stable magnetic-luminescent magnetite nanocomposites.

These nanostructures display intense luminescence when excited under UV light. The nanocomposites also demonstrate magnetic properties and could be easily separated from the CdTe QD solution using an external magnetic field. We have also shown that the luminescent magnetic nanocomposites can be organized in long parallel "chains-like" structures when dried in a parallel magnetic field and could be detected by confocal microscopy.

We believe that these magnetic-fluorescent nanocomposites can find a range of applications in chemistry and biology.

4.5. References

1. H. Yan, S.H. Park, G. Finkelstein, J.H. Reif, T.H. Labean., *Science.*, (2003), 301, 1882.

2. H. A. Becerril, R.M. Stoltenberg, D.R.Wheeler, R.C. Davis, J.N. Harb, A.T. Woolley., *Journal of American Chemical Society.*, 127, (2005), 2828.

3. N.C. Seeman., *Nature*, 421, (2003), 427.

4. S.J. Byrne, S.A. Corr, Y.K. Gun'ko, J.M. Kelly, D.F. Brougham, S. Ghosh., *Chemical Communications.*, 22, (2004), 2560.

5. J. Philip, O. Mondain-Monval, F. Leal-Calderon, J. Bibette., *Journal of Physics D: Applied Physic*s., (1997), 30, 2798.

6. E. Furst, C. Suzuki, M. Fermigier, A. Gast., *Langmuir.*, (1998), 14, 7334.

7. S.L. Biswal, A.P. Gast., *Physical Review.*, (2003), 68, 021402.

8. C. Goubault, P. Jop, J. Baudry, E. Bertrand, M. Fermigier, J. Bibette., *Physical Review Letters*, (2003), 91, 260802.

9. C. Goubault, F. Leal-Calderon, J.-L. Viovy, J. Bibette., *Langmuir.*, (2005), 21, 3725.

10. H. Singh, P.E. Laibinis, T.A. Hatton., *Nano Letters.*, (2005), 5, 2149.

11. J. F. Berret, N. Schonbeck, F. Gazeau, D. El. Kharrat, O. Sandre, A. Vacher, M. Airiau., *Journal of American Chemical Society.*, (2006), 128, 1755.

12. H. Singh, P.E. Laibinis, T.A. Hatton., *Langmuir.*, (2005), 21, 11500.

13. A. Ditsch, P.E. Laibinis, D.I.C. Wang, T.A. Hatton., *Langmuir.*, (2005), 21, 6006.

14. R. Sheparovych, Y. Sahoo, M. Motornov, S.M. Wang, H. Luo, P.N. Prasad, I. Sokolov, S. Minko., *Chemistry of Materials.*, (2006), 18, 591.

15. http://www.malvern.com/LabEng/technology/zeta_potential/zeta_potential_L DE.htm 12.08.2009

16. R.T.M. Cornell, U. Schewertman., The Iron Oxides. Structure, Properties, Reactions, Occurrence and Uses., Wiley-VCH Verlag GmbH, (2003), 128.

17. S. Corr. New magnetic nanocomposite materials. Thesis for degree of Doctor of Philosophy. University of Dublin. Trinity College, (2006).

18. S. Nasrazadani and A. Raman., *Corrosion Science,* (1993), 34, 8, 1355-1365.

19.   M.A. Morales, T.K. Jain, V. Labhasetwar, D.L. Leslie-Pelecky., *Journal of Applied Physics.*, 97, (2005).

20.   V.T. Binh, S.T. Purcell, V. Semet, F. Feschet., *Applied Surface Science.*, 130–132, (1998), 803.

21.   H. Kachkachi, A. Ezzir, M. Nogues and E. Tronc., *European Physical Journal B*, 14, (2000), 681.

22.   J.F. Hochepied., *Nanotechnology*, ., 2(1), (2001).

23.   J.M.D. Coey., *Physical Review Letters*, 27, (1971), 1140.

24.   W.W. Wang, Y.J. Zhu, and M.L. Ruan., *Journal of Nanoparticle Research*, 9, (2007), 419–426.

25.   X. Hong, J. Li, M. Wang, J. Xu, W. Guo, J. Li, Y. Bai, and T. Li., *Chemistry of Materials.*, 16, (2004), 4022-4027.

26.   N. Gaponik., *Nano Letters*, 3 (3), (2003), 369-372.

27.   M.A. Walling, J.A. Novak and J.R.E. Shepard., *International Journal of Molecular Science.*, (2009), *10*, 441-491.

28.   V. Zucolotto, M. Ferreira, M.R. Cordeiro, C.J.L. Constantino, D.T. Balogh, A.R. Zanatta, W.C. Moreira, and O.N. Oliveira., *Journal of Physical Chemistry B.*, 107, (2003), 3733.

29.   J. Park, Y.W. Choi, K.B. Kim, H. Chung, and D. Sohn., *Bulletin of the Korean Chemical Society.*, 29, 1, (2008).

30.   B. Gillot, A.F. Rousset, G.Dupre., *Journal of Solid State Chemistry.*, 25, (1978), 263–271.

Chapter 5

5.1. Bimodal luminescent-magnetic nanocomposites

5.1.1.   Introduction

The combination of both magnetic and fluorescent properties in one nanocomposite can provide new "two-in-one" multifunctional nanomaterials with a broad range of potential applications. For example, these nanocomposites could serve as multimodal assays for *in vitro-* and *vivo-* bioimaging applications such as MRI and fluorescence microscopy. They can also be used as bimodal agents for anticancer therapy, encompassing photodynamic and hyperthermic capabilities. Fluorescent-magnetic nanocomposites may also be utilised as a multimodal diagnostic and therapeutic tool, which could be used, for example, to identify, diagnose and simultaneously treat various diseases. Other exciting applications of these nanocomposites include cell tracking, cytometry and magnetic separation, which could be easily controlled and monitored using fluorescent microscopy and MRI.

Quantum dots (QDs), which were considered in the previous chapter, exhibit many advantageous optical properties, however many inorganic semiconductor materials are quite toxic, effectively limiting their use in biological systems [1].

A lot of work has been carried out in recent years on the development of new fluorescent markers based on standard fluorescent labels such as organic dyes for molecular imaging, cell labelling and tracking, multiplexed analyses, and DNA detection [2, 3].

One of the common fluorescent dyes is Rhodamine B (RhB). Rhodamine B (**Fig. 5.1**) molecules usually have a positive charge and good solubility in water, methanol and ethanol [4, 5]. Rhodamine dyes are used extensively in biotechnology applications such as fluorescence microscopy [6], biology [7] and medicine [8] to highlight structures in biological tissues for viewing, often with the aid of different microscopy techniques. Rhodamine dye modifications may be used to define and

examine bulk tissues (highlighting, for example muscle cells [9], cell populations instance, or organelles within individual cells [10]).
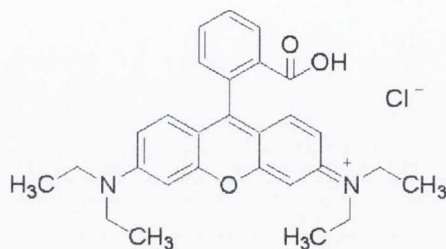
Figure 5.1. Chemical formula of *N*-[9-(2-Carboxyphenyl)-6-(diethylamino)-3*H*-xanthen-3-ylidene]- *N*-ethylethanaminium chloride (Rhodamine B).

Previously it was reported that by using standard organic synthesis methods Rhodamine B could be directly coupled with magnetite nanoparticles [11, 12].

The main aim of this part of our work is to prepare and investigate new "two-in one" fluorescent–magnetic nanocomposites, which are based on Rhodamine B coated polyelectrolyte stabilised magnetite nanoparticles. These nanomaterials can potentially serve as new multimodal MRI contrast agents and fluorescent markers for various biomedical applications. In addition we would like to explore these materials as potential drug delivery systems.

5.2. Preparation and investigation of new luminescent cobalt ferrite based nanocomposites

In this work we are going to apply a Layer by layer (LbL) technique [13-18] to prepare Rhodamine B coated magnetic (cobalt ferrite and magnetite) nanocomposites, where the fluorescent dye is bound *via* ionic interactions to the magnetic nanoparticle.

5.2.1. Preparation and characterisation of cobalt ferrite (CoFe₂O₄-PSSS) nanocomposites

$CoFe_2O_4$-PSSS nanocomposites have been prepared by the co-precipitation technique as described in Chapter 3, using 2: 4 mmoL ratios of Co^{2+}/ Fe^{2+} precursors.

114

The prepared nanocomposite products and their colloidal suspensions were analysed using TEM, FTIR, Raman spectroscopy, XRD, PCS, Zeta potential measurements and SQUID magnetometry techniques.

FTIR spectra of the $CoFe_2O_4$-PSSS revealed a stretch at 580 cm^{-1}, which is assigned to the Fe-O bonds. Co-O bonds are reported to have a stretch at 670 cm^{-1} [19, 20]. In the spectra (**Fig. 5.2 a)**) this peak appears as a shoulder on the Fe-O stretch. As with the magnetite samples, the PSSS-functionalised cobalt ferrite nanoparticles show stretches for aromatic C-C bonds, CH$_2$ bonds, sulfonate bonds and aromatic C-H bonds [20, 21]. Raman spectra (**Fig. 5.2 b)**) have displayed the main characteristic peaks of cobalt ferrite at 200, 315, 470, 627 and 688 cm^{-1} for the sample [22].
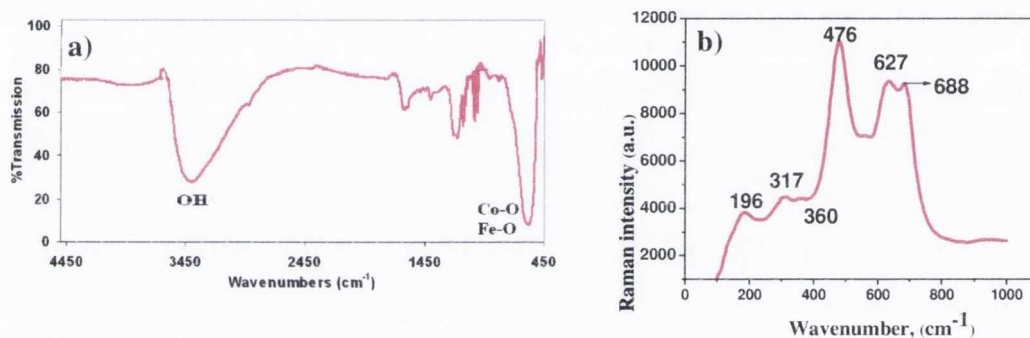
Figure 5.2. a) FTIR spectra of $CoFe_2O_4$-PSSS nanoparticles, b) Raman spectra $CoFe_2O_4$-PSSS nanoparticles.

TEM images (**Fig. 5.3**) showed cross-linked nanoparticles with an average particles diameter of 19.3 ± 3 nm.
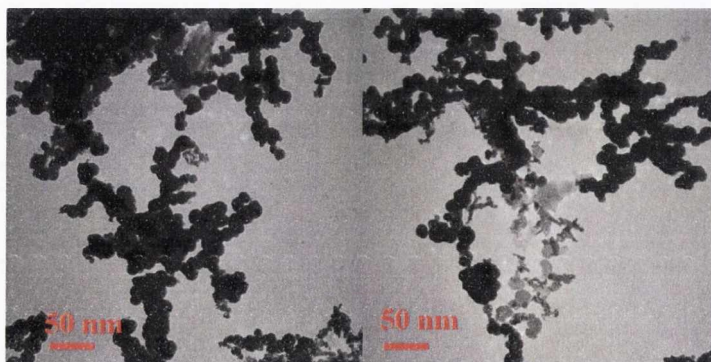
Figure 5.3. TEM images of $CoFe_2O_4$-PSSS nanoparticles.

115

PCS measurements were taken to check the suspension's stability in water and also to obtain the average particles size in diameter. Unfortunately, the sample showed some clustering in solution. **Fig. 5.4** shows the presence of two peaks at 90 nm and 700 nm (PDI 0.567). The presence of the larger particles (clusters) could be explained by the cross-linking of primary magnetic particles.
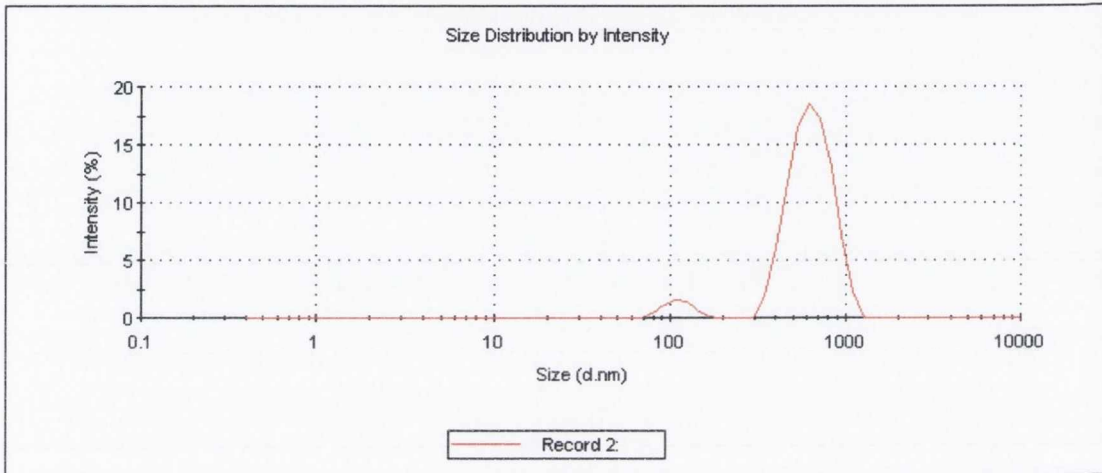
Figure 5.4. Hydrodynamic radius distributions of $CoFe_2O_4$-PSSS nanoparticles in Millipore water.

When the sample was analysed with SQUID magnetometry, PSSS functionalised $CoFe_2O_4$ nanoparticles showed no hysteresis and demonstrated clear superparamagnetic behaviour at 300 K (**Fig. 5.5**) with the magnetisation (M_S) of 26 $Am^2kg^{-1}K$.
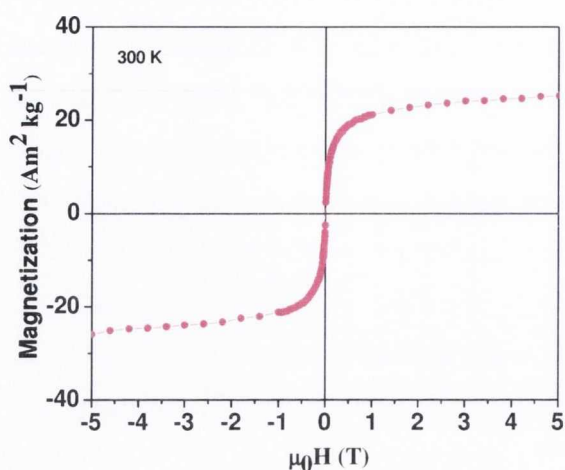
Figure 5.5. Magnetisation curve versus magnetic field for $CoFe_2O_4$-PSSS powder.

Thus the properties and stability of the sample with small particles size made PSSS stabilised cobalt ferrite nanoparticles a suitable candidate for the further synthesis of fluorescent-magnetic nanocomposites.

5.2.2. Preparation of multilayered $CoFe_2O_4$-PSSS-RhB nanocomposites

We chose cobalt ferrite nanoparticles stabilised with PSSS polyelectrolyte as magnetic templates because of their potentially high magnetic moment. It was expected that the ionic interaction between the positively charged RhB and the negatively charged polyelectrolyte coated magnetic cobalt ferrite nanoparticles would lead to the formation of new luminescent-magnetic nanocomposites.

A modified LbL technique [13-18] was used to prepare cobalt ferrite nanoparticles with multilayer polyelectrolyte coating. LbL technique has several potential advantages, which include simplicity, universality, and thickness control at the nanoscale level, compared with the other available assembly techniques. Simultaneously, LbL provides the opportunity to combine optical and magnetic properties in one nanomaterial. A multilayered polyelectrolyte coating should cover and isolate the magnetic nanoparticle cores from direct contact with the fluorescent Rhodamine B molecules and prevent paramagnetic quenching of the dye. The quenching is strongly dependent on the separation distance between RhB and magnetic cores and the luminescence intensity is expected to drastically increase with

117

increasing distance between the magnetic shell and the luminescent dye. The Zeta potential measurements were used to monitor the successful deposition of PE layers using LbL technique. **Fig. 5.6** shows the changes of Zeta potential during the formation of multilayered nanocomposites using positively and negatively charged PE (PSSS, PAH) and LbL technique.
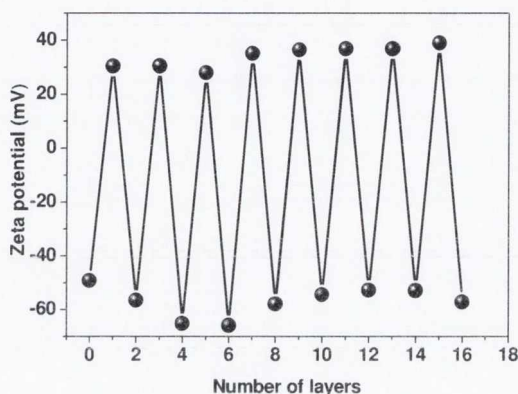
Figure 5.6. Zeta potential of the negatively charged $CoFe_2O_4$-PSSS coated PAH/PE_{16} nanoparticles as a function of polyelectrolyte layers numbers for PAH/PSSS coatings.

When 10, 12 and 14 layers of PE were deposited on the surface of the nanoparticles and Rhodamine B was added to the suspension, complete quenching of luminescence was observed. This suggests that the distance between the magnetic core and the organic dye is not sufficient to prevent the quenching of the RhB emission. However, the $CoFe_2O_4$ sample with 16 PE layers (shell) was used as a template for the preparation of magnetic- fluorescent nanocomposites as it demonstrated some luminescence under UV light. A summary of these feasibility studies is shown in **Table 5.1**. These findings indicate that multilayered $CoFe_2O_4$-PSSS-PAH/PE_{16} nanocomposites could be used as a template in future synthesises of magnetic luminescent nanocomposites. This fact also confirms that control of the distance between the organic luminescent dye and magnetic cores is crucial for the fabrication of magnetic luminescent nanocomposites. An attempt to introduce more than 16 PE layers resulted in very low stability of magnetic suspension (PDI = 1, from PCS), which leads to the precipitation of the final materials. Note that, zeta potential measurements were on the limit of detection of the machine (see **Appendix**

118

4). Therefore, in our following preparation of magnetic luminescent nanocomposites we used $CoFe_2O_4$-PSSS nanoparticles with 16 layers of PE coating. A series of samples with RhB were prepared at various dye concentration (see **Table 5.2**).

Table 5.1. Summarised data of the multilayered $CoFe_2O_4$-PSSS nanocomposites.

Sample	Number of layers of PE	Concentration RhB (M)	Stability	Presence of Luminescence
$CoFe_2O_4$-PE	10	4.2×10^{-5}	stable	no
$CoFe_2O_4$-PE	10	$1.2 \cdot 10^{-4}$	stable	no
$CoFe_2O_4$-PE	10	$1.8 \cdot 10^{-4}$	stable	no
$CoFe_2O_4$-PE	10	$2.1 \cdot 10^{-4}$	stable	no
$CoFe_2O_4$-PE	12	$2.1 \cdot 10^{-4}$	stable	no
$CoFe_2O_4$-PE	12	$2.1 \cdot 10^{-4}$	stable	no
$CoFe_2O_4$-PE	14	$2.1 \cdot 10^{-4}$	stable	no
$CoFe_2O_4$-PE	16	$2.1 \cdot 10^{-4}$	stable	**yes**

Schematic illustration of the fabrication of magnetic luminescent nanocomposites is presented in **Fig. 5.7**.
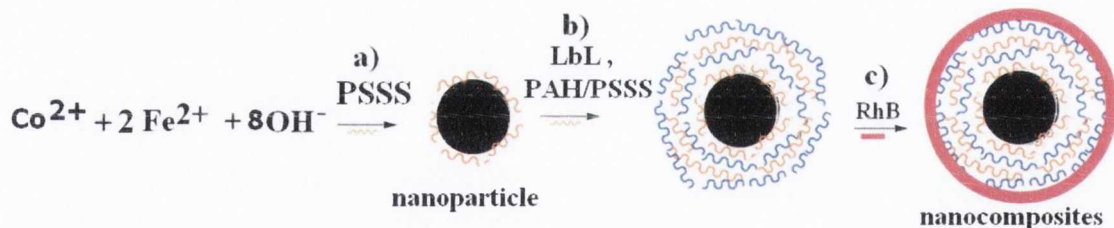
Figure 5.7. Schematic illustration of fabrication magnetic luminescent nanocomposites using the LbL technique.

Table 5.2. Summaries of results of $CoFe_2O_4$-PSSS-PAH/PE_{16}-RhB nanocomposites. $CoFe_2O_4$-PSSS-PAH/PE_{16} (5.8×10^{-4} g/mL).

Sample	$CoFe_2O_4$ with 16 layers PE	Rhodamine B	Concentration RhB (M)
15	2 mL	0.5 mL	4.2×10^{-5}
16	2 mL	1 mL	$1.2 \cdot 10^{-4}$
17	2 mL	2 mL	$1.8 \cdot 10^{-4}$
18	2 mL	3 mL	$2.1 \cdot 10^{-4}$

5.2.2.1. TEM microscopy studies of CoFe₂O₄-PSSS-PAH/PE₁₆-RhB nanocomposites
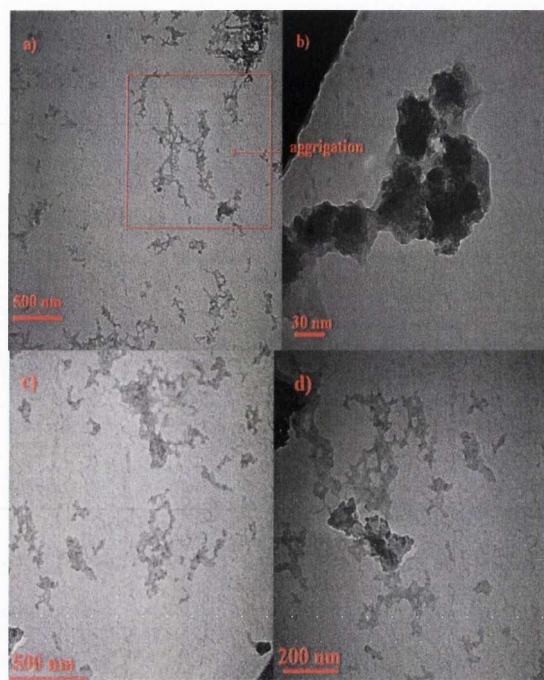
TEM images of $CoFe_2O_4$-PSSS-PAH/PE$_{16}$ nanocomposites showed the presence of the highly aggregated $CoFe_2O_4$ nanoparticles coated with polyelectrolytes. The average particles size was 19.3 ± 3 nm in diameter (**Fig. 5.8**). TEM images displayed the formation of a series of self-assembled interconnected long chains or array structures which are formed due to cross-linking of $CoFe_2O_4$-PSSS nanoparticles by PE molecules. This was accompanied by an increase in the average particle size with the addition of polymer coating (shell) to 25.6 ± 4.2 nm.
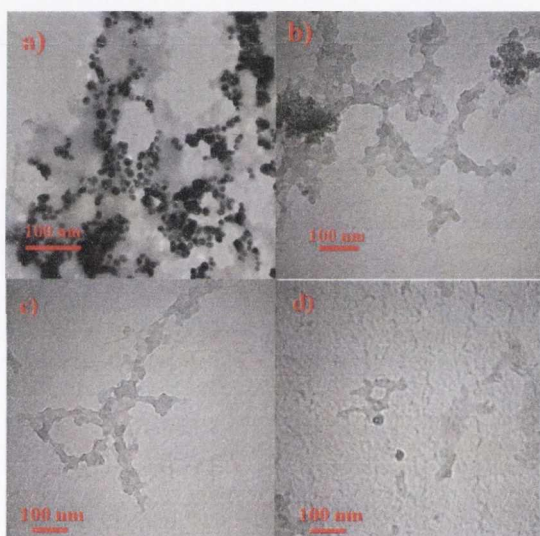
Figure 5.8. TEM images of $CoFe_2O_4$-PSSS and $CoFe_2O_4$-PSSS_PAH/PE$_{16}$ nanocomposites. a) initial $CoFe_2O_4$ –PSSS particles, (b-d) $CoFe_2O_4$-PSSS particles coated with 16 layers of PE.

After the treatment with RhB, the particles size distribution increased to 52.7 ± 12 nm due the aggregation process (**Fig. 5.9**). Both samples treated with higher RhB concentrations (**Samples 17 a**nd **18**) showed similar results.

Figure 5.9. TEM images of selected $CoFe_2O_4$-PSSS_PAH/PE_{16}-RhB nanocomposites. (a, b) **sample 16**, (RhB, 1.2×10^{-4} M), (c, d) **sample 15**, (RhB, 4.2×10^{-5} M).

In the presence of an external parallel 0.5 T magnetic field, all samples formed linear chain-like assemblies with specific orientation in the direction of the applied magnetic field. Once this alignment occurs, the attraction between the particles is strong enough so that the formed chains retain their orientation after removing the magnetic field (**Fig. 5.10**).
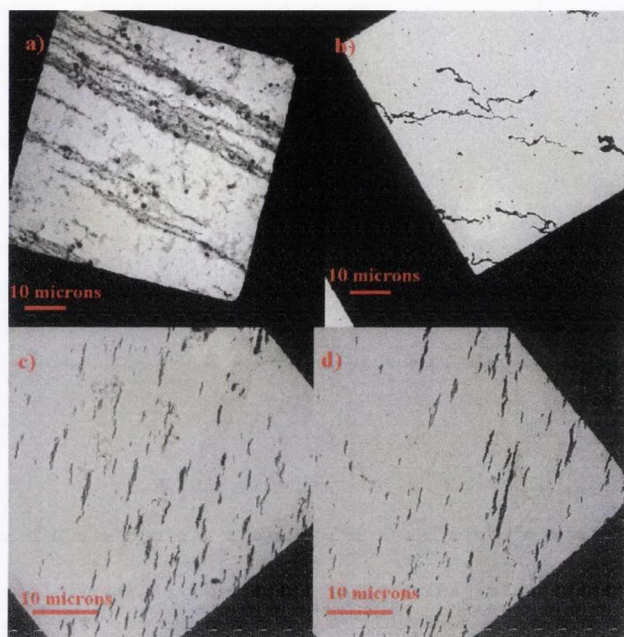
Figure 5.10. TEM images of $CoFe_2O_4$-PSSS_PAH/PE$_{16}$-RhB nanocomposites in 0.5 T parallel magnetic field. a) and b) **sample 16**, (RhB, 1.2×10^{-4} M), c) and d) **sample 15**, (RhB, 4.2×10^{-5} M).

5.2.2.2. FTIR spectroscopy studies of $CoFe_2O_4$-PSSS-RhB nanocomposites

FTIR spectra were recorded for all samples and compared with pure RhB. **Fig. 5.11** shows characteristic O-H stretching vibration at 3420 cm^{-1}. The stretching vibration peak characteristic of Co-O bond is hidden due to its proximity with Fe-O bond peak around 580 cm^{-1} [19] (**Fig 5.11**). The green curve of $CoFe_2O_4$-PSSS-RhB nanocomposites shows weak characteristic bands C=O 1651-1694 cm^{-1} of Rhodamine and C-H stretching vibrations at 2974 and 2883 cm^{-1} [23]. Peaks of aromatic C=C bonds appear at 1600-1400 cm^{-1} (**Fig 5.11**). There are also C-H peaks around 2980 cm^{-1} arising from organic groups. Stretches at 1350 and 1150 cm^{-1} represent S=O bonds from PSSS coating. Thus the RhB dye was still present on the surface of particles even after being washed several times with Millipore water. However, because of the small concentration of surface molecules relative to the metal oxide core, this type of characterisation is not very accurate in detecting of the changes of surface composition.
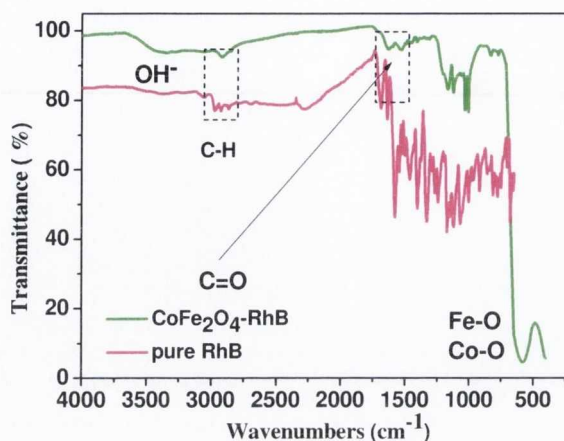
Figure 5.11. FTIR spectra of selected $CoFe_2O_4$-PSSS_PAH/PE$_{16}$ nanocomposites. **Key:** (green) $CoFe_2O_4$-RhB nanocomposite, **sample 16** (RhB, $1.2 \cdot 10^{-4}$ M), (magenta) pure Rhodamine B.

5.2.2.3. UV-vis and PL spectroscopy of $CoFe_2O_4$-PSSS-PAH/PE$_{16}$-RhB nanocomposites

For further confirmation of the presence of RhB on the surface of our multilayered $CoFe_2O_4$-PSSS nanocomposites after washing, the last washing fraction was used for spectroscopic studies and compared with particles re-dispersed in distilled water. Because of its fully conjugated structure, pure RhB has the characteristic intense red colour with the maximum absorbance at 555 nm [4]. **Fig. 5.12** shows **a)** UV-vis and **b)** excitation spectra of pure RhB and prepared samples before washing procedure. The luminescence absorbance spectra of the $CoFe_2O_4$-PSSS_PAH/PE$_{16}$-RhB samples show a similar peak around ~555 nm [4, 24]. This indicates that the origin of their luminescence is due the presence of RhB on the surface of the multilayered magnetic nanocomposites (**Fig. 5.13**).
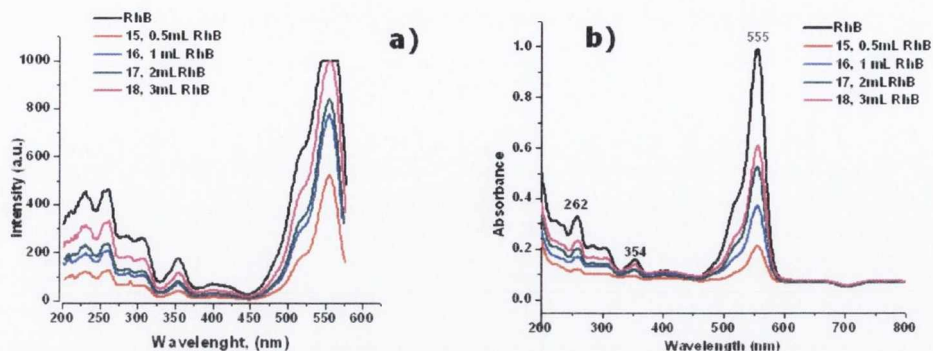
Figure 5.12. Room temperature a) Excitation spectra of magnetic luminescent $CoFe_2O_4$ nanocomposites with various concentration of Rhodamine B in samples; b) Absorbance spectra of Fe_3O_4-PSSS_PAH/PE_{16} RhB nanocomposites. **Key**: (black) Rhodamine B, (magenta) **sample 18**, (RhB, 2.1×10^{-4} M), (dark cyan) **sample 17**, (RhB, 1.8×10^{-4} M), (blue) **sample 16**, (RhB, 1.2×10^{-4} M), (red) **sample 15**, (RhB, 4.2×10^{-5} M).
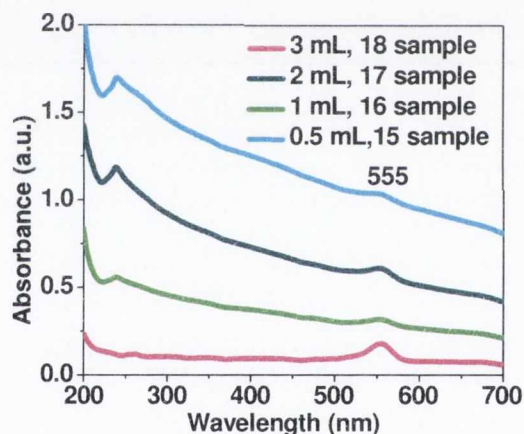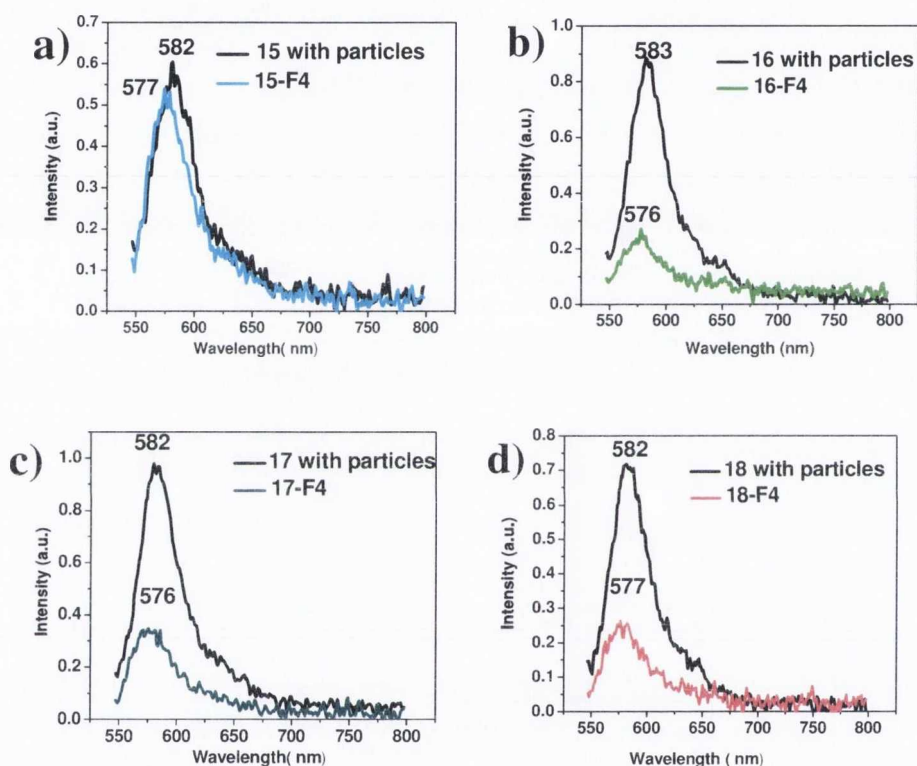

Figure 5.13. Absorbance spectra of $CoFe_2O_4$_PSSS-PAH/PE_{16} RhB nanocomposites with various concentration of RhB in a sample (last wash with particles). **Key**: (magenta) **sample 18,** (RhB, 2.1×10^{-4} M), (dark cyan) **sample 17**, (RhB, 1.8×10^{-4} M), (green) **sample 16**, (RhB, 1.2×10^{-4} M), (cyan) **sample 15**, (RhB, 4.2×10^{-5} M).

$CoFe_2O_4$-PSSS_PAH/PE_{16}-RhB nanocomposites still contained their characteristic magenta colour in solution, thus indicating the generation of Rhodamine B in the final product for all samples (**Fig. 5.13, 5.14**). Importantly, the final washings of the **samples 15–17** were almost colourless, with their UV–Vis spectra devoid of absorbance bands above 550 nm. A red shift around 5-6 nm was

observed in all spectra of new nanocomposites. It was estimated that less then ~1 % of the original RhB used for the synthesis was incorporated on the surface of multilayered $CoFe_2O_4$ nanoparticles.

Unfortunately, the luminescence intensity of the nanocomposites was much weaker than expected (**Fig. 5.14**). This can be explained by still quite a significant quenching of RhB by $CoFe_2O_4$ nanoparticles.

Figure 5.14. Room temperature emission spectra of $CoFe_2O_{44}$-PSSS_PAH/PE_{16}-RhB nanocomposites with various concentration of RhB in the sample. (λ_{ex} = 555 nm). **Key**: black curve corresponds to the last filtrate. a) **sample 15**, (RhB, 4.2×10^{-5} M), b) **sample 16**, (RhB, 1.2×10^{-4} M), c) **sample 17**, (RhB, 1.8×10^{-4} M), d) **sample 18**, (RhB, 2.1×10^{-4} M).

5.2.2.4. Effect of time on optical properties of $CoFe_2O_4$-PSSS-PAH/PE_{16}-RhB nanocomposites

To monitor the effect of time and the presence of excess PE on the stability and optical properties of $CoFe_2O_4$-PSSS_PAH/PE_{16}-RhB nanocomposites, aqueous

solutions of the composites with various RhB concentrations in the sample were kept in darkness at the room temperature over period of 3 days.

A reduction in the luminescence was observed for all samples after 3 days due to complete quenching (**Fig. 5.15**), followed by coagulation and precipitation of the colloidal suspension. This is most likely due to the slow elimination of deposited PE shells, which in turn led to the formation of the larger aggregates (clusters) with time. This process also resulted in quenching of RhB species, which were not separated by PE shells from $CoFe_2O_4$ nanoparticles.
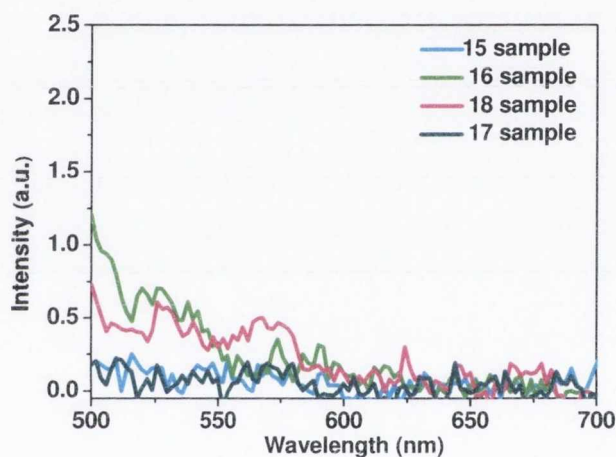
Figure 5.15. Room temperature emission spectra of $CoFe_2O_4$-PSSS_PAH/PE$_{16}$-RhB nanocomposites with various concentration of RhB in the sample after 3 days. ($\lambda_{ex} = 555$ nm). **Key**: (cyan) **sample 15**, (RhB, 4.2×10^{-5} M), (green) **sample 16**, (RhB, 1.2×10^{-4} M), (dark cyan) **sample 17**, (RhB, 1.8×10^{-4} M), (magenta) **sample 18**, (RhB, 2.1×10^{-4} M).

TEM images have confirmed the intensive aggregation of the nanocomposites after 3 days (**Fig. 5.16**).
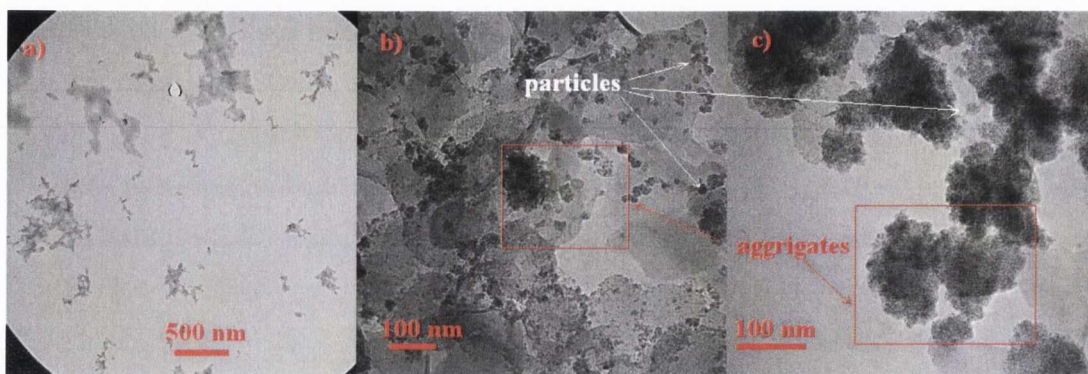
Figure 5.16. Selected TEM images $CoFe_2O_4$-PSSS_PAH/PE$_{16}$-RhB nanocomposites after 3 days. **Sample 15**, (RhB, 4.2×10^{-5} M). a), b) and c) formation of aggregates after 3 days.

Attempts to measure average particle size in solution using PCS were unsuccessful, due to the low stability of the nanocomposites in water.

A series of other tests were performed on the $CoFe_2O_4$-PSSS_PAH/PE$_{16}$-RhB nanocomposites in order to improve their optical properties and the stability of suspension of luminescent nanocomposites.

Our next goal was to deposit extra polyelectrolyte shells on the top of the $CoFe_2O_4$-PSSS_PAH/PE$_{16}$-RhB nanocomposites. It was expected that the extra coating might prevent or reduce dissolution and diffusion of RhB molecules from the surface into the surrounding media, which would improve the luminescent properties of the nanocomposites.

Following the standard procedure from **Fig. 5.7** extra layers of PAH and PSSS were deposited on the surface of $CoFe_2O_4$-PSSS_PAH/PE$_{16}$-RhB.

Unfortunately, this resulted in the aggregation and strong decreased in luminescence intensity after each addition of PE. See **Fig. 5.17** and summarised data in **Table 5.3**.
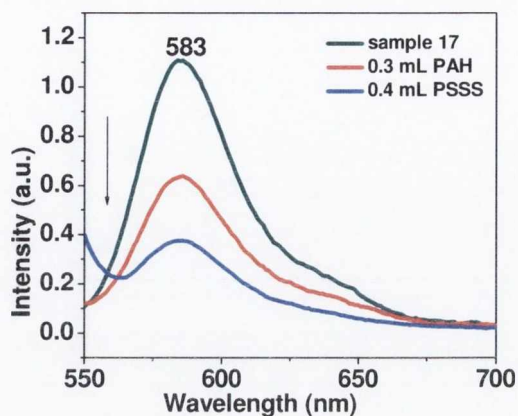
Figure 5.17. Room temperature emission spectra of selected CoFe$_2$O$_4$-PSSS_PAH/PE$_{16}$-RhB nanocomposites. **Sample 17**. (λ_{ex} = 555 nm) **Key**: (dark cyan) uncoated CoFe$_2$O$_4$-PSSS_PAH/PE$_{16}$-RhB nanocomposite, (red) 0.3 mL PAH (blue) 0.4 mL PSSS.

Sample 17 after coating showed a decrease in PL signal when compared to the uncoated sample. The PCS data recorded for the coated CoFe$_2$O$_4$-PSSS_PAH/PE$_{16}$-RhB showed evidence of large amounts of aggregation after depositing the extra layer of PAH (**Table 5.3**). After the addition of an extra PSSS layer precipitation of the nanocomposites was observed. These phenomena could be explained by the partial replacement of RhB by polyelectrolyte during the introduction of extra PE layers. As a result free non-attached RhB was washed and we have obtained only highly aggregated unstable nanocomposites with low RhB content and consequently with a very weak emission.

Table 5.3. Summarised data of results of CoFe$_2$O$_4$-PSSS-PAH/PE$_{16}$-RhB nanocomposites before and after deposition of extra PE layers.

Name	Zeta potential (mV)		Size from PCS (nm)		Suspension stability	
	before	after	before	after	before	after
Extra PAH	-30.6	+35.4	332.1 (PDI=238)	437.4 (PDI=0.407)	stable	non-stable
Extra PSSS	+35.4	-29.7	437.4 (PDI=0.407)	664.7 (PDI=0.832)	non-stable	non-stable

5.3. Preparation and investigation of new luminescent magnetite based nanocomposites

Unfortunately, as shown above $CoFe_2O_4$-RhB nanocomposites have demonstrated quite weak luminescence as they were not very resistant to quenching. In addition, due to the presence of cobalt in $CoFe_2O_4$-RhB nanocomposites are potentially toxic for use in biological studies. Therefore, we decided to prepare similar magnetite based nanocomposites.

5.3.1. Preparation and characterisation of magnetite (Fe_3O_4-PSSS) nanoparticles

According to previous studies of S. Corr [19] and C. Seymour [25] polyelectrolytes (PSSS or PAH) stabilised magnetite nanoparticles provided sufficient electrostatic stabilisation avoiding agglomeration for long periods of time. In the reaction solution, the molar ratio of precursors $FeCl_3$ to $FeCl_2$ was fixed at 2 : 1, which was consistent with the theoretical atomic ratio of Fe^{3+} to Fe^{2+} in Fe_3O_4 nanoparticles. As a result we have prepared well-dispersed magnetite (Fe_3O_4) PSSS stabilised particles with average size in diameter than 10 nm [19].

In our work we used an optimised co-precipitation method to prepare PSSS stabilised magnetite nanoparticles. 1 : 2 mmoL ratio of Fe^{3+} and Fe^{2+} precursors, and 2.3×10^{-4} M PSSS solution were used for the synthesis of stable magnetic fluid of magnetite nanoparticles in distilled water. Freshly synthesised materials have been characterised by FTIR spectroscopy, magnetisation measurements, TGA, TEM, PCS, Zeta potential and NMRD studies.

When the FTIR spectra were compared with those of the uncoated Fe_3O_4 particles, the same absorption peaks in the spectrum of the modified particles confirmed the successful coating of polymer on the surface of nanoparticles (**Fig. 5.18 a)**). FTIR spectra of Fe_3O_4 nanoparticles without PSSS gave stretches at 570-580 cm^{-1} for Fe-O bond [19, 25], and 3440-3460 cm^{-1} OH⁻ groups and a weak peak at 2345 cm^{-1} attributed to the adsorbed H_2O on a surface of the particle. The spectra of pure PSSS (in green) show the characteristic bands of arenes with represent peaks of

129

aromatic C=C bonds (1600-1400 cm^{-1}) and C-H peaks slightly below 3000 cm^{-1}. Stretches at 1350 and 1150 cm^{-1} represent S=O bond [26, 27] (**Fig. 5.18 a)**). Analysis had confirmed the formation of magnetite-PSSS nanocomposites. Raman spectra of the PSSS coated magnetite nanoparticles. (**Fig. 5.18 b)** showed a main peak at 670 cm^{-1}[20, 28], which characteristic for pure Fe_3O_4 phase.
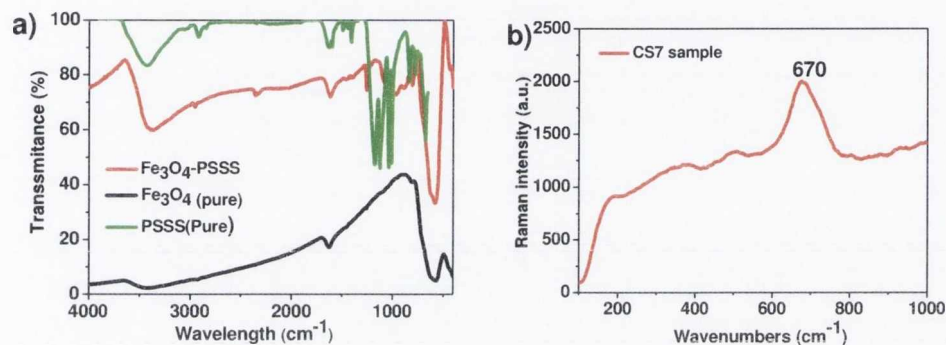
Figure 5.18. FTIR spectra of Fe_3O_4-PSSS sample. **Key**: (black) pure Fe_3O_4, (red) Fe_3O_4-PSSS, (green) pure PSSS. b) Raman spectra of Fe_3O_4-PSSS nanoparticles (**CS7$_r$ sample** – repeated sample).

PSSS functionalised magnetite samples demonstrated no hysteresis and typical superparamagnetic behaviour at 300 K. Magnetisation (M_S) was 67.79 Am^2kg^{-1} K (**Fig. 5.19**).
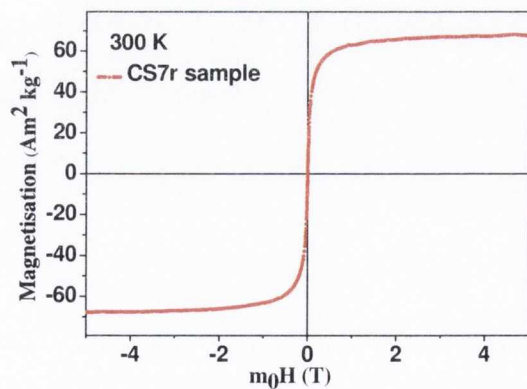
**Figure 5.19.** Magnetisation curve versus magnetic field for Fe_3O_4-PSSS nanoparticles. Measurements were carried out at 27 °C. (**CS7r sample**)

The TGA measurements for PSSS coated magnetite nanoparticles (**Fig. 5.20**) showed 0.4-1 % weight lost around 50-70 °C, which corresponds to adsorbed

molecules of H_2O on surface on PSSS coated magnetite nanoparticles. The apparent weight loss of ~5 % was observed around 260 °C, corresponds to the decomposition of polyelectrolyte on the surface of the Fe_3O_4 nanoparticles.
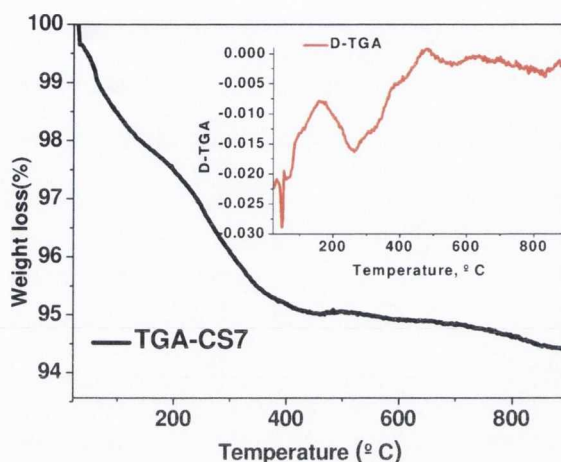
Figure 5.20. TGA spectra of Fe_3O_4-PSSS nanoparticles. **Key**: (black) Fe_3O_4-PSSS (**CS7$_r$ sample**). The insert shows D-TGA curve of Fe_3O_4-PSSS.

TEM analysis (**Fig. 5.21 c)**) of the Fe_3O_4-PSSS nanocomposites showed highly aggregated nanoparticle assemblies with quite narrow size distribution (7.9 ±1.5 nm) for primary nanoparticles. Under an external 0.5 T magnetic field, Fe_3O_4-PSSS nanoparticles form long chains, which are parallel to the field applied (**Fig. 5.21 c**). The average chain diameter of these nanocomposites was 4.3 ± 3.5 µm.
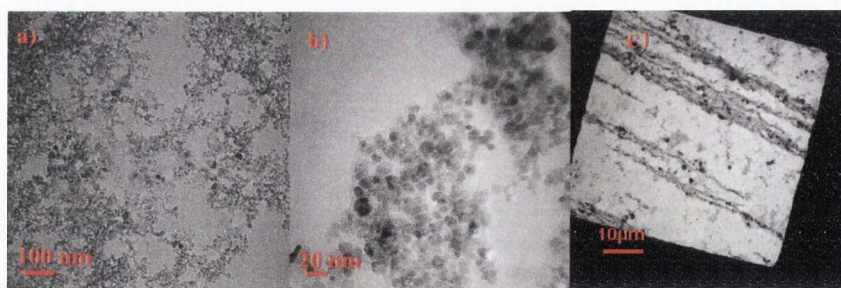
Figure 5.21. TEM images of Fe_3O_4-PSSS nanoparticles. a), b) without external 0.5 T magnetic field (0.5 T c) under external parallel magnetic field (0.5 T).

Then the stable magnetic suspension (last filtrate) was analysed by PCS. These measurements in general, confirmed TEM data and showed the presence of

nanoparticle aggregates with an average hydrodynamic diameter of 141.4 nm (PDI 0.141).

NMRD studies of Fe_3O_4-PSSS nanocomposites in Millipore water (**Fig. 5.22**) demonstrate curves, which are typical for superparamagnetic magnetite nanoparticles. The **sample CS7$_r$** (with Fe/PSSS ratio of 283) has shown the highest relaxivity of ~ 73.43 s^{-1} at lower field (0.62 MHz). To confirm the suspension stability and reproducibility of NMRD measurements, they were repeated after 3 days. No decrease in suspension stability was observed. **Fig. 5.22** (red data points on the black curve) shows no change of the NMRD curve at the selected frequencies (0.023, 0.034, 0.06, 9.28, MHz) after 3 days. Relaxation time measurements gave $T_1 = 1.97x10^{-2}$ (error 0.04%) and $T_2 = 3.25x10^{-3}$ (error 0.21%) values.

The PCS data obtained for the PSSS coated magnetite nanoparticles do not show any evidence of extra aggregation after NMR field. In fact PCS data showed a slight decrease in average of the hydrodynamic diameter of magnetite particles size (**Table 5.4**).
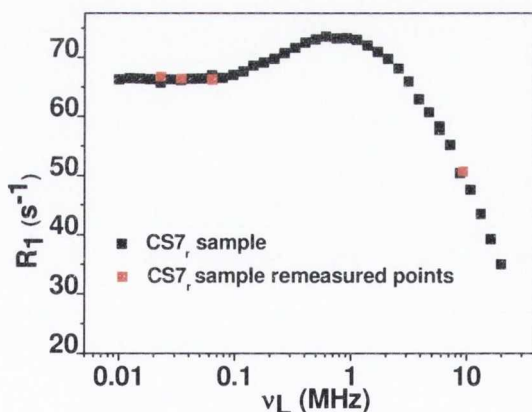

Figure 5.22. NMRD relaxation curve recorded at a measuring frequency of 20 MHz for Fe_3O_4-PSSS nanoparticles in Millipore water. **Key**: (black) PSSS coated nanoparticles, (red) data points correspond to the re-measured NMR of sample after 3 days. Measurements were carried out at 24.8 ±1°C. **CS7$_r$ sample**.

Table 5.4. Summarised PCS and TEM data of Fe_3O_4-PSSS nanoparticles before and after NMR measurements.

| Name	Before NMR field		After NMR field	
	TEM (nm)	PCS (nm)	TEM (nm)	PCS (nm)
CS7$_r$	8.8±0.6	171.6, PDI 0.203	9±1	138.2, PDI 0.203

According to TEM images, no change in the particles size and morphology were observed after NMRD measurements were performed on the tested sample (**Fig. 5.23**).
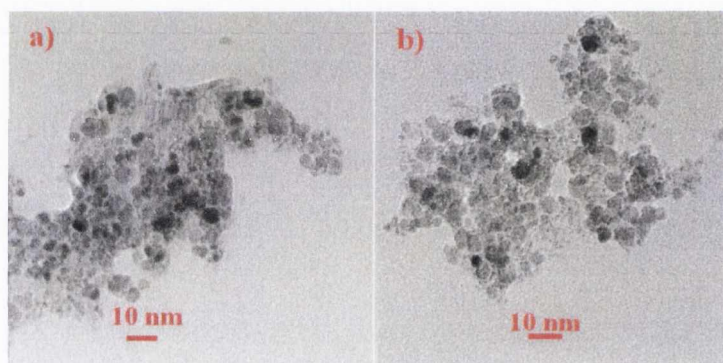
Figure 5.23. TEM images of Fe_3O_4-PSSS nanoparticles before and after NMR measurements. **CS7$_r$ sample**.

### 5.3.2. Fabrication of multilayered Fe_3O_4-PSSS-PAH/PE$_{10}$-RhB nanocomposites

In this part of our work, Fe_3O_4-PSSS-PAH/PE$_{10}$ nanocomposites were used as templates for electrostatic binding of RhB to the surface of the nanoparticles. Similarly, above LbL deposition technique [15] was used for the fabrication of Fe_3O_4-PSSS nanoparticles coated with 10 layers of PE (see Chapter 4). Schematic illustration of the LbL deposition is presented in **Fig. 5.24** below. Driven by electrostatic interactions, the positively charged RhB molecules were deposited as a final layer on the negatively charged multilayered Fe_3O_4-PSSS-PAH/PE$_{10}$ nanoparticles via electrostatic bonding.
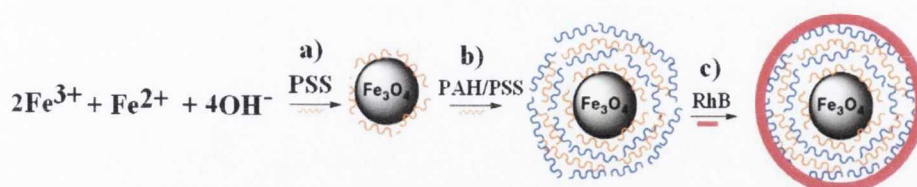
Figure 5.24. Schematic illustration of fabrication magnetic luminescent nanocomposites using the LbL technique.

Fig. 5.25 shows the monitoring of Zeta potential as a function of deposited number of polyelectrolyte layers for negatively charged Fe_3O_4-PSSS. The measurement of Zeta potential was performed at each stage during the preparation of new nanocomposites. 10 layers of PE were successfully deposited on the Fe_3O_4-PSSS nanoparticles. Zeta potential of multilayered Fe_3O_4-PSSS-PAH/PE$_{10}$ nanoparticles was -36.1 mV. A series of experiments were done to treat multilayered structures of Fe_3O_4-PSSS-PAH/PE$_{10}$ with RhB. These nanocomposites were mixed with RhB solution ($2.1 \cdot 10^{-4}$M) overnight, and changes in Zeta potential were monitored. The **sample 25** demonstrated the best stability and has shown the Zeta potential of -26.8 mV with standard deviation of -6.3 mV for the final product. Summarised experimental data for the optimised sample is presented in the **Table 5.5**. Unfortunately, the nanocomposites with higher RhB ratios were unstable in solution and did not give reliable results.
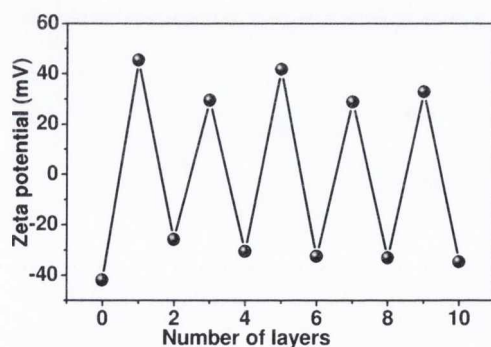
Figure 5.25. Zeta potential of the negatively charged Fe_3O_4-PSSS coated PAH/PE$_{10}$ nanoparticles as a function of polyelectrolyte layers numbers for PAH/PSSS coatings.

Table 5.5. Summaries of results for the optimised Fe_3O_4-PSSS-PAH/PE_{10}-RhB nanocomposite.

Sample	Fe_3O_4 with 10 layers PE	Rhodamine B (mL)	Concentration RhB (M)	Zeta potential before (mV)	Zeta potential after (mV)
25	10	3	$2.1 \cdot 10^{-4}$	-36.8	-26.8

### 5.3.3. UV-vis and PL spectroscopy of Fe_3O_4-PSSS-PAH/PE_{10}-RhB nanocomposites

Synthesised nanocomposites have demonstrated visible remnant luminescence (**Fig. 5.26**). This indicates that the reaction between multilayered Fe_3O_4-PSSS-PAH/PE_{10} nanocomposites and RhB resulted in the formation of new luminescent nanocomposites. UV-Vis scans were also carried out on the washings to confirm the absence of RhB from the final washing (**Fig. 5.26 a**) dotted line). However, a red shift of ~3 nm occurred in both absorbance spectra, indicating a possible increase in the particle size. PCS measurements were also indicative of the formation of new nanocomposites, showing a slight increase in the average diameter of the particles, from 203 nm (PDI 0.205) before the reaction to 223 nm (PDI 0.450) after the reaction. A significant drop in the luminescence was still observed due partial quenching of RhB molecules by superparamagnetic core. It was estimated from UV-vis spectra (**Fig.5.26 a)**) that only ~11.3 % of the original RhB ($2.1 \cdot 10^{-4}$ M used for the synthesis) was deposited on the surface of the nanocomposites.
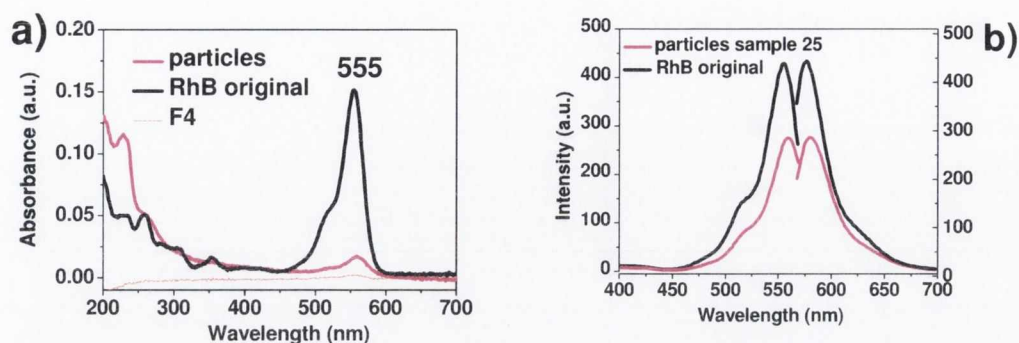
Figure 5.26. Room temperature spectra of Fe_3O_4-PSSS_PAH/PE_{10} –RhB nanocomposites. a) luminescence and excitation spectra **Key**: (black) Original RhB solution, (magenta) particles-RhB in water, **Sample 25,** b) luminescence (λ_{ex} = 555 nm) and excitation spectra. Dotted orange line shows last washing (F4).

The remnant luminescence intensity of 284 a.u. was observed for **sample 25** (**Fig. 5.26 b**)). In comparison of Fe_3O_4-PSSS_PAH/PE_{10} with $CoFe_2O_4$-PSSS_PAH/PE_{16} nanocomposites, magnetite samples demonstrated much stronger luminescence and there were not so much quenched as corresponding cobalt ferrite derivatives. There is no free RhB observed after repeated washing of Fe_3O_4-PSSS_PAH/PE_{10}-RhB nanocomposites with Millipore water, indicating the stable binding of RhB molecules within Fe_3O_4-PSSS_PAH/PE_{10}. Thus the Fe_3O_4-PSSS_PAH/PE_{10} sample still possesses sufficient emission for biological imaging applications.

The Fe_3O_4-PSSS-PAH/PE_{10}-RhB nanocomposites consist of magnetic iron oxide (**Fe_3O_4-**) core, which can be directed to specific locations when manipulated by an external magnetic field. In this case, the nanocomposites movement can be easily monitored through the luminescence of the particles. **Fig. 5.27** shows images of an aqueous dispersion of luminescent magnetic of Fe_3O_4-PSSS-PAH/PE_{10}-RhB nanocomposites under UV radiation (365 nm). While in the absence of a magnetic field the luminescence is observed from the whole dispersion (**Fig. 5.27, a**)), when a handheld magnet is placed below the glass vial, the nanocomposites accumulate near it over a period of a few hours (**Fig. 5.27, b**)).
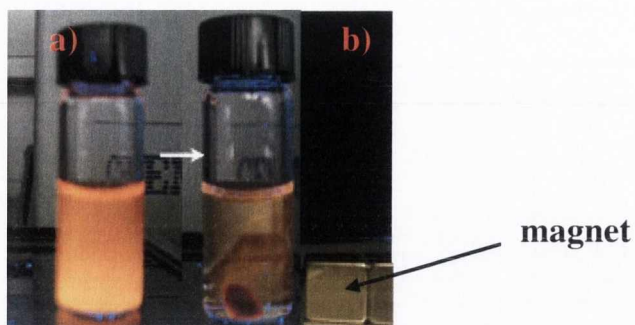
Figure 5.27. Image of selected Fe_3O_4-PSSS-PAH/PE_{10}-RhB nanocomposites (**sample 25**), under UV radiation without (a) and with (b) the presence of an external magnetic field.

The nanocomposites can be re-dispersed again with the formation of stable luminescent suspensions. Importantly this process could be repeated many times without any visual degradation of the Fe_3O_4-PSSS-PAH/PE_{10}-RhB nanocomposites.

5.3.4. TEM microscopy studies of Fe_3O_4-PSSS-PAH/PE_{10}-RhB nanocomposites

Some changes in the final product morphology and an increase of average size of the nanocomposites were observed by TEM due to some aggregation. The average nanocomposites size was 13.8 ± 2.5 nm for **sample 25** (**Fig. 5.28**).
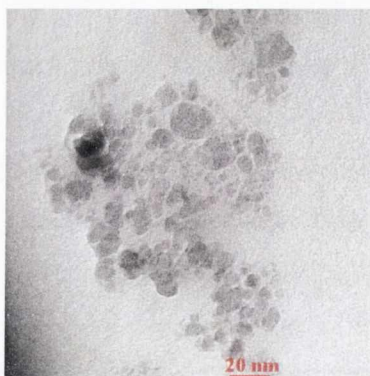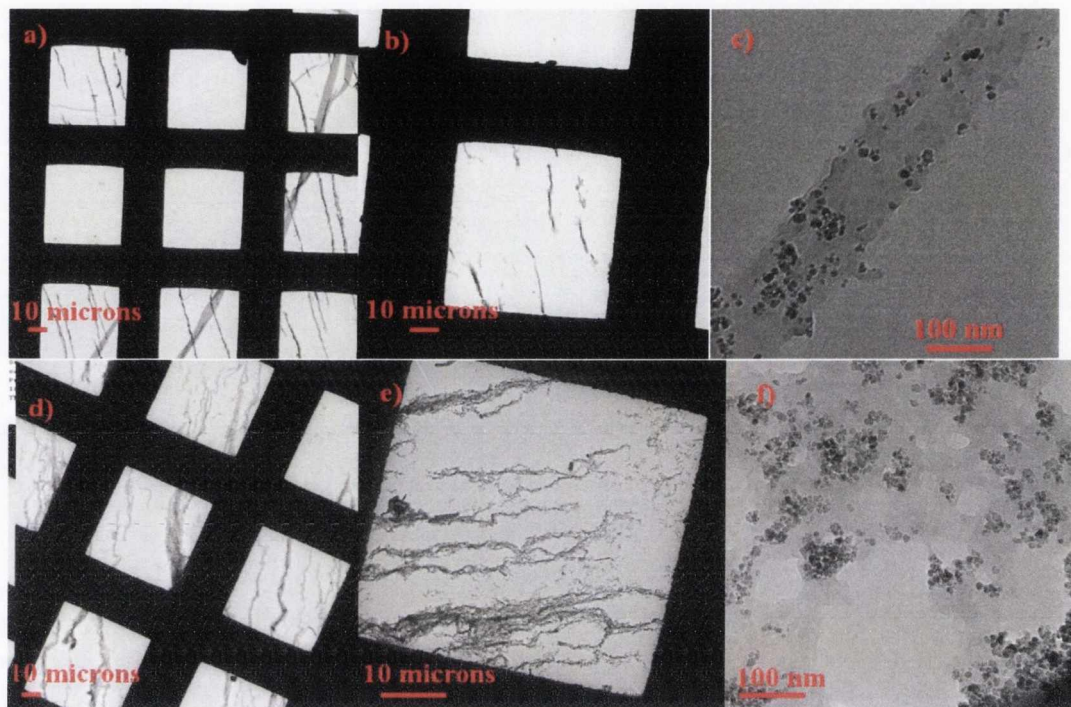

Figure 5.28. TEM images of Fe_3O_4-PSSS-PAH/PE_{10}-RhB nanocomposites. **sample 25**.

The effect of an external magnetic field was observed and analysed for **sample 25**. Nanocomposites were exposed to 0.5 T and 7 T parallel magnetic field and left overnight at the room temperature. In **Fig. 5.29** the linear chain-like assemblies formed by the nanoparticles can be seen quite clearly. There were no significant

137

changes observed in the average size of the primary particles. Under 0.5 T parallel magnetic field, the size was 10.8 ± 2 nm, and in 7 T field the size was 9.7 ± 2.3 nm.
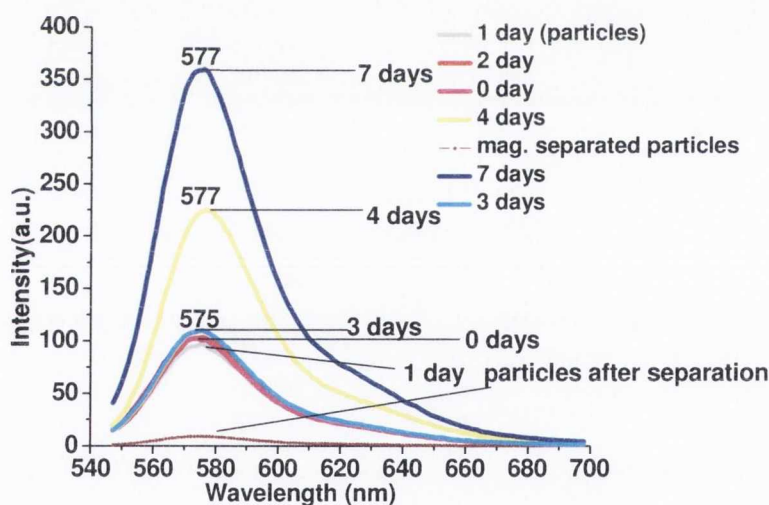

Figure 5.29. TEM images of Fe_3O_4-PSSS-PAH/PE_{10}-RhB nanocomposites increasing magnification. (a, b, c) sample in parallel 7 T magnetic field, (d, e, f) sample in 0.5 T parallel magnetic field. **Sample 25.**

5.3.5. Effect of time on optical properties of Fe_3O_4-PSSS-PAH/PE_{10}-RhB nanocomposites

Information about changes in optical properties of magnetic luminescent Fe_3O_4-PSSS-PAH/PE_{10}-RhB nanocomposites is of particular importance, especially in their biological applications, including confocal imaging, drug delivery and release studies.

Freshly prepared **sample 25** was kept in the darkness over period of time (7 days) and changes in suspension stability and optical properties were monitored, PL and Uv-vis measurements were performed. Room temperature PL (**Fig. 5.30**) and Uv-vis (**Fig. 5.31**) spectra demonstrated that **Sample 25** showed the ability to release luminescence species (RhB molecules) from the surface of the multilayered Fe_3O_4-PSSS-PAH/PE_{10}-RhB nanocomposites back into the surrounding media. The ionic

bonds formed between RhB molecules and final layer (PSSS) on multilayered Fe_3O_4-PSSS-PAH/PE_{10} nanocomposites hold RhB on the surface of the nanocomposites for period of 3 days. No visible decrease of luminescent intensity was observed due to the possible presence of the free oxygen in the system, which could result in bleaching of RhB. **Fig. 5.30** shows that the luminescence of the suspension has increased and red shifted (2 nm) and after the period of 4 days. This indicates the beginning of leakage of RhB molecules back into the surrounding media. After 7 days in total, an increase in PL intensity was observed. The difference between the two curves in **Fig. 5.30** before and after magnetic separation (after 7 days) indicated that significant decrease (approximately by 98 % in total) in the PL signal, because of all released RhB was removed out of the solution. After magnetic separation was performed and Fe_3O_4-PSSS-PAH/PE_{10}-RhB nanocomposites were re-dispersed in Millipore water, it showed only very weak residual luminescence.

Figure 5.30. Changes in emission spectra of Fe_3O_4-PSSS_PAH/PE_{10} –RhB nanocomposites. (λ_{ex} = 555 nm) **Key:** (magenta) 0 day (grey) after 1 day (red) after 2 days, (cyan) after 3 days, (yellow) after 4 days, (navy) after 7 days, (wine) particles after magnetic separation.

A comparison in the Uv-vis spectra is shown in **Fig. 5.31.** The difference in the absorbance intensity between two spectra of freshly prepared nanocomposites (0 day)

and red shift of ~2 nm for magnetically separated nanocomposites after 7 days confirmed PL results.
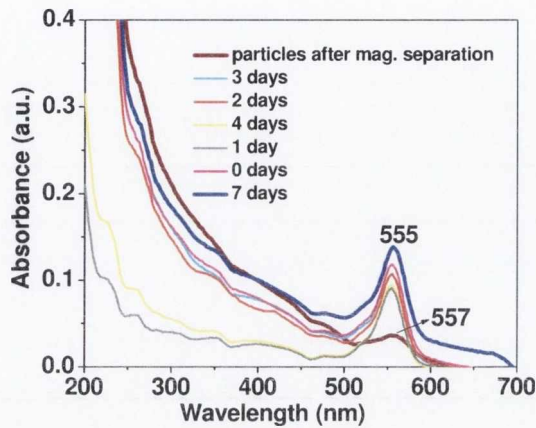
Figure 5.31. Changes in absorbance spectra of Fe_3O_4-PSSS_PAH/PE_{10} –RhB nanocomposites. (**sample 25**). **Key:** (magenta) 0 day (grey) after 1 day (red) after 2 days, (cyan) after 3 days, (yellow) 4 after days, (navy) 7 after days, (wine) particles after magnetic separation.

We have also monitored changes in the surface charge (Zeta potential) of the Fe_3O_4-PSSS-PAH/PE_{10} nanocomposites over 5 days. Measurements of Zeta potential (see **Fig. 5.32**), suggests that charge of the last layer deposited of the multilayered Fe_3O_4-PSSS-PAH/PE_{10} changes in time. This demonstrates that the deposited PE layer is desorbing from the surface of the nanocomposites, resulting in the degradation of the multilayered structure of Fe_3O_4-PSSS-PAH/PE_{10} nanocomposites (**Fig. 5.32 b**)) The appearance of the second peak suggests the formation of species with different surface charge of the nanocomposites (presents of two type charged species) and as a result, desorption of PSSS into surrounding media.
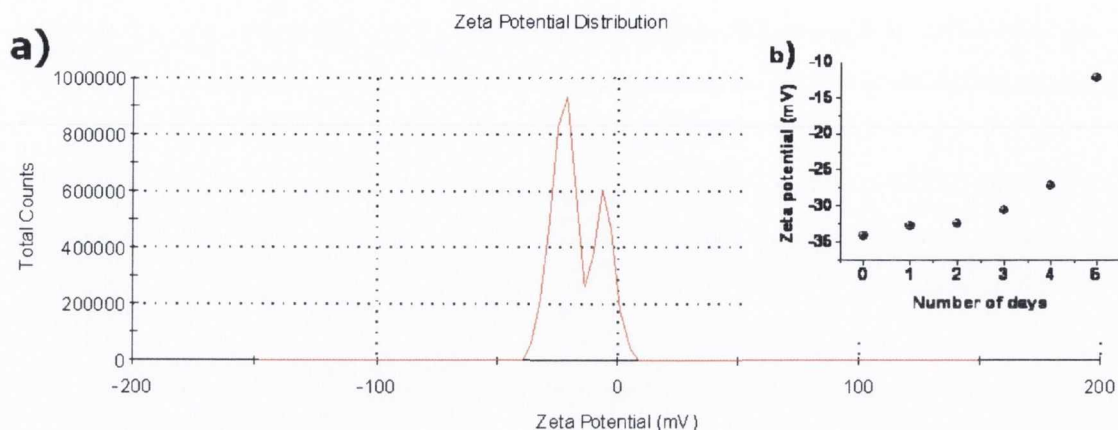
Figure 5.32. Changes in zeta potential of the Fe$_3$O$_4$-PSSS-PAH/PE$_{10}$ in time. a) Zeta potential of Fe$_3$O$_4$-PSSS-PAH/PE$_{10}$ nanocomposites after 5 days, b) changes in zeta potential in the period of 5 days.

PCS data showed increase in average size from 240 nm (PDI 0.350, 0 day) to 560 nm (0.603) after 7 days. TEM images show strong aggregation of the nanocomposites (**Fig. 5.33**), confirming PCS data.
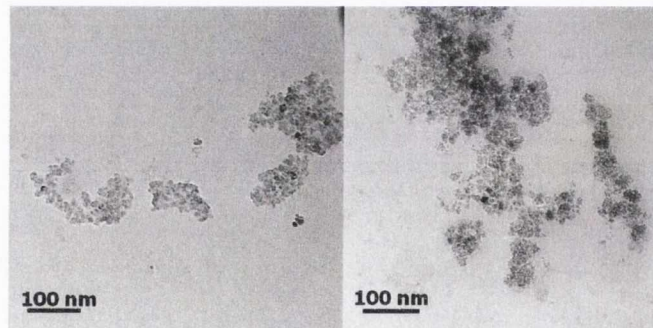
Figure 5.33. TEM images of Fe$_3$O$_4$-PSSS_PAH/PE$_{10}$ –RhB nanocomposites the after 7 days.

5.3.6. Coating Fe$_3$O$_4$-PSSS_PAH/PE$_{10}$ –RhB nanocomposites with extra PE layers

In an attempt to protect the RhB layer on magnetic luminescent nanocomposites we performed a coating of an extra layer of PE (see scheme in **Fig. 5.34**). It was expected that the extra polyelectrolyte coating would allow for higher stability and slower degradation of the nanocomposites in solution. To investigate how the extra

PE coating affects the PL, Uv-vis spectra of the Fe_3O_4-PSSS-PAH/PE_{10}-RhB nanocomposites were measured before and after the deposition. (**Table 5.6**).

nanocomposite with RhB

PAH   PSSS
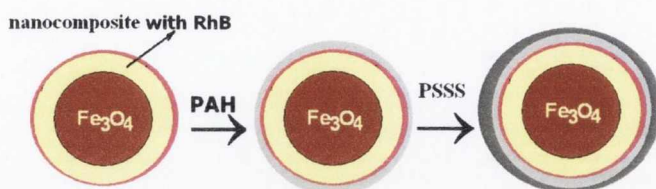
Figure 5.34. Schematic illustration of the extra coating magnetic luminescent nanocomposites using the LbL technique.

2 mL of **sample 25** was used for the tests, and coated with extra layers of PE according scheme in **Fig. 5.34**. Changes in suspension stability and optical properties were monitored by PL and Uv-vis measurements after each extra PE layer was deposited.

Table 5.6. Summaries of Zeta potential measurements of Fe_3O_4-PSSS-PAH/PE_{10}-RhB nanocomposites before and after deposition of extra PE layers.

Coating with PAH		Coating with PSSS	
Zeta potential before	Zeta potential after	Zeta potential before	Zeta potential after
-28.5 ±4.3 mV	+12.5 ±5.7 mV	+12.5 ±5.7 mV	-20.3 ±7.5 mV

We found that the initial sample showed a higher PL intensity than the nanocomposite, which was coated with extra PE layers as seen in **Fig. 5.35**. Thus, the extra deposited layer of 0.4 mL of PAH resulted in reduced luminescence of the sample with some blue-shift in the emission spectra (4 nm). This quenching of luminescence is most likely due the partial replacement of RhB molecules with PAH molecules. On the other hand, the stability of the Fe_3O_4-PSSS-PAH/PE_{10}-RhB nanocomposites against clustering and aggregation in suspension are influenced by the charge and number of the deposited layers. PAH is known as positively charged polyelectrolyte. With addition of 0.4 mL PAH in to solution there was a change in Zeta-potential from -28.5.5 to +12.5 mV that means a decrease in suspension

stability. In that case, some aggregates can be easily formed leading to the precipitation of the nanocomposites.

However, red-shift (7 nm) in PL spectra of nanocomposites was observed after addition of 0.3 mL PSSS compared with uncoated nanocomposites. This indicates the formation of larger species, which confirmed PCS data (243. 7 nm (PDI 0.232) size before addition of PAH, size after 654 nm (PDI 0.475)). This is analogous to the situation of the $CoFe_2O_4$-PSSS-PAH/PE_{16}-RhB nanocomposites aqueous solutions.
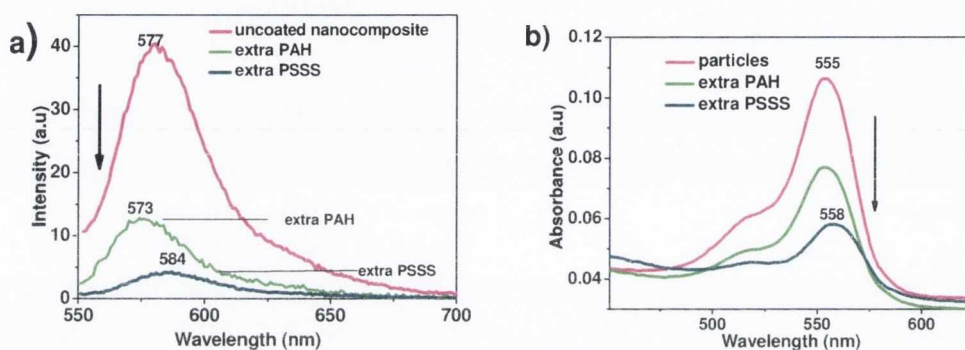

Figure 5.35. Changes in emission and absorbance spectra of Fe_3O_4-PSSS_PAH/PE_{10} –RhB nanocomposites. (λ_{ex} = 555 nm) **Key:** (magenta) Fe_3O_4-PSSS_PAH/PE_{10} –RhB nanocomposite, (green) after PSSS deposition, (dark cyan) after PAH deposition. a) emission spectra, b) absorbance spectra.

Careful inspection of spectra in **Fig. 5.35 b)** reveals that the absorption from the uncoated Fe_3O_4-PSSS_PAH/PE_{10} –RhB nanocomposites was higher in comparison with nanocomposites coated with an extra layer. Again the possible suggestion for the weakness of the absorption might indicate a degradation of PSSS_PAH/PE_{10} –RhB due to the replacement of RhB molecules from the surface of the nanocomposites by the capping layer of PAH and later PSSS.

TEM images showed aggregations and clumps of nanocomposites (**Figure 5.36**). This can be seen in the TEM images below.
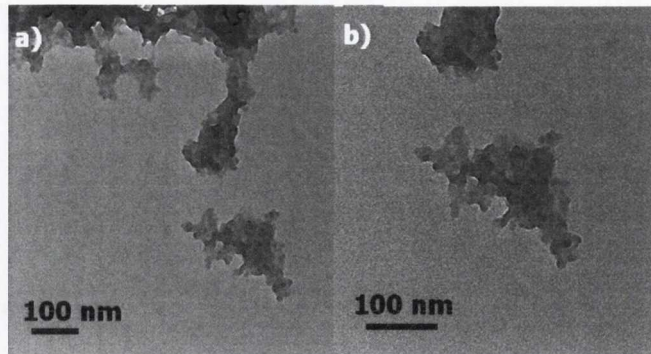
Figure 5.36. TEM images of Fe_3O_4-PSSS_PAH/PE_{10} –RhB after extra coating with PE. a) after coating with 2 extra layers of PE, b) the same sample with higher magnification.

5.3.7. Confocal and light microscopy studies of Fe_3O_4-PSSS_PAH/PE_{10} – RhB nanocomposites

Investigations into the localisation of the magnetite-RhB nanocomposites into cells were conducted by J.J. Gallagher and Dr. C.M. Kerskens in the Neuroscience Department of Trinity College Dublin. Confocal imaging carried out on luminescent nanocomposites. The sample was left in a 7 T field overnight. In **Fig. 5.37** it can be clearly seen that the nanoparticles form linear chain-like assemblies, white arrows on each of the images illustrate this. This particles' behaviour could be very useful for the *in vivo* or in *vitro* studies. For example, if the driving field is parallel to the magnetic luminescent particles the repulsive forces would force formation of the one dimensional self-assembled chains.
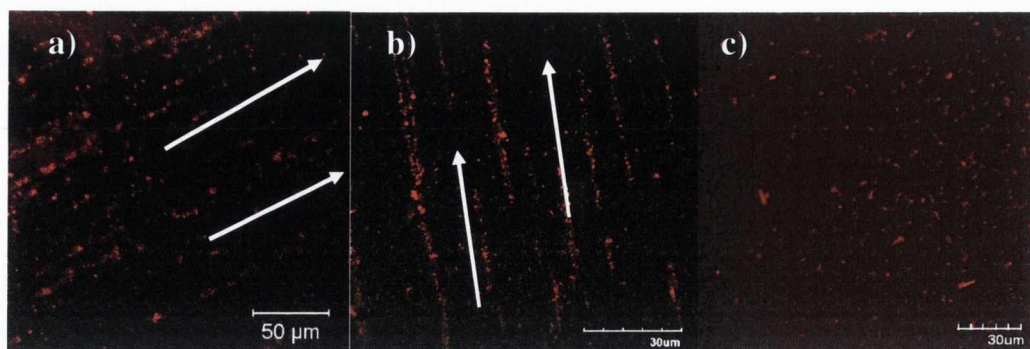
Figure 5.37. Confocal microscopy of nanoparticles fixed following overnight placement in a 7 T magnetic field increasing magnification. The white arrows highlight the directions of the linear chain-like assemblies formed. a) magnification = 40x, b) magnification = 60x, c) nanocomposites without magnetic field magnification = 60x

In order to evaluate magnetite –RhB nanoparticles as MRI contrast agent and fluorescent markers, these nanoparticles were incubated with microglial cells

5.3.8. Biolabelling and live intracellular visualisation studies of Fe_3O_4-PSSS_PAH/PE$_{10}$ –RhB nanocomposites

We considered the ability of magnetite nanoparticles to act as magnetic labels for the cell labelling. We also tested samples to confirm that bound Rhodamine caused the luminescence. Nanocomposites uptake by microglial cells was visualized using confocal microscopy. For these tests microglial cells cultures were stained for iron detection by a Prussian blue reaction [29]. The control sample without Fe_3O_4-PSSS-PAH/PE$_{10}$-RhB nanocomposites was tested as well. **Fig. 5.38** demonstrates the uptake of nanocomposites in cells. Cells without the nanocomposites (control sample) showed no staining with the Prussian blue agent. Only microglial cell cultures with Fe_3O_4-PSSS-PAH/PE$_{10}$-RhB nanocomposites showed the presence of detectable amounts of iron as demonstrated by the blue precipitates (**Fig. 5.38 b), d)**). These results indicate a high uptake of the nanocomposites nanoparticles by the cells. Nanocomposites are also rapidly accumulated in to the cell.
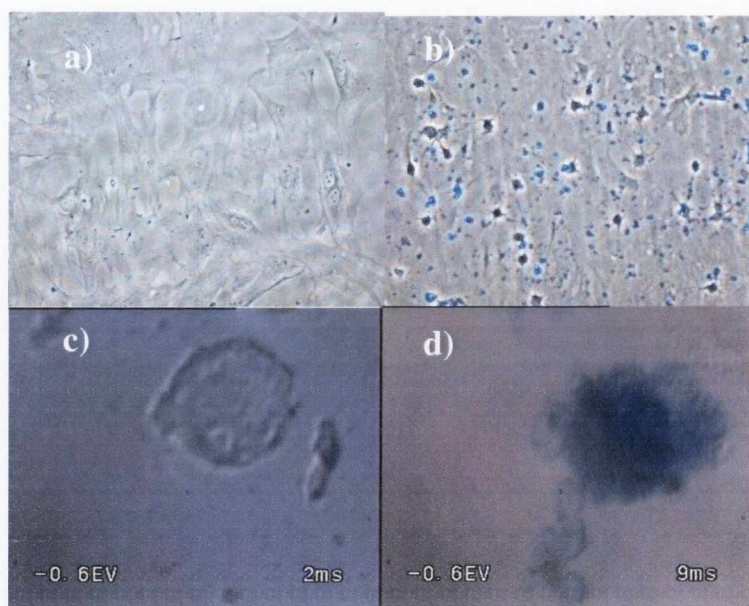
Figure 5.38. Prussian Blue Staining of unlabelled and labelled cells at different magnification. a) unlabelled glia cells, b) labelled glia cells, at x10 magnification, c) single unlabeled, d) labelled cell stained with Prussian Blue at x60 magnification.

The surface charge of the nanoparticles is a property that is very important for cellular uptake. It has previously reported that negatively charged CdTe QDs can be taken up by various phagocytic cells [30]. In our work (**Fig. 5.39, 5.40**) negatively charged Fe_3O_4-PSSS_PAH/PE$_{10}$ –RhB nanocomposites are also easily taken up and accumulated in the nucleus of microglia cells. At the same time the size of the nanocomposites a critical parameter too. The nanocomposites should be big enough to avoid fast renal elimination and to guarantee long blood circulation life. On the other hand, it should be small enough to elude the recognition processes operated by the phagocytes. Optimal sizes for intravenous injection range normally from 10 to 100 nm [31].

This may be a stage in the process of endocytosis, in which microglial cells internalise the nanocomposite but it could also reflect phagocytic activity of microglial cells
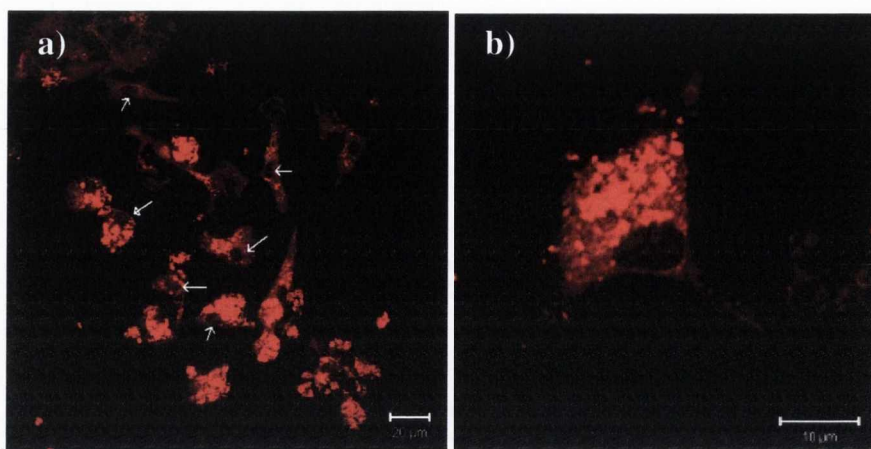
Figure 5.39. Sample image of microglia and particles under different magnification. **Sample 25**. Large field of view demonstrating the internalisation of the nanocomposites and the delineation of several cell nuclei. a) Magnification 40x, b) Smaller field of view image at magnification 40x.

The spatial distribution of nanostructures, in the cytosol and localised to the cell membrane, is demonstrated in the **Fig. 5.40**. The top images (**a***, **b***) show cells defined by the absence of fluorescence under light microscopy. Fluorescence and distribution throughout the cell body and cell nuclei (**a**, **b**) can be seen under confocal microscopy.
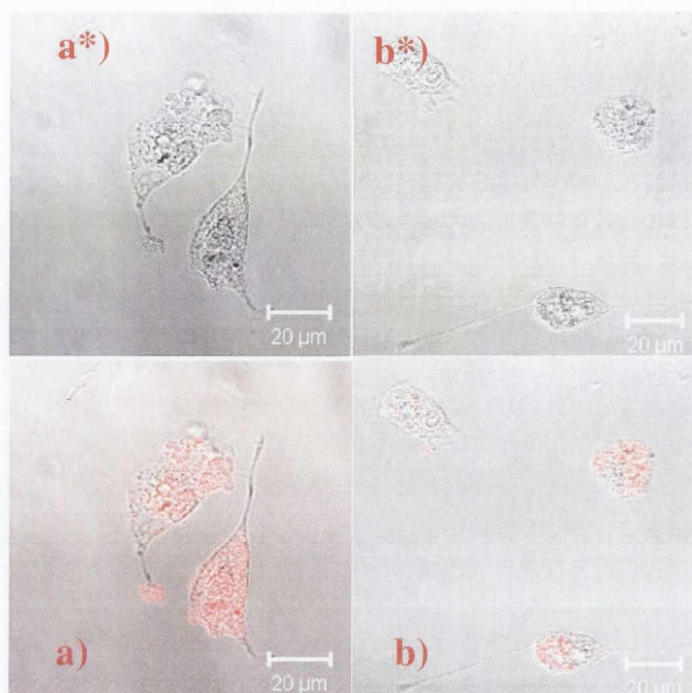
Figure 5.40. Use of phase contrast fluorescence microscopy to investigate nanocomposite spatial distribution within cells following 2 hour incubation period. (a* - b*)Corresponding light micrograph and overlay is also shown. a) Fluorescence is visible on cell membrane, b) Fluorescence appears more distinctly within the cell and can be seen to delineate the nucleus. Magnification = 40x

This phenomenon indicates that our magnetic luminescent nanocomposites show great potential as a biomarker for *in vivo* cellular imaging.

5.3.9. Cytotoxicity studies of Fe$_3$O$_4$-PSSS_PAH/PE$_{10}$ –RhB nanocomposites

Emerit *et.al.* have reported, that an intracellular iron overload may lead to cytotoxicity and cell death due to free radical formation and oxidative stress [32].

The cytotoxicity studies of prepared nanocomposites were also evaluated on the cortical glial cultures from 1 day old Wistar rats. Incubation of cells in the presence of various concentration of nanocomposites for 2, 18, 24 and 48 hours revealed no evidence of a reduction in cell viability [33] (**Fig. 5.41**).
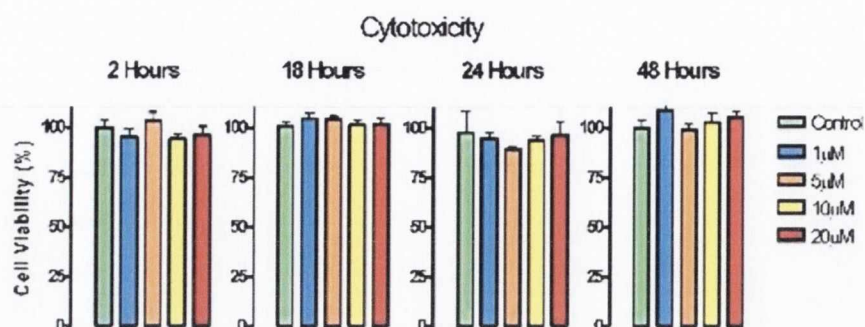
Figure.5.41. Analysis of the cytotoxic effects of nanostructures. Incubation of cells in the presence of nanostructures (0.46x10^{-4}, 2.31 10^{-4}, 4.62x10^{-4}, 9.24x10^{-4} g/mL of Fe$_3$O$_4$) for 2, 18, 24 and 48 hours revealed no evidence of a reduction in cell viability.

5.4. Conclusions

We have developed new procedure for the preparation of "two-in-one" magnetic-luminescent nanocomposites using the magnetite and cobalt ferrite nanoparticles as a magnetic core and Rhodamine B as a luminescent component.

These new nanocomposites have been fully characterised by FTIR, Raman, TEM, PCS, Zeta-sizer, UV-vis and PL spectroscopy, Confocal microscopy, feasibility studies.

Our studies have shown that the utilisation of commercially available PSSS and PAH polyelectrolytes for the preparation multilayered magnetic core/shell nanoparticles using LbL technique. The optimised LbL synthetic procedure allows us to prepare magnetic-luminescent nanocomposites (CoFe$_2$O$_4$-PSSS_PAH/PE$_{16}$-RhB and Fe$_3$O$_4$-PSSS_PAH/PE$_{11}$-RhB nanocomposites) and have shown good reproducibility of the results.

The colloidal suspensions of Fe$_3$O$_4$-PSSS_PAH/PE$_{11}$-RhB nanocomposites in water showed the presence of luminescence and possessed the best colloidal stability. However, CoFe$_2$O$_4$-PSSS_PAH/PE$_{16}$-RhB nanoparticles gave only a very weak luminescence and were not very stable in aqueous solution. The most likely

149

explanation of these differences is related to stronger magnetic interactions in cobalt ferrite nanocomposites.

In our microscopy studies we have found that after coating magnetic particles with PE layers, particles were organised in long "chain" structures, which are linked together in the presence of an external magnetic field. We have also demonstrated that for $CoFe_2O_4$-PSSS nanoparticles, the addition of extra layers of deposited polyelectrolytes layers on the surface of the particles (shell growth), could give aggregation and clustering. We also observed complete quenching of luminescence of $CoFe_2O_4$_PSSS-PAH/PE_{16}-RhB over time.

Our results show that the presence of a polyelectrolyte shell together with the encapsulated magnetic nanoparticles (Fe_3O_4-PSSS) is a promising approach to the simple manipulation of nanostructures by magnetic fields. We have demonstrated that the new "two-in-one" magnetic-luminescent nanostructures can be detected by their fluorescence.

Our biological studies in live microglial cells have shown that the Fe_3O_4-PSSS_PAH/PE_{10}-RhB could be effective cell labelling agents.

We believe that more detailed investigations of these new magnetite nanocomposites with fluorescent dyes and ionic drugs would allow for further development the applications of magnetite nanocomposites in biology and medicine.

5.5. References:

1.   A.M. Derfus, W.C.W. Chan, S.N. Bhatia. *Nano Letters., 4,* (2004), 11-18.

2.   W.W. Yu, E. Chang, J.C. Falkner, J.Y. Zhang, A.M. Al-Somali, C.M. Sayes, J. Johns, R. Drezek, and V.L. Colvin., *Journal of the American Chemical Society.,.* 129, (2007), 2871–2879.

3.   L.E. Rikans, T. Yamano., *Journal of Biochemical and Molecular Toxicology.,* 14, (2000), 110-117.

4.   H. Du, R.A. Fuh, J. Li, A. Corkan, J.S. Lindsey., *Photochemistry and Photobiology.,* 68, (1998), 141-142.

5.   X. Hong, J.Li, M. Wang, J. Xu, W. Guo, J. Li, Y. Bai, and T. Li., *Chemistry of Materials.* 16, (2004), 4022-4027.

6.   T. Kon, S. Nakakura, K. Mitsubayashi., *Nanomedicine: Nanotechnology, Biology and Medicine 1,* (2005), 159–163.

7.   T. Matsunaga, Y. Namba, T. Nakajima. *Bioelectrochemistry and Bioenergetics.,* 13, (1984), 393-400.

8.   A.L.K. Roberts, M.H. Rees, S. Klebe, J.M. Fletcher and S. Byers., *Molecular Genetics and Metabolism,* 1-2, 92, (2007), 115-121.

9.   D.D. Kunkel, L.K Lee and J. Stollberg., *BMC Neuroscience.,* 2-19, (2001), 1-12.

10.   http://www.absoluteastronomy.com/topics/Rhodamine

11.   F. Srinivasan, and X. Huang., *Chirality.,* 20, (2008), 265–277.

12.   A.A. Mamedov, N.A. Kotov., *Langmuir.,* 16, (2000), 5530–5533.

13.   S. Srivastava and N.A. Kotov., *Accounts of Chemical Research.,* 41, 12, (2008), 1831–1841.

14.   Q. Jiao, Z. Yi, Y. Chen, F. Xi., *Polymer.,* 49, (2008), 1520-1526.

15.   L. Wang, X. Wang, M. Xu, D. Chen, and J. Sun., *Langmuir,* 24, (2008), 1902-1909.

16.   J. Sun, M. Gao, M. Zhu, J. Feldmann and H. Mohwald., *Journal of Materials Chemistry.,* 12, (2002), 1775–1778.

17.   Y.H. Lin, C. Jiang, J. Xu, Z. Lin and V.V. Tsukruk., *Soft Matter*, 3, (2007), 432–436.

18.   X. Zhang, H. Chen and H. Zhang., *Chemical Communications.*, (2007), 1395–1405.

19.   S. Corr. New magnetic nanocomposite materials. Thesis for degree of Doctor of Philosophy. University of Dublin. Trinity College, (2006).

20.   O.N. Shebanova and P. Lazor., *Journal of Solid State Chemistry.*, 174, (2003), 424–430.

21.   M. Szekeres, A. Szechenyi, K. Stepan, T. Haraszti, I. Dekany., *Colloid and Polymer Science.*, 283, (2005), 937–945.

22.   S.W. da Silva, T.F.O. Melo, M.A.G. Soler, E.C. D. Lima, M.F. da Silva, and P.C. Morais., *IEEE Transactions on Magnetics.*, 39, 5, (2003).

23.   T. Moadhena, H. Elhouicheta, L. Nosova, M. Oueslati., *Journal of Luminescence.,* 126, (2007), 789–794.

24.   http://omlc.ogi.edu/spectra/PhotochemCAD/html/rhodamineB.html 13.08.2009.

25.   C. Seymour. Development of Polyelectrolyte Stabilised Magnetite Nanocomposites. Fourth year project. University of Dublin. Trinity College., (2007/2008).

26.   S. Bi, X.Wei, N. Li, Z. Lei., *Materials Letters.*, 62, (2008), 2963–2966.

27.   L. Chen, G. Lu., *Journal of Electroanalytical Chemistry.*, 597, (2006), 51–59

28.   D.L.A. de Faria, S.V. Silva and M.T. de Oliveirs., *Journal of Raman Spectroscopy.*, 28, (1997), 873.

29.   F.Y. Lee, T.S. Lee, C.C. Pan, A.L. Huang, L.Y. Chau., *Atherosclerosis*, 138, (1998), 281–288.

30.   S.J. Byrne, S.A. Corr, T.Y. Rakovich, Y.K. Gun'ko, Y.P. Rakovich, J.F. Donegan, S. Mitchell and Y. Volkov, *Journal of Materials Chemistry.*, (2006), 16, 2896–2902.

31.   S. Mornet, S. Vasseur, F. Grasset, and E. Duguet. *Journal of Materials Chemistry.*, 14, (2004), 2161–2175.

32. J.E. Merit, C. Beaumont, F. Trivin., *Biomedicine & Pharmacotherapy.,* 55, (2001), 333–339.

33. J. Gallagher, R. Tekoriute, J.A. O'Reilly, C. Kerskens, Y.K. Gun'ko and M. Lynch., *Journal of Materials Chemistry.,* 19, (2009), 4081–4084.

Chapter 6

6.1. Magnetic luminescent nanocomposites based on Magnetite-DNA nanoparticles

6.1.1. Introduction

DNA is potentially an excellent template for nanoassemblies due to its appropriate size (approximately 2 nm in diameter) and repeating structure (a helical pitch of 3.4 – 3.6 nm) and its functional groups [1]. The use of DNA as cross-linking template agent for nanoparticles has been extensively investigated. For example, previously it was reported that herring sperm DNA can acts as a template for the preparation of magnetic chain-like assemblies, which form very stable aqueous suspensions and exhibit unprecedentedly high relaxivity at low field, suggesting that the material may be a potentially useful reagent for MRI [2].

It is well known that there are a number of dyes that can interact with DNA via electrostatic interactions or an intercalation of the dye molecules between two successive base pairs in the double helix [3]. Intercalation into DNA (insertion between a set of base pairs) is a critical step in the function of developing new anti-cancer drugs [4] and in site-specific manipulation of DNA [5]. One of type of intercalation dye is Acridine Orange (AO), see **Fig. 6.1** [6-7].
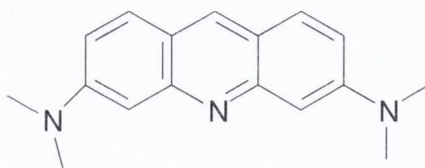

Figure 6.1. Chemical structure of N,N,N',N'-tetramethylacridine-3,6-diamine (Acridine Orange).

Once in the interior of the cell, Acridine Orange can complex with deoxyribonucleic acid (DNA) and with ribonucleic acid (RNA). Intercalation may occur in the denatured DNA samples due to the presence of a small number of base pairs, which may form during the partial renaturation of DNA, which can occur during cooling. At the same time interaction of AO with DNA is complex. The

154

heterocyclic bases, which are the primary centres of photoreactivity in DNA, could be detected by UV-vis spectrometer because their absorption maximum lie in the region between 250-270 nm. The chemistries of these complexes affect the wavelength of the emitted radiation. Intercalation between the base pairs could be detected by spectroscopic methods.

Classical intercalators include ethidium bromide, amniacridine and proflavine. Acridine Orange, these wavelengths are shifted to longer wavelengths when bound as single cations, while the reversal of this trend is seen when the Acridine is bound as dimers or aggregates [8]. In the case of the Acridine Orange-DNA complex, the emitted radiation is green. In the case of the complex formed with RNA, the emitted light is orange [8-13]. This sort of information allows detailed analysis of the DNA replication cycle in microorganisms.

Fig. 6.2 presents schematic representation of Acridine Orange intercalating between base pairs of the polynucleotide chains of DNA.
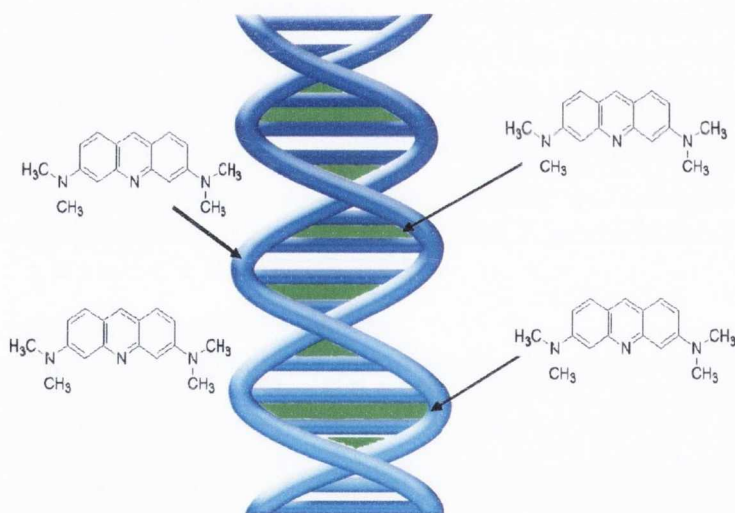
Figure 6.2. Schematic representation of intercalating dye – Acridine Orange lodges between base pairs of the polynucleotide chains of DNA and forms a coloured band.

The main aim of this work is to develop new fluorescent-magnetic nanoparticles, which are based on DNA-magnetite nanocomposites and intercalating dyes such as Acridine Orange. We plan to perform these studies using the double and single stranded forms of Herring Sperm DNA. Herring sperm DNA was chosen for study as the DNA target for AO intercalation due to its availability, purity, and biological

155

relevance. After the synthesis of stable magnetite-DNA fluids nanocomposites, intercalation studies of Acridine Orange into DNA will be carried out in order to synthesise new *"two-in-one"* magnetic-luminescent nanocomposites. Then we aim to investigate these new materials by various instrumental techniques.

6.2. Preparation and characterisation of magnetite-DNA nanocomposites

Synthesis of magnetite-DNA nanocomposites was carried out according to published procedure [2] by co-precipitation of Fe^{3+}/Fe^{2+} salt solutions in the presence of single (ssDNA) or double (dsDNA) stranded Herring sperm DNA using aqueous ammonia.

6.2.1. Spectroscopy studies of magnetite-DNA nanoparticles

In order to confirm that there is dsDNA and ssDNA present on the surface of the particles, absorbance spectra of last filtrates were recorded (**Fig. 6.3**). Characteristic peak for DNA could be seen for the Herring Sperm DNA sample (**sample 7**), ssDNA and dsDNA (**sample 8**) at around 260 nm [14].
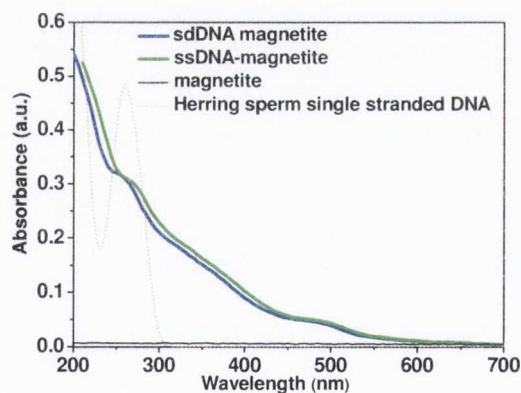

Figure 6.3. Room temperature absorbance spectra of magnetite –DNA nanocomposites. **Key**: (black) magnetite (red) double stranded Herring sperm DNA, (blue) **Sample 8**, double stranded Herring Sperm DNA (green) **Sample 7**, single stranded Herring Sperm DNA.

FTIR spectra of the dried DNA-magnetite nanocomposites are shown in **Fig. 6.4**. All samples reveal stretches at 3432, 1647, 1220, 1084 and 580 cm^{-1}. These represent OH⁻ groups on the particle surface, associated water molecules with the surface, asymmetric and symmetric phosphate stretches and a Fe-O stretch respectively [15, 16].
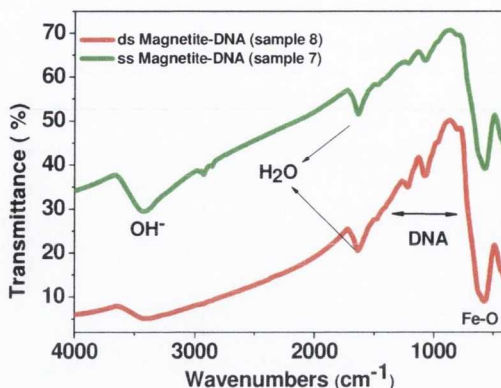
Figure 6.4. FTIR spectra of selected samples magnetite –DNA nanocomposites: **Key**: (red) **sample 8,** magnetite coated with double stranded Herring Sperm DNA, (green) **Sample 7,** magnetite coated with single stranded Herring Sperm DNA.

The Raman spectra was recorded for **sample 8** (see **Fig. 6.5**). **Fig. 6.5** shows the main peaks at 475 and 685 cm^{-1} characteristic for vibration mode for pure magnetite (Fe_3O_4) [17] was observed for magnetite-PSSS nanocomposites. These peak might be shifted 20 cm^{-1} according M. Mandal *et al.* due to small size of magnetite [18]. Literature suggests a beginning of magnetite phase oxidation, especially then a weak slight shifted peak at 185, 290 and 630 cm^{-1} are also visible due to oxidative laser effects, which caused decomposition of the sample [19].
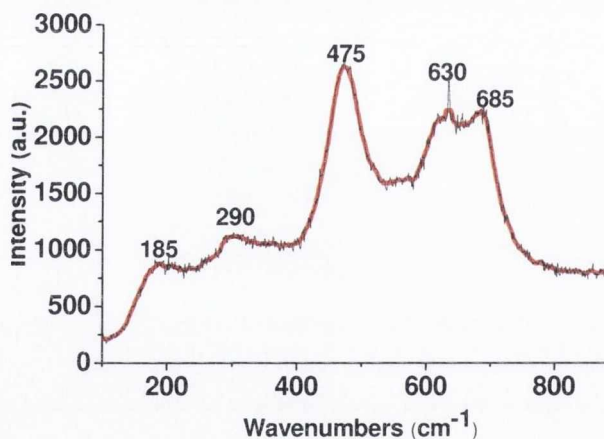
Figure 6.5. Characteristic Raman spectra of selected magnetite-DNA nanocomposite. **Key:** (black) **sample 8**, magnetite coated with double stranded Herring Sperm DNA (red) smoothed spectra for **sample 8**.

6.2.2. XRD analysis of magnetite-DNA nanoparticles

XRD patterns (**Fig. 6.6**) coincide with the data available for magnetite, with all peaks matching to those in the JCPDS database. Diffraction peaks shown in this pattern correspond to the (111), (220), (311), (400), (422), (511), (440), and (533) plane reflections of cubic Fe_3O_4 phase [20]. The broadening of the peaks implies that the magnetite –DNA nanoparticles are very small in size.
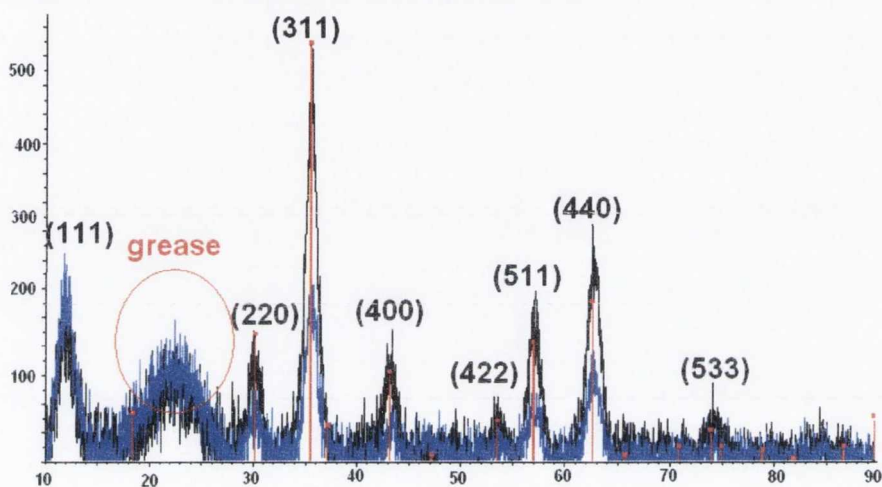
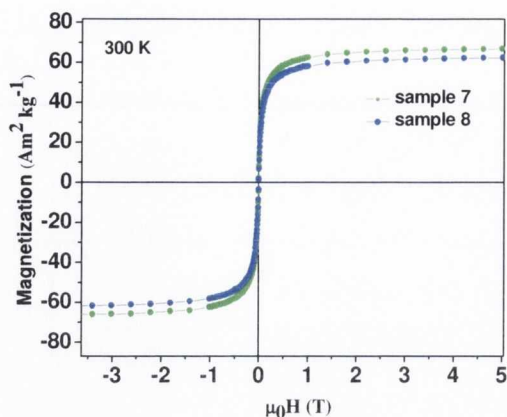**Figure 6.6.** XRD patterns (λ=1.54056 Å) of magnetite-DNA samples. **Key**: (back) **sample 8**, magnetite coated with double stranded Herring Sperm DNA (blue) **sample 7**, magnetite coated with single stranded Herring Sperm DNA, (red) Fe_3O_4 from JCPDS database.

6.2.3. Magnetic measurements (SQUID) of magnetite-DNA nanoparticles

Magnetisation curves (**Fig. 6.7**) of DNA-magnetite samples did not show any hysteresis and almost zero coercivity (H_c = 0.0004 T) indicating that particles are superparamagnetic. Almost no effect of different type of DNA on saturation magnetization (M_s) values for **sample 7** and **8** were observed. The saturation magnetisation was 62.9 Am^2/kg (**sample 8**) and 67.3 Am^2/kg for **sample 7,** which are relatively lower than that of the bulk value of Fe_3O_4 92 Am^2/kg [21, 22].

Figure 6.7. Magnetisation curves versus magnetic field for magnetite-DNA powders. **Key**: (blue) **sample 8**, magnetite coated with double stranded Herring Sperm DNA, (green) **sample 7**, magnetite coated with single stranded Herring Sperm DNA.

6.2.4. TEM microscopy studies of Fe_3O_4-ssDNA and Fe_3O_4-dsDNA nanoparticles

The samples were prepared by placing a 10 µL onto a copper formvar grid and dried over night. Small aggregation of some nanoparticles could be seen in **Fig. 6.8.** due to cross linking. DNA stabiliser works as linkage between the single magnetite nanoparticles lids formation of long cross-linked between each other non-orientated assemblies. TEM images of aqueous magnetite nanoparticles coated with DNA have revealed the presence of almost spherical shape of the magnetite particles. DNA coating has remained surrounding magnetite nanoparticles. The average particle size was 8.2 ± 1.9 nm (**sample 8**), and 9.3 ± 1.4 nm (**sample 7**).

We note that upon application of 0.5 T parallel magnetic field, formation of 1-D nanostructures were not observed (see **Fig. 6.8 c), d)**).
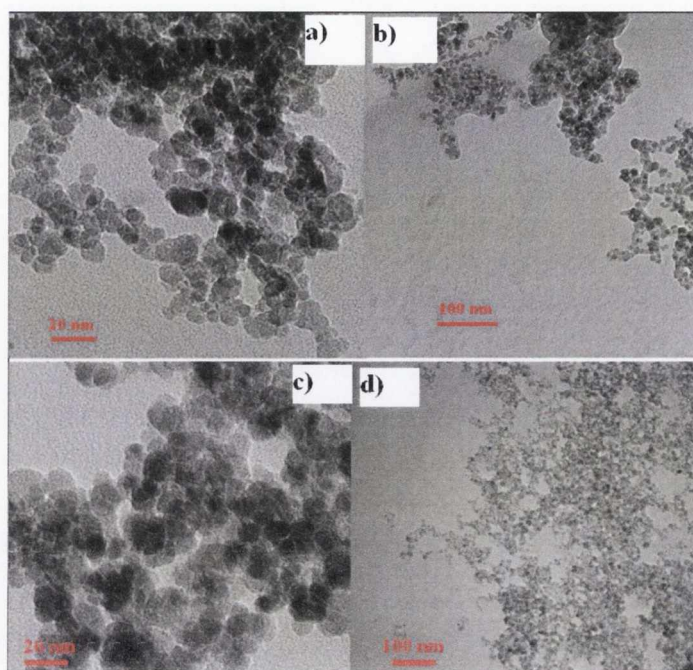
Figure 6.8. TEM images of Fe$_3$O$_4$-ssDNA and Fe$_3$O$_4$-dsDNA nanoparticles (a, b, c) **sample 7,** particles coated with single stranded Herring Sperm DNA (d, e, f) **sample 8,** particles coated with double stranded Herring Sperm DNA

These results are similar to those obtained for Cobalt ferrite DNA stabilised particles (**Chapter 3,** Cobalt ferrite DNA nanoparticles).

PCS measurements showed average particle size as for **sample 7** and **sample 8** 192.1 nm (PDI = 0.243). For coated nanoparticles, dPCS includes the effective radius of orbit of the attached polymers and water, as a part of the diffusive mass of the nanoparticles [23]. The difference between measured (PCS) and calculated (TEM) average primary particle size could be mainly attributed to the aggregation of magnetite-DNA nanoparticles in the aqueous solutions.

6.3. Acridine Orange (AO) titration

6.3.1. Single stranded Herring Sperm DNA (ssDNA) titration of AO

To investigate interaction between AO molecule and DNA molecule, freshly prepared stock ssDNA and dsDNA solutions were titrated with AO in phosphate buffer solution.

Optical absorbance experiments were performed using aliquots varying in volume from 1 to 200 μL taken from the prepared stock AO solution (7.54x10^{-5} M),

and titrated into cuvette containing 2.0 mL (0.0030 M) of ssDNA solution. The AO solution was scanned before the start of each titration series to quantitatively monitor any changes in the absorbance spectra. After the first addition of AO (2 µL) in to the system the intensity of 490 nm peak decreased slightly from 0.24 to 0.13 (8 µL). The red-shift from 490 nm to 500 nm in the absorbance spectra was observed after addition of 20 µL of AO. This suggests that the reaction system might be at equilibrium at the absorbance minimum point. Increasing aliquots of intercalating agent AO, a secondary peak 500 nm begins to increase in amplitude but peak position remains unchanged (see **Appendix 5**). Hypochromism was extremely weak (3 %), suggesting that no significant interaction with the single stranded DNA.

The fluorescence intensity of free AO is 220 a.u. with characteristic green strong fluorescence λ_{max} = 530 nm (see **Appendix 6**). After first additions of ssDNA into the system fluorescence intensity decreasing to 36 (10 µL). After addition of 20 µL of DNA increase of the fluorescence intensity was recorded.

6.3.2. AO titration of Single stranded herring sperm DNA coated magnetite nanoparticles

Stable colloidal suspensions of magnetite nanoparticles stabilized with Herring Sperm DNA were used. To study AO intercalation onto surface of Fe_3O_4-ssDNA nanocomposites, optical absorbance titration experiments on the samples were performed according earlier described procedure. **Appendix 7** shows do not present of interaction and intercalation of AO molecules with Fe_3O_4-ssDNA particles (**sample 7**).The black curve corresponds to the last wash of the Fe_3O_4-ssDNA particles Alternatively spectral analyses of each next addition of AO into the system considerably accelerate increase of the absorbance intensity without any red shift of characteristic peak at 480 nm. **Fig. 6.9** shows changes in emission and excitation spectra of the Fe_3O_4-ssDNA-AO nanocomposite. Dotted curve corresponds to the original AO in the phosphate buffer solution. Thus, there was no indication of AO intercalation with the single stranded Herring DNA. An increase in the peak intensity could be attributed to increase of the AO concentration [24] in the titrated solution.
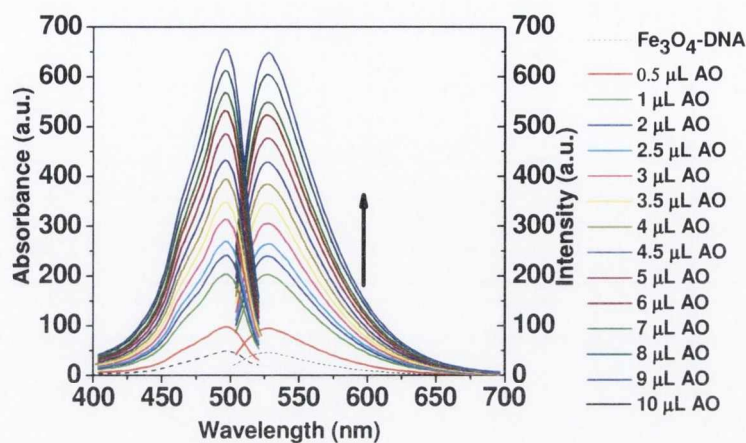
Figure 6.9. Room temperature emission spectra and excitation of Fe_3O_4-ssDNA nanocomposites intercalated with AO (**Sample 7**). (λ_{ex} = 490 nm, (λ_{em} = 527 nm). Dotted curve shows original AO in phosphate buffer solution. The legend shows the curves as 10 µL of AO in phosphate buffer solution added.

6.3.3. TEM microscopy studies of Fe_3O_4-ssDNA-AO nanocomposites

TEM analysis showed slight aggregation of the nanocomposites with increase of an average particle size to 11.5 ± 3.2 nm. The PCS data did not show any changes in average size of the particles (198±4 nm, PDI 0.234). Under external 0.5 T magnetic field nanocomposites were re-orientated into the self-assemblies with an average length 10.2 ± 1.9 µm (**Appendix 8**).

### 6.4. Double stranded Herring Sperm DNA (dsDNA) titration of AO

Initial attempts to evaluate AO intercalation onto DNA were made by titrating measured quantities of a stock solution of AO (7.54×10^{-5} M) to a known volume of the dsDNA solution (0.0030 M) and monitoring the resulting changes in the absorption and emission spectrum of the AO. After the first addition of stock AO (1 µL) to the system the absorbance intensity of 490 nm peak increased from 0.35 to 0.45, due presents of free unbound AO in the system. Spectral analyses of AO aliquots of 5 µL or less do not exhibit this secondary peak. After increasing the aliquots to 50 µL, the absorbance intensity was decreased due to quenching. (**Fig. 6.10**). Note: after 60 µL of AO, an increase in absorbance intensity was recorded. The

change in the peak position to 490 nm (slight red shift) has been proposed to be indicative of the intercalation of AO to dsDNA.
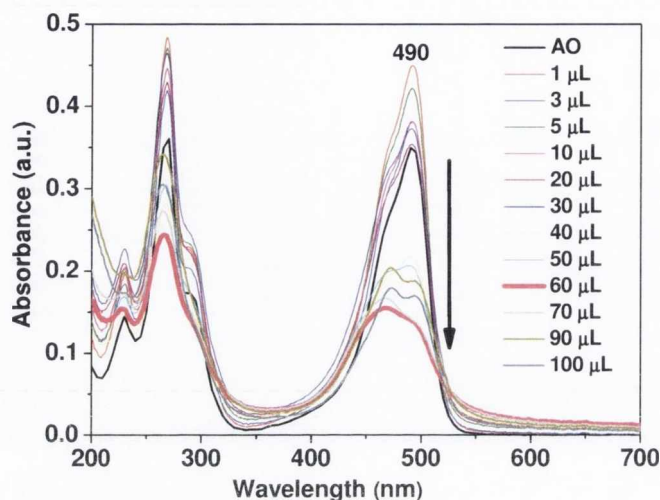
Figure 6.10. Room temperature absorbance spectra of double stranded Herring DNA intercalated with AO. (λ_{ex} = 490 nm. The black curve is original Acridine Orange in phosphate buffer solution and the legend shows the curves as 100 µL of AO solution added.

The growth in shoulder peak at ~470 nm after addition 70 µL of AO could be considered as further evidence for AO molecules intercalation into dsDNA structure. **Fig. 6.11** shows the change in emission spectra after addition of AO. As the AO intercalation started an increased in fluorescence intensity was observed due to formation of the luminescent species (magnetic luminescent nanocomposites).
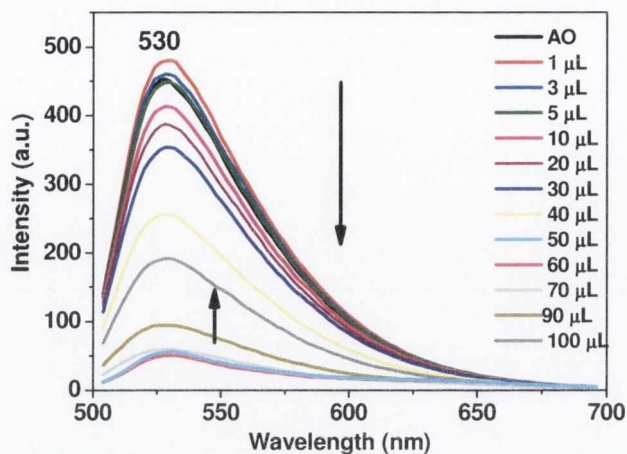
Figure 6.11. Room temperature emission spectra of double stranded Herring DNA intercalated with AO. (λ_{ex} = 490 nm). The black curve is original Acridine Orange in phosphate buffer solution and the legend shows the curves as 100 µL of AO solution added.

6.5. AO titration of double stranded herring sperm DNA coated magnetite nanoparticles

Using the same optical titration procedure Fe_3O_4-dsDNA nanocomposites was titrated with AO in buffer solution. The changes of optical properties in the absorbance spectra of Fe_3O_4-dsDNA nanocomposites (**sample 8**) were recorded. Absorption maxima were slightly broadened and red-shifted compared with free AO (see **Fig. 6.12**). Red shift about 4 nm was observed in the room temperature emission spectra (see **Fig. 6.13**) after 8 µL of AO solution was added. This suggested AO intercalation onto the surface of Fe_3O_4-dsDNA nanocomposites. Alternatively, when AO molecules intercalate into dsDNA enhancement of fluorescence was recorded due to the binding of AO to base pairs of dsDNA.
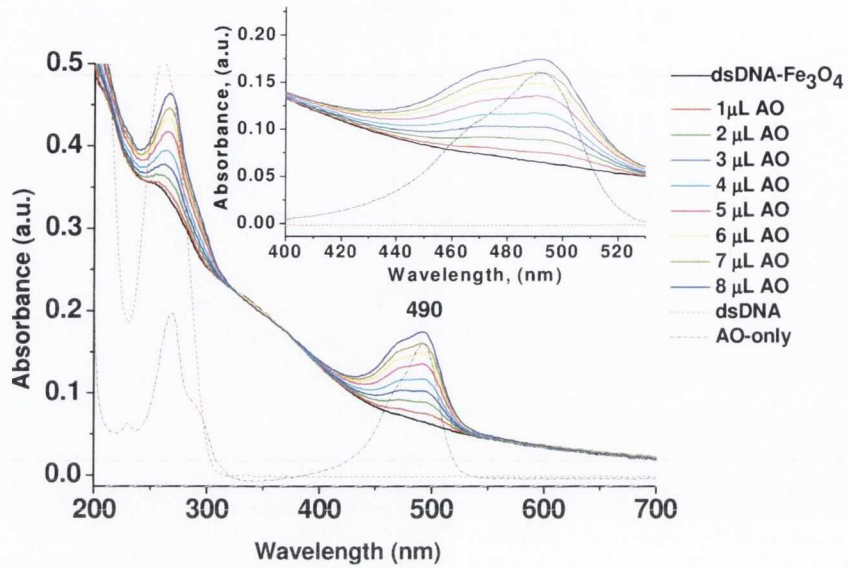
Figure 6.12. Room temperature absorbance spectra Fe₃O₄-dsDNA nanocomposite intercalated with AO (**Sample 8**). (λ_{ex}= 490 nm). Insert shows changes in 480 nm band. The black curve is original Fe₃O₄-dsDNA and the legend shows the curves as 8 µL of AO in phosphate buffer solution added.
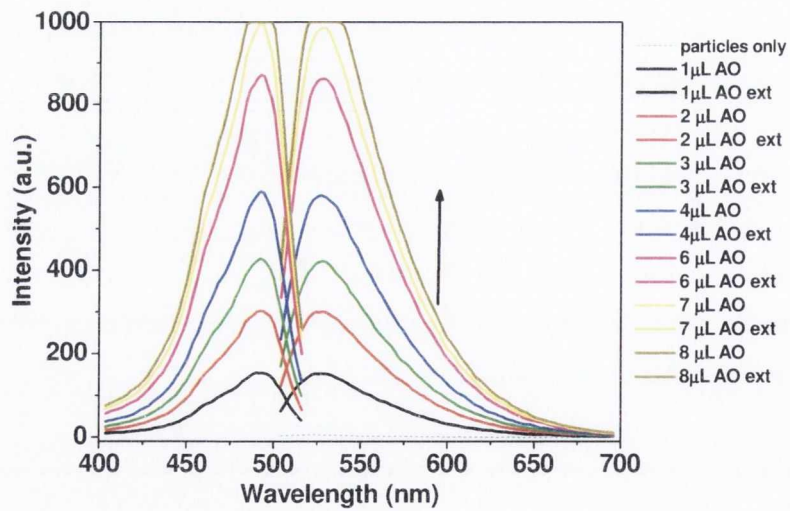

Figure 6.13. Room temperature emission spectra and excitation of Fe₃O₄-dsDNA nanocomposites intercalated with AO (**Sample 8**). (λ_{ex} = 490 nm, (λ_{em} = 527 nm). Dotted curve shows original AO in phosphate buffer solution. The legend shows the curves as 8 µL of AO in phosphate buffer solution added.

TEM analysis showed no changes in an average particle size of 8.9 ± 1.9 nm (see **Fig. 6.14 1, 2)**). In the presence of an external 0.5 T parallel magnetic field the formation of arranged chain-like nanostuctures was observed (**Fig. 6.15 1, 2**).
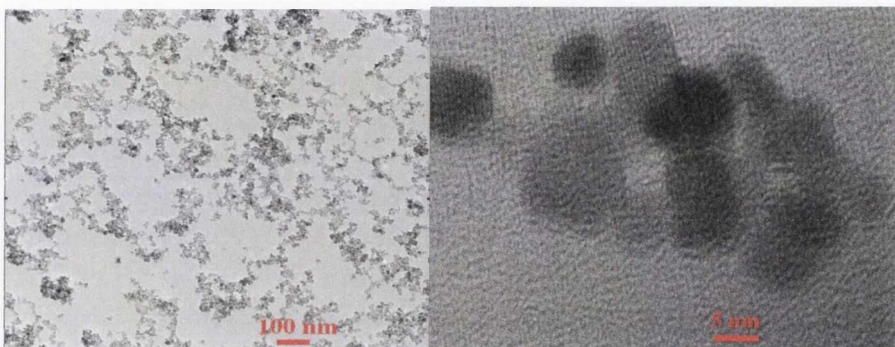
Figure 6.14. TEM images of Fe_3O_4-ssDNA-AO nanocomposites (**Sample 8**). 1) and 2) Without external magnetic field.
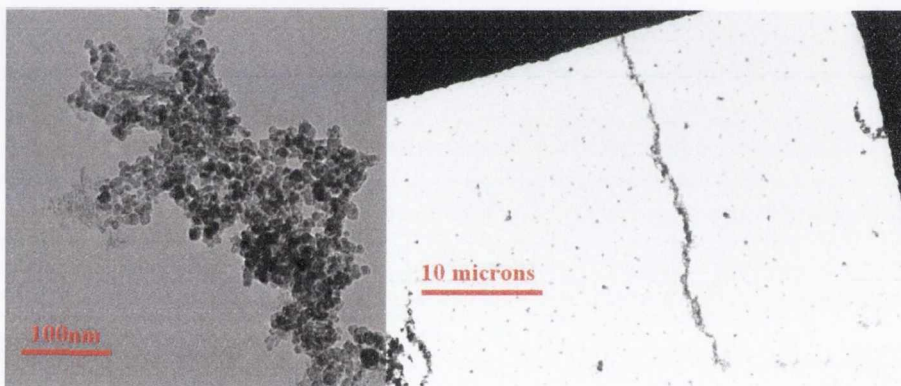
Figure 6.15. TEM images of Fe_3O_4-ssDNA-AO nanocomposites (**Sample 8**). 1) and 2) in 0.5 T external parallel magnetic field.

6.6. Confocal microscopy studies of Fe_3O_4-dsDNA-AO nanocomposites

To support our findings confocal microscopy studies of AO intercalated Fe_3O_4-dsDNA nanocomposites were performed. 400 µL of the sample was placed onto a glass slide and placed into an external 0.5 T parallel magnetic field over night. Confocal micrograph images of Fe_3O_4-dsDNA-AO nanocomposites are shown in **Fig. 6.16**. This observation demonstrates that the final product of this synthesis is both magnetic and fluorescent and certainly contains AO species. When AO intercalates as occurs with dsDNA it has an emission at $\lambda_{max} = 530$ nm [25]. **Fig. 6.16** shows clear evidence of presence of fluorescence dye AO on the surface of magnetic

nanocomposites. The results showed the formation of arranged linear nanoassemblies (average length 27.5 microns) under an external 0.5 T parallel magnetic field. The results derived from UV-vis spectroscopy and cofocal measurements are consistent with each other. Thus, AO molecules intercalate into dsDNA strands staining linear magnetic nanoassemblies a bright green colour.
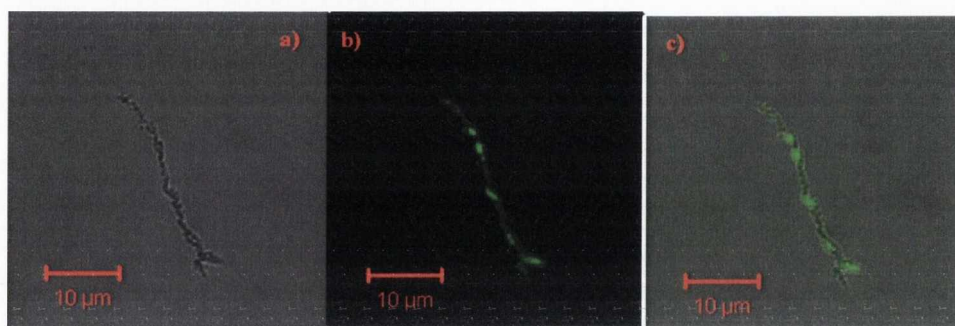
Figure 6.16. a) Transmitted light microscopic image of the Fe_3O_4-dsDNA-AO nanocomposites interacting with AO. Remaining Fe_3O_4-dsDNA particles are seen as black-brown linear assemblies in transmitted light. (b, c) Corresponding fluorescent images of the same microscopic field taken one after another. Ext 488 nm. **Sample 8** in external parallel 0.5 T magnetic field.

It should also be noted that according to PCS measurements the hydrodynamic average particle size of Fe_3O_4-dsDNA-AO nanocomposites was 100 nm (PDI 0.201) (see **Appendix 9**). These results showed great potential for biomedical applications as larger particles have a shorter half-life in the blood stream, being efficiently removed by the immune system.

Taken together the above spectroscopic and microscopy findings, we believe these results suggest new quick in situ synthetic approach for the preparation magnetic luminescent nanocomposites. More experiments are underway to develop and investigate new physical and chemical properties of these nanocomposites.

6.7. Conclusions

• Thus, new "two-in-one" magnetic luminescent nanocomposites were successfully prepared. Water-soluble herring sperm DNA indeed stimulates formation of stable magnetic fluids, which contain magnetic chain-like assemblies of magnetite-DNA nanoparticles.

- Studies of the interaction between DNA-magnetite nanocomposites and Acridine Orange dye have shown intercalation of Acridine and enhancement of the luminescence in the case of double stranded DNA samples.

- Confocal microscopy studies suggest that the final product of exhibit magnetic and luminescent properties. By contrast, denatured (single stranded) DNA magnetite nanocomposites have shown no intercalation and did not result in the formation of fluorescent-magnetic nanocomposites.

- TEM and PCS measurements of stable magnetic fluids showed that DNA coated iron oxide nanoparticles might be suitable candidates for NMRD studies and might in future for MRI applications.

We believe that these new fluorescent-magnetic nanocomposites can be potentially utilised as probes for *in vitro* and *in vivo* biological imaging.

6.8. References

1.   N.C. Seeman, *Nature*, (2003), 421, 427.

2.   S.J. Byrne, S.A. Corr, Y. K. Gun'ko, J. M. Kelly, D. F. Brougham, S. Ghosh, *Chemical Communications.*, (2004), 2560-2561.

3.   R.W. Armstrong, U.P. Strauss, T. Kurucsev., *Journal of the American Chemical Society.*, (1970), 92, 3174.

4.   a) S. Neidle, M. Waring., *Molecular Aspects of Anticancer Drug-DNA Interactions*; (1993); Vol. 1 and 2; b) M. D'incalci, C. Sessa., *Expert Opinion* on *Investigational Drugs.*, (1997), 6, 875.

5.   E. Kimura, T. Ikeda, M. Shionoya., *Pure and Applied Chemistry.*, 69, (1997), 2187.

6.   H. Du, RA. Fuh, J. Li, A. Corkan, J.S. Lindsey., *Photochemistry and Photobiology.*, 68, (1998), 141-142.

7.   L.C. Lim, Y.F. Liu, K. Schell, S.D Lovrich, S.M Callister, and R.F Schell., *Clinical and Diagnostic Laboratory Immunology.*, 1, (1994), 44–50.

8.   R.M. Acheson, A. Weissberger, E.C. Taylor., Acridines. The Chemistry of Heterocyclic Compounds, Interscience Publishers Inc, New York, (1956).

9.   E. Gurr., Synthetic dyes in biology, medicine and chemistry. Academic Press, London, England. (1971).

10.   V.K. Sharma, P.D. Sahare, R.C. Rastogi, S.K. Ghoshal and D. Mohan., *Spectrochimica Acta Part A.*, 59, (2003), 1799-/1804.

11.   M. B. Lyles, I.L. Cameron., *Biophysical Chemistry.*, 96, (2002), 53–76.

12.   F. Lauretti, F.L. de Melo, F.J. Benati, E. de Mello Volotao, N. Santos, R.E. Linhares, C.J. Nozawa., *Journal of Virological Methods.*, 114, (2003), 29-35.

13.   G.P. Moloney, D.P. Kelly, P. Mack., *Molecules.*, 6 (3), (2001), 230-243.

14.   M. Gong, T. Han, C. Cai, T. Lu, J. Du., *Journal of Electroanalytical Chemistry.*, 623, (2008), 8–14.

15.   S. Corr. New magnetic nanocomposite materials. Thesis for degree of Doctor of Philosophy. University of Dublin. Trinity College, (2006).

16.   Y. Qu, H. Yang, N. Yang, Y. Fan, H. Zhu, G. Zou., *Materials Letters.*, 60, (2006), 3548–3552.

17.   M. Mandal, S. Kundu, S.K. Ghosh, S. Panigrahi, T.K. Sau, S.M. Yusuf, T. Pal., *Journal of Colloid and Interface Science.*, 286, (2005), 187–194.

18.   O.N. Shebanova and P. Lazor., *Journal of Solid State Chemistry*, 174, (2003), 424–430.

19.   J. Dunnwald and A. Otto., *Corrosion Science.*, 29, (1989), 1167–1176.

20.   Y.B. Khollam, S.R. Dhage, H.S. Potdar, S.B. Deshpande, P.P. Bakare, S.D. Kulkarni, S.K. Date., *Materials Letters.*, 56, (2002), 571–577.

21.   K. Landfester and L.P. Ramirez., *Journal of Physics: Condensed Matter.*, 5, (2003), 1345.

22.   J. Popplewell and L. Sakhnini., *Journal of Magnetism and Magnetic Materials.*, 149, (1995), 72.

23.   K.E. Kellar, D.K. Fujii, W.H.H. Gunther, K. Briley-Sab, A. Bjornerud, M. Spiller, and S.H. Koenig., *Journal of Magnetic Resonance Imaging.*, 11, (2000), 488–494.

24.   H. Robinson, A. Loffler and G. Schawrz., *Journal of the Chemical Society, Faraday Transactions 1.*, (1972), 56.

25.   R.P. Haugland., *Methods Cell Biology B.*, 42, (1994), 641–663.

Chapter 7

7.1. Conclusions and Future Work

7.1.1. Conclusions

We have prepared and investigated a number of new magnetic nanocomposite materials, which are expected to find a range of potential applications.

In situ co-precipitation technique is a very convenient method for the preparation of various DNA and polyelectrolyte stabilised magnetite and cobalt ferrite nanocomposites. This method has several advantages over other existing procedures: it is a quick, inexpensive, one step experiment, which is reproducible and whose parameters can be varied to produce various magnetic fluids. We have also demonstrated that by choosing appropriate iron and polyelectrolyte concentrations and ratios, we potentially can tune the nanoparticle size, their aggregation as well as their magnetic properties and relaxivities.

It was found that the higher concentration of DNA and polyelectrolyte results in formation of smaller primary particles. This can be explained by polyelectrolyte coating, which stabilises the nanoparticles and prevents their further growth. However, it was found that excessive DNA and polyelectrolyte could also cause aggregation of the nanoparticles via their cross-linking.

It was found that PSSS coated magnetite nanoparticles showed great potential as magnetic templates for the fabrication "two-in-one" magnetic luminescent nanocomposites by the LbL approach. We have demonstrated that various CdTe QDs coated with a stabiliser (PAH) could be linked to the surface of the multilayer-polyelectrolyte coated magnetite nanoparticles and as a result produce stable magnetic-luminescent magnetite-QD nanocomposites. In this case controlled thickness multilayer polyelectrolyte coating prevents quenching of quantum dot luminescence by magnetic core.

We have also developed a similar LbL approach for the synthesis of new "two-in-one" magnetic luminescent nanocomposites using polyelectrolyte stabilised magnetite and cobalt ferrite nanoparticles as a magnetic core and Rhodamine B as a the luminescent component. We have demonstrated that the Fe_3O_4-PSSS_PAH/PE_{10}-RhB

nanocomposites, showed the best stability and good luminescent properties. However, similar CoFe$_2$O$_4$-based nanocomposites were not very stable and had only a very weak luminescence, which was not sufficient for their further biological testing. All attempts to deposit an extra protective polyelectrolyte layer on the top of the luminescent layer resulted in quenching of the luminescence and aggregation of the nanocomposites. We have demonstrated that Fe$_3$O$_4$-/PE-RhB nanocomposites can be effectively manipulated using an external magnetic field and simultaneously detected by their fluorescence. Our investigation of the stability of these nanocomposites in an aqueous solution showed no release of Rhodamine B for the first three days following fabrication. However, almost all Rhodamine B was released after 7 days. This nanostructure degradation with dye release gives potential opportunities for their utilisation as subcellular imaging contrast agents or as targeted drug delivery systems. In fact our biological studies in glial cell cultures have demonstrated an excellent cellular internalisation and proved the potential of Fe$_3$O$_4$-/PE-RhB composites as effective cell labelling agents.

Finally we have demonstrated that new fluorescent magnetic nanocomposites can also be produced by intercalation of Acridine Orange into DNA in magnetite - DNA nanocomposites. The intercalation studies have demonstrated that the double stranded DNA structure is not compromised during the preparation and readily intercalates with Acridine orange to provide magnetic-fluorescent nanocomposites. Strong quenching of the fluorescence for the single stranded DNA-magnetite nanocomposites was observed. This is because, since the double helix is no longer intact, the Acridine orange can only electrostatically bind to the DNA, leaving it more open to quenching by the magnetic particles. This is an exciting outcome as these nanocomposites could provide a new method for biological imaging, medical diagnostic and therapy.

In conclusion, we believe that our work will contribute to the further development of nanotechnology applications in biomedical research.

7.2. Future work

Future work will include further research and development on magnetic nanowires, magnetic-fluorescent nanocomposites and also magnetic nanoparticle-drug conjugates for various biological applications.

7.2.1. Development of new magnetite- or cobalt ferrite-based polyelectrolyte nanocomposites

The successful utilisation of PSSS and PAH as stabilisers for the formation of water stable magnetic fluids has been encouraging. Future work will involve the development of similar types of nanocomposites using a variety of commercially available polyelectrolytes such as poly (diallyldimethylammonium chloride) and polyethylenimine. We expect that many of these materials will give stable magnetic fluids with high relaxivities, which can be investigated by NMRD. Of course the biological behaviour and toxicity of these new materials must be studied prior to their further applications. New magnetic fluids of these nanocomposites with high relaxivities and good biocompatibility can be potentially utilised as contrast agents for *in vivo* MRI diagnostics.

7.2.2. DNA modified nanoparticles and intercalation studies

Our initial intercalation studies using Acridine Orange have shown that the dye can effectively intercalate into double stranded DNA-magnetite nanocomposites. In future work we plan to use other intercalates such as thiazole orange (e.g. TOTO), or oxazole yellow (e.g. YOYO) derivatives and ruthenium - (diethoxyphosphorylmethyl)dipyrido[3,2-a:2',3'-c] phenazine (dppz) complexes (e.g. [Ru(phen)$_2$dppz]Cl$_2$) to produce new fluorescent DNA functionalised magnetic nanowires. These nanowires then can be manipulated by an external magnetic field that would allow us to build new fluorescent –magnetic nanostructures with potential chemo- and bio-sensing properties.

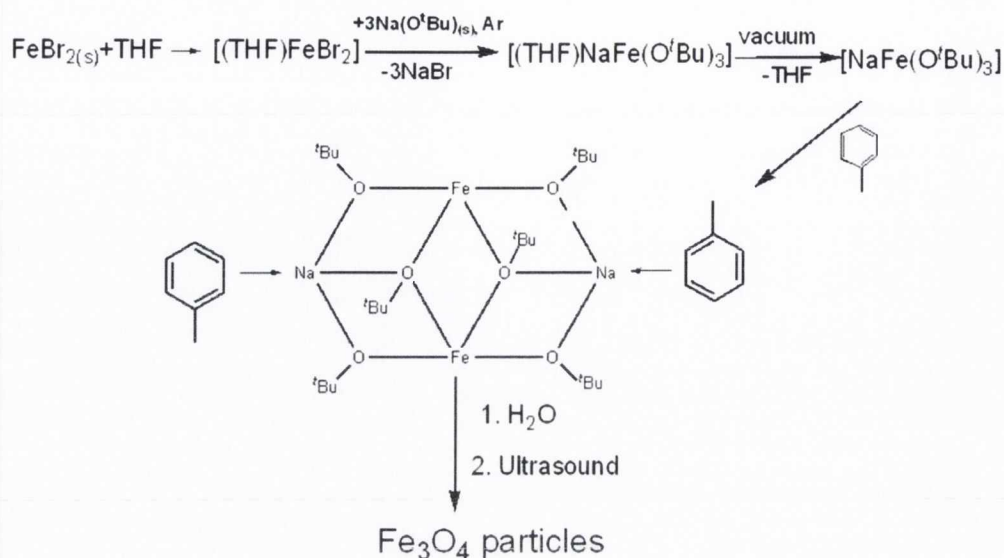### 7.2.3. Drug-functionalised magnetic nanoparticles

It has been demonstrated in this work that magnetic nanoparticles have some attractive potential applications, including conjugation with drugs to provide targeted drug delivery. Current chemotherapies have major disadvantages in that they are relatively non-specific and lead to negative side effects, where the active drug attacks normal healthy cells. The use of magnetic nanoparticles as drug carriers could provide a site-specific drug delivery system where an external magnetic field could be used to concentrate the bound drug to the target site. We plan to utilise our LbL approach to produce magnetic nanoparticles- polyelectrolyte –drug nanocomposites. In these can

173

we plan to coat magnetic core by alternating polyelectrolyte layers of opposite charge (e.g. PSSS /PAH). Then charged possibly fluorescent drug molecules will be incorporated into the top layer. The stability of the nanocomposites and potential drug release will be studied by spectroscopic techniques (UV-vis and PL). These strategies can be used to develop the nanocomposite containing anti-inflammatory (aspirin), pro-apoptotic (e.g. cardiolipin) and anti-proliferative (e.g. doxorubicin hydrochloride) agents. These potentially bioactive magnetic nanoparticle-polyelectrolyte-drug nanocomposites will be investigated in various cell cultures to fully understand their transport mechanism and biological properties. It is expected that our approach would open up new possibilities in the administration of biologically active molecules and their targeted delivery to sites of disease may be achieved.

7.2.4. Hollow magnetic nanostructures for medical diagnostics and drug delivery

The aim of this work will be to develop new hollow magnetic iron oxide nanostructures with a broad range of potential applications. We plan to use metallorganic $[Fe(OBut)_2(THF)]_2$ [1, 2] and $[NaFe(BuO^t)_3]_2$ [3] precursors and controlled hydrolysis. To demonstrate the feasibility of our approach we have performed some preliminary studies using the $[NaFe(O^tBu)_3]_2$ precursor. A schematic description of Fe_3O_4 synthesis procedure from single-source metallorganic precursor is presented in **Scheme 7.1**. Metallorganic precursor $[NaFe(O^tBu)_3]_2$ was prepared according using $FeCl_2$ and $Na(O^tBu)$ in a molar 1:3 ratio (see **Scheme 7.1**). Then the required amount of $[NaFe(O^tBu)_3]_2$ dissolved in dry toluene and hydrolysed using small controlled volumes of distilled water (0.1 mL, 0.2 mL) under ultrasonication for 30 minutes at 50 °C. Two other samples were prepared using the same method, but water was mixed with 10 mL of dry ethanol, and the this EtOH-water mixture was injected in reaction mixture of toluene-$[NaFe(O^tBu)_3]_2$. The preliminary characterisation of the obtained products was performed by TEM microscopy and Raman spectroscopy.

$$FeBr_{2(s)} + THF \longrightarrow [(THF)FeBr_2] \xrightarrow[-3NaBr]{+3Na(O^tBu)_{(s)}, Ar} [(THF)NaFe(O^tBu)_3] \xrightarrow[-THF]{vacuum} [NaFe(O^tBu)_3]$$

1. H_2O

2. Ultrasound

Fe_3O_4 particles

**Figure 7.1.** Schematic description of Fe_3O_4 synthesis from metallorganic precursor.

Summarised experimental data of different morphologies of iron oxide synthesized using ultrasonication method from single-source $[NaFe(O^tBu)_3]_2$ metallorganic precursor are given in the **Table 7.1**.

Table 7.1. Summarised experimental data of properties of different morphologies iron oxide nanomaterials synthesised using single-source metallorganic precursor.

Sample	Toluene volume (mL)	Volume of water (mL)	Synthesis time (min)	Temperature (°C)	Morphology	Average size (nm)
1	20	0.1	30	50	nanorings	78± 15
2	20	0.2	30	50	nanorings	187± 43
3	20	0.1+EtOH	30	50	nanocubes	56 ± 6
4	20	0.2+EtOH	30	50	nanocubes	173± 64

TEM images of the iron oxide nanomaterials are presented in **Fig. 7.2.** It should be noticed that with absence of a stabilising agent, no any clustering or aggregation was observed. Images showed that various shaped (nanorings or nanocubes, nanosquares) nanocrystalline iron oxide particles are well distributed across the TEM grid.

The formation of the hollow structures can be explained most likely by the Kirkendall Effect, in which the mutual diffusion rates of two components in a diffusion couple differ by a considerable amount. In this case the hydrolysis is taking place at the toluene-water interface, where ultra small droplets of water hydrolyse the metallorganic $[NaFe(O^tBu)_3]_2$ precursor resulting in the formation of hollow nanostructures for the **sample 1, 2.** The addition of ethanol obviously has an effect on the toluene-water interface that affects the diffusion of the reagents and the mechanism of hydrolysis. As a result the morphology of the nanoparticles is different and results in the formation of nanocubes.
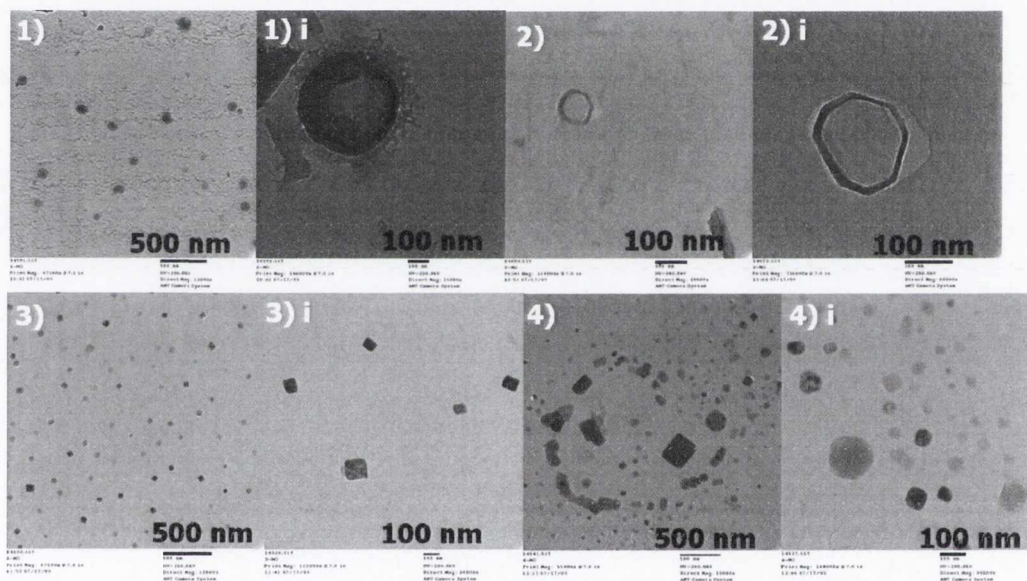
Figure 7.2. TEM images of different morphologies of iron oxide nanomaterials produced from single-source metallorganic precursor. 1) **1 sample**, 0.1 mL water, 2) **2 sample**, 0.2 mL water 3) **3 sample**, 0.1 mL+EtOH, 4) **4 sample**, 0.2 mL+EtOH, i) samples at the higher magnification.

The samples were left for a period of 3 weeks and investigated by TEM again (**Fig. 7.3**). Dramatically changes in original morphology were observed for both samples. After period of 3 weeks **Sample 2, 4** changes in the shape and morphology from nanocubes (100-240 nm varied depending on the sample) to hollow spheres (core-shell structures) with the average diameter of 120 ±19 nm for **Sample 2**, 166 ±60 nm for Sample 4. It should be noted that TEM images of the single nanosphere (**Fig. 7.3. 1 (i), 2 (i)**) show a reduced electron density of the spheres (compared to the

previous results, see **Fig. 7.2**), suggesting that hollow nanoparticles were synthesized. Quit uniform wall thickness of spheres with average 17 ±2 nm is estimated by TEM (from the darker area around the perimeter of the hollow sphere) for **Sample 2**. For the **Sample 4** non-uniform wall thickness of spheres could be clearly seen **Fig.7.3. 2i**).
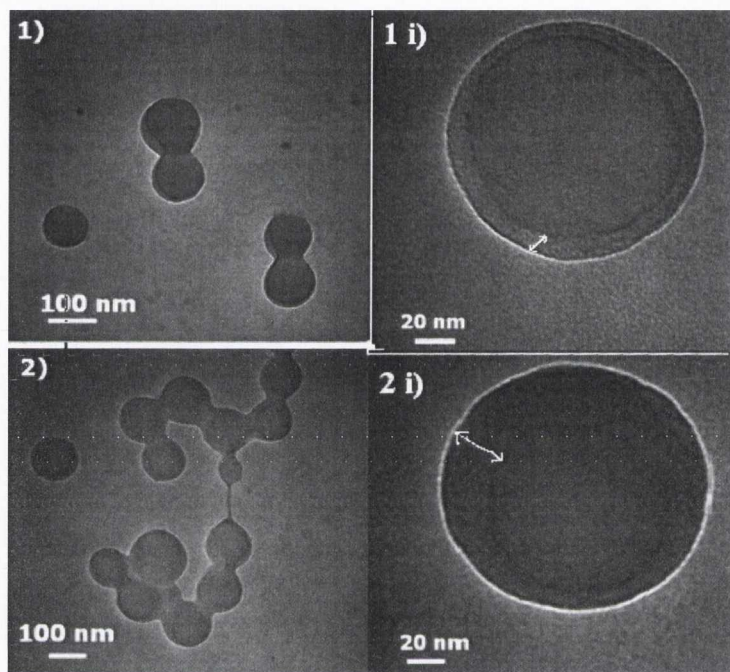

Figure 7.3. TEM image of selected iron oxide nanomaterials produced from single-source metallorganic precursor after 3 weeks. 1) **Sample 2**, 2) **Sample 4**, i) Corresponding images for the same samples under higher magnification.

The detailed mechanism of the formation of these nanoparticles is currently unclear and will require further investigations. Further work will also include the optimisation of the synthesis to prepare hollow magnetite nanospheres with narrow size distribution. We believe that these hollow magnetic nanoparticles could potentially serve as smart contrast agents and drug carriers.

7.3. References:

1. Y.K. Gun'ko, U. Cristmann, and V.G. Kessler., *European Journal of Inorganic Chemistry.,* (2002), 1029-1031.

2. G.B. Biddlecombe, Y. K. Gun'ko, J.M. Kelly, S.C. Pillai, J.M.D. Coey, M. Venkatesan and A.P. Douvalis., *Journal of Materials Chemistry.,* 11, (2001), 2937–2939.

3. S.A. Corr, Y.K. Gun'ko, A.P. Douvalis, M.Venkatesan, and R.D. Gunning., *Journal of Materials Chemistry.,* 14, (2004), 944–946.
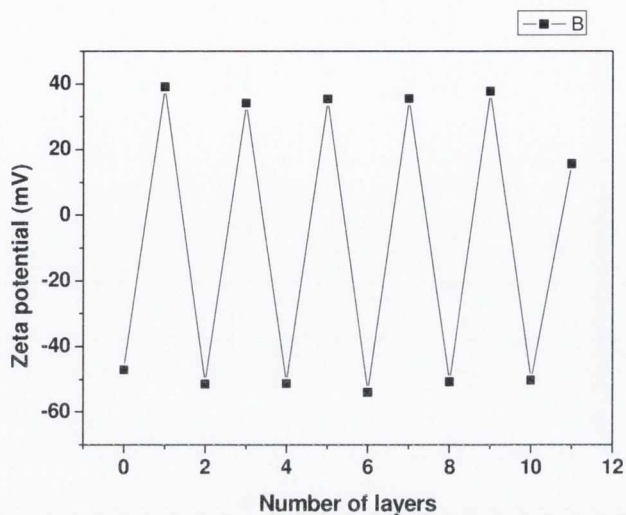
Chapter 8 Appendices
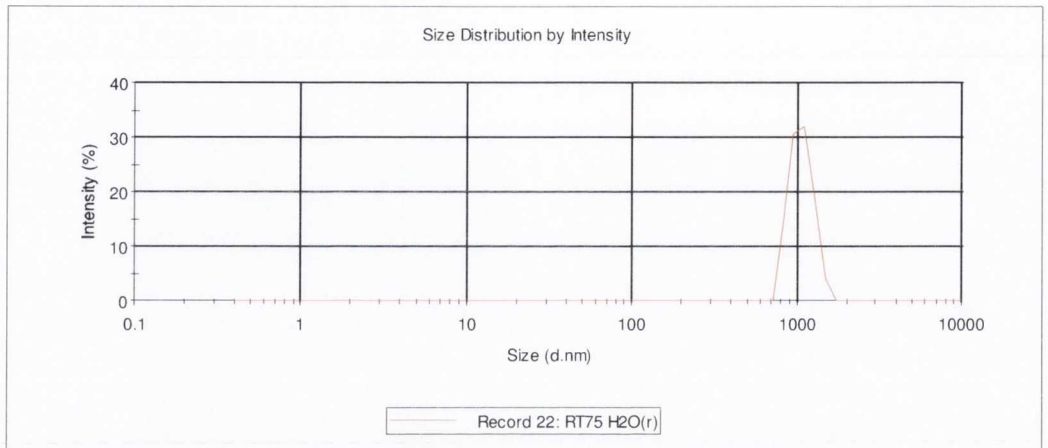
Appendix 1. Hydrodynamic radius of size distributions of cobalt ferrite-DNA composites in Millipore water (a) pure cobalt ferrite particles.
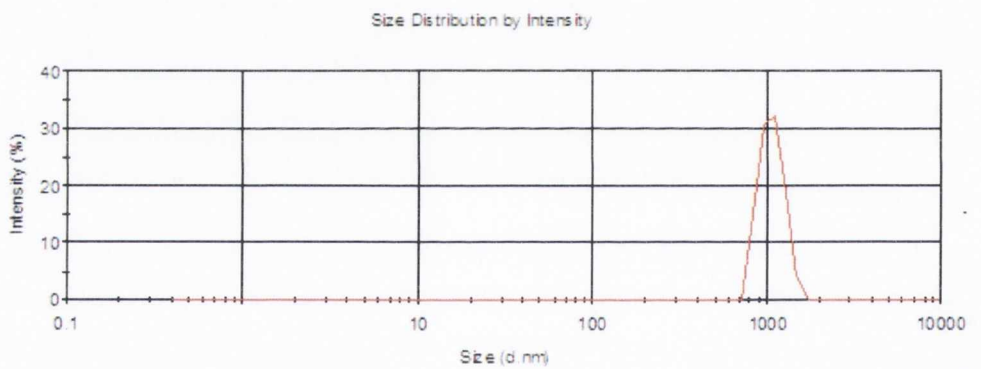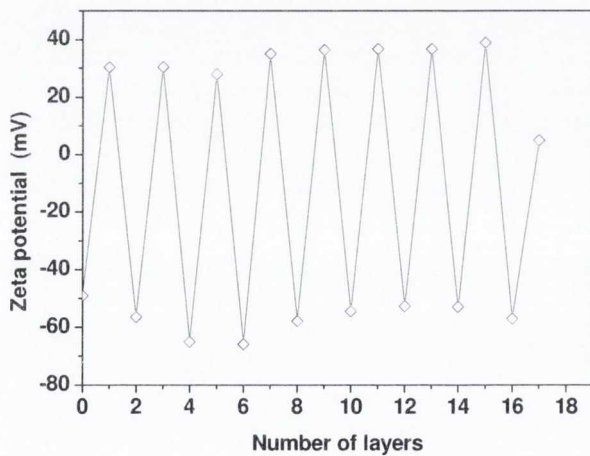

Appendix 2. Hydrodynamic radius of size distributions of cobalt ferrite-DNA composites in Millipore water: **RT51** sample (0.06 g DNA).
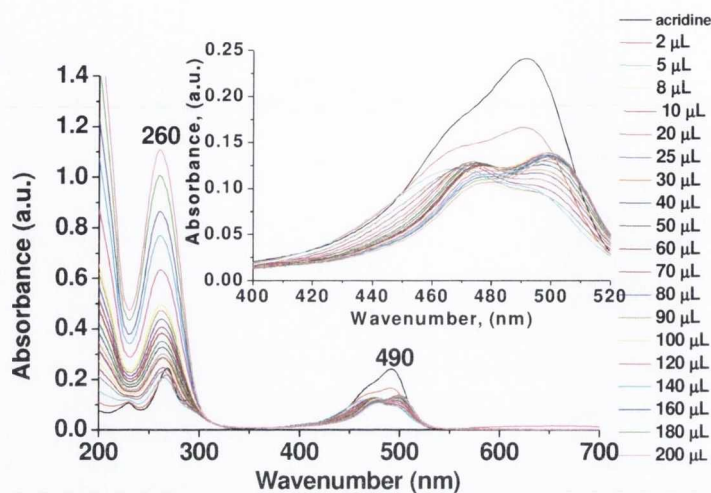
Appendix 3. Zeta potential of the negatively charged Fe_3O_4-PSSS coated PAH/PE_{11} nanoparticles as a function of polyelectrolyte layers numbers for PAH/PSSS coatings.


Appendix 4. Zeta potential of the negatively charged $CoFe_2O_4$-PSSS coated PAH/PE_{17} nanoparticles as a function of polyelectrolyte layers numbers for PAH/PSSS coatings.

Appendix 5. Room temperature absorbance spectra of single stranded Herring DNA intercalated with AO. (λ_{ex} = 490 nm). Insert shows changes in 480 band. The black curve is original Acridine Orange in phosphate buffer solution. and the legend shows the curves as 200 µL of AO solution added.
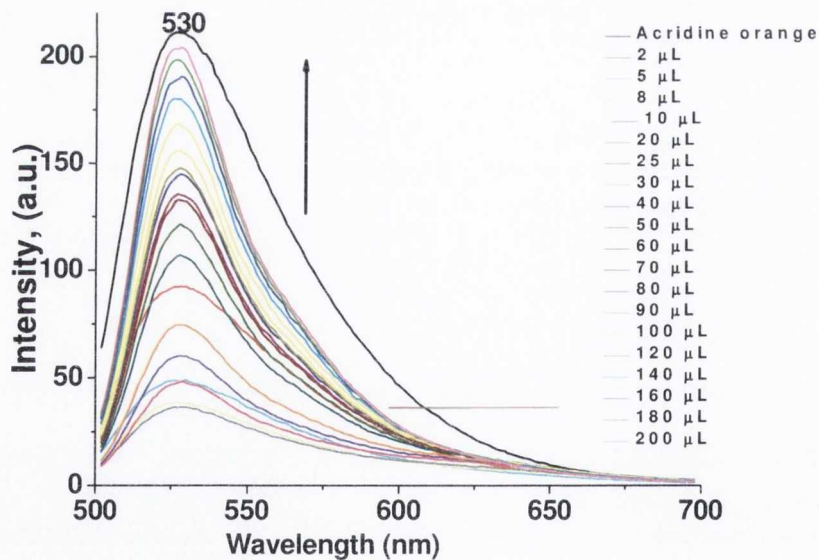
Appendix 6. Room temperature emission spectra of single stranded Herring DNA intercalated with AO. (λ_{ex} = 490 nm). The black curve is original Acridine Orange in phosphate buffer solution. The legend shows the curves as 200 µL of AO solution added.
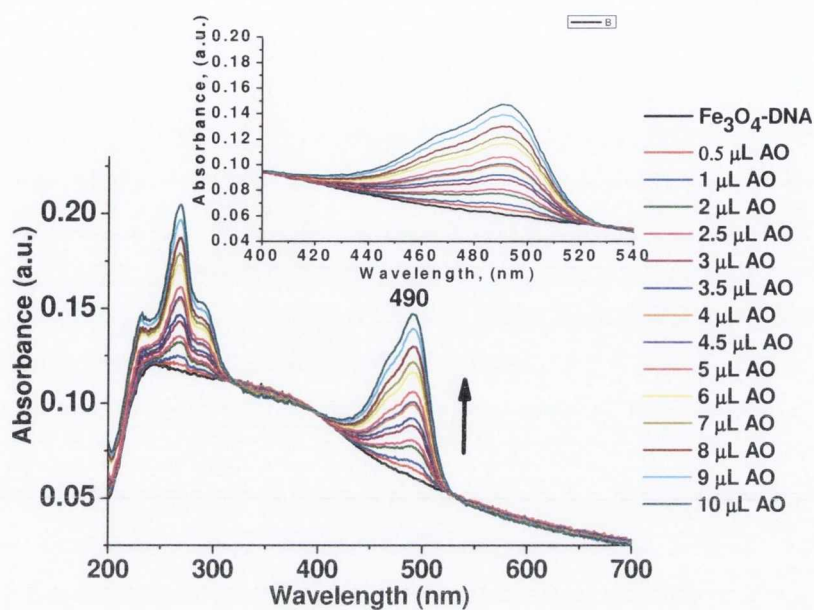
Appendix 7. Room temperature absorbance spectra of Fe_3O_4-ssDNA nanocomposite intercalated with AO (**Sample 7**). (λ_{ex} = 490 nm). Insert shows changes in 480 band. The black curve is original magnetite-dsDNA and the legend shows the curves as 10 µL of AO in phosphate buffer solution added.
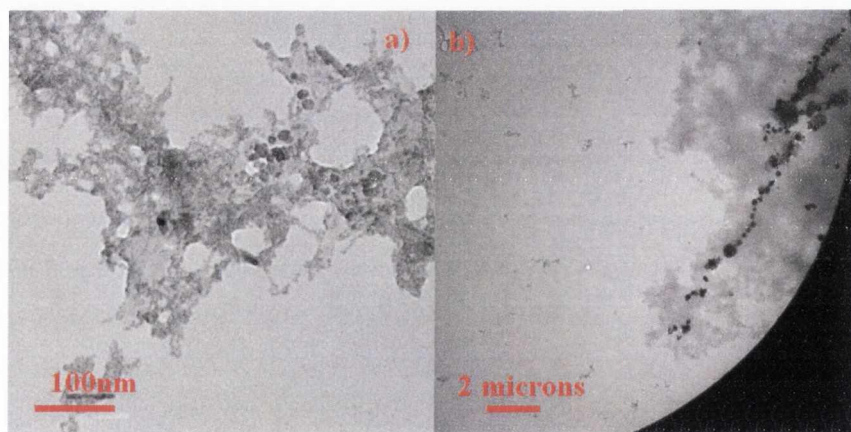
Appendix 8. TEM images of Fe_3O_4-ssDNA-AO nanocomposites (**Sample 7**). a) Without external magnetic field b) in 0.5 T external parallel magnetic field.
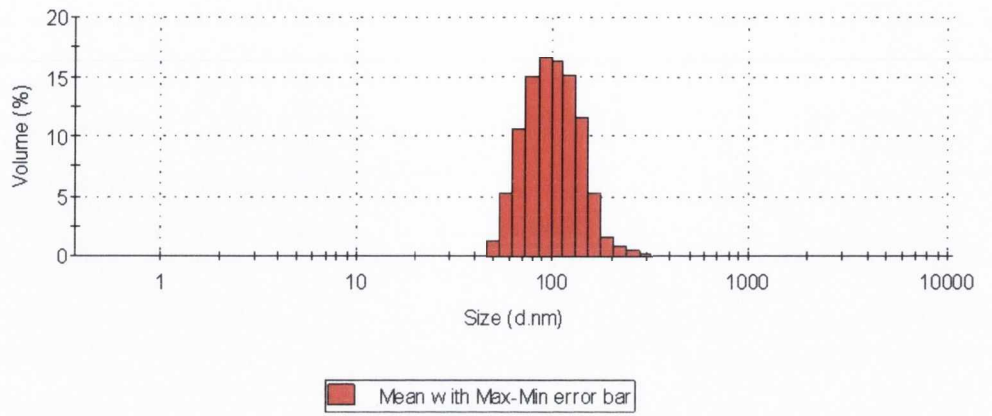
Appendix. 9. Hydrodynamic radius of average particle size distribution in Millipore water.

List of publications:

1. Linear Assemblies of Magnetic Nanoparticles as MRI Contrast Agents

Serena A. Corr, Stephen J. Byrne, Renata Tekoriute, Carla J. Meledandri, Dermot F. Brougham, Marina Lynch, Christian Kerskens, Laurence O'Dwyer, and Yurii K. Gun'ko. *Journal of American Chemical Society.*, 2008, 130 (13), 4214 - 4215.

2. Poly(sodium-4-styrene)sulfonate-Iron Oxide Nanocomposite Dispersions with Controlled Magnetic Resonance Properties

Serena A. Corr, Yurii K. Gun'ko, Renata Tekoriute, Carla J. Meledandri, and Dermot F. Brougham., *Journal of Physical Chemistry C,* 2008, 112, (35), 3324 – 13327.

3. The First Magnetic Nanoparticle-Supported Chiral DMAP Analogue: Highly Enantioselective Acylation and Excellent Recyclability

Oliver Gleeson, Renata Tekoriute, Yurii K. Gun'ko, and Stephen J. Connon. *Chemistry – A European Journal.*, 2009, 15, (23), 669 – 5673.

4. Bimodal magnetic-fluorescent nanostructures for biomedical applications

Joseph J. Gallagher, Renata Tekoriute, Julie-Ann O'Reilly, Christian Kerskens, Yurii K. Gun'ko, and Marina Lynch. *Journal of Materials Chemistry.*, 2009, 19, 4081 – 4084.

5. Precursor and Solvent Effects in the Nonhydrolytic Synthesis of Complex Oxide Nanoparticles for Bioimaging Applications by the Ether Elimination (Bradley) Reaction

Robert Pazik, Renata Tekoriute, Sebastian Hakansson, Rafal Wiglusz, Wieslaw Strek, Gulaim A. Seisenbaeva, Yurii K. Gun'ko, and Vadim G. Kessler. *Chemistry - A European Journal.*, 2009, 15, 6820 – 6826.